THE INTERACTION OF BREAKING SOLITARY WAVES WITH AN ARMORED BED

Thesis by

Catherine M. Petroff

In Partial Fulfillment of the Requirements for the Degree of Doctor of Philosophy

California Institute of Technology

Pasadena, California

1993

(Submitted February 26, 1993)

ACKNOWLEDGEMENTS

The findings presented here are a result not only of the author's original work but of the considerable assistance that was provided to her by the Caltech community and by her family. I would like to extend the warmest thanks to my advisor, Dr. Fredric Raichlen, for directing (and focusing) my research, for answering my questions and challenging me with his questions, for offering suggestions at times of impasse and also for allowing me the latitude to conduct the experiments described here in the manner and pace of my choosing. I also thank Dr. Norman H. Brooks and Dr. John List for their assistance with the concept of turbulent shear and their efforts to make me a competent hydraulicist. My gratitude is extended to Dr. Vito Vanoni for his support and encouragement during his visits to the Keck sub-basement lab and for his ability to put things in their proper perspective.

The actual experiments themselves were completed because of the hard work of several people whom I would particularly like to thank: Rich Eastvedt, for installing, removing, assembling, disassembling, lifting, moving, finding, fixing and keeping a watchful eye on just about everything concerned with the wave tank; Joe Fontana, for machining most of the special equipment involved in the experiments, usually on short notice; Hai Duc Vu, for maintaining calm in times of panic when the switch was flipped and nothing happened; Monica Holboke, for always having the time and inclination to help with some strenuous and very repetitious portions of lab work; Regina Dugan, for keeping flexibility, patience and a sense of humor while sharing the wave tank / flume / tank / flume / tank; and finally Jerry Ramsden, for collaborating with me in bringing the lab into the age of the personal computer, for always maintaining a sense of cooperation, and for standing me as an officemate for five years. I would also like to recognize the contributions of Fran Matzen who facilitated purchasing, travel, and most day-to-day problems (e.g., where are

the transparencies and how do I mail this after 5 p.m.?) and who assisted with the typing of this thesis.

Financial support for the research reported here was provided by the National Science Foundation through Grant No. CTS-8812187. Thanks are also due to the California Institute of Technology for their financial assistance during my period of residence here and to the ARCS Foundation for their support in 1988-1989.

Finally, I would like to thank my husband, Ed Lambert, not only for acting as editor and cheerleader in chief during the writing of this document, but for standing by me with understanding, patience, and encouragement during the time that I have spent as a doctoral student. I would like to dedicate this work to him and to my children, James and Sophie, who have always had the utmost faith in their mother.

February, 1993

Catherine M. Petroff

ABSTRACT

This study investigates the interaction of breaking waves with a bed of loose angular material with a median grain size of 4.8 mm. It is motivated by the engineering problem of determining rock sizes for revetments used as protection for structures in the coastal zone and by the need for an understanding of the mechanics of material movement under waves. Both the effect of the bed on the velocities and accelerations in breaking and non-breaking waves, and the effect of breaking waves on the movement of bed material is measured.

Velocities in breaking waves are measured at elevations approaching the bottom boundary, both for the case of a level bed of graded angular material and for a flat plate at the same location. By changing the water depth and the initial conditions of the incident wave, the relative size of the rock with respect to the breaking wave height is varied. Material movement resulting from the wave passage is measured and compared to the breaking wave height and to the turbulent shear determined near the bed. Using velocity and acceleration records near the rock bed together with observations of rock motion, the mechanics of material movement under waves are investigated.

The roughness elements in the bed are found to have a large effect on both the mean and fluctuating velocities in the wave near the bottom. Evidence is shown of the existence of an inner layer where individual pieces of bed material influence the flow over the bed. A method for determining the maximum mean shear under a single wave is presented. Mean vertical velocities are measured to be not negligible near the bed and are shown to produce convective accelerations of the same order as the accelerations due to turbulent fluctuations.

The movement of bed material is compared with the calculated shear on the bed and with local velocities and accelerations measured very close to the individual rocks. The mean size of the material moved in the bed is found to vary with the amount of shear on the bed. When adjusted for the mean size of the moved material, the calculated shears correspond well with the criterion for critical shear from the Shields curve used in steady flow. From the observed movement of particles during the passage of a wave and the measured velocities and accelerations in the wave, inertial forces are found to contribute to particle movement, especially in the regions before and after wave crest passage.

TABLE OF CONTENTS

LIST OF FIGURES

LIST OF TABLES

LIST OF SYMBOLS

A_p	=	projected area of particle;
a	=	water particle excursion under solitary wave;
C	=	wave celerity, $\sqrt{gh}$;
C_D	=	drag force coefficient;
C_L	=	lift force coefficient;
C_M	=	inertial force coefficient;
D	=	sphere diameter;
D_{50}	=	mean grain size diameter;
D_{90}	=	90th percentile grain size diameter;
D_a, D_b, D_c	=	orthogonal particle cross-sectional diameters;
D_S	=	grain size;
e_i	=	direction of LDV scatter beam;
e_o	=	LDV observation direction;
F_x	=	hydrodynamic force in x direction;
F_y	=	hydrodynamic force in y direction;
f_w	=	wave friction factor;
g	=	acceleration of gravity;
H	=	wave amplitude;
H_b	=	wave amplitude at breaking;
H_p	=	wave amplitude at generation;
h	=	still water depth;
h_b	=	still water depth at breaking location;
h_p	=	still water depth at wave plate;
I(t)	=	output current from photodetectors;
k	=	von Karman constant (=0.4);

k_s = Nikuradse equivalent sand grain roughness;

L = Length of test section (1.5 m);

M_H = overturning moment, equation (1.12);

M_R = restoring moment, equation (1.13);

n = index of refraction of water;

p = pressure;

p_d = dynamic pressure;

p_h = hydrostatic pressure;

q = total water particle velocity;

r = autocorrelation coefficient;

Re = flow Reynolds number, $\frac{u_{max}\, h}{\nu}$;

$S(\omega)$ = amplitude spectral intensity;

S_f = shape factor, $\frac{D_a}{\sqrt{D_b\, D_c}}$;

T = wave period;

t = time;

u = horizontal water particle velocity;

u = mean horizontal velocity component;

u' = turbulent horizontal velocity component;

u_* = shear velocity;

u_i, u_j, u_k = velocity components in orthogonal directions;

u_{max} = maximum horizontal velocity away from boundary layer;

u_o = horizontal velocity at top of boundary layer;

V = volume of particle;

V_s = volume of sample;

v	=	vertical water particle velocity;
v	=	mean vertical velocity component;
v'	=	turbulent vertical velocity component;
v_{max}	=	maximum vertical velocity away from boundary layer;
W	=	weight of particle;
W_s	=	weight of sample;
x	=	distance from upstream edge of test section;
x_b	=	distance from upstream edge of test section to breaking location;
z	=	elevation from bottom surface;
z_m	=	measured elevation from rock bed;
α_m	=	particle shape and orientation coefficient;
η	=	water surface elevation;
ϕ	=	contact angle of particle resting on bed;
γ_s	=	specific gravity of solid (grain);
γ_w	=	specific gravity of water;
λ	=	vacuum wavelength of laser light;
μ	=	viscosity;
ν	=	kinematic viscosity;
$\Delta\upsilon$	=	change in Doppler frequency;
ρ	=	water density;
ρ_s	=	solid (grain) density;
θ	=	Shields parameter;
σ_g	=	standard deviation of grain size distribution;
τ	=	shear stress;
τ_{cr}	=	Shields criterion critical shear stress;

τ_o	=	bed shear stress;
τ_{max}	=	maximum shear; and
ω	=	angular frequency.

INTRODUCTION AND LITERATURE SURVEY

1.1 INTRODUCTION

The protection of coastal structures from erosion often involves the placement of pavements of large rock on the natural sea bed. In the nearshore region, such pavements have been used to armor ocean outfalls and other large pipelines against the effects of extreme waves. Other nearshore structures which could be endangered by bottom erosion are also often protected with blankets of large scale material. The rock armor, when properly sized and placed, prevents the structure from being undermined. If the design of the armor is inadequate, however, erosion caused by large storm waves can result in the differential settlement and, possibly, the failure of the structure. Because velocities near the sea bed in the region of wave breaking are not clearly understood, the engineering design of rock pavements is by necessity quite conservative.

The objective of this study is to investigate the interaction of breaking waves with an armored section of the sea bed under conditions where rocks are moved during the passage of the wave. Because of the size of the material and the breaking wave heights chosen for these experiments, the velocity measurements and material movement observations in this study also apply to the motion of gravel on shingle beaches and to the mechanics of bottom particle motion under waves in general.

1.2 LITERATURE REVIEW

1.2.1 Experimental Investigations

While numerous studies have been made of mobile beds in steady flow, very few experiments are available which directly examine water particle velocities and the consequent movement of bed material under waves. For a steady flow, the initiation of particle motion is usually based on the concept of dimensionless shear as presented by

Shields (1936). Since the major problem of interest for these experiments is often the transport of sediments, accurate velocity measurements near the bed are difficult to obtain using laser Doppler velocimetry because of optical interference from the sediment grains. Hence, relatively few steady flow studies are available for comparison of velocity data near the bed. In studies that address the probability of material movement, Gessler (1965) and Bayazit (1976) have calculated statistical shear stress and velocity distributions, respectively, for steady flows in channels of large relative roughness.

Madsen and Grant (1975) used previously obtained experimental data for a granular bed oscillating in still water to show that Shields' diagram could be applied to oscillatory flows. Using a mobile bed, Rance and Warren (1968) conducted initiation of motion experiments for coarse material exposed to an oscillating flow in a water tunnel. Most of the recent experimental work concerning water particle velocity and shear stress measurements has been conducted in oscillatory water tunnels with the flow being observed over particles firmly attached to a rigid plate.

A number of experimental investigations of the turbulent wave boundary layer are available in the literature. The flow Reynolds numbers, $\frac{u_{max}h}{\nu}$, in the present experiments ranged between 4.7×10^4 and 1.1×10^5. For similar flows with a similar size of rock as the one used in this study, Naheer (1977), Kamphuis (1975) and others have confirmed that the flow is in the fully rough turbulent regime. Since both Sleath (1988) and Justesen (1988) give extensive summaries of recent investigations conducted in this area, only an overview of some of these experiments is presented here.

Early work by Jonsson and Carlsen (1976) using a miniature (5 mm diameter) propeller meter yielded an extensive set of velocity measurements over a triangular roughness element for oscillatory flow in a water tunnel. Kamphuis (1975) conducted

many experiments with different sizes of material in different flow regimes to obtain friction factors for a wide range of wave motion. Kamphuis' experiments employed shear stress measurements for material fixed to a plate and were also carried out in an oscillating water tunnel.

With the increasing use of laser Doppler velocimetry, (LDV), a number of investigators have obtained non-intrusive measurements of oscillatory flow near a rough boundary. Jensen et al. (1989) investigated water particle velocities and turbulence at large Reynolds numbers, while measurements made by Sleath (1987) covered a range of regimes including smooth and transitional wall flows. Sumer et al. (1990) studied the effect on oscillatory water particle velocities of a sudden change in roughness, from a smooth bed to a roughness element of 4.8 mm and noted greatly increased turbulent velocities over the rock when compared to the smooth bed. The LDV measurements were again carried out in a U-shaped water tunnel with a single layer of sand, gravel or pebbles glued to a flat surface. Measurements in oscillatory water tunnels, while able to achieve high Reynolds numbers and insure a fully developed rough turbulent boundary layer, may not accurately model the flow under waves in the open ocean. In the ocean, convective accelerations are present which is not the case in oscillating tunnels. In addition, while in the tunnel vertical velocities are constrained to be small, this is not necessarily the case near the sea bed.

The number of studies with experiments concerning the direct measurement of turbulent water particle velocities and material movement under waves is fairly limited. In experiments carried out in a wave tank, Deigaard et al. (1991) examined the bed shear stress in periodic breaking and non-breaking waves with a hot film probe placed in a smooth constant slope bed. Naheer (1977) derived shear stress measurements for angular material under solitary waves by measuring wave attenuation with distance over an

extensive bed of rock. Within the range of literature references surveyed, the measurements carried out in the present study appear to be unique.

1.2.2 Velocities and Shear Stresses in Waves

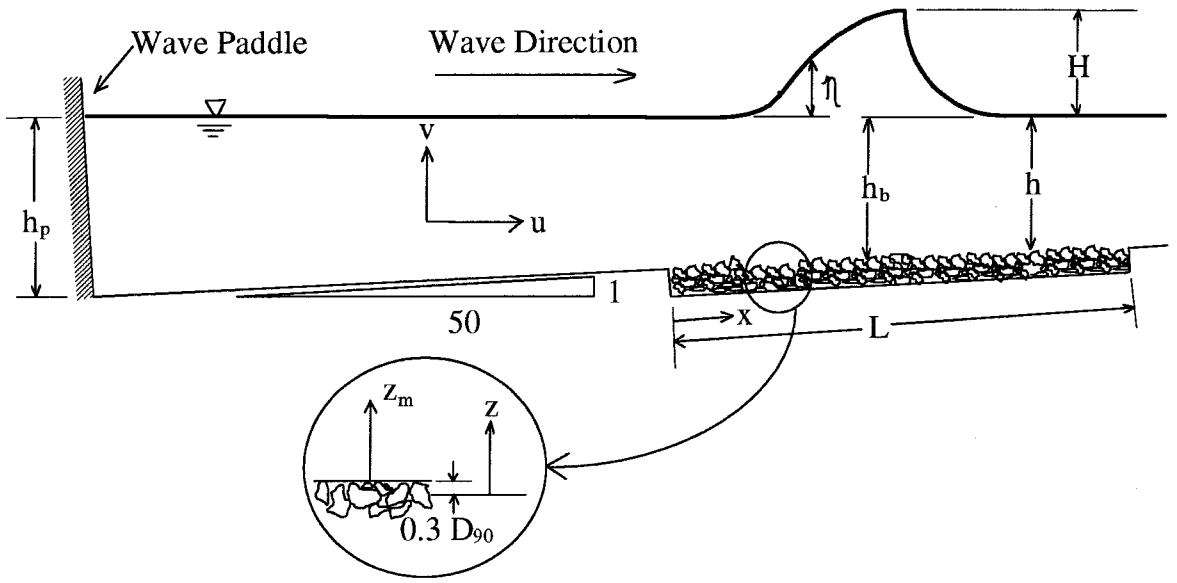

FIG. 1.1. Definition Sketch.

A definition sketch for the experiments in this study is shown in Figure 1.1. The zero level of the bottom boundary was measured as suggested by Kamphuis (1974) in oscillatory flow over a single layer of particles fixed to a plate.

$$z = z_m + 0.3D_{90} \tag{1.1}$$

where z_m is measured from the top of the material, and D_{90} refers to the grain diameter larger than 90 percent of the particles in a grain size distribution. The elevation z is measured from the $0.3D_{90}$ datum of Kamphuis (1974) who estimated a theoretical elevation for the bed calculated by fitting measured velocities to a logarithmic velocity profile. The equation

$$\frac{u - u_{max}}{u_*} = \frac{1}{k} \ln \frac{z}{h}. \tag{1.2}$$

was solved for z using measured velocities and a shear velocity, u_*, computed from the slope of the water surface.

It is expected that for the waves used in this study the amplitude and water particle velocities in the wave at the point of generation are nearly those in a solitary wave. As the wave propagates in the wave tank at a slope of 0.02 m/m (unless otherwise noted), the changing water depth along the length of the tank causes the wave to shoal and eventually to break. For the purposes of discussion, in this study, waves which have not yet reached the breaking point will be referred to as shoaling waves. Waves at and after breaking will be referred to as breaking and broken waves, respectively. Near the bottom boundary, even for the case of a breaking wave, the water particle velocities still retain the general features of solitary waves. For reference, the second order solution of Boussinesq (1872) for the wave amplitude and velocities in a solitary wave is presented below:

Wave Profile:

$$\eta = H\left[\operatorname{sech}\sqrt{\frac{3}{4}\frac{H}{h}}\frac{X}{h}\right]^2 \tag{1.3}$$

where X = x-Ct, and $C = \sqrt{gh\left(1+\frac{H}{h}\right)}$.

Water Particle Velocity, Horizontal Component:

$$\frac{u}{\sqrt{gh}} = \frac{\eta}{h}\left[1 - \frac{1}{4}\frac{\eta}{h} + \frac{h}{3}\left(\frac{h}{\eta}\right)\left(1 - \frac{3}{2}\frac{z^2}{h^2}\right)\frac{d^2\eta}{dX^2}\right] \tag{1.4}$$

Water Particle Velocity, Vertical Component:

$$\frac{v}{\sqrt{gh}} = \frac{-z}{h}\left[\left(1-\frac{1}{2}\frac{\eta}{h}\right)\frac{d\eta}{dX}+\frac{1}{3}h^2\left(1-\frac{1}{2}\frac{z^2}{h^2}\right)\frac{d^3\eta}{dX^3}\right] \tag{1.5}$$

It is noted from the expressions for velocities that the horizontal velocity has a maximum at the wave crest and varies weakly with elevation in proportion to the second derivative of η. The vertical velocity, since it is proportional to the first derivative of η, goes to zero under the wave crest and varies more strongly with elevation. These equations were developed assuming inviscid conditions and hence are only valid for flow outside the bottom boundary layer.

The concept of turbulent shear used in the many investigations of turbulent boundary layers can be developed by introducing fluctuating velocities, $u_i = \bar{u}_i + u_i'$ into the Navier-Stokes equations and taking a time average over a sufficiently long interval such that the term $\overline{u_i'}=0$. This yields:

$$\frac{\partial \overline{u_i}}{\partial t}+\overline{u_j}\frac{\partial \overline{u_i}}{\partial x_j} = -\frac{1}{\rho}\frac{\partial \bar{p}}{\partial x_i}+g_i+\frac{\partial}{\partial x_j}\left(-\overline{u_i' u_j'}\right)+\nu\frac{\partial^2 \overline{u_i}}{\partial x_j \partial x_j} \tag{1.6}$$

where ρ is the fluid density, p is the pressure, and ν is the kinematics viscosity of the fluid. The term including the product of the fluctuating velocities is commonly referred to as the Reynolds stress or the turbulent shear stress.

In derivations of the equations for a two dimensional shear boundary layer by Justesen (1988), Nielsen (1992) and others, Equation 1.5 is generally reduced to the single expression

$$\frac{\partial \bar{u}}{\partial t}+u\frac{\partial \bar{u}}{\partial x}+v\frac{\partial \bar{u}}{\partial y}=-\frac{1}{\rho}\frac{\partial \overline{p_d}}{\partial x}-\frac{\partial \overline{u'^2}}{\partial x}-\frac{\partial \overline{u'v'}}{\partial y}+\nu\left(\frac{\partial^2 \bar{u}}{\partial x^2}+\frac{\partial^2 \bar{u}}{\partial y^2}\right) \qquad (1.7)$$

by assuming that the flow equation for vertical velocities can be discarded for flows with $\bar{u}>>\bar{v}$. It is generally further assumed that the gradient of u in the y-direction is much larger than the gradient in the x-direction, allowing the term $\frac{\partial^2 \bar{u}}{\partial x^2}$ to be ignored. Most investigators make the further assumption that the flow in the boundary layer is essentially horizontal (v = 0), and that convective accelerations may be omitted. This yields the equation

$$\rho\frac{\partial \bar{u}}{\partial t}=-\frac{\partial p}{\partial x}+\frac{\partial \tau}{\partial y}, \qquad \text{where}\ \tau=\mu\frac{\partial \bar{u}}{\partial y}-\rho\overline{u'v'} \qquad (1.8)$$

By evaluating the term $\frac{\partial p}{\partial x}$ at an elevation where τ is zero, the shear stress can then be calculated using

$$\tau=\rho\int_y^{\infty}\frac{\partial\left(\bar{u}_{\infty}-\bar{u}\right)}{\partial t}dy \qquad (1.9)$$

Jonsson, (1975), Sleath (1987) and others have evaluated the shear in an oscillatory flow over a rough boundary using this integral method. Equation 1.9, however, is only applicable when the general Navier-Stokes equation can be linearized as in Equation 1.8.

Nielsen (1992) gives three requirements for the use of the linearized Navier-Stokes equation. First, the vertical flow inside the boundary layer must be negligible. If small

vertical velocities are present near the bed, however, the convective inertia term $\bar{v}\frac{\partial \bar{u}}{\partial y}$ can not be ignored. The second requirement is the horizontal uniformity of the velocity $\bar{u}$ away from the bottom boundary. While this condition for $\bar{u}$ is satisfied in oscillating water tunnels, under real waves, there may be significant convective accelerations. The third criterion is that non-uniformities in the horizontal velocity caused by the individual roughness elements or rock pieces should be restricted to a layer which is considerably thinner than the boundary layer itself. This concept of an inner layer where the shape of individual particles affect the flow velocities is shown graphically in Figure 1.2.

It can be seen that in the inner layer the flow around the individual particles results in substantial convective accelerations. In addition, in this inner layer the definition of the

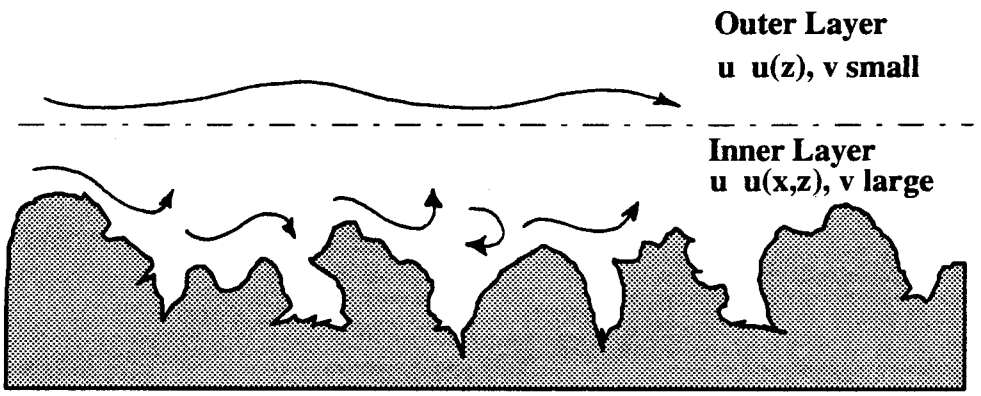

FIG. 1.2. Inner Layer near Rock Bed (After Nielsen (1992)).

mean and fluctuating portions of the instantaneous velocities may not be the same as outside the inner layer and hence the time averages taken for Equation 1.6 may not be applicable.

In general, the flow under ocean waves does not appear to always allow the use of the linearized Navier-Stokes equations. In the present study, shear is evaluated using

direct measurements of the fluctuating velocities u' and v'. In addition, the relative magnitudes of the terms in the Navier-Stokes equation (Equation 1.7) are calculated from the measured flow velocities in the boundary layer. Water particle velocities are measured very close to the bottom boundary in order to observe the characteristics of flow in the inner layer.

1.2.3 Mechanics of Material Movement

The forces acting on a particle resting on the surface of the bed are illustrated in a very simple way in Figure 1.3. Here the particle is shown as an idealized sphere but, in practice, it may be arbitrary in shape.

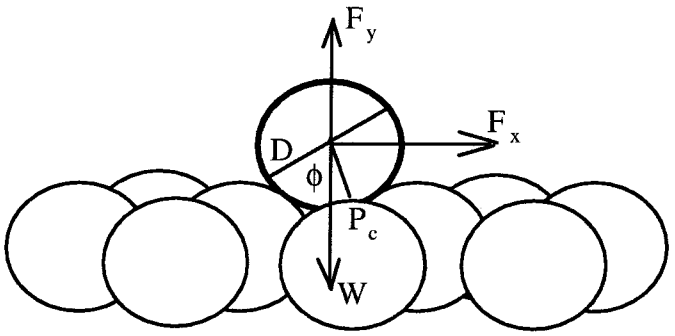

FIG. 1.3. Forces Exerted on a Sphere under Waves.

Here, F_x and F_y are the horizontal and vertical components of the hydraulic force, W is the submerged particle weight, and φ is the contact angle of the particle to the bed. Using the approach developed by O'Brien and Morison (1952) for defining drag, lift and inertial forces acting in concert on the particle, the applied forces can be calculated using:

$$F_x = \frac{1}{2}\rho C_D A_p u^2 + \rho C_m(V)\frac{du}{dt} \qquad (1.10)$$

$$F_y = \frac{1}{2}\rho C_D A_p v^2 + \rho C_m(V)\frac{dv}{dt} + \frac{1}{2}\rho C_L A_p u^2 \qquad (1.11)$$

where ρ is the density of the fluid, A_p is the projected area of the particle in the appropriate flow direction, and V is the volume of the particle. C_D, C_M and C_L are drag, inertia and lift coefficients, respectively, whose values are dependent in the geometry of the particle and on the Reynolds number of the flow. The total moment on the particle is given by the difference between the applied hydrodynamic moment and the restoring moment due to the submerged weight of the particle.

$$\text{Overturning Moment,} \quad M_H = F_x \frac{\alpha_m D}{2}\cos\varphi + F_y \frac{\alpha_m D}{2}\sin\varphi \qquad (1.12)$$

$$\text{Restoring Moment,} \quad M_R = W\frac{\alpha_m D}{2}\sin\varphi \qquad (1.13)$$

Here α_m is a proportionality coefficient which depends on the specific size, shape and position of the particle on the bed. Using velocities and accelerations measured in the immediate vicinity of the rock pieces, this study investigates the relative importance of inertial forces to the particle motion under waves.

1.3 EXPERIMENTAL CONSIDERATIONS

Naheer (1977) notes that as successive waves pass over a bed of angular rocks, the number of rocks moved in the bed decreases by a factor of almost one hundred between the passage of the first and the thirtieth waves. The process where rocks move from their initial locations into a more stable configuration is referred to as the packing of the bed. Part of this study was concerned with evaluating the wave conditions causing movement in a rock pavement for the worst case condition of a single large storm event occurring soon after the initial placement of the rock. For this case, the pavement has not been exposed to waves sufficiently large to cause rock motion and hence is still in its original,

unpacked state. Accordingly, the experiments were carried out on an unpacked bed of material and the material was actively maintained in the unpacked state.

Generally, the placement of rock armor occurs only in the direct vicinity of a protected coastal structure. Prior to passing over the armor, waves travel over the relatively smooth boundary of the sea bed. In the case of the shingle beach, the sorting process which occurs because of smaller fall velocities at smaller grain sizes also results in a relatively smooth sand bed seaward of the shingle. The test section containing the angular material was positioned on the shoreward end of a smooth flat sloping bottom in order to simulate this configuration. In addition, since in practice the thickness of an armor layer is only a few rock diameters deep, the test section was limited to a depth of roughly five rock diameters.

The movement of material under waves is not a uniform process. Vanoni (1964), Sutherland (1966), and others have observed that for turbulent flow over a sand bed, material motion occurs in bursts over small areas of the bed. Although this effect is not as pronounced for the motion of larger material, local variations in the number of particles moved are still readily observable. The rock size for this study was chosen to allow a significant amount of movement under the breaking waves produced in the tank. In this way, the effect on rock motion of different stages in wave breaking and varying breaking wave heights could be measured with a minimal number of repetitions of the same experiment.

The waves used in this study were breaking and non-breaking solitary waves. Solitary waves were chosen for several reasons. The nearshore waves which cause the most damage in storm events are long waves generated at sea, which propagate, transform and break in the nearshore region. In a qualitative sense these waves have shapes similar to solitary waves with wide trough areas and narrow crest regions. At breaking, solitary

waves represent well some of the important characteristics of breaking periodic waves, exhibiting the same plunging jet interaction with the front face of the wave. In addition, the solitary wave is a single positive disturbance propagating into a still undisturbed fluid. Using the wave generation system described in Chapter 2, this type of wave can be reproduced accurately in successive experiments and is well defined by existing wave theories. Since these experiments required many repetitions of identical wave conditions, this accuracy was deemed to be an important factor in the choice of wave type. Since for the solitary wave there is no interaction of incident and reflected waves, the effect of a single wave passing over the rock bed could be measured separately from the effect of return flow. Finally, one technique used in this study required the recording of the material in the bed with a still water surface both before and after the passage of a single wave. The solitary wave was hence an appropriate choice of wave for this method of observing material movement.

CHAPTER 2

EXPERIMENTAL EQUIPMENT AND PROCEDURES

2.1 TILTING WAVE TANK

2.1.1 Tank Characteristics

The experiments in this investigation were conducted in the 40 meter precision tilting flume located in the W.M. Keck Hydraulics Laboratory. The construction and assembly of the flume, shown schematically in Figure 2.1, are detailed by Vanoni et al. (1967). The flume was modified for use as a wave tank by the installation of a piston type wave generator at one end. The tank is 109 cm wide and 61 cm deep with a stainless steel plate bottom plane to within ± 2.5 mm. The side walls of the tank are composed of 1.5 meter long panels of 1.3 cm thick tempered glass. The flume is mounted on two 30 inch steel I beams which rest on a central pivot. Dual power driven jacks both upstream and downstream of the pivot allow the tank to be tilted continuously from the horizontal to a maximum slope of 1 vertical to 50 horizontal. A photograph is presented in Figure 2.2 showing the author for scale with the tank in the level position. Instrument carriages are supported above the tank by two 3.8 cm diameter stainless steel rails. Prior to the start of the experiments, these rails were leveled to within ± 0.01 cm with the tank in a horizontal position using the still water surface as a reference point. A metric steel measuring tape is located on the top edge of the tank to allow the accurate measurement of relative distances between locations.

In order to reduce the resonant oscillation of the flume piping, the pump inlets were blocked with wooden blinds. A constant water level was maintained in the tank during the experiments by means of an overflow tube attached to the reservoir at the

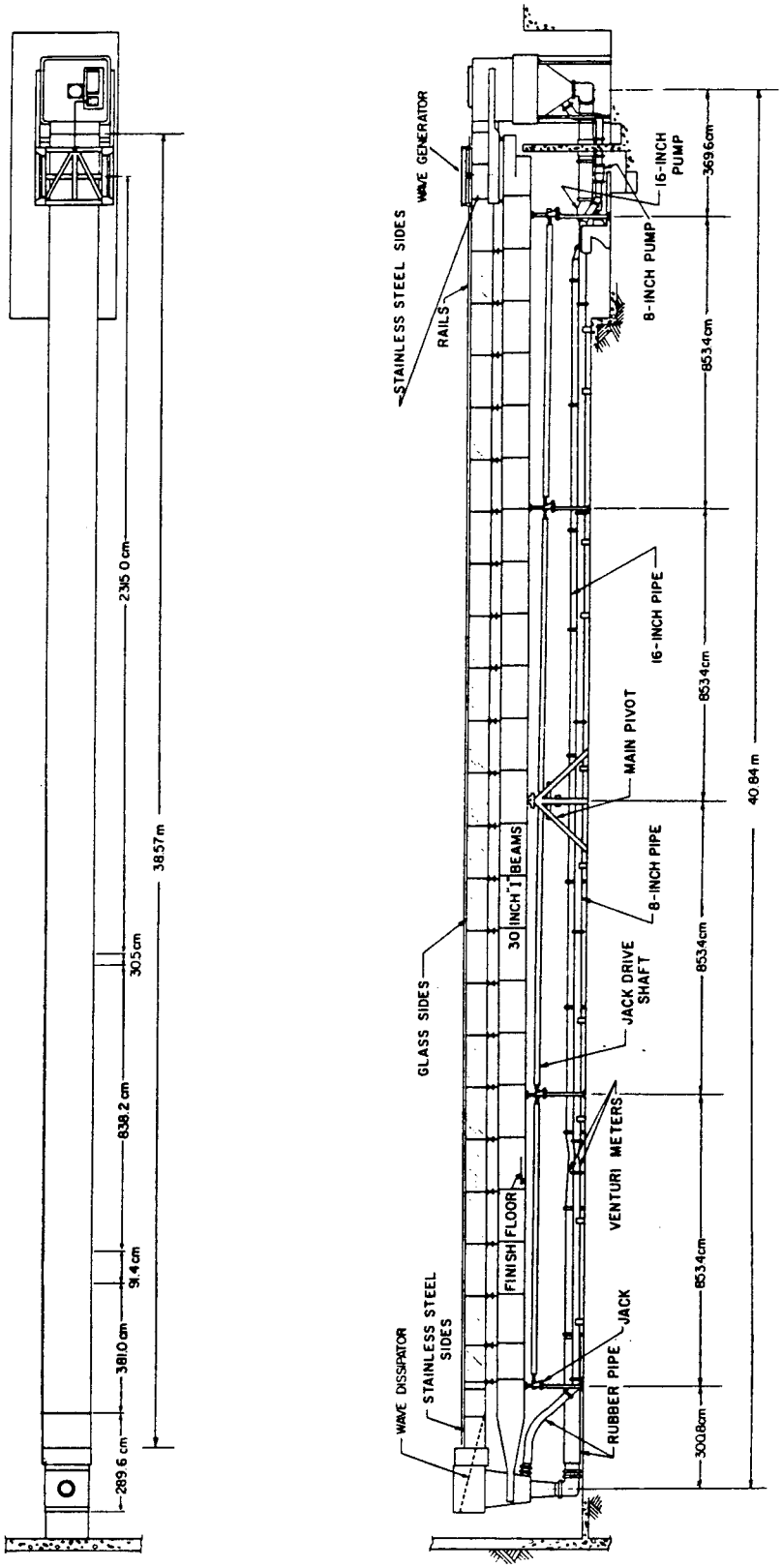

FIG. 2.1. Schematic of Wave Tank.

FIG. 2.2. Photograph of Level Wave Tank.

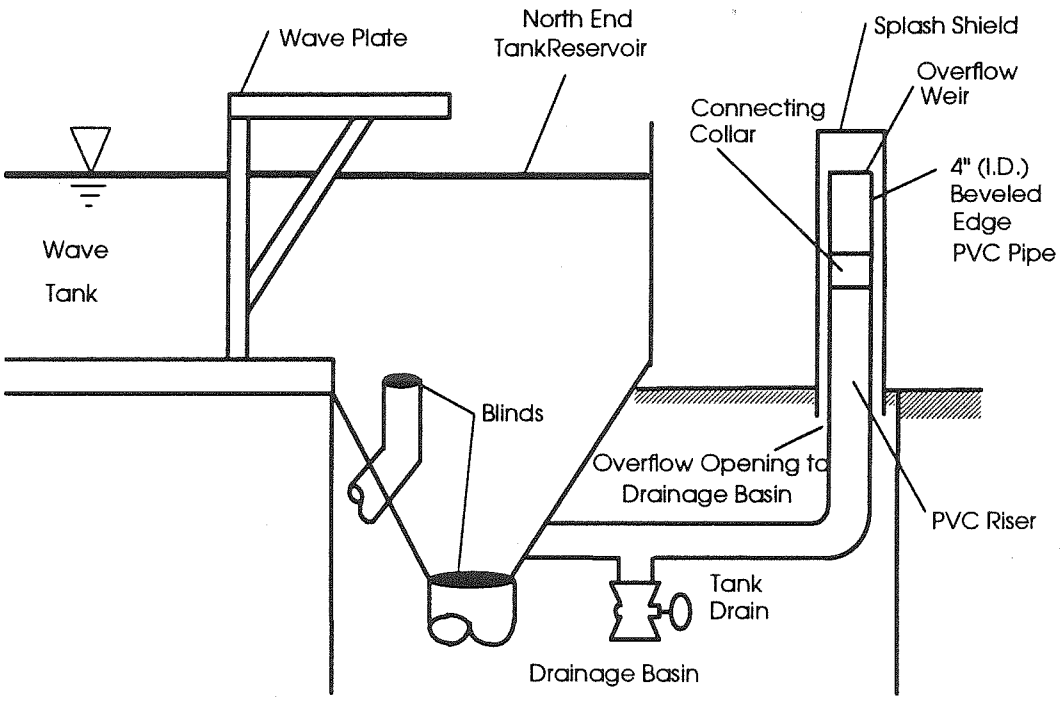

FIG. 2.3. Schematic of Overflow Tube.

North end of the tank (Figure 2.3). A small amount of water was constantly piped into the reservoir in order to replace water in the tank lost to evaporation or leakage. The balance spilled over the edge of the overflow pipe allowing an accurate setting of the water level in the tank.

2.1.2 False Bottom

This investigation required laser measurements as close as 1 mm above the bottom of the tank. This was not possible initially because of distortions present in the stainless steel plates forming the bottom of the tank. In addition, a recessed area was needed in which to place the rock fill. For this purpose a false bottom was installed in the tank, extending from underneath the wave generator a distance of 28.3 m upstream. The presence of the false bottom reduced the usable tank depth to 48 cm.

The false bottom is composed of 27 segments, each designed as a module that rests on the tank bottom. A picture of a typical false bottom section is shown in Figure 2.4. Each of 22 panels (Figure 2.5) consists of a pane of tempered glass 1.3 cm thick mounted on a galvanized steel frame such that the module stands 12.7 cm high, 108.6 cm wide and 121.9 cm long. The glass panes are sealed to the steel frame, to the side walls of the tank and to each other with a clear silicone RTV sealant. Sealing details are shown in Figure 2.6. Two additional glass and steel panels, one 61 cm long and one 91.4 cm long allow for adjusting the position of three test sections relative to the joints in the 1.5 m side wall panels of the tank. Seven of the glass and steel modules have been modified to allow for the connection to the test sections (described in Section 2.1.3).

When submerged the glass panels have a calculated maximum deflection of 0.05 mm. The maximum deflection in the steel frame is 0.03 mm. Welds in the frame were

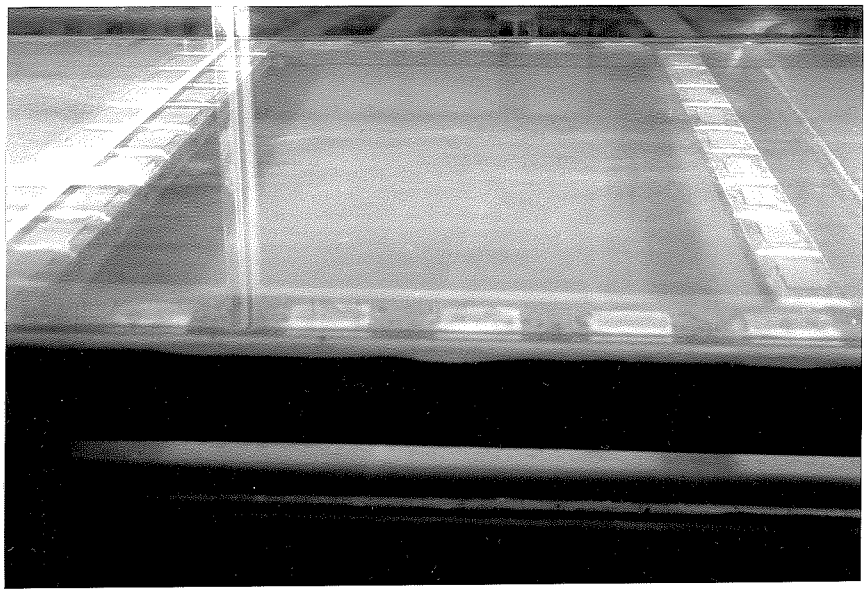

FIG. 2.4. Photograph of False Bottom.

sized to withstand transportation and installation live loads. The members in the steel frame were designed for a maximum deflection of less than 0.2 mm under the uplift forces from the trough of a 30.5 cm wave. At this loading the maximum deflection in the glass, occurring in the center of the panel, is calculated to be less than 1.5 mm. The first harmonic of the submerged glass pane when acting as a diaphragm simply supported on four sides is calculated at 84.7 Hertz.

Each false bottom module is supported on four leveling screws attached to the steel frame. A detail of the leveling screw is shown in Figure 2.7. The panels were installed in the tank by first placing the steel frames on the tank bottom without the glass. Two special glass panes, notched in the corners to allow access to the leveling screws, were then placed upon adjacent steel frames. This allowed the panes to be leveled while simultaneously aligning the top surfaces of the glass. The leveling screws were then

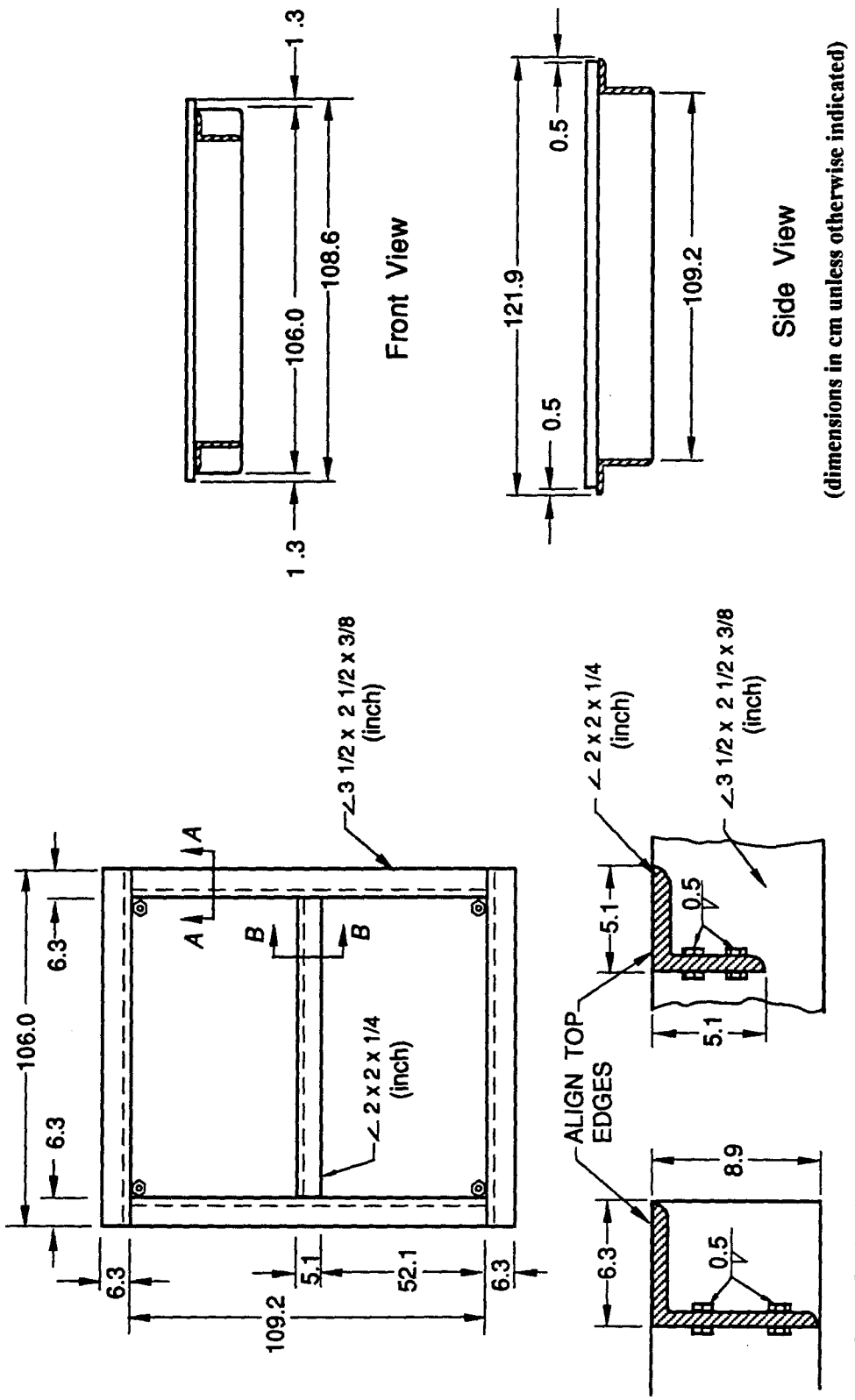

FIG. 2.5. Drawing of a Typical False Bottom Panel.

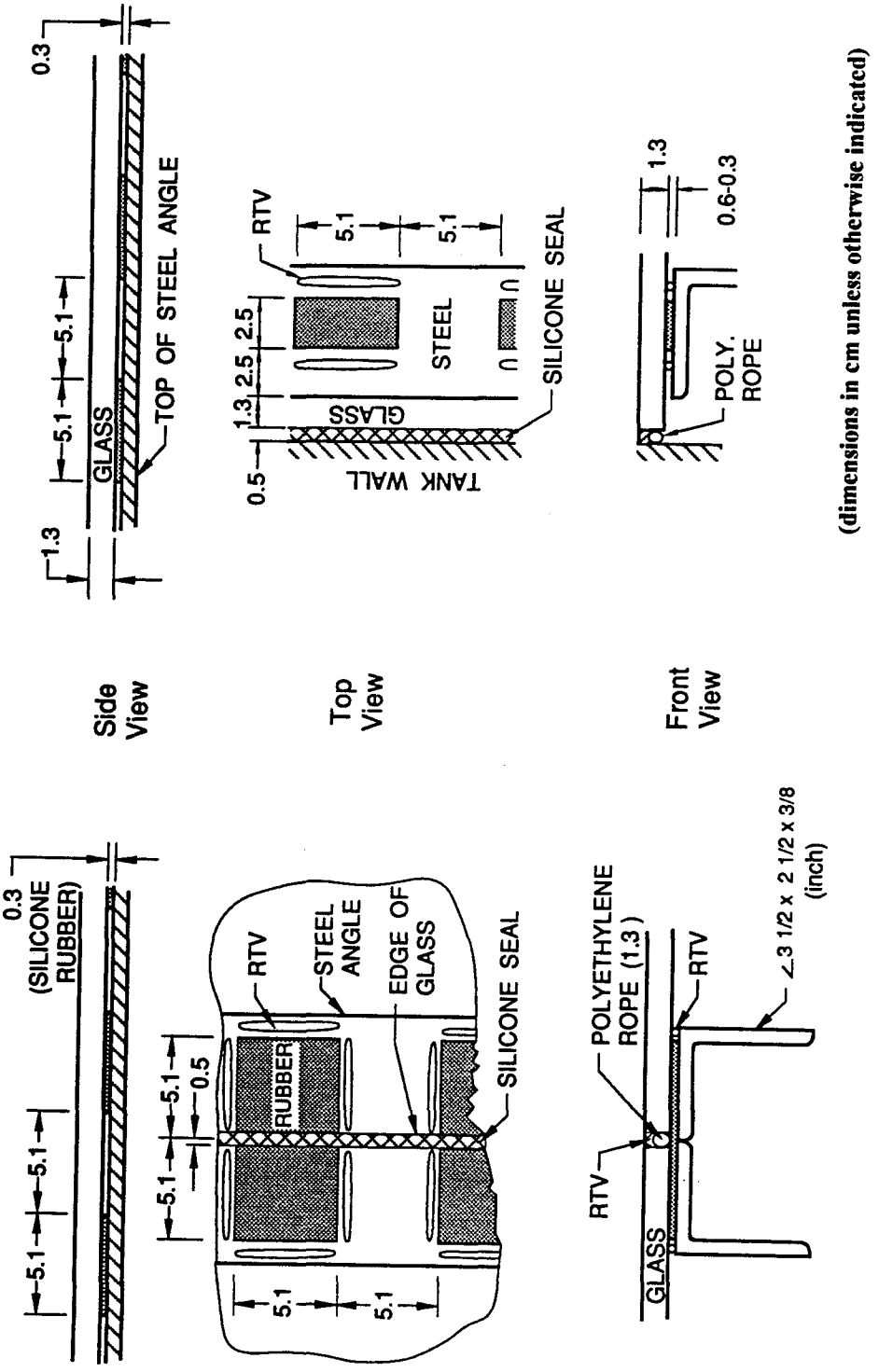

(a) Sealing detail @ plates

(b) Sealing detail @ tank wall

FIG. 2.6. Joint Details of False Bottom Panels.

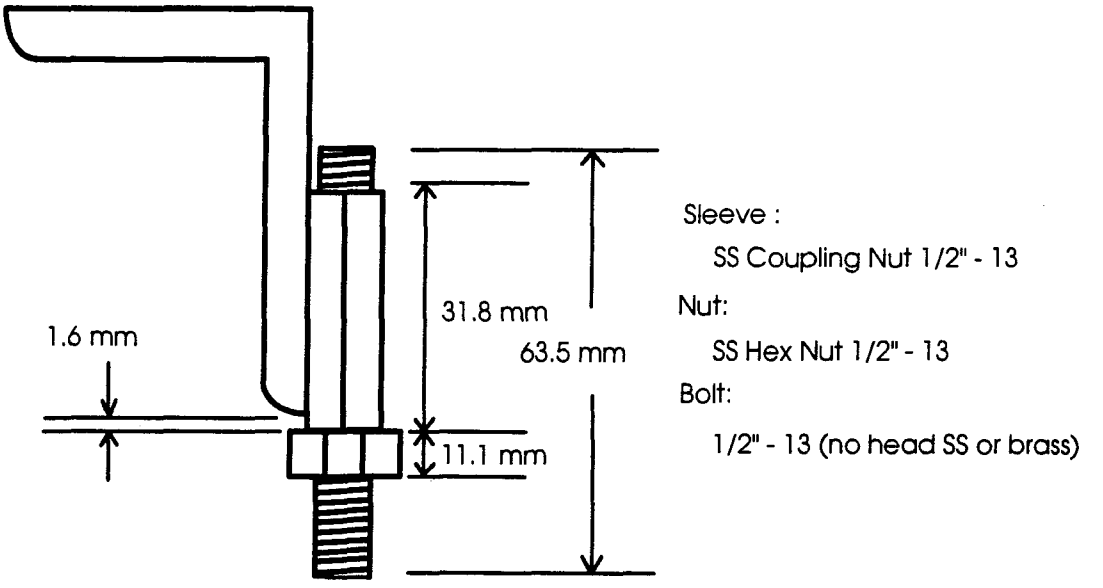

FIG. 2.7. Leveling Screw Details.

tightened. One pane of glass was moved to the next steel frame and the process was repeated down the tank. The steel frames were leveled to within ± 0.13 mm at the corners. The final glass panels were then placed upon the frames and sealed in place.

The initial false bottom section extended a distance of 25 cm behind the resting or initial position of the wave paddle. The steel frame for this section was braced to the wave tank as shown in Figure 2.8 in order to stabilize it during the motion of the wave paddle. The blind placed at the end of the section was sealed with silicone sealant to the walls of the tank and to the false bottom panel. This barrier was needed in order to minimize the communication between the reservoir behind the wave paddle and the space under the glass bottom occupied by the steel frames. This cavity was filled with water during these investigations and was thus capable of transmitting a pressure to the underside of the glass bottom during wave generation if not isolated.

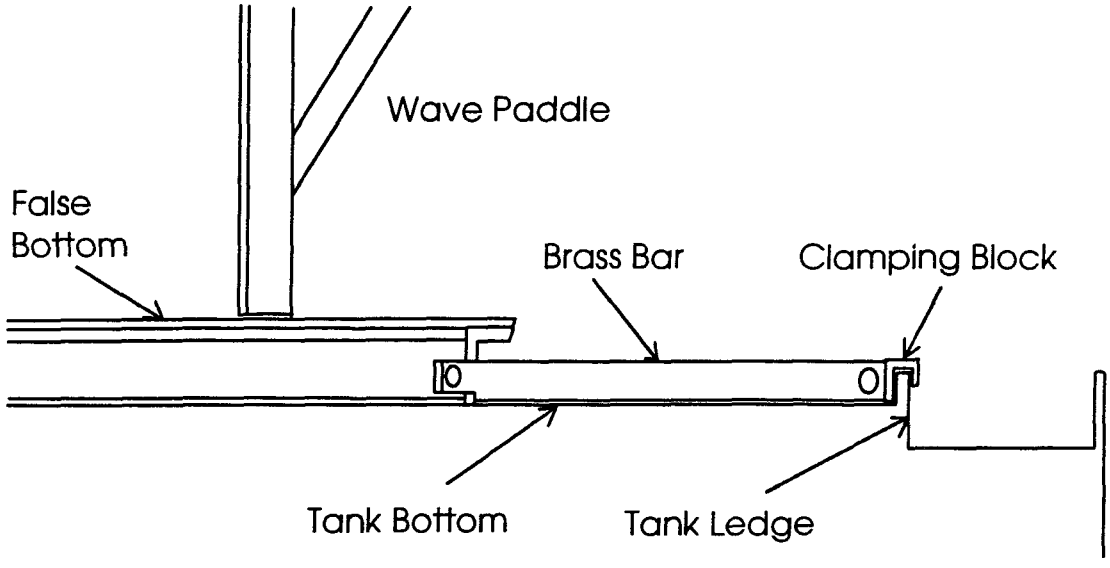

FIG. 2.8. False Bottom Bracing.

2.1.3 Test Sections

The false bottom modules were installed to leave space for three test Sections 1.5 m in length (shown as the dimension L in Figure 1.1). These spaces occurred on centerline at 13.70 m, 18.25 m and 29.20 m from the initial position of the wave paddle. All the experiments described herein were conducted in the first of these locations, from 12.95 m to 14.45 m from the wave paddle. This location coincided exactly with a glass side panel so that the test section was observable over its entire length. Two types of test sections were used: a flat anodized aluminum panel and a wooden panel providing a 2.5 cm deep recess for the test material.

2.1.3.1 Aluminum Plates

A 1.6 cm thick clear anodized aluminum panel measuring 152.2 cm long by 109.1 cm wide was used for experiments requiring a flat plate bottom. Details of the plate construction appear in Figure 2.9. The plate and supporting channel were designed to sustain a maximum deflection of 0.8 mm when acted on by the uplift force from the trough

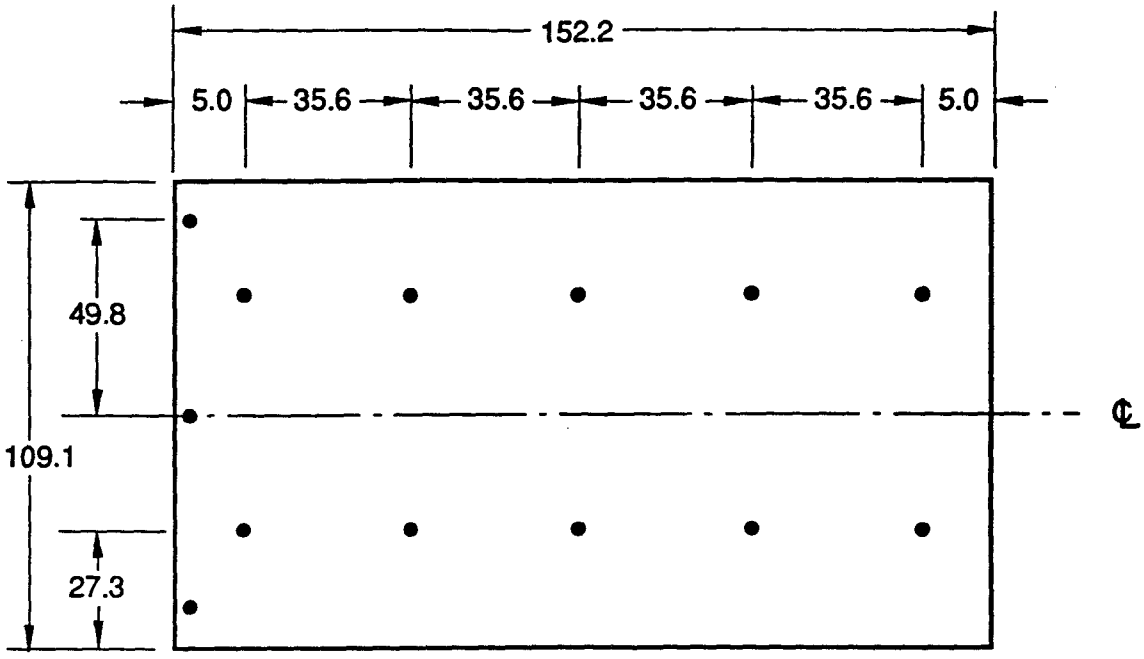

(a) Top View

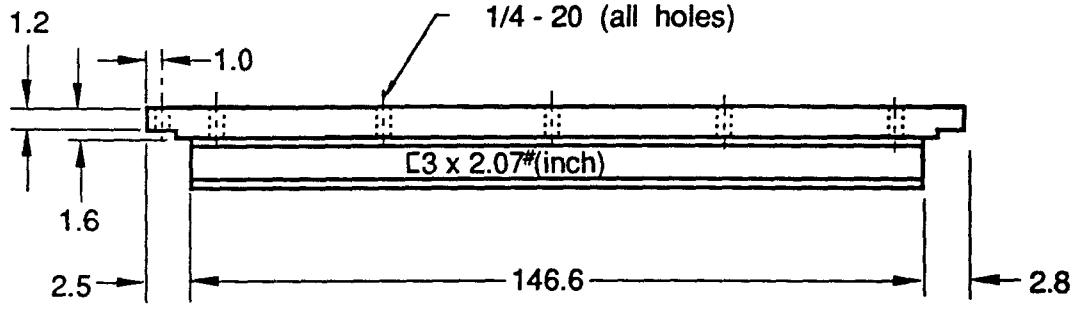

(b) Side View

FIG. 2.9. Drawing of Aluminum Test Section.

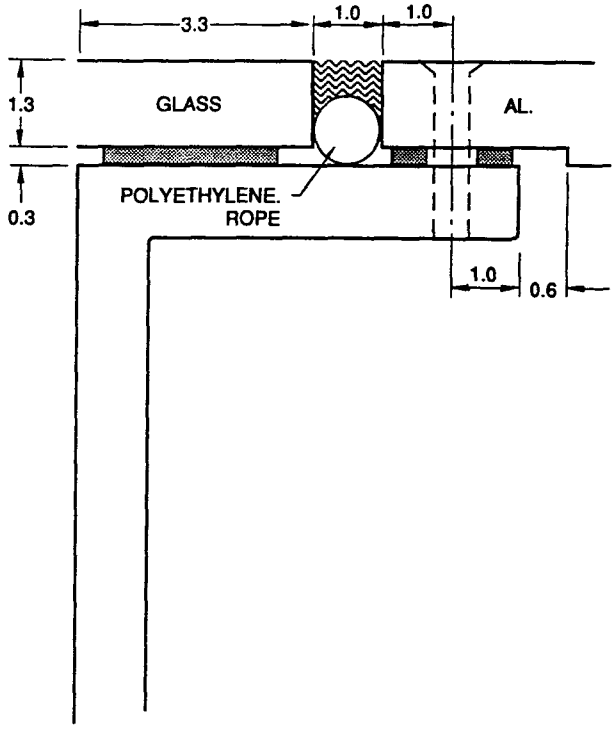

FIG. 2.10. Aluminum-to-Glass Joint Detail.

of a 30.5 cm wave. The aluminum panels were supported at the ends upon the steel frames of the adjoining glass false bottom and secured with resin coated brass screws to minimize galvanic action. Figure 2.10 shows a detail of the joint. The ends of each panel were shimmed to match the level of the adjoining glass.

2.1.3.2 Recess panel for Rock Fill

For the experiments requiring a bed of graded angular rock, the aluminum panel was replaced with a composite sheet metal and wood base. This panel was designed to hold a 2.5 cm deep layer of rock and is shown in Figure 2.11. The galvanized sheet metal edges were mounted to wooden strips and screwed to the steel frames of the adjoining false bottom sections. The joint detail appears in Figure 2.12. The wooden panel was designed to deflect a maximum of 1.0 mm under the trough of a 30.5 cm wave. The panel was weighted with 2 lead bricks weighing 25 pounds each in order to obtain a negative

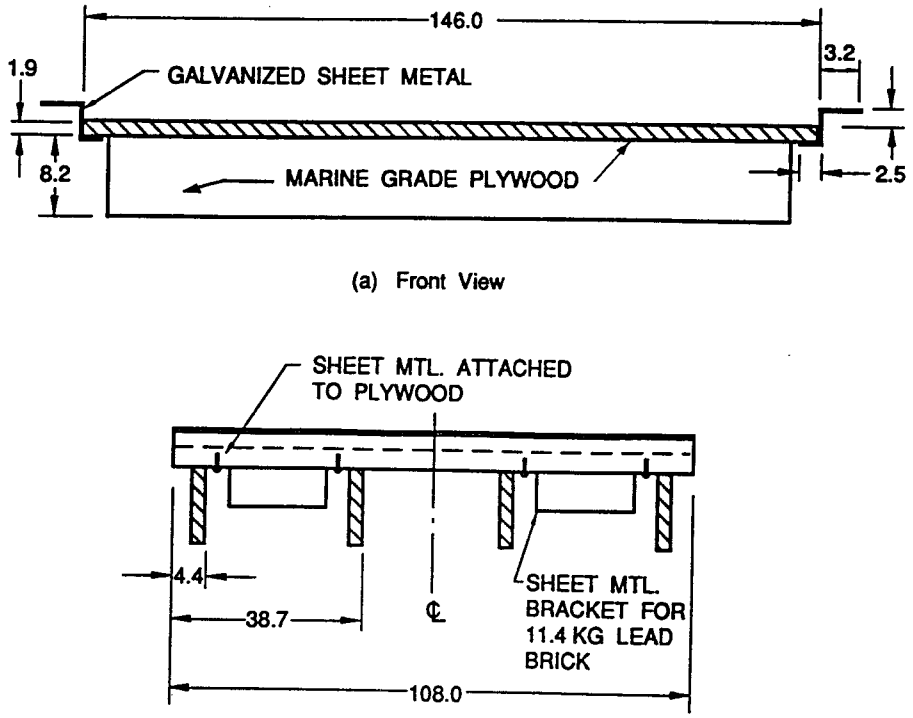

FIG. 2.11. Drawing of Wooden Recess Panel.

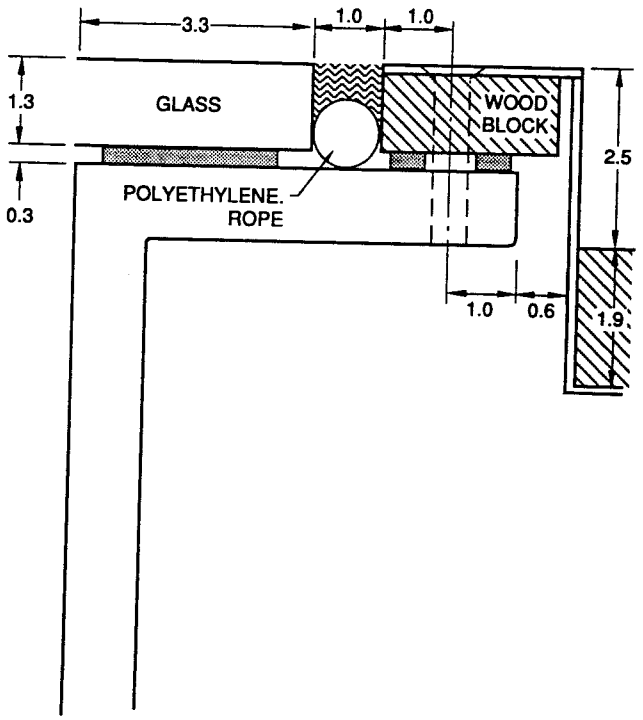

FIG. 2.12. Recess Panel-to-Glass Joint.

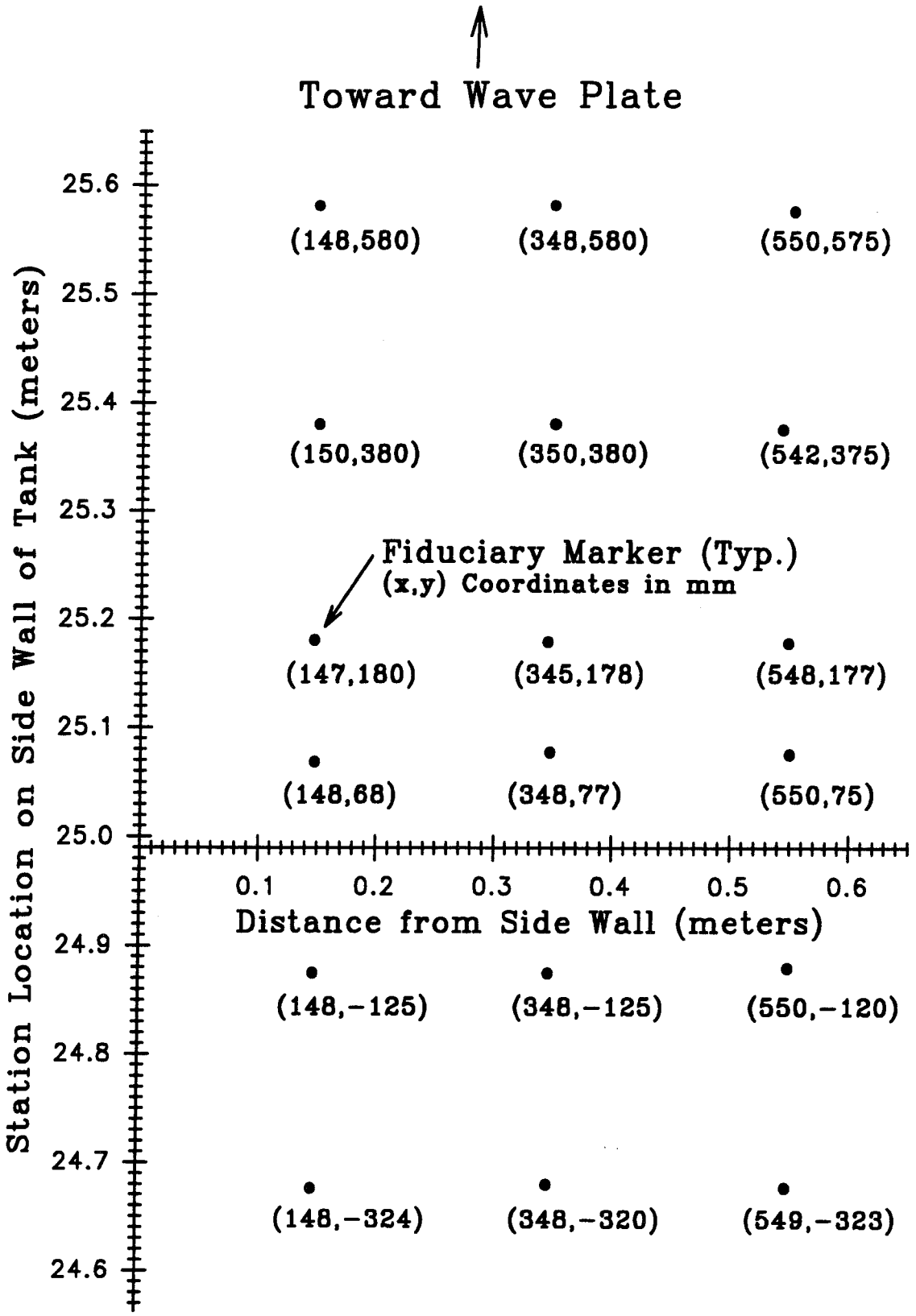

FIG. 2.13. Fiduciary Marker Layout.

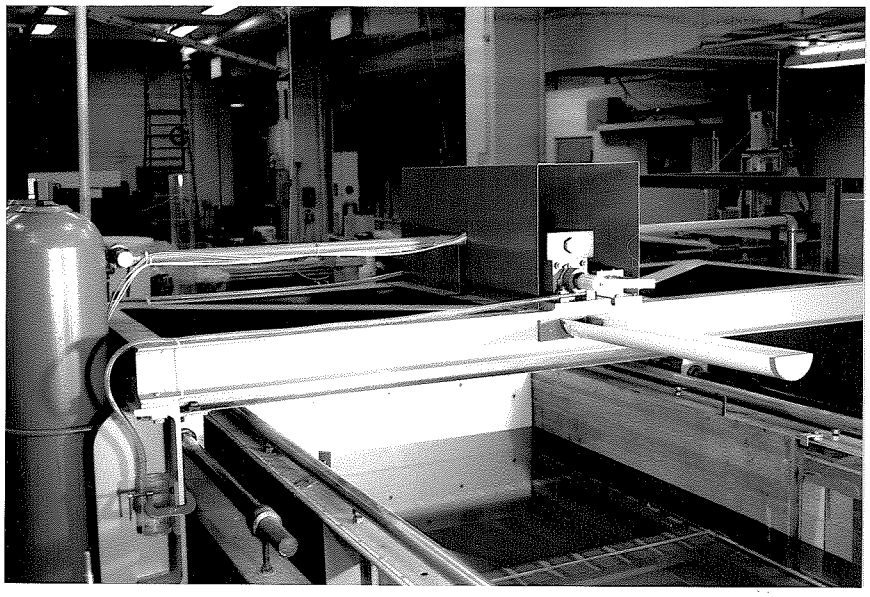

FIG. 2.14. Photograph of Wave Generator.

buoyancy. For the purposes of calibrating video images of particles resting in the recess, brass screws were added to the wooden base as fiduciary markers. The layout of these markers with respect to an origin at the 25 meter mark on the tank side wall is given in Figure 2.13. The coordinates of each marker are given with respect to the origin in millimeters. It was noted that during the course of the experiments, the wooden portion of the recess panel, which was sealed with lacquer, experienced very little warping or distortion.

2.2 WAVE GENERATION

2.2.1 Hydraulic System

The waves used in this investigation were produced using the programmable bulkhead wave generator shown in Figure 2.14. The entire assembly is supported on the

same frame as the tank and tilts integrally with the tank. A new wave paddle was manufactured to accommodate the installation of the glass false bottom. The paddle, made of 6.4 mm anodized aluminum, is mounted to a carriage which travels on 3.8 cm diameter steel rails using pillow block ball bushings. A seal to the tank walls is maintained during the motion of the paddle by rubber windshield wiper blades attached around the perimeter of the paddle.

Figure 2.15 shows the hydraulic system used to control wave generation in the tank. A variable displacement pump rated at 1.9 liters per second (30 GPM) supplies the hydraulic system with oil at an operating pressure of 1.7×10^7 Pascals (2500 psi). The pump is powered by a 56 KW, 1800 rpm electric motor and draws oil from a 680 liter reservoir. The temperature of the oil is controlled by a water-cooled heat exchanger rated for 1.3 liters per second at 23.9 degrees centigrade. An unloading valve located downstream of the pump directs flow to the servo-valve when the downstream pressure falls below the 1.7×10^7 set point. In this manner a constant pressure supply of oil is always available to the hydraulic cylinder. Six accumulators of varying capacities have been installed in the line to act as dampers for any transients, to reduce noise associated with vibration, and to provide some temporary storage capacity.

The servo-valve (Moog, Model 72-103) directs the flow of hydraulic fluid to either side of the hydraulic cylinder depending on the current provided to it by the servo-controller (Moog, Model 82D300). The valve is rated at 3.8 liters per second for a current of 40 mA with a pressure drop of 2.7×10^6 Pascals across the valve. The hydraulic cylinder (Miller, Model DR-77B) has a bore of 8.25 cm and a rod diameter of 3.49 cm with a maximum travel distance of 63.5 cm. The original seals in the cylinder have been replaced with step seals (Shamban Model S32573-126) in order to allow a free movement of the stainless steel rod, especially for very small amplitudes of motion.

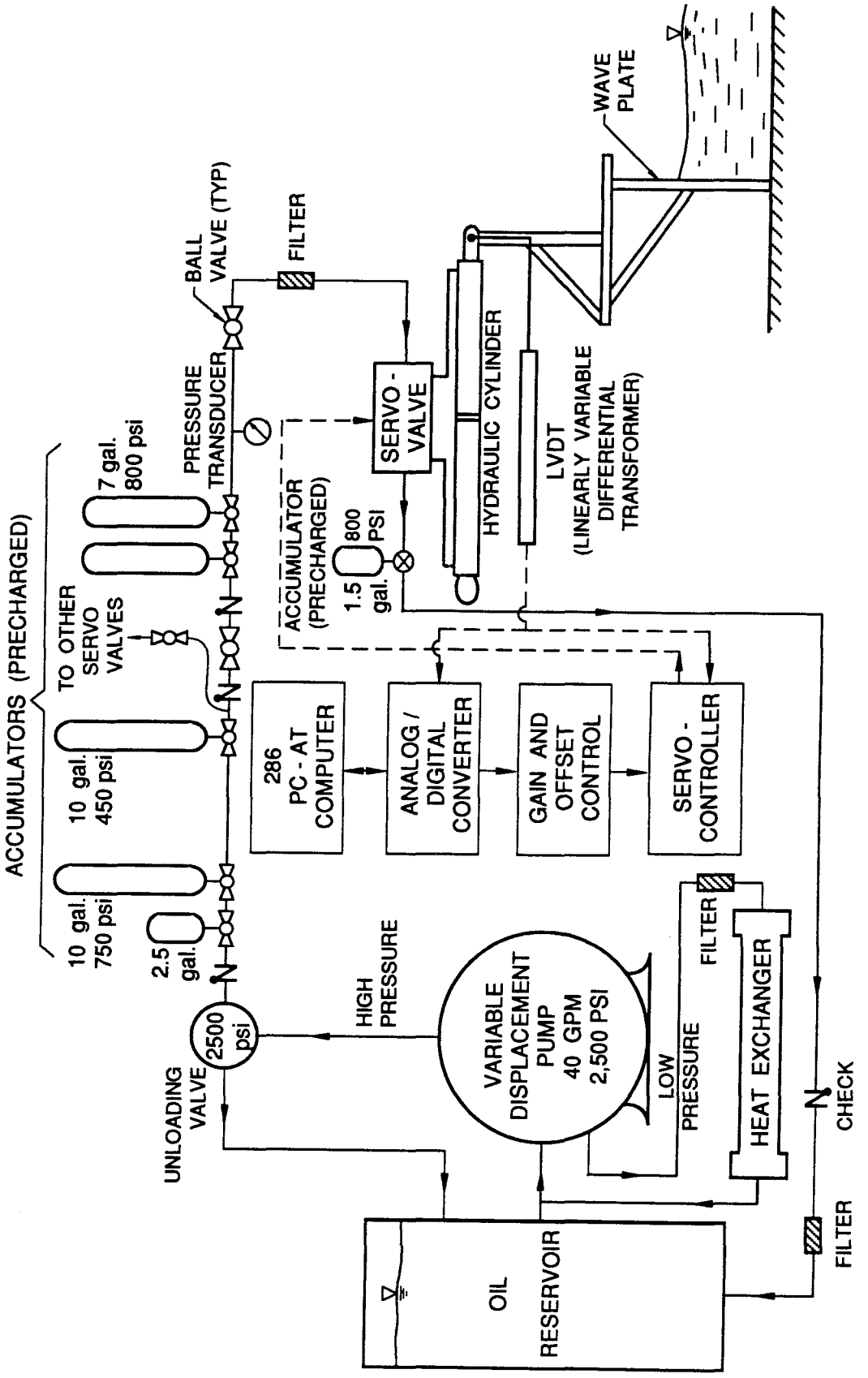

FIG. 2.15. Schematic of Hydraulic System.

The displacement of the wave paddle is monitored by a Linear Variable Differential Transformer (LVDT) (Collins Model LMT-811T41). The signal from the LVDT is used as a feedback input to the servo-controller. The servo-controller then accelerates or decelerates the motion of the piston depending on the difference between the desired trajectory of the wave paddle and the actual displacement measured by the LVDT.

2.2.2 Trajectory Generation

The desired trajectory of the wave paddle was supplied to the servo-controller as a time series of discrete voltage levels. The trajectories were generated using the method described by Goring (1979) with a microcomputer (IBM AT compatible). The signal was transferred from the computer to the servo-controller by means of a 12 bit analog-to-digital and digital-to-analog converter card (Omega Model DAS-16F). The maximum excursion of the paddle is adjusted by changing the gain on the analog output of the Omega card. In addition, the initial position of the wave paddle can be adjusted by adding or subtracting an offset voltage from the signal to the servo-valve. Figure 2.16 shows the calibration curve used to adjust the gain setting for the maximum excursion of the wave to match the desired stroke distance. Throughout this investigation, the initial offset position of the piston was maintained at the value of 20 noted on the calibration curve. The gain settings used in the experiments ranged from 510 to 773.

Figure 2.17 shows a sample trajectory output from the computer program along with the recorded LVDT output for that wave during the motion of the wave paddle. Both signals have been normalized by their maximum amplitudes. At very high speeds the response of the wave paddle shows a slight lag behind the desired trajectory. This is seen in the second half of the signal in Figure 2.17 where the deceleration of the paddle lags the desired deceleration and results in a slight overshoot of the wave plate. This response lag was not deemed to be significant for any of the waves generated in this investigation.

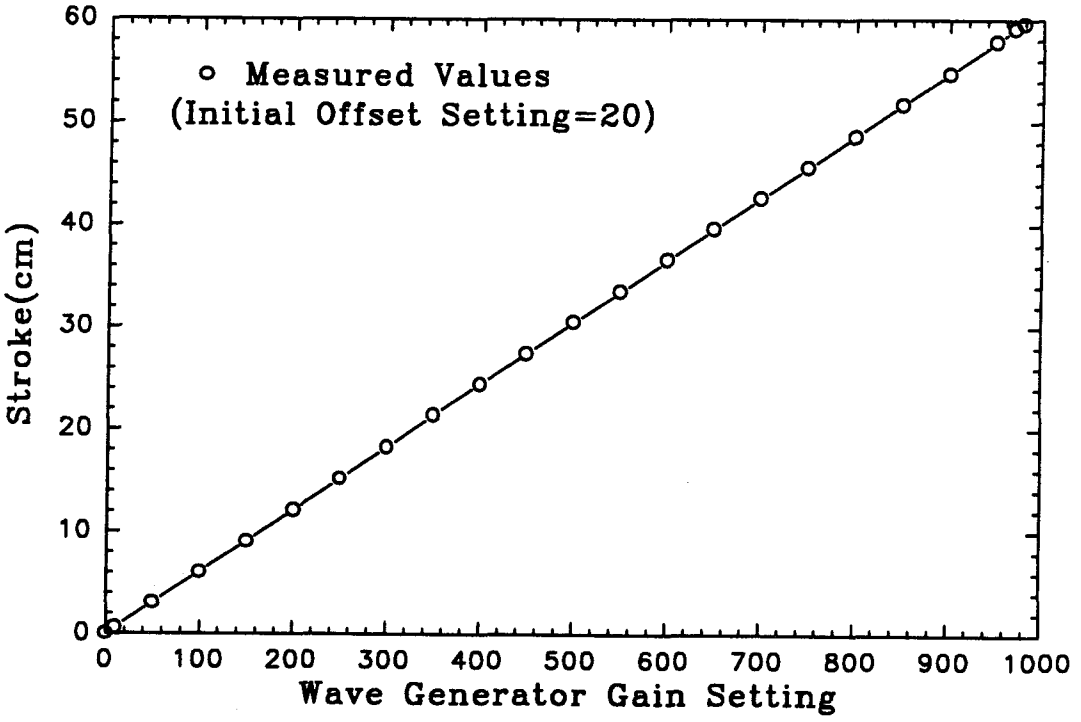

FIG. 2.16. Calibration Curve of Wave Generator Signal Gain to Stroke of Paddle Motion.

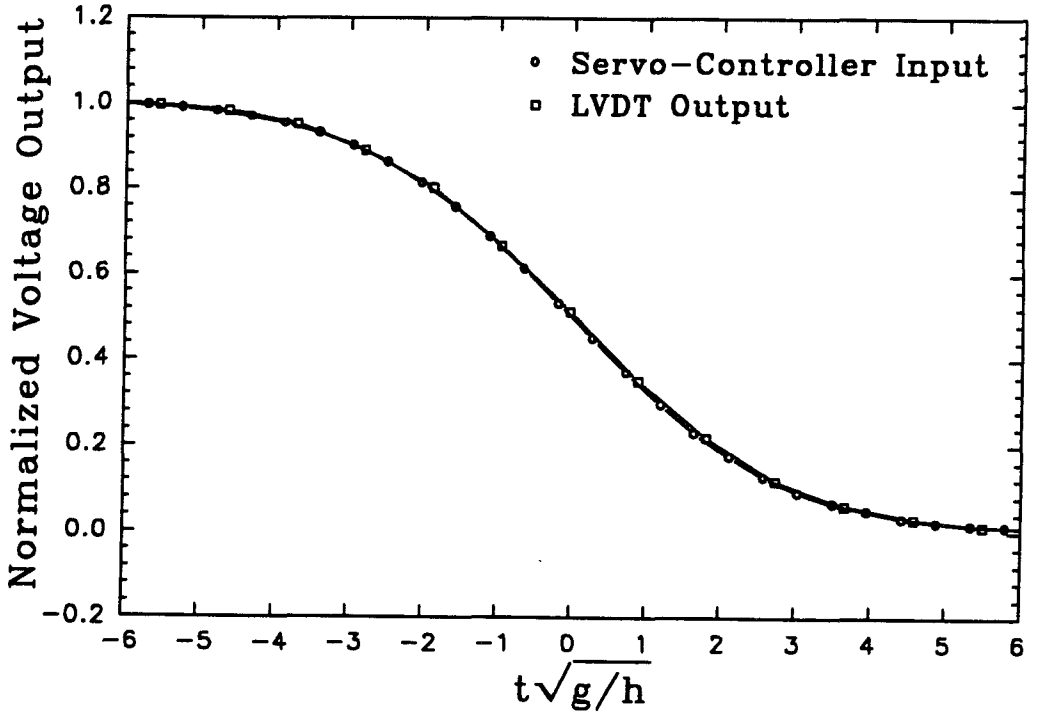

FIG. 2.17. Comparison of Wave Generator Signal to Displacement of Wave Paddle.

2.3 ROCK CHARACTERISTICS AND PLACEMENT

2.3.1 Rock Characteristics

One of the objectives of this investigation was to observe particle movement with respect to the phase of the breaking wave. For this purpose, a significant amount of motion was needed in the bed under each wave. The particles used in the experiments were selected with a mean grain size small enough to provide a readily observable amount of motion yet not allow scouring of large areas of the test section. In addition, the size of the material allowed video observations of the bed to cover a wide area while retaining the capability to resolve individual particles in the video image.

2.3.1.1 Particle Composition, Density, Angularity

The particles used in the experiments were prepared from natural crushed white rock (Brubaker-Mann Inc. natural colored white crushed rock, Barstow, California and Gibbel Bros. Inc. decorative rock, white, 3/8 inch, size 1, Sun Valley, California). The composition of the rock was primarily calcite, as determined by visual inspection and by exposing whole and crushed samples to hydrochloric acid.

The specific gravity of the rock material was obtained by weighing three samples in air and then measuring the volume of water displaced when the samples were submerged. The specific gravity was then calculated as:

$$\frac{\gamma_s}{\gamma_w} = \frac{W_s / V_s}{\gamma_w} \tag{2.1}$$

where γ_s is the specific weight of the rock, γ_w, the specific weight of water (at 20 degrees centigrade), W_s is the weight of the sample and V_s is the volume of water

displaced by the sample. For the prepared test material, γ_s / γ_w ranged between 2.48 and 2.50.

The material chosen for experiments was angular and very highly fractured. Before the start of the experiments, a fracture count of a sample of 129 particles showed that 120 or 93 percent of the grains were fractured on at least one face. The fracture count was made prior to the treatment of the particles with colored epoxy paint as detailed below. Since the paint covered the majority of the grain surfaces, a similar count was not possible later in the investigations.

The angularity of the material used in the experiments was characterized by a shape factor defined as $S_f = D_a / \sqrt{D_b D_c}$. The dimension of the particle in three orthogonal directions are defined as D_a, D_b and D_c with origin at the estimated center of mass of the particle. The largest possible diameter is D_c , and D_a is the smallest diameter perpendicular to D_c and passing through the origin. The value of S_f has a maximum value of 1.0 for a spherical particle and is a minimum for flat disk-shaped particles. Figure 2.18 shows the shape factor distributions obtained for two forty-particle samples of the test material: one taken before experiments began and one taken after the conclusion of the investigation. The distributions show that the particles experienced some degree of wear during the course of the experiments and the more angular particles were affected the most by the experimental procedures.

2.3.1.2 Particle Preparation and Gradation

The test material was prepared by using a large shaker fitted with heavy duty 46.5 cm square sieves. The rock was separated into three different size fractions using three sieves of mesh openings 9.5 mm, 4.8 mm, and 3.6 mm respectively. The material collected on the 4.8 mm, 3.6 mm sieves and in the pan was retained. Each sieving run

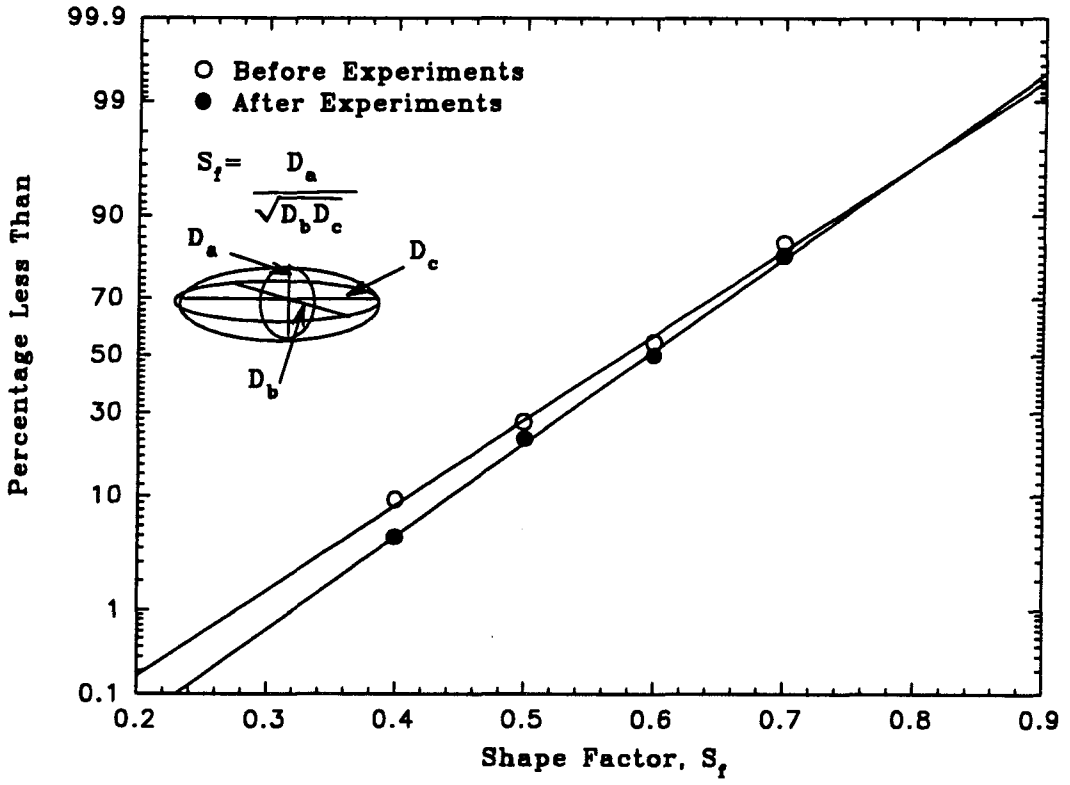

FIG. 2.18. Shape Factor Distribution for Test Material.

processed approximately 18.2 kg of material. Sieving time was set at ten minutes. The different size fractions were then sprayed with an epoxy paint (Krylon epoxy spray enamel). The largest size fraction, 9.5 mm to 4.8 mm, was colored green; the next largest, 4.8 mm to 3.6 mm, was painted yellow and the remaining material, 3.6 mm and less, received a white coat. The particles were mixed and resprayed until all observable surfaces were colored. The choice of the colors is detailed in Section 3.1.1.

The three size fractions were combined by weight in the ratio of 1:2:1 of green, yellow and white respectively. Since this was approximately the distribution of the original material, the resulting gradation was fairly smooth. Figure 2.19 shows a grain size analysis of the colored rock at three stages during the course of the experiments. Each curve is the average of three grab samples of material sieved for ten minutes in a testing sieve shaker (RO-TAP No. 2855, W. S. Tyler Co.). Although the standard deviation,

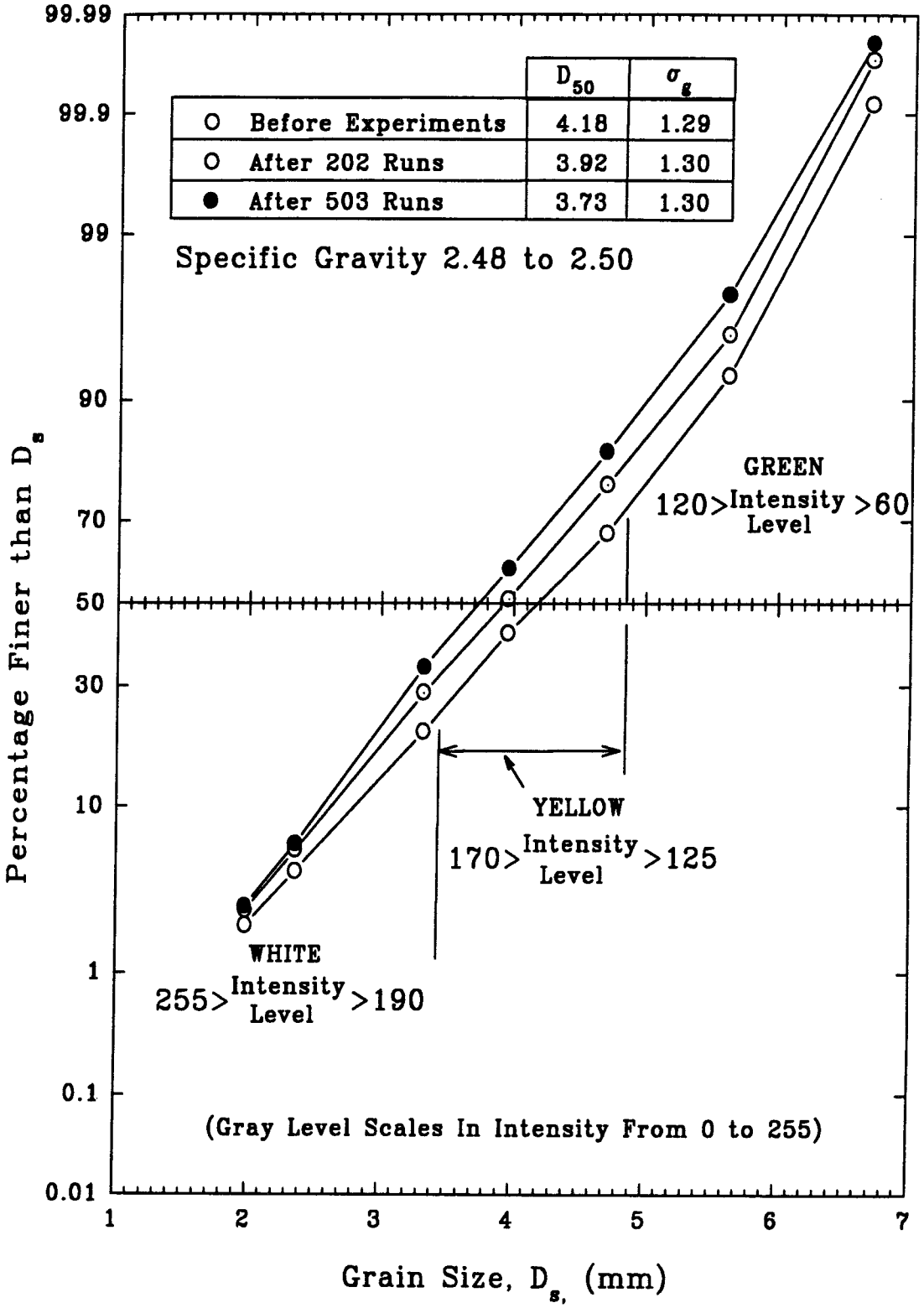

FIG. 2.19. Grain Size Analysis.

FIG. 2.20. Photograph of Test Material in Recess.

σ_g, remains nearly the same at 1.30, the mean diameter of the material has decreased by 10.7 percent. This decrease would imply a mean particle weight and volume change of nearly 30 percent. Fortunately, as described in Section 2.3.2, some self sorting of the material does occur during its placement in the test section and the composition of the top layer of rock in the bed remained constant throughout the experiments.

2.3.2. Placement of Rock in Test Section

Figure 2.20 shows the colored material as it appears when placed into the 2.5 cm recess. As mentioned in Section 1.1, the investigation was concerned with wave interaction with unpacked material on the bottom. For this purpose, the bed was raked and leveled after each wave passage.

2.3.2.1 Rake/Leveler Assembly and Unpacking Procedure

The test section was initially filled with material by placing approximately 0.030 cubic meters in the recess and roughly leveling the material by hand. The capacity of the recess is 0.024 cubic meters when the top of the rock is level with the edge of the false bottom. The excess material was then removed using a milled aluminum angle attached to a rake and leveler assembly.

In order to maintain a consistent level at the top of the material, the bed was smoothed using the assembly shown in Figure 2.21. The rake and leveler assembly consists of an aluminum frame which is mounted to a heavy steel carriage. The carriage moves on the tank rails thus controlling the vertical position of the leveler. The assembly extends most of the way across the tank, leaving a 0.6 cm clearance on either side between the leveler and the side walls of the tank. A milled aluminum angle serves as the surface by which the rock is leveled. The rake portion consists of a series of pointed brass rods brazed to a brass bar. The bar rides on two 8 mm brass rods and can be hoisted up out of the way to allow the use of the leveler alone. The vertical position of the leveler is controlled by means of slotted connections in the aluminum frame. The extent to which the brass rods extend below the edge of the leveler is controlled by raising or lowering the position of the C3 channel depicted in detail "A" of Figure 2.21. During these investigations the raking rods extended 1.9 cm below the edge of the leveler. This allowed the bed to be raked without scraping the wooden recess below.

The original intent of the rake and leveler assembly was to accomplish the unpacking and leveling in one pass. It was noted, however, that the passage of the rake left furrows in the bed that were not removed during leveling. The schematic in Figure 2.22 illustrates the procedure used in the experiments to achieve the unpacking and leveling of the bed. The rake/leveler assembly was kept in the dry section of the tank,

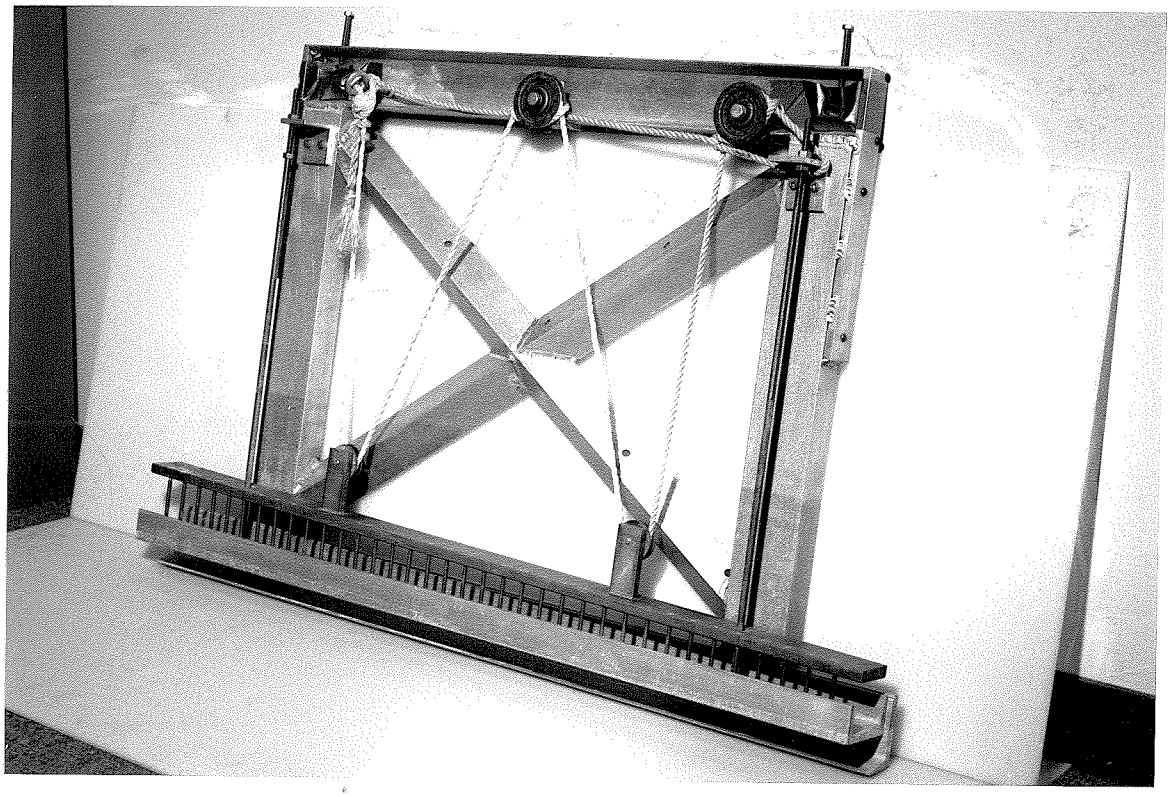

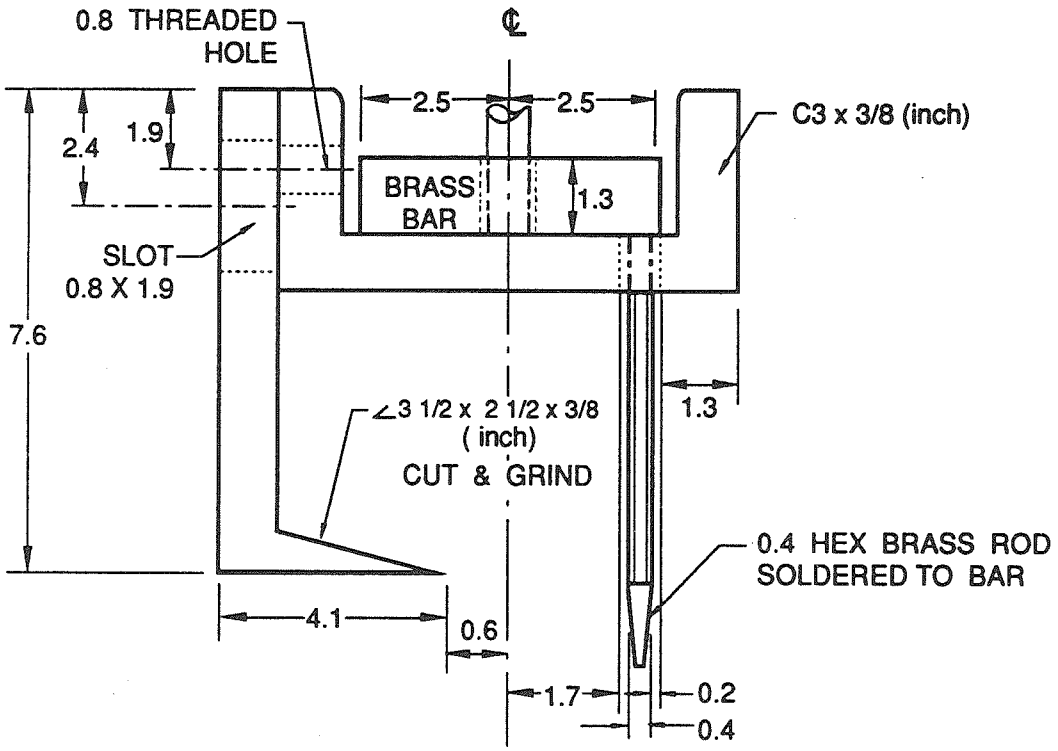

FIG. 2.21. Rake/Leveler Photograph and Schematic.

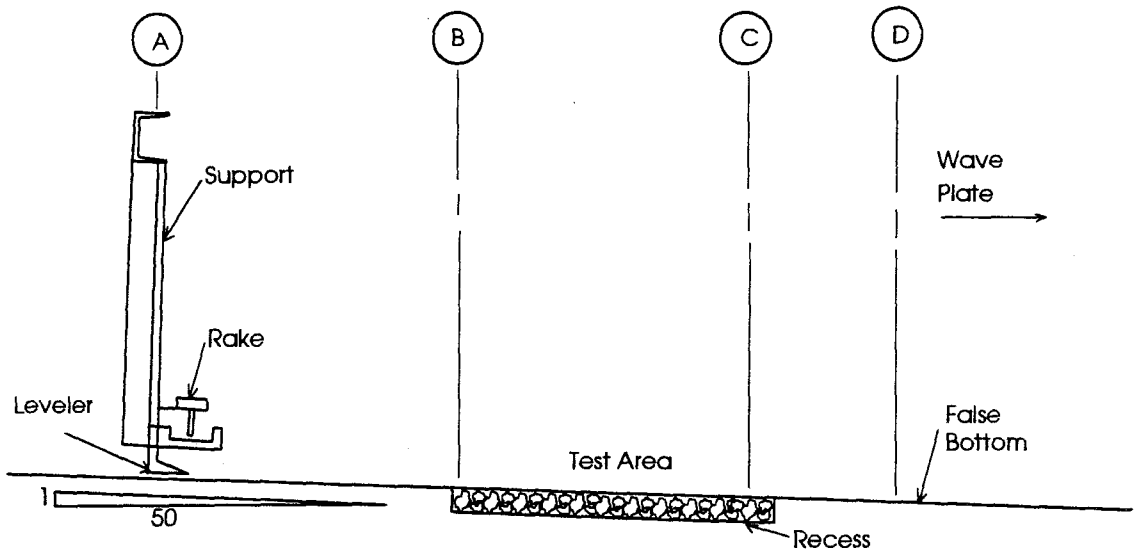

FIG. 2.22. Schematic of Rake and Leveler Positions.

position A, during the passage of a wave. In order to unpack the bed, the assembly was moved to position B and the rake was lowered. The carriage was then pushed along the bed to position C where the rake was raised out of the way. The assembly was moved to position D and extra material was added to the bed. The bed was then leveled by moving the assembly back to position B. The excess material removed by the leveler was cleared away to allow passage of the assembly and the leveler was returned to position A.

The above procedure provided the most consistent bed composition. Because of the size fraction differentiation by color, several phenomena were observed to occur in the test section. As the bed was leveled it was noted that a greater amount of the finer material occupied the lowest 1 cm of the 2.5 cm recess. This was observable through the glass sidewalls of the tank and occurred with the initial leveling of the bed. This self-armoring process meant that the material on the top surface, although not packed, was generally larger in mean diameter than the supplied mixture. As the bed was repeatedly unpacked and leveled, the addition of excess material during the leveling process appeared to minimize any increase in self-armoring. The other observed effect occurred as a result

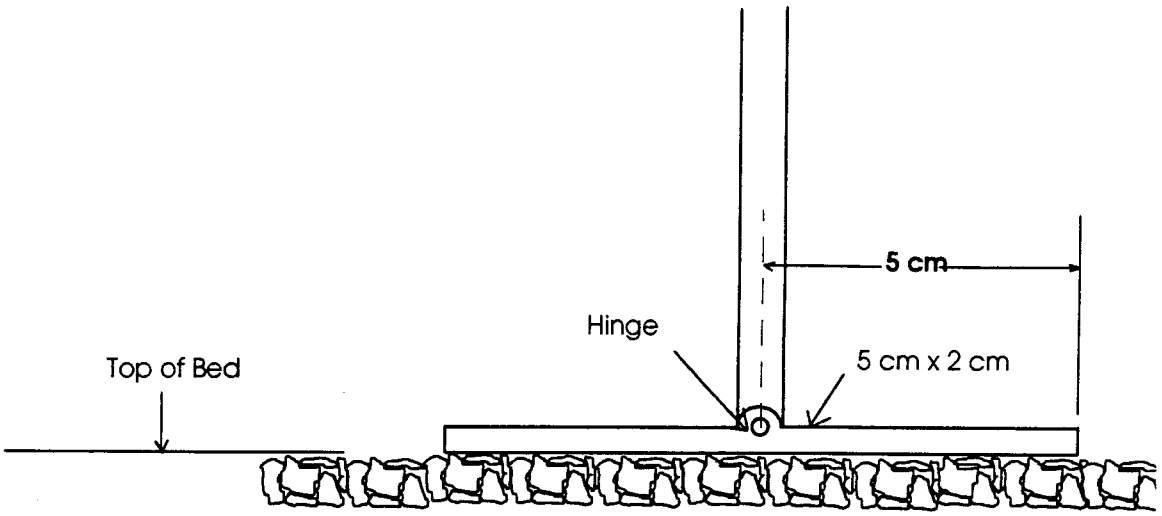

FIG. 2.23. Schematic of Foot Gauge.

of the leveling process. As the leveler was moved along the bed, from position C to position B in Figure 2.21, the material carried in advance of the leveler contained increasingly more of the large green particles. After a number of unpacking repetitions, the bed near position B appeared increasingly greener while the region near position C contained more of the smaller white particles. The mixture of particles in the area of the bed where experimental measurements were made, however, remained unchanged. To control the particle segregation problem, the entire bed was remixed by hand and reset with the rake/leveler after every ten experimental runs.

2.3.3.2 Determination of Bed Elevation

The level of the material in the recess was determined using the "foot" gauge shown in Figure 2.23. The foot gauge was lowered until it just came into contact with the tops of the particles. To find the mean bed elevation, eight measurements were taken along the centerline of the tank in the test section in different locations. The average elevation from these measurements was then compared to the elevations of the adjoining false bottom sections. The rake/leveler assembly was adjusted to produce a bed elevation 2 mm to 3 mm above the false bottom. This is as close as possible to Kamphuis (1975)

criterion of $0.3D_{90}$. For the case of the material on the top of test section, $0.3D_{90} = 1.8$ mm. It was not possible to adjust the rake/leveler assembly any lower because the leveler would then jam particles between the leveling angle and the false bottom.

2.4 PARTICLE MOVEMENT MEASUREMENTS

Video images of the particles in the test section were recorded with two video cameras: a Magnavox model VR9244/46AV full size Super VHS (S-VHS) format camera, and a Mitsubishi model HS-C-30U compact S-VHS format camera. Both cameras recorded at a rate of 30 frames per second with a maximum shutter speed of 1/1000 of a second. The S-VHS format records 480 lines per image with 512 pixels per line. The images were recorded on videotape so that they could be processed later with a computer image processing system.

2.4.1 Overhead Observations

Video recordings were taken of the bed before and after the passage of a wave in order to find the net movement of particles under the wave. To observe the bed from a position directly overhead, the camera was mounted on a swivel bracket attached to the inner frame of a traveling carriage described in Section 2.5.1. A picture of the Magnavox camera in this position is shown in Figure 2.24. The camera elevation and lens were adjusted to encompass a field of view of approximately 600 cm^2 centered on the centerline of the tank and including two fiduciary marker screws. This allowed the largest field of view, given the size of the bed material. Figure 2.25 shows a schematic of the experimental setup for overhead observations.

The Magnavox camera was used for those experiments where only overhead images were recorded. For experiments which included both sideview and overhead observations, the Mitsubishi camera, the focal length of which was unsuitable for

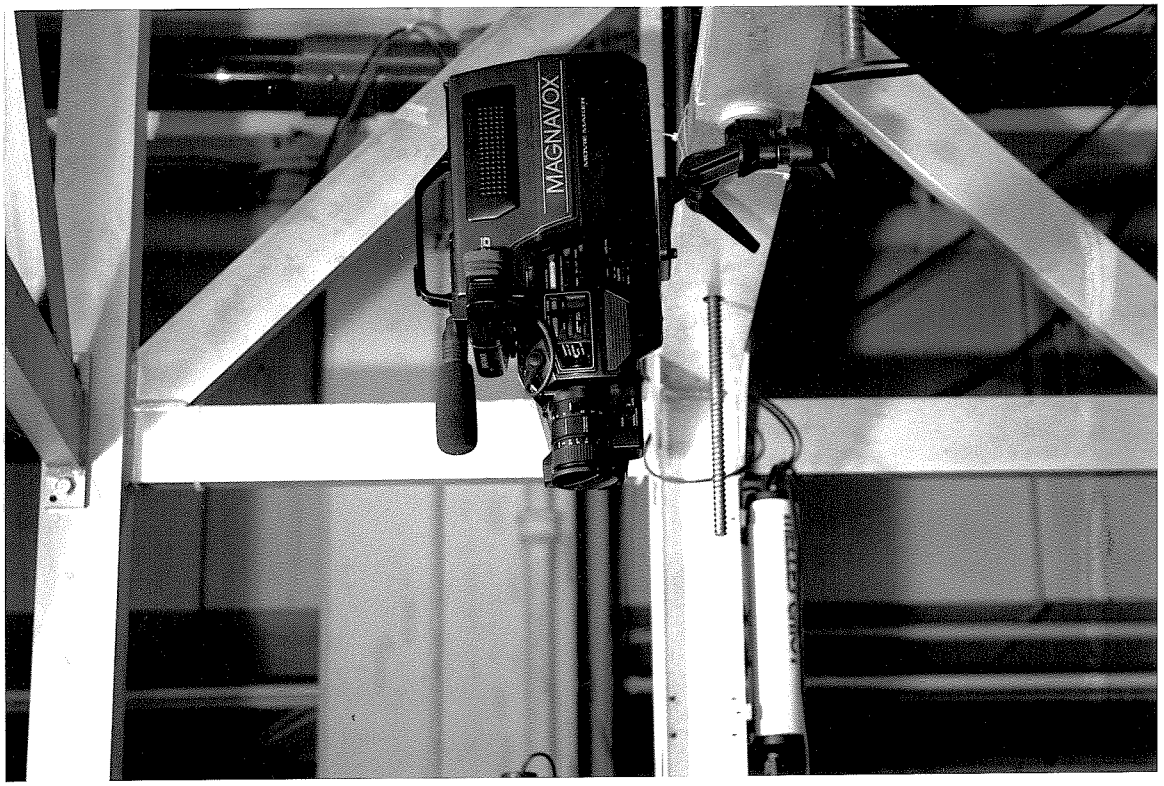

FIG. 2.24. Photograph of Overhead Video Camera.

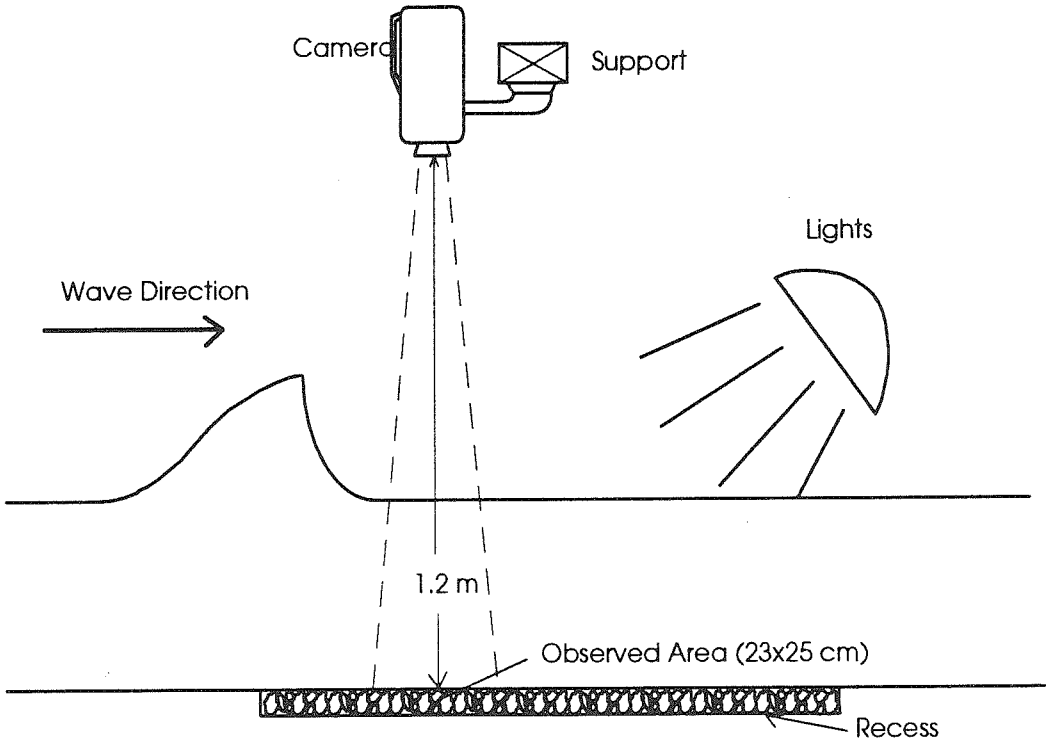

FIG. 2.25. Schematic of Overhead Observation Camera.

sideviews, was positioned over the bed. The full size S-VHS camera had a much better light sensitivity and depth of view as well as more flexible focusing than the compact S-VHS camera.

The test section was illuminated with two 200 watt photographer's bulbs. The bulbs were mounted on an instrument carriage over the test section at a low angle in order to give the most definition to individual grains in the bed. The relative location of the lights with respect to the observation area appears in Figure 2.25.

2.4.2 Oblique Sideview Observations

The movement of particles during wave passage was recorded by viewing a portion of the bed through the sidewalls of the tank at an oblique angle. Figure 2.26 shows a schematic for these observations. The Magnavox S-VHS camera was mounted on a tripod and placed a sufficient height and distance away from the tank so that both the wave and a portion of the test section were in the field of view. The observed area of the

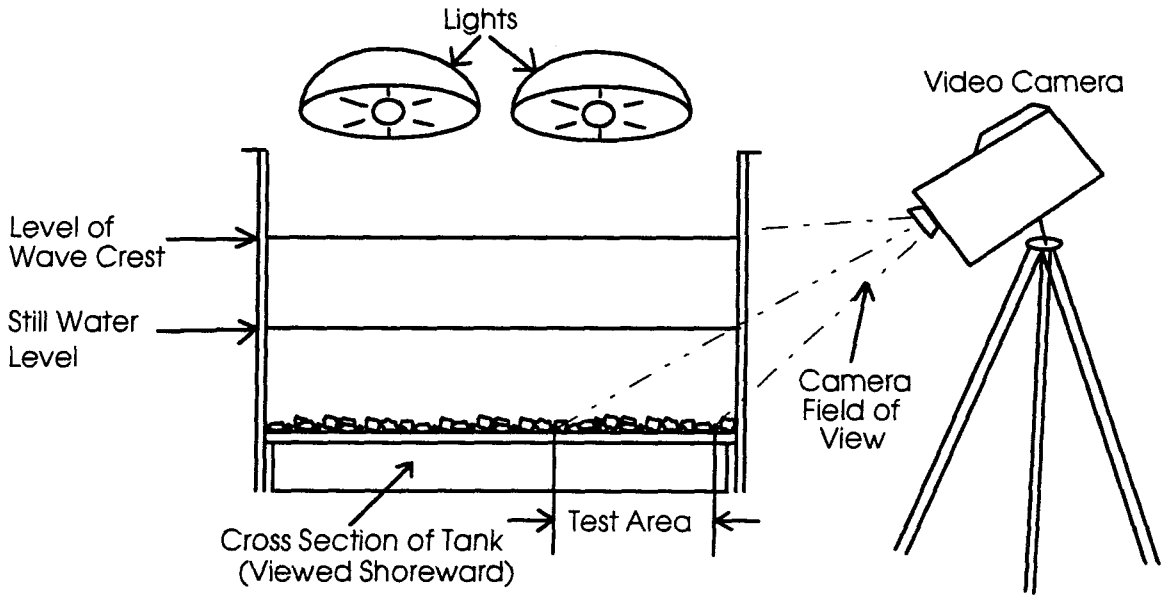

FIG. 2.26. Schematic of Sideview Observation Camera.

test section started 15 cm from the sidewall and extended at least an additional 20 cm towards the center of the tank. At the still water level, the entire observed area could be viewed through the glass without crossing the top surface of the water. The shutter speed on the camera was set to 1/1000 second for all sideview observations.

An opaque lucite panel was placed on the far side of the test section to provide a uniform background for the oblique angle observations. This panel was not illuminated since this would direct light into the video camera and cause the particles in the bed to be underexposed and difficult to define. The bed was illuminated with the two 200 watt bulbs, located as described in Section 2.4.1. This lighting arrangement allowed the simultaneous recording of overhead and sideviews of the bed during the same experiment.

2.4.3 Data Acquisition / Image Processing

The images recorded on videotape were digitized using a frame grabber card (Imaging Technologies Inc. Model: PC- Vision Plus) installed on an IBM AT compatible minicomputer. The control software package for the frame grabber card, entitled VICAR, was developed by Jean Lorre and Mark Mosher of the Jet Propulsion Laboratory in Pasadena, California. The VICAR package also contained programs for performing image manipulation and analysis of the data digitized with the frame grabber card.

The system used to acquire the digitized images is described in Figure 2.27. The output from video camera or videotape editor (Panasonic Model AG-7500) is digitized by the frame grabber card at a rate of 30 frames per second. The color pixel inputs are converted to integer gray level intensities ranging from 0 for black to 255 for white. Any particular digital image may be loaded into the computer memory by the image processing software. The procedure of saving an image can take as long as several seconds for a 480 x 512 pixel image. For this purpose, the videotape editor was capable of advancing recorded images incrementally by scrolling video frame. This allowed the accurate

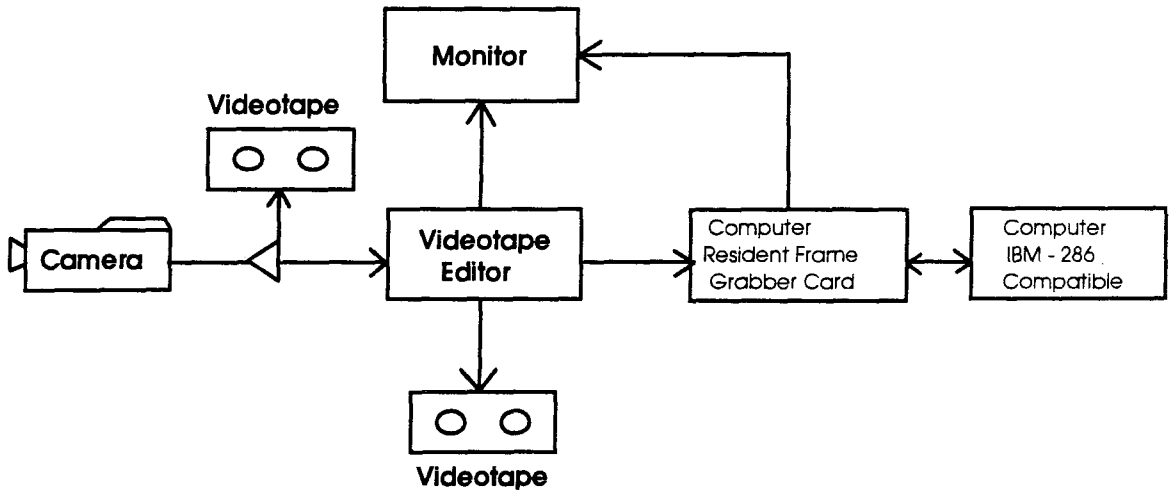

FIG. 2.27. Schematic of Image Acquisition and Processing System.

positioning of the frame to minimize flutter and video synchronization problems. Some small fluctuation of the still video images did occur, causing distortions in the digitized frames. The correction of these distortions is discussed in Section 3.1.2.

2.5 WATER PARTICLE VELOCITY MEASUREMENTS

2.5.1 Laser Doppler Velocimeter

A two dimensional Laser Doppler Velocimeter (LDV) developed by Skjelbreia (1987) was used to measure water particle velocities in the tank. The laser, optical elements and photodetectors are mounted on a traveling carriage suspended from tracks on the ceiling of the laboratory, as shown in Figure 2.28. The entire LDV apparatus rests on an inner frame which may be raised and lowered by means of twin screw jacks. The elevation of the inner frame can be determined within 0.1 mm by means of a Vernier scale.

The LDV employs an optical arrangement in which the reference beam is not required to pass through the focal volume. Thus, measurements can be taken very close to either the free surface or the bottom boundary. In the downward looking mode the reference beam is passed above the scatter beam while in the upward looking mode the

FIG. 2.28. Photograph of the LDV Carriage.

optics are adjusted so that it passes below the scatter beam. These experiments employed both observation modes. Velocity measurements were obtained as close as 1 mm from the false bottom of the tank.

A schematic for the LDV apparatus is shown in Figure 2.29. This arrangement is identical to that used by Skjelbreia except that a Melles Griot polarized 10 mW Helium-Neon laser (Model 05-LHP-991) was substituted for the original 5 mW scattering and reference beam laser. The use of a higher wattage laser resulted in a better signal input for the signal processor. This was especially true for measurements over the bed of particles when the signal was occasionally reduced by the presence of rock dust in the water.

Figure 2.30 shows pictures of the transmitting and receiving optics of the LDV. The beam from the 10 mW laser is divided with a polarizing beam splitter cube so that 90 percent of the laser power is directed toward the scatter beam while 10 percent of the power goes into the reference beam. The beams are then both passed through Bragg Cells (Coherent Model 305) so that the relative frequency shift between the two beams is 500 KHz. The beams are then passed through the tank by a system of right angle prisms and mirrors. After passing through the tank, the reference beam is split and directed into two photodetectors (photo-diode model EG&G DT-25-8237).

A second laser (Melles Griot model 05-LHP-151) with a power of 5 mW is used for alignment purposes only and is switched off during LDV operation. The beam from this laser is split into four parts. Two beams define the observations directions for the upward looking mode and two beams define the downward looking mode. These beams are optically directed to intersect with the scatter beam and form a focal volume with a maximum diameter of 0.7 mm and a maximum length transverse to the tank of 1.3 cm. The observation direction of the receiving optics is adjusted by focusing light from the alignment beams on the two photodetectors, one photodetector for each direction. During

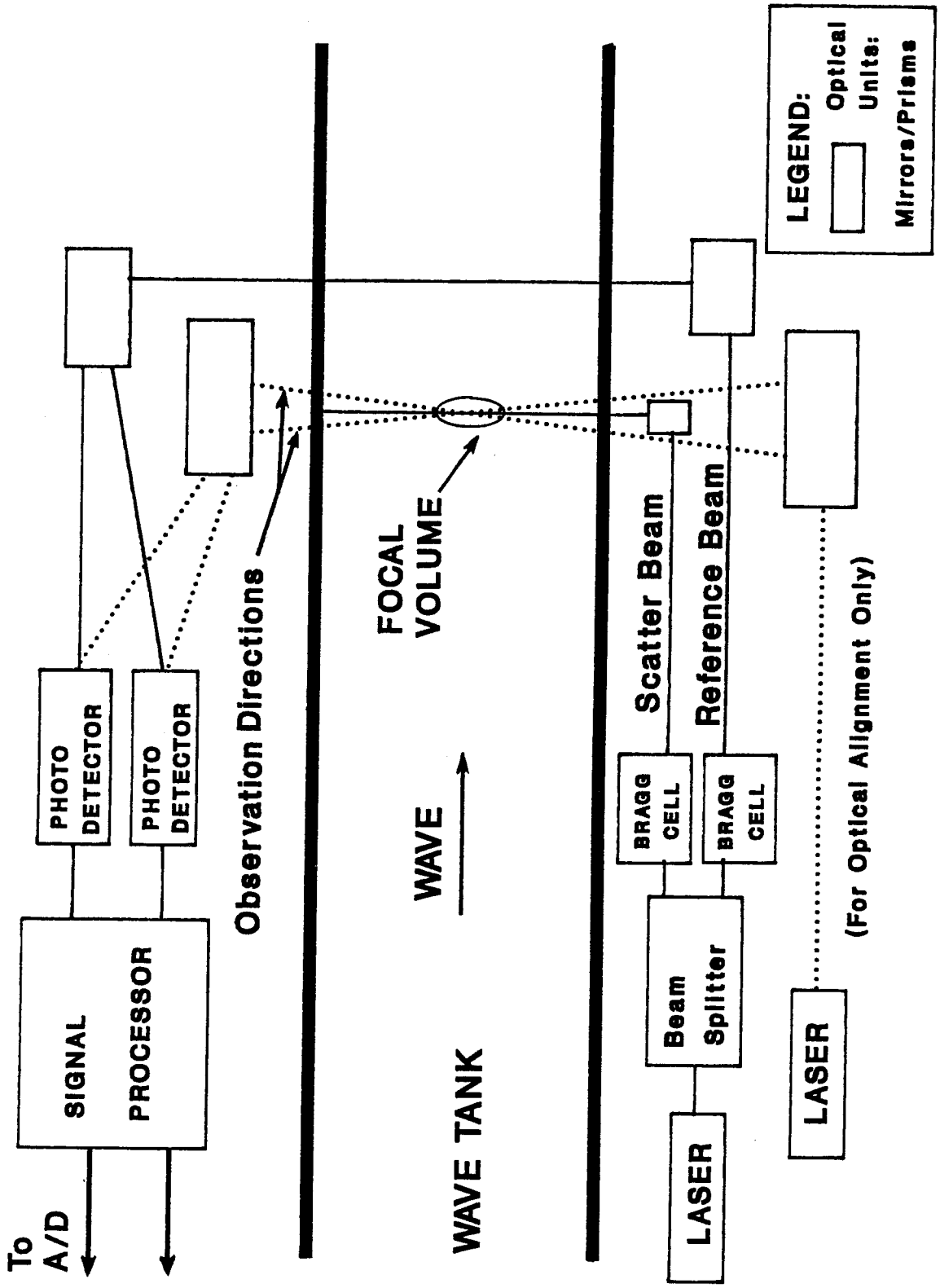

FIG. 2.29. Schematic of the Laser Doppler Velocimeter.

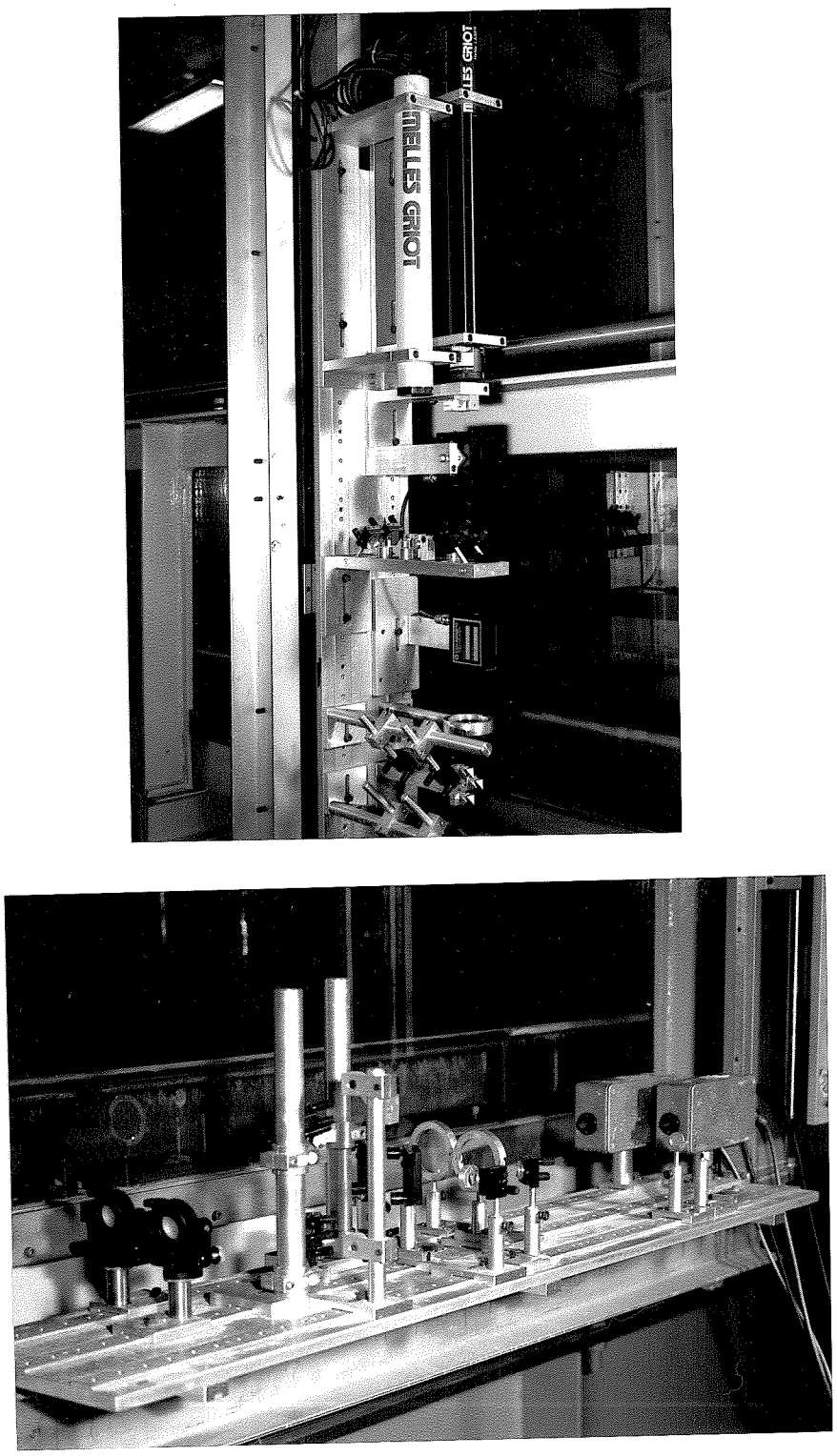

FIG. 2.30. Photographs of Transmitting and Receiving Optics.

the operation of the LDV, the alignment laser is switched off and the scattered light from the focal volume radiating in the observation directions is mixed with the reference beam signal. Further details of the construction of the LDV and the LDV carriage are discussed by Skjelbreia (1987).

As a small particle in the water crosses the focal volume, the frequency of the observed light scattered from the scatter beam by the particle is shifted by an amount dependent upon the particle velocity and the observation direction. This shifted or Doppler frequency can be expressed as:

$$\Delta\upsilon = \frac{n}{\lambda}\vec{q}\left(\vec{e}_i - \vec{e}_o\right) \tag{2.2}$$

where $\Delta\upsilon$ is the difference between the frequency of the incident beam and the observed frequency, n is the index of refraction of water, λ is the vacuum wavelength of the laser, $\vec{q}$ is the particle velocity, and $\vec{e}_i$ and $\vec{e}_o$ are unit vectors in the scatter beam and observation directions respectively. As a result of this frequency shift, the frequency difference between the scattered light and the reference beam is no longer 500 KHz, but is greater or smaller depending on the motion of the particle. The output current, I(t), of the photodetectors reflects the difference between the two frequencies:

$$I(t) = A(t)\cos(500 - \Delta v)t + C(t) \tag{2.3}$$

A(t) and C(t) are functions determined by the intensity of the mixed laser light and by the characteristics of the particles. LDV measurements made in this investigation used the particles naturally present in the local water supply. No additional particles were added to the water.

2.5.2 Signal Processing

The signal from the photodetectors is filtered, amplified and then processed by a signal processor developed by Gartrell (1979). The components of the signal processor are shown in schematic form in Figure 2.31.

The output of the photodetectors is sent to a highpass and lowpass filter combination in order to eliminate signal noise outside the range of interest. During the experiments, the output of the bandpass filter was restricted to frequencies between 400 KHz and 600 KHz. The filtered amplified signal is passed into a level detector which identifies the Doppler-shifted burst of scattered light caused by the passage of a particle. The counter measures the frequency of the burst and converts that frequency into a voltage output. After setting the gain and offset for the output voltage, the signal processor was calibrated with a frequency generator. A typical frequency calibration curve appears in Figure 2.32. The curve uses a second order polynomial least squares fit

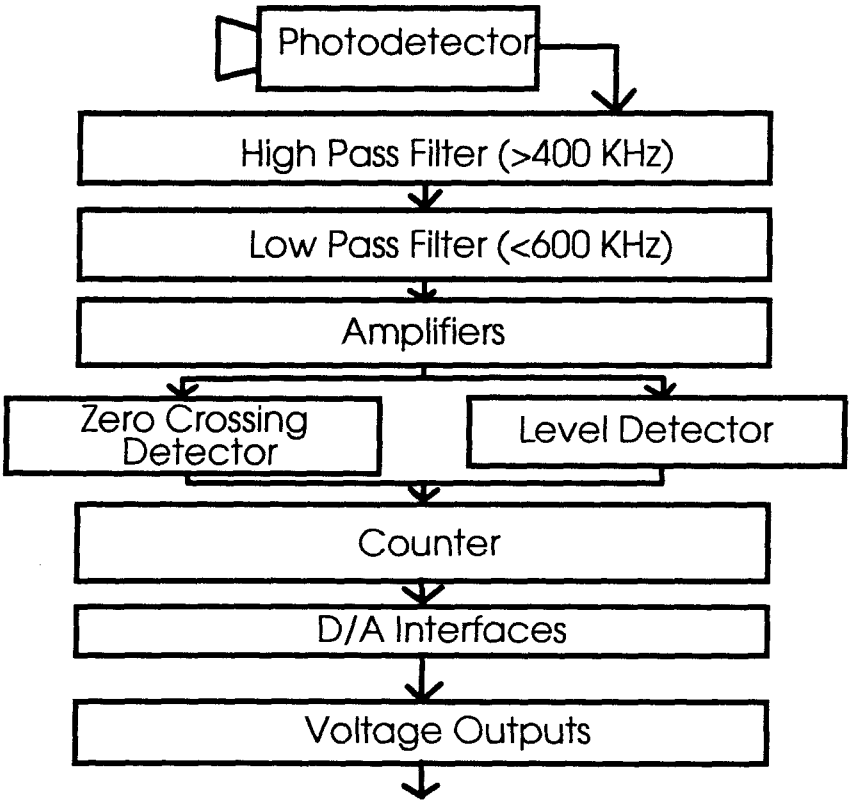

FIG. 2.31. Schematic of Signal Processor.

curve appears in Figure 2.32. The curve uses a second order polynomial least squares fit to define the relation between the input frequency and the output voltage of the signal processor for each channel of the signal processor.

2.6 WATER SURFACE ELEVATION MEASUREMENTS

Water surface time histories were measured with resistance wire wave gauges. A typical schematic of a wave gauge appears in Figure 2.33. The resistance between the two 0.23 mm stainless steel wires varies with their depth of immersion in water. The gauge acts as a variable resistor in the Wheatstone bridge circuit shown in Figure 2.34. The bridge circuit is balanced with the gauge immersed at the still water level. As the water level changes, the voltage imbalance caused by the changed resistance of the gauge is registered by a carrier preamplifier (Hewlett Packard Model 8848A). In addition to conditioning and amplifying the signal from the wave gauge, the carrier preamplifier also provides the excitation signal for the Wheatstone bridge.

The wave gauges used in these experiments were calibrated using a Vernier scale accurate to 0.1 mm. A typical calibration curve is shown in Figure 2.35. Since only solitary waves were used for this investigation, calibration curves were only obtained for water surface elevations above the still water level. The depth of immersion of the gauge was varied in increments of 0.5 cm while recording the resulting voltage change. After recording the datum at each immersion depth, the gauge was returned to the still water, or zero, position to compensate for any dynamic effects due to the passage of a wave. The effect of varying the position of the wave gauge rather than the water level during the calibration process is discussed by Ramsden (1993), and errors caused by the approach of the gauge to the bottom are not significant for the purposes of this investigation.

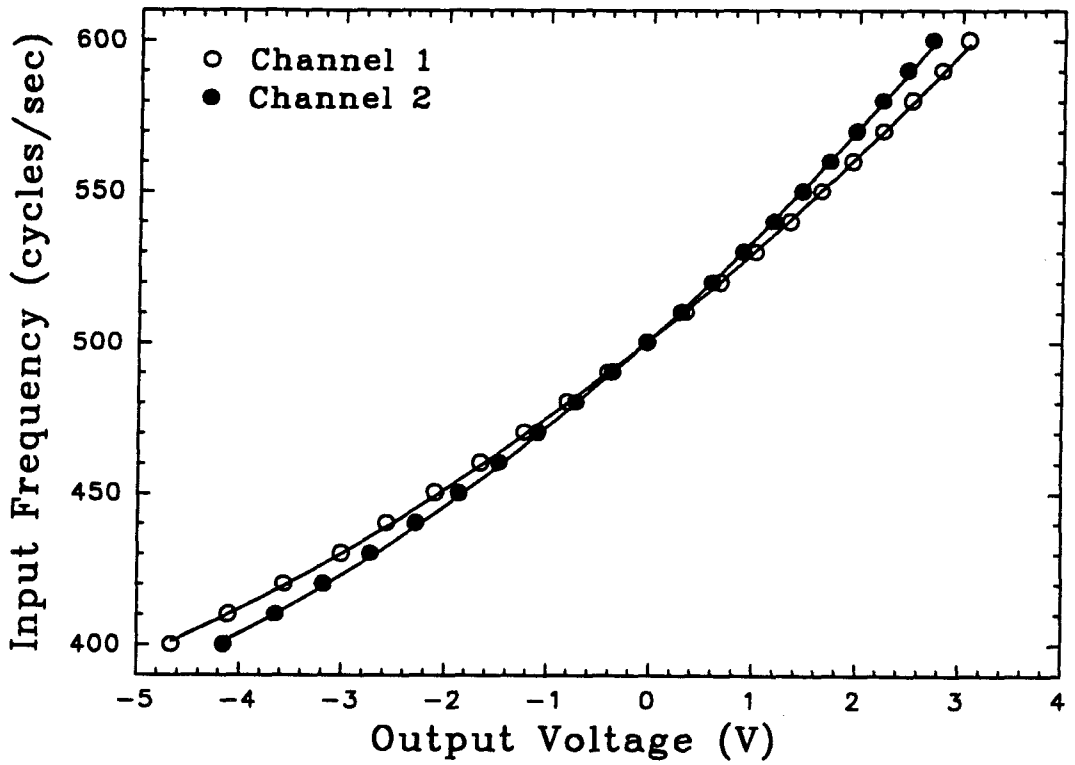

FIG. 2.32. Frequency Calibration Curve for LDV.

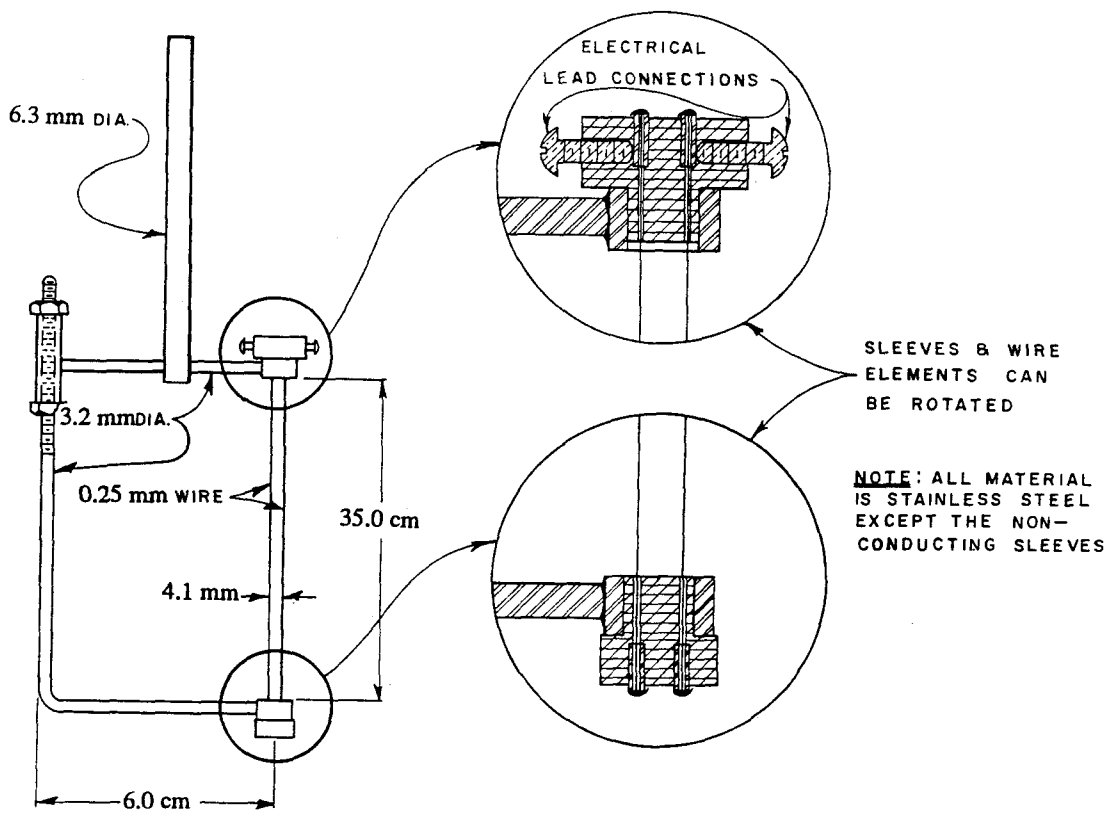

FIG. 2.33. Schematic of Wave Gauge.

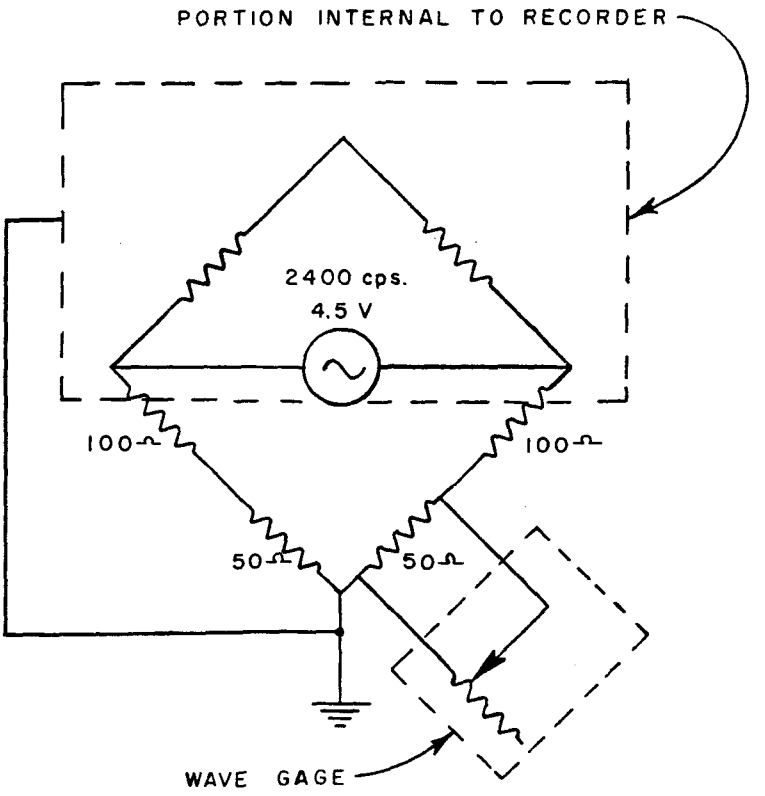

FIG. 2.34. Circuit Diagram of Wave Gauge.

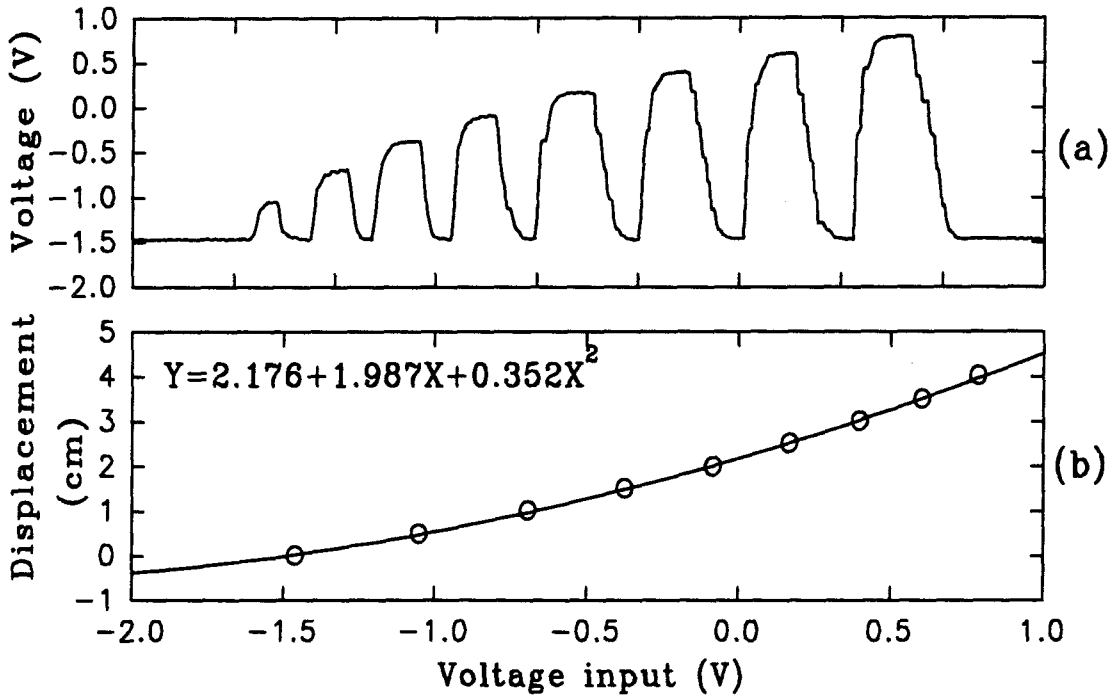

FIG. 2.35. Wave Gauge Calibration Curve.

2.7 DATA ACQUISITION

The voltage signals from the wave gauges, the laser Doppler velocimeter, the LVDT at the wave paddle and the analog/digital interface output to the servo-valve were acquired in digital form with a microcomputer. The computer, an IBM-AT compatible, is equipped with a 12 bit resolution analog to digital interface card with a maximum sampling rate of 1 MHz and a buffer size of 128 Kilobytes. In order not to exceed this buffer size and to monitor several channels of data for the full duration of each experiment, the sampling rate was set at 200 Hz.

2.8 EXPERIMENTAL PROCEDURES

Prior to each experimental series, the slope of the tank was set using a Vernier scale, accurate to within 0.03 mm, located 17.07 m away from the central pivot of the tank support ($\pm$ 1.01 x 10^{-4} degrees). As mentioned earlier, the water level in the tank was maintained by means of an overflow tube and a small amount of water was kept flowing into the tank during the course of the experiments. To generate a plunging, breaking wave, the water level and the amplitude of the solitary wave were adjusted, with the tank tilted to its maximum slope of 0.02, until the wave broke at a distance of 13.4 m from the wave paddle. This breaking location was 0.43 m shoreward from the leading edge of the bed. The breaking location of the wave was determined by visually observing the point where the front face of the wave first became vertical.

2.8.1 Overhead Video Observations

All overhead video observations were made over the bed of angular material in one of three areas located on the centerline of the tank. These areas are defined from the leading edge of the test sections: from 0.33 m to 0.53 m, from 0.63 m to 0.83 m and from 0.93 m to 1.13 m . Two wave gauges were positioned at 7.5 m and 11.1 m from the wave

plate to verify the height and shape of the wave incident on the bed. The camera was positioned as described in Section 2.4.1 and was left with its power on.

Prior to the passage of a wave, the bed was raked and leveled and the water in the tank was allowed 15 minutes to become still. The raking and leveling process itself created a long period wave which required this amount of time to dissipate. The two wave gauges were then calibrated using the method described in Section 2.7. The lights were turned on and the camera was given time to adjust to the increased lighting level. The videotape editor was then turned on to record the video camera image of the bed before the passage of the wave.

The recording time was set at a minimum of 20 seconds to allow for the startup of the editor and to establish a constant tension on the videotape. Recorded segments shorter than 10 seconds were found to contain a distorted signal. In addition, each portion of videotape was used only once, since re-recording over the same part of the tape often caused a noisy or blurred signal.

After recording the initial bed configuration, a wave was generated. The motion in the tank was allowed to dissipate for another 20 minutes. The variation in the water surface of the tank was monitored with the wave gauges to insure that this length of time was adequate for the water to become still and return to its original level. The re-establishment of the original water surface was critical for the overhead observations, since a small change in depth resulted in a significant reduction or magnification of the bed in the video image. After the water in the tank was still, the lights were turned on and a second video segment was taped of the bed configuration after the passage of the wave. This segment was also a minimum of 20 seconds long.

The length of time required for a single run was typically between 45 and 50 minutes long. This included the time to set the bed, wait for the water motion to cease, run

the wave and again wait for motion to cease. In addition, because of the size segregation problems mentioned in Section 2.3.2.1, the entire bed was remixed after every nine or ten runs. Since the remixing process often reduced the clarity of the water, the tank was flushed overnight after it was remixed.

Each experiment for a given wave in a given location was repeated from 15 to 20 times. This was done in order to form an ensemble average of the movement of particles at a given location.

2.8.2 Oblique Sideview Observations

Recordings of particle movement during the passage of a wave were made for each of the cases used for overhead observations. These sideview observations were taken in some instances simultaneously with overhead observations and in some instances in separate experiments.

When conducting a separate experiment to obtain a sideview of particle movement, a single wave gauge was positioned 11.1 m from the wave generator to monitor the wave incident on the bed. The bed was raked and leveled and the motion in the tank was allowed 20 minutes to cease. While the wave motion in the tank was decreasing, the camera shutter speed was adjusted to operate under ambient lighting conditions. The camera then recorded on videotape as a pointed rod was placed on each of four fiduciary markers in the camera field of view. This served as the means to calibrate the scale of the video image and also to provide a square grid by which the oblique view could be rotated.

When the water in the tank was still, the wave gauge was calibrated. Then the camera shutter speed was set to 1/1000 second and the lights were turned on. The recorder was started and a wave was produced. The recorder remained on until the wave

had passed, and then both the recorder and the lights were switched off. The bed was then leveled and raked again for the next run. Each sideview experiment took approximately 30 minutes to perform. Since the oblique views of the bed of material were more sensitive to any cloudiness in the water than the overhead views, the water in the tank was replaced after every five runs.

When sideview observations were conducted simultaneously with overhead observations, the calibration procedure explained above was performed after the bed had been raked and leveled. The initial bed configuration was then recorded with the overhead camera and then the sideview recording was made during the passage of the wave. It should be noted that the overhead views and sideviews observed different portions of the bed during the same experiment and so were not directly related.

2.8.3 Water Particle Velocity Measurements

LDV measurements were obtained for each wave condition both with the test section filled with angular material and then with the anodized aluminum plate in place of the bed of particles.

Water particle velocity measurements were made at several elevations over the bed for each incident wave. The scatter beam from the LDV apparatus was positioned at a longitudinal location corresponding approximately to the center of area observed by the video cameras. The elevation of the top of the bed was determined by the "foot" gauge. The foot gauge was then moved over to a fixed location on the glass false bottom and the relative difference, Δz, in elevation was recorded. A pointed brass rod, or point gauge, was then substituted for the foot gauge and was raised a distance $(5+\Delta z)$ cm above the glass false bottom. The scatter beam from the laser was positioned so that the tip of the pointed rod blocked out approximately one half of the beam. This elevation was then fixed as 5 cm above the top of the bed. This elevation was chosen to allow a clear view of

the alignment laser. The vernier scale on the LDV support carriage was used to measure the elevation of the laser after the initial position was established. For the aluminum plate experiments, the elevation of the top of the plate was measured directly with the point gauge and the elevation of the laser beam was determined similarly by intersecting the laser with the tip of the point gauge at a measured distance of 5 cm over the plate.

In order to minimize the amount of time that the LDV signal was blocked by moving particles at the lower observation elevations, the scatter beam was slightly inclined from the horizontal at an angle of 1.1 degrees down towards the bed. This had the effect of allowing particles near the side walls of the tank to travel with the wave without interrupting the beam path to the observation volume. The focal volume of the LDV itself was only slightly distorted by this alteration. The scatter beam was left in the horizontal position for measurements over the anodized aluminum plate.

Two wave gauges were placed in the tank, one at a distance of 11.1 m from the wave generator at its rest position and one directly over the laser beam. In some instances, the depth of the water was insufficient to allow both the wave gauge and the laser to occupy the same location, and the second wave gauge was placed a distance of 2 cm behind or shoreward of the laser beam.

After aligning the laser at a given location and elevation, the bed was raked and leveled and motion in the tank was allowed 20 minutes to cease. The wave gauges were then calibrated. The desired wave was then generated. The data acquisition system was triggered to capture the signals from the LDV, wave gauges and wave plate LVDT at start of motion by the hydraulic wave generator. The data were acquired for at least 20 seconds, which allowed time for the wave to travel from the wave generator through the test area and for the wave plate to reset to its original position.

The bed was then raked and leveled and the motion in the tank was allowed to dissipate for at least 20 minutes. The water particle velocities were monitored to insure that no residual motion was present in the tank. The amount of time for each experiment varied from a minimum of 30 minutes depending on whether the elevation of the laser was changed. If the LDV positioned was changed, a realignment of the laser was performed. After passage of a given wave, the resulting LDV signal was examined to determine if any portion of the signal had been blocked by the passage of a particle. At elevations close to the bed, several runs were required in order to obtain an adequate signal.

The experimental conditions for the LDV runs over the bed of particles were duplicated with the aluminum plate at the same location in place of the rock. LDV, wave gauge and LVDT data were again acquired for a 20 second interval after the start of the signal to the wave generator. Wave motion was allowed to dissipate for 20 minutes and was again monitored by means of the LDV. Typically, for the flat plate experiments, a single measurement was recorded for each wave condition, elevation and location along the tank.

CHAPTER 3

METHODS OF ANALYSIS FOR VIDEO IMAGES

Each of the video images recorded during these experiments was digitized into an array of 480 by 512 pixels. The direction along the tank contained 480 lines per video frame while each line consisted of 512 samples taken perpendicularly in the direction across the tank. At each point in the array, the video information was recorded as a light intensity ranging from 0 for black to 255 for white. As mentioned in Chapter 2, the rock in the test section was colored according to size fraction: white rock, less than 3.6 mm, registered at intensity levels from 190 to 255; yellow rock, between 3.6 mm and 4.8 mm, gave intensity levels from 125 to 170; and green rock, between 4.8 mm and 9.5 mm, showed intensity levels of 60 to 120. Intensities below 60 occurred chiefly because of deep shadows between particles. Using the intensity level as an indicator of rock color, it was possible to analyze the composition of the rock bed in the video images.

3.1 DETERMINATION OF BED COMPOSITION

Figure 3.1 shows photographs of the digitized images of two typical bed configurations prior to the passage of a breaking wave. In each photograph the left side shows the rock bed at the station in the tank closest to the wave plate while the right side is the station furthest shoreward. Section 2.3.2.1, it will be recalled, described the unfeasibility of achieving a completely uniform bed of material for the experiments. In Figure 3.1(a) it can be observed that there appears to be more of the smaller lighter colored material near the left and more of the larger darker material at the right of the photograph. Figure 3.1(b) shows the result of averaging the measured light intensities for a given station across the 512 pixel width of the image. Here, the average intensity at a location is given as a percentage of the maximum intensity of 255. For example, at 50

(a)

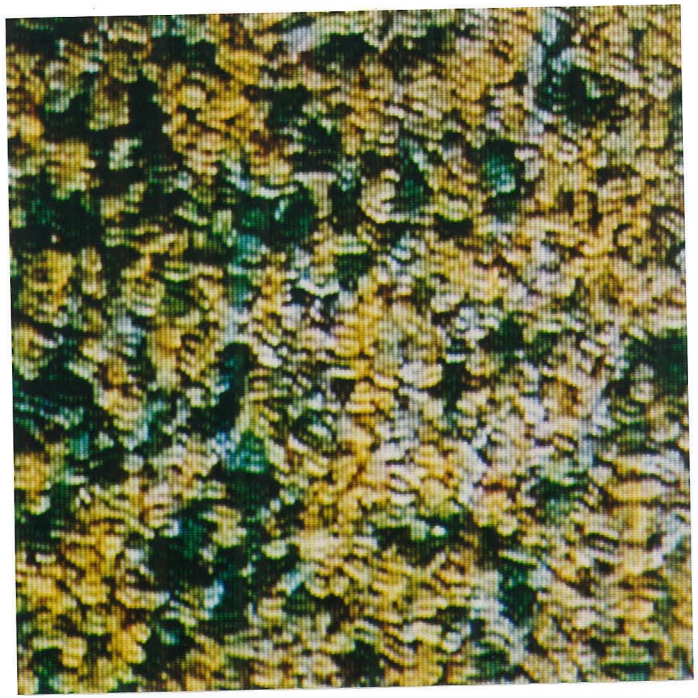

(c)

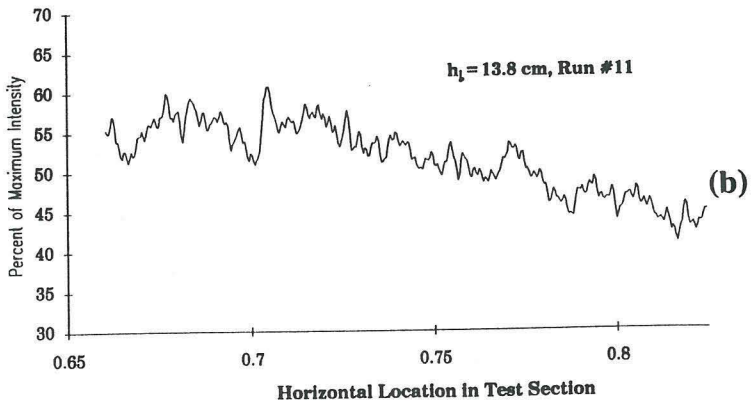

(b)

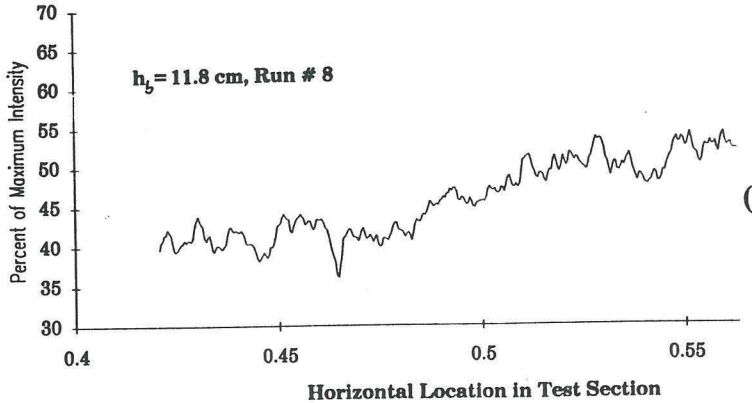

(d)

FIG. 3.1. Views of Typical Bed Composition.

percent of maximum intensity, the average value of all 512 pixels is 128 indicating that about half the pixel values came from yellow and white particles and half from green particles and deep shadows. For the experiment shown in Figure 3.1(b), the average intensities decrease in the downstream direction along the bed. This is in accordance with the relative decrease of the small light colored particles compared to the large darker ones going from left to right in the image. In addition, local maxima and minima in the average intensities occur as a result of patches of similar colored material which substantially affect the local average intensities.

In Figure 3.1(c), in a different experiment, the number of light colored particles appears to increase in going from left to right in the image. The average intensity record in Figure 3.1(d) confirms this observation. Again, clusters of light or dark particles produce local minima and maxima in the intensity record. During this study, the average intensity of the bed was not observed to increase or decrease consistently in any one direction, but rather was different with each different experiment.

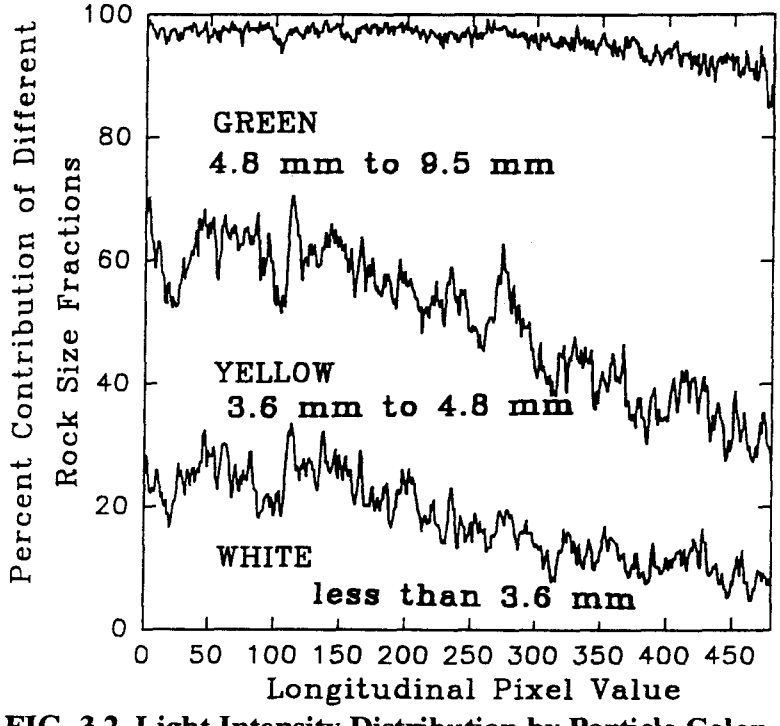

FIG. 3.2. Light Intensity Distribution by Particle Color.

If the image of the rock bed is decomposed into the light intensities corresponding to each color of rock, an estimate of size distribution can be obtained. Figure 3.2 shows the result of counting the number of pixels in each of the three ranges of light intensities for the colored rock at each of the 480 longitudinal stations in the image of the particle bed. The graph shown in Figure 3.2 corresponds to the image shown in Figure 3.1(a).

Since the maximum size of the rocks in each color range is known, a distribution of particle sizes can be plotted for the cumulative fractions of white, yellow and green rocks at each longitudinal pixel value in Figure 3.2. In addition, although the size distribution consists of only two points, the mean particle size can be roughly estimated from these plots. For example, in Figure 3.2 at a longitudinal pixel value of 50, the relative proportions of green, yellow and white rock are 31.7 percent, 38.8 percent and 29.5 percent respectively. This indicates that at this particular longitudinal location 68.3 percent of the material is smaller than 4.8 mm and 29.5 percent is smaller than 3.6 mm. If these two points are plotted on a grain size distribution, the D_{50} diameter occurs at a grain size of 4.25 mm. From Figure 3.1(b), the average light intensity at the same longitudinal location (pixel value = 50) is 146 or 57 percent of the maximum value of 256.

Estimating the D_{50} grain size at different locations in the bed and comparing these mean grain size estimates to the average light intensity at those locations results in a curve relating intensity to mean particle size. Figure 3.3 shows the result of plotting the estimated mean grain size at several locations in Figure 3.2 against the average intensity observed at those locations. The data have been fitted with a least squares fit to a second order curve. This curve may then be used to estimate the grain size at a given location along the tank using the average light intensity level at that location. When several curves were plotted for different images of the rock bed in different experiments, the correspondence curves did not vary appreciably in slope or curvature. Hence, the

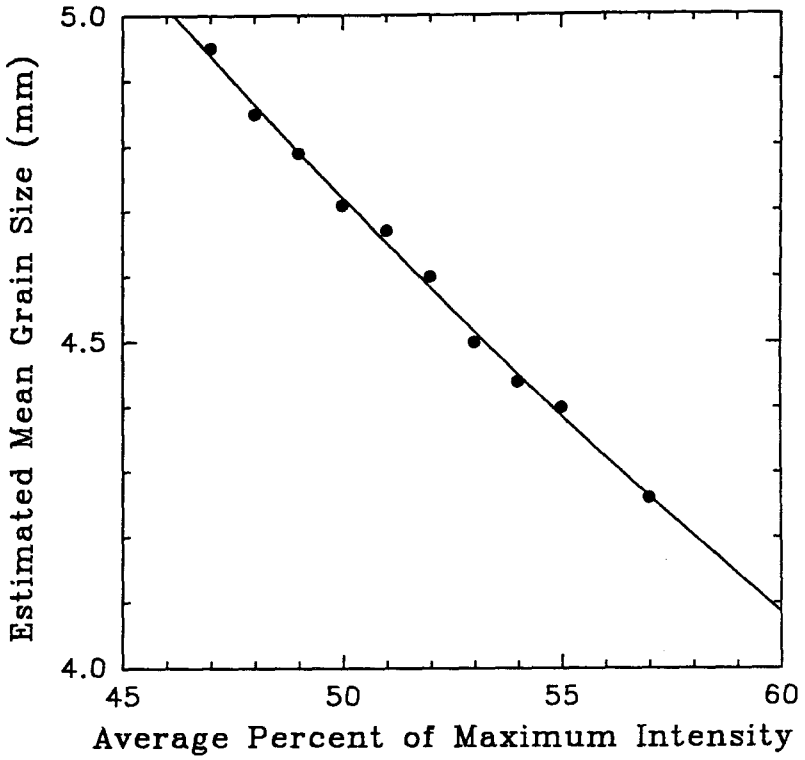

FIG. 3.3. Calibration Curve for Determination of Mean Grain Size.

calibration curve shown in Figure 3.3 was used throughout the study to estimate the composition of the rock bed.

It is to be noted that for all the recorded images in all the experiments, the average light intensity for the whole image ranged between 123 and 130, with an average value of 125.5. At this light intensity (average percent of maximum = 49.2) the overall mean grain size for the bed in all experiments was computed to be 4.76 mm.

3.2 FILTERING AND ANALYSIS OF OVERHEAD VIEWS

Figure 3.4 shows a typical pair of images used to compute the amount of material movement under a wave from a view directly above the rock bed. The photographs in Figure 3.4(a) and 3.4(b) show the video record of the rock bed before and after the passage of the breaking wave, respectively. The corresponding photographs in Figure 3.4(c) and 3.4(d) are the black and white digitized images of 3.4(a) and 3.4(b). If the two

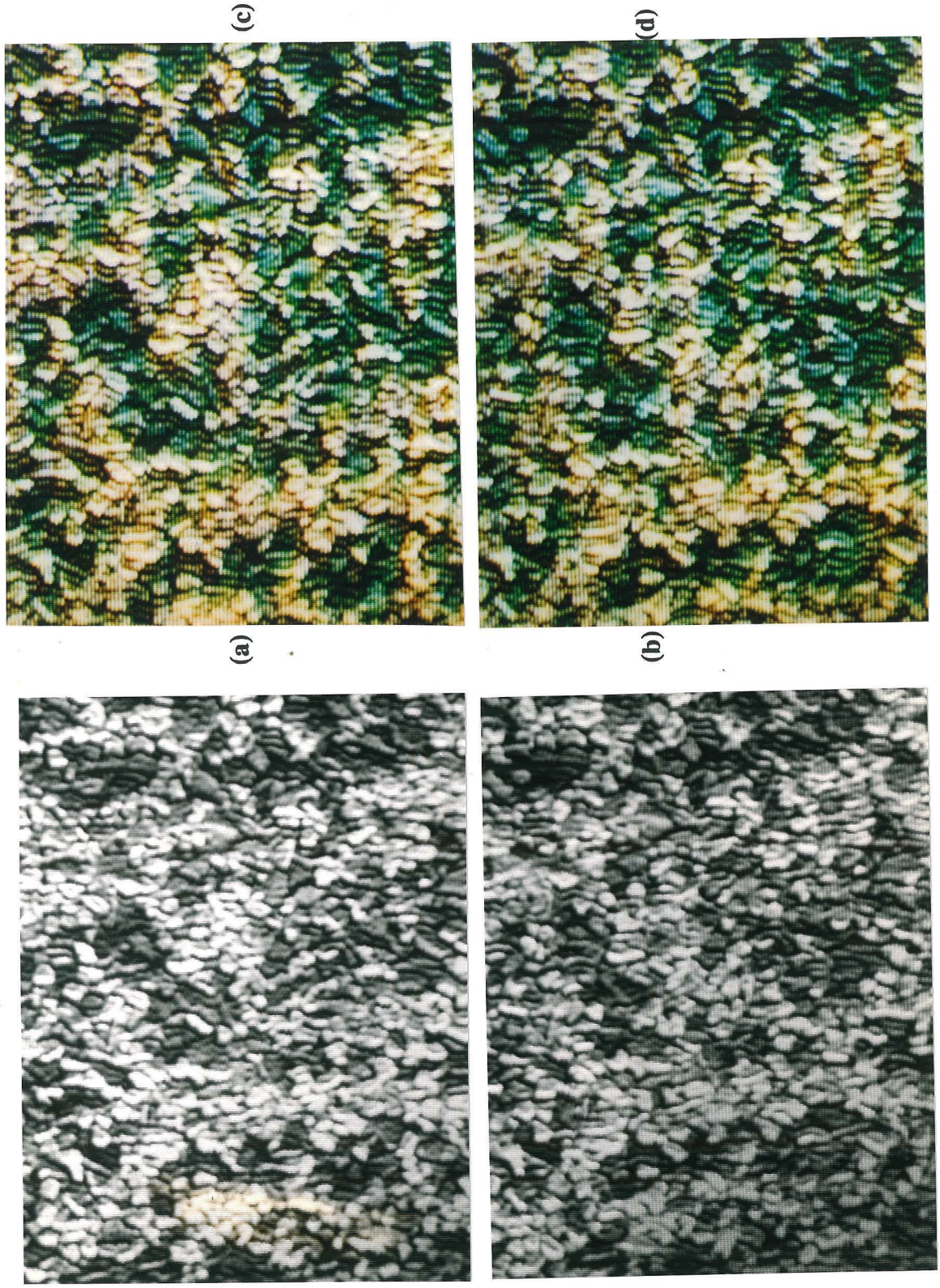

FIG. 3.4. Typical Video Images and Digitized Light Intensity Images.

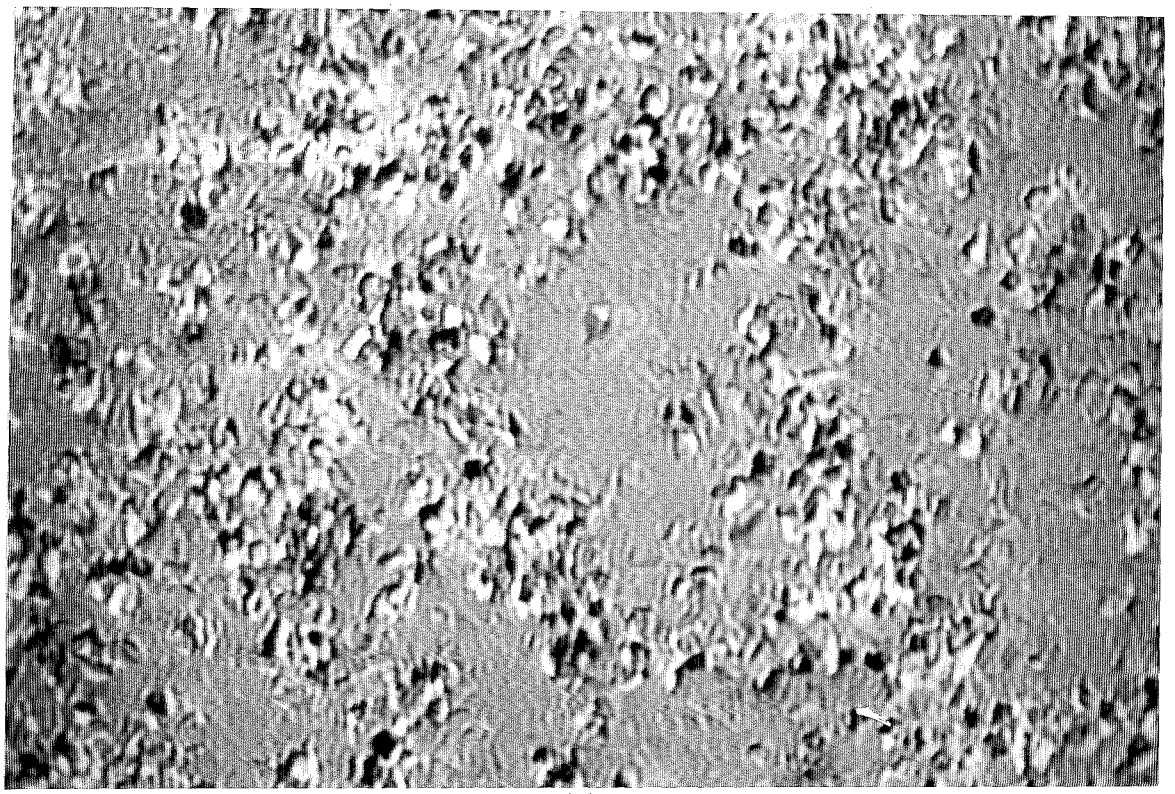

(a)

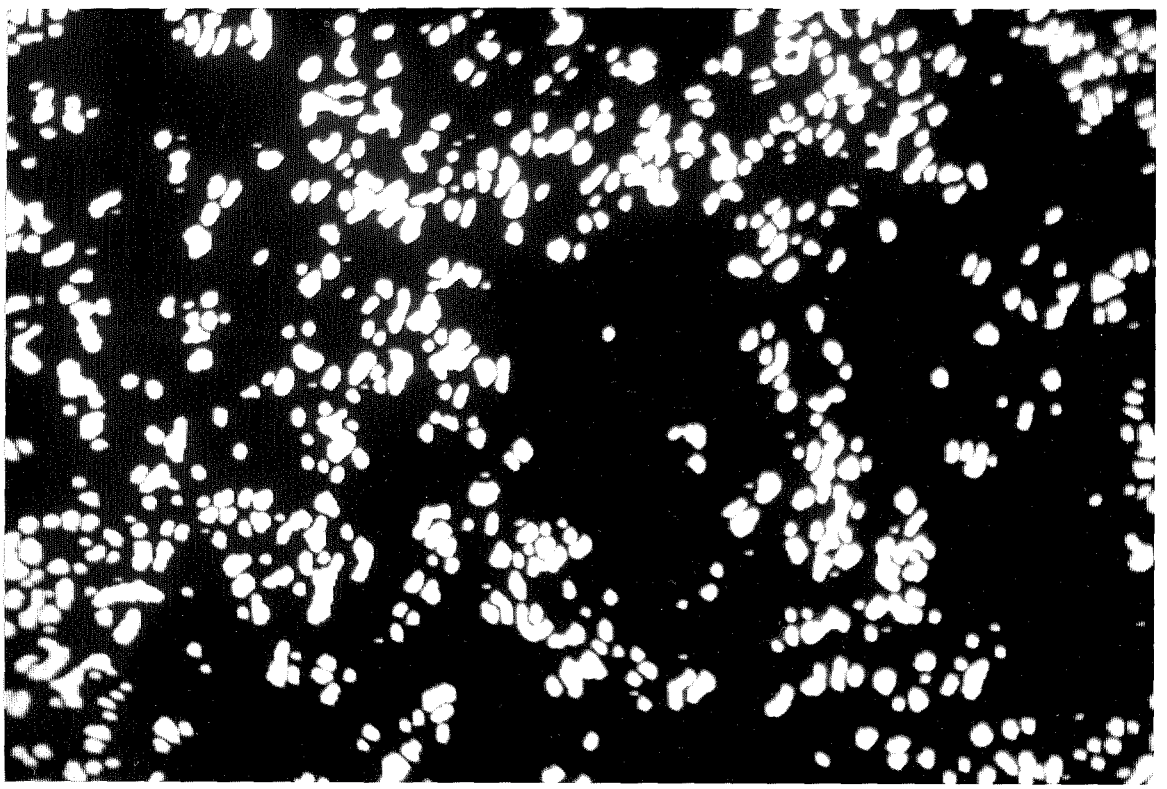

(b)

FIG. 3.5. Typical Image Comparison and Resulting Filtered Image.

views of the particle bed are compared carefully, differences can be observed in the positions of the rocks in the bed.

The negative of one image can be obtained by subtracting the measured light intensity in each pixel from the maximum value of 255. By adding intensities from the negative of the image of the bed before wave passage to the intensities in the image of the bed after wave passage and dividing the sum by two (to keep the range of intensities between 0 and 255), a visual comparison of the two frames is produced.

This comparison is shown in Figure 3.5(a). Here if, after the wave, a dark particle is in a position occupied formerly by a light particle, the comparison shows a dark spot. If a light particle is in a position formerly occupied by a dark particle, the image shows a lightened area. Because of the different colors of the particles and the range of intensities in each color, even particle removal or deposition from a cluster of same colored particles is observable. The only case in which it is difficult to see particle movement with this type of comparison is when a particle is removed from a cluster of the same colored particles and another particle of the same color is concurrently deposited in the same position without greatly affecting any of the surrounding particles. This study did not estimate the frequency of this type of occurrence.

Another feature that is observable in Figure 3.5(a) is the appearance of thin light and dark shadows in the comparison between the two images. These shadows have two main causes. Any small variation in the depth of the water at the observation location changes the magnification of the image of the rocks below. Thus, if the water level in the view of the bed after wave passage is slightly different than that before wave passage, or if a small ripple occurs at the time of observation, the two images no longer match exactly. The difference results in the appearance of small edges or shadows around the individual

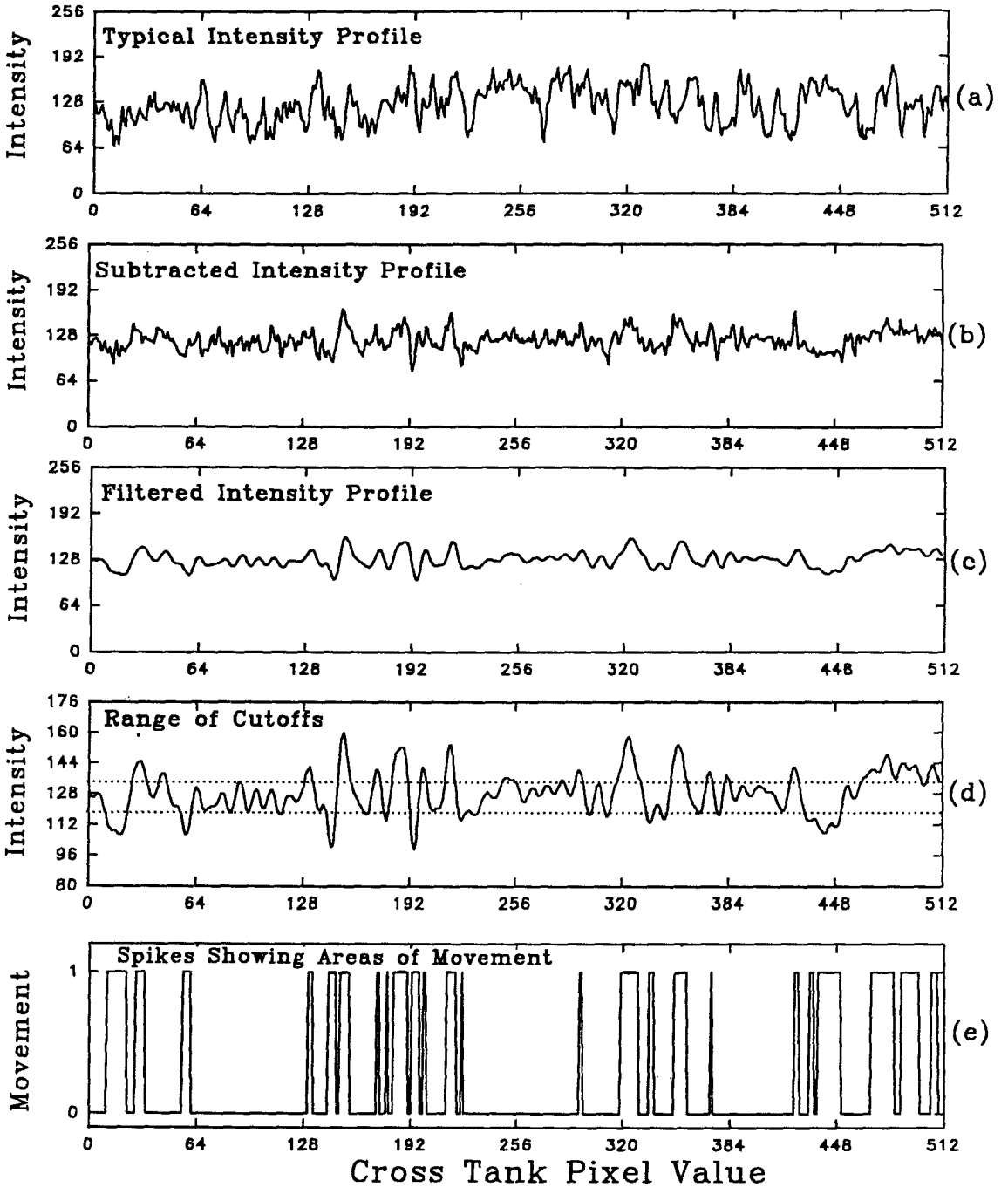

FIG. 3.6. Criteria for Filtering of Overhead Image.

rock pieces. In addition, if a rock is slightly displaced but does not move out of its original position, this movement also appears as a line or shadow in the compared image.

Since the lines and shadows in the image comparison make it difficult to quantify the amount of particle motion in the experiment, the comparison images were filtered to reduce this effect. The result of filtering the comparison image in Figure 3.5(a) is shown in Figure 3.5(b). Figure 3.6 illustrates the method used to filter comparison images. The graphs in Figure 3.6 are for intensities observed at a single longitudinal location in the tank during a typical experiment. Thus only one line of data, taken in the direction across the tank is being shown. The actual images consist of 480 such lines.

Figure 3.6(a) is a typical measured intensity in the bed before the passage of the wave. Figure 3.6(b) shows the result of superimposing the negative image of the intensities in the bed before the wave and the positive image of the intensities after the passage of the wave. Here, an intensity of 128 would denote no observed difference between the two images. Along with the larger definite peaks due to movement, many high frequency oscillations are visible in the superimposed image. These correspond in part to the effects mentioned above and in part to the physical features of the moved rock pieces.

In order to reduce the high frequency oscillations, the image was transformed using a two-dimensional FFT in the spatial domain. Since the oscillations occurred over small distances, a cutoff filter was employed that eliminated any oscillations smaller than the size of the smallest rock in the bed. For example, for the image in Figure 3.6, the smallest rock would have a width and breadth of four pixels. This corresponds to a spatial frequency of 64 cycles per line in the image. Accordingly, oscillations of frequency higher than 64 cycles per line were removed by multiplying the transformed image by a filter

window with a value of 1 for frequencies less than 64 cycles, decreasing exponentially to a value of 0 for frequencies greater than 66 cycles.

Figure 3.6(c) shows the filtered intensity profile. Although some small oscillations are visible, the large scale differences have been enhanced. Figure 3.6(d) shows the final stage in the filtering of the comparison image where the data above and below the range shown with dotted lines were retained as evidence of material movement. The range for the cutoff values was determined by trial and error by observing the values for which the filtered image showed an abrupt jump in total calculated movement and by visually comparing the filtered image with the unfiltered one. Note that the ordinate in Figure 3.6(d) is greatly magnified with respect to the ordinates in Figures 3.6(a), (b) and (c).

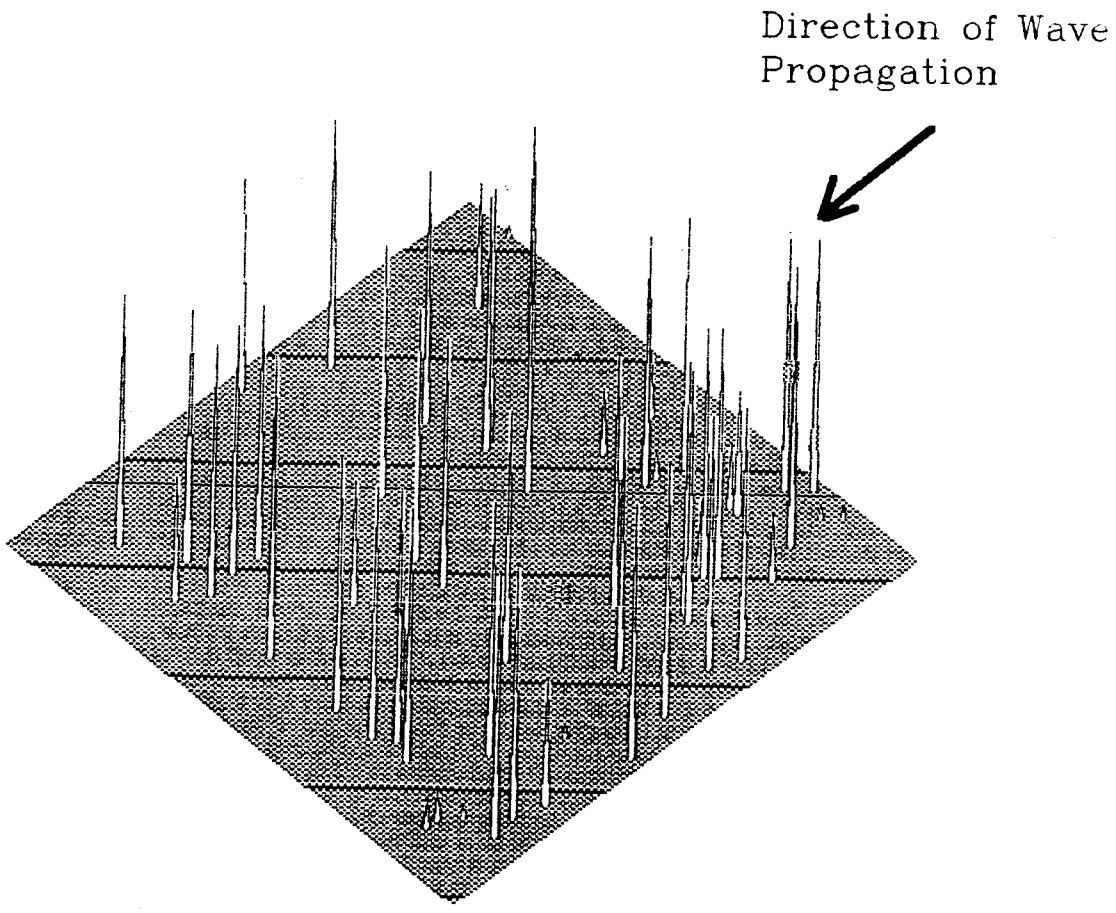

FIG. 3.7. Section of Filtered Image Showing Movement Locations.

Figure 3.6(e) shows the final step in the processing of the comparison of the rock before and after the passage of the wave. After adjusting the width of the movement peaks for the values lost in the cutoff process, the image was adjusted to show a value of 1 for pixels where movement occurred and a value of 0 where there was no material movement. In Figure 3.7, a small area of a filtered image is shown in three-dimensional view. Here the spikes represent particle movement, either the removal or the deposition of material.

The calculated movement at each longitudinal location along the tank was averaged over the 512 pixel width to obtain the percentage of particle movement at that location. For example, if all 512 pixels were of value 1, then the percentage was calculated to be 100 percent; if 256 of the 512 pixels were of value 1, then the percent movement was 50, and so on. In this way the filtered image comparison was related to the total area of the rock bed disturbed during the passage of the wave. Figure 3.8 shows

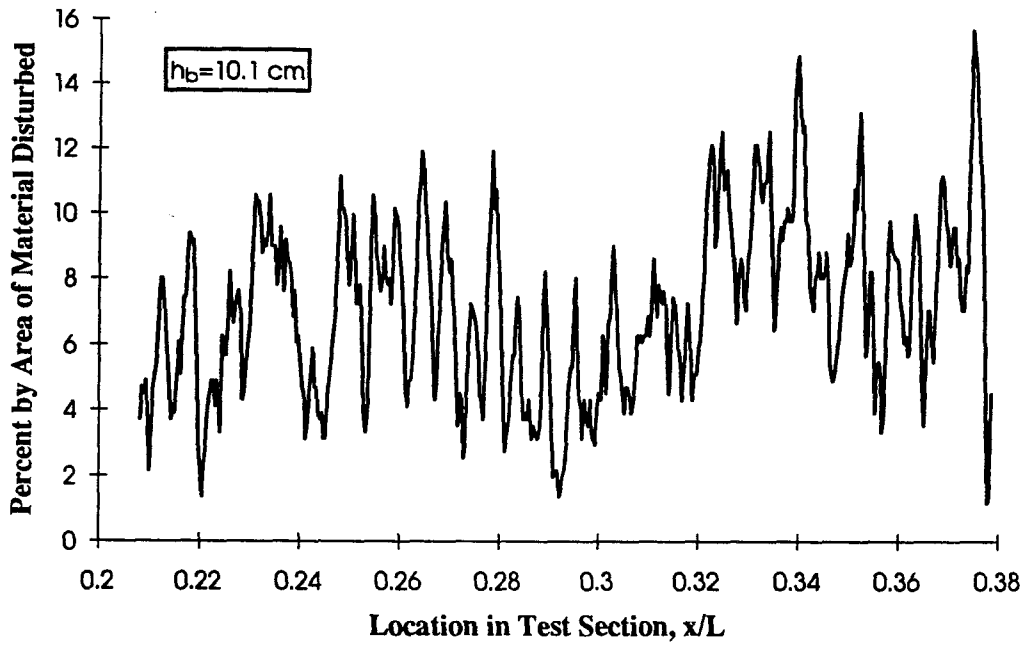

FIG. 3.8. Typical Movement Intensity Record.

a typical calculated movement intensity in a single experiment for a wave with a breaking depth of 10.1 cm at an observation location centered at x/L = 0.29. For this particular experimental run, the percent of total area disturbed varied from about four percent at x/L = 0.22 to about ten percent near x/L = 0.35. Between 15 and 20 repetitions of each experiment were averaged at each longitudinal pixel location in order to obtain an average amount of movement in a particular location under a given wave.

3.3 FILTERING AND ANALYSIS OF SIDEVIEWS

Figure 3.9 shows a photograph of a typical sideview video image of the bed during the passage of a breaking wave. Both the passing wave and the rock bed were recorded in the field of view to allow the direct comparison of particle movement with the location of the wave crest. After the wave had broken, the crest was defined to be at the point of highest elevation in the wave. By comparing successive frames from the video recording, 1/30 of

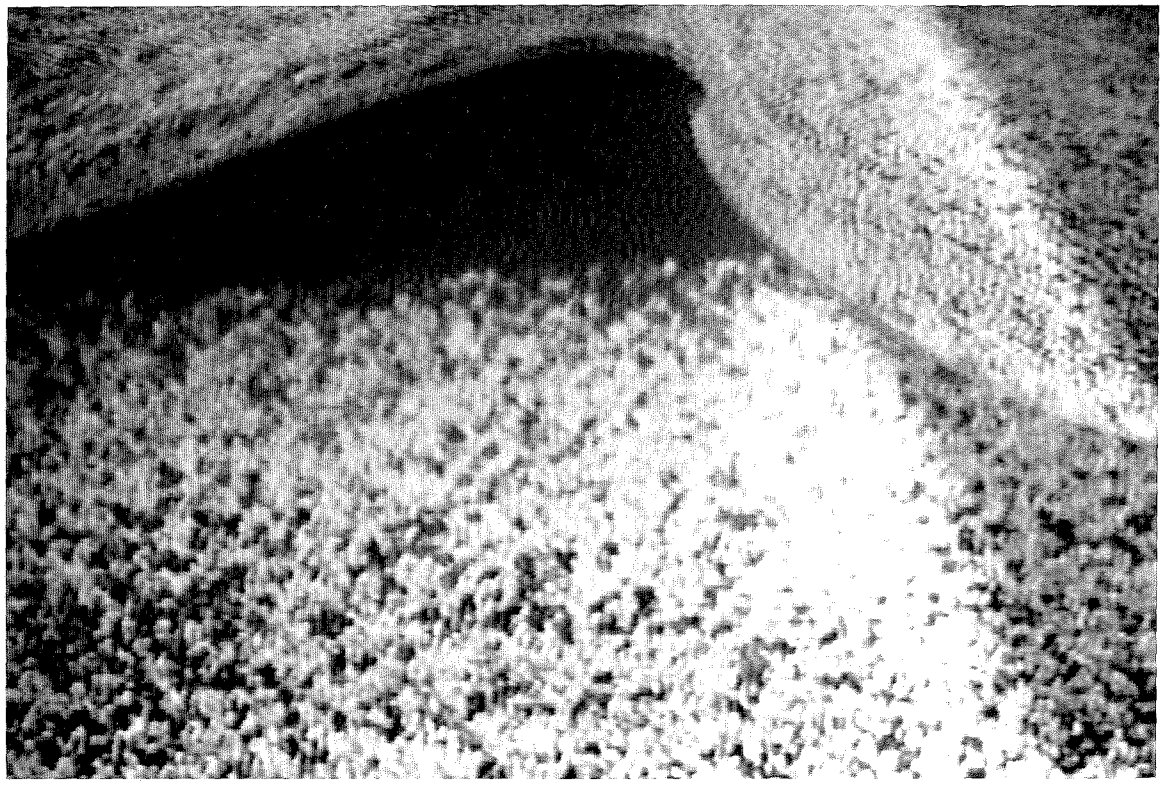

FIG. 3.9. Typical Video Image of Sideview Observations.

a second apart, the incremental movement of material could be measured as the wave passed by the field of view. Slightly to the right of the center of Figure 3.9, a band of bright light is visible. This increased light level is the result of the focusing of the ambient lighting by the curvature of the water surface, and was present to some extent in all of the wave sideviews.

The same procedure used to filter the overhead views of the rock bed was employed to filter the views of the bed taken through the tank sidewalls during passage of a wave. The procedure was adjusted to filter out long frequency spatial variations such as the lighting shift described above. In the case of the focused light under the wave, the spatial frequency was observed to be lower than 6 cycles per line of the image. Accordingly, the filter shape in the frequency domain was adjusted to be zero for frequencies of 5 cycles per line or less as well as for the frequencies above the size of the smallest particle. In addition, the filtered image was cropped to only include the area from 15 cm to 35 cm from the tank sidewalls (see Figure 2.26).

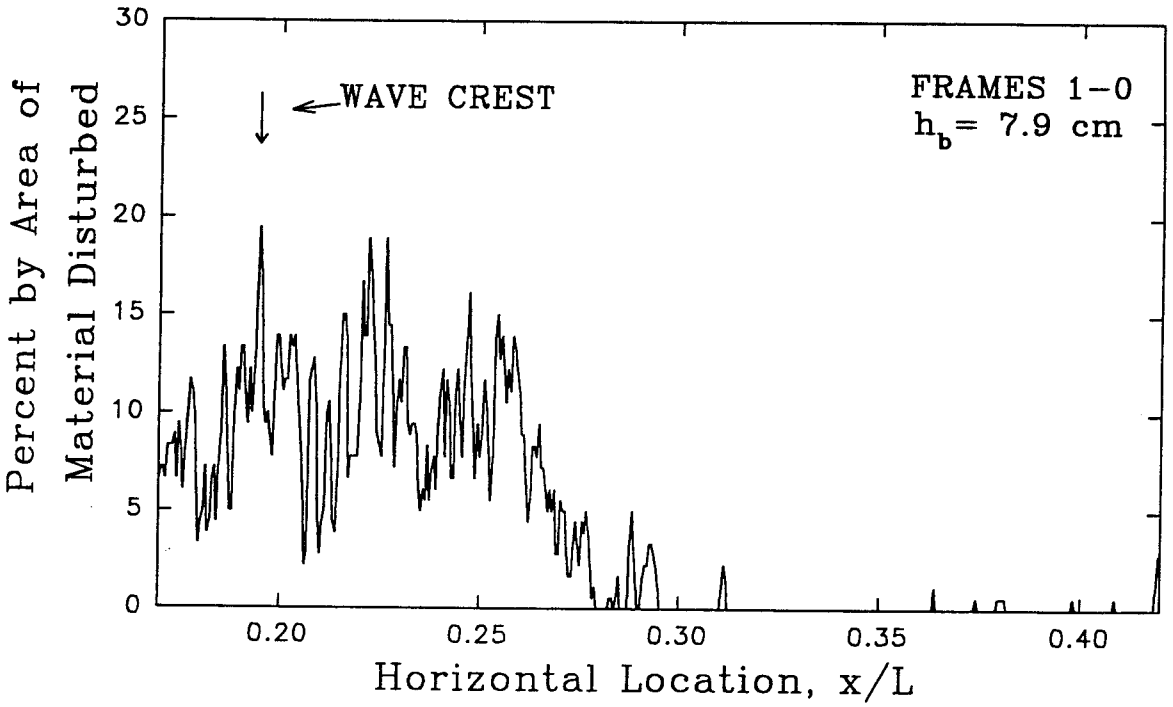

FIG. 3.10. Typical Incremental Movement Intensity Record.

Figure 3.10 shows a typical result of filtering and averaging across the 20 cm observation width for the comparison between two sideviews. In this case, an image of the bed before the appearance of the wave in the frame and the first image containing the wave crest have been superimposed to show the movement of material as the wave first begins to pass over the observation location centered at x/L = 0.29. For this experimental run, small amounts of movement occur well ahead of the wave crest, but general particle motion does not begin until near x/L = 0.30. The amount of material movement is seen to vary widely as the wave crest approaches. As seen in the side views, several runs of sideview observations must be averaged in order to see the general trends in particle movement. The sideview observations, however, provide good records of the actual process of material movement under a single wave.

CHAPTER 4

PRESENTATION AND DISCUSSION OF RESULTS

The results presented in this study are based on two types of measurements of the interaction between breaking and non-breaking solitary waves and a bed of angular material on the tank bottom. Water particle velocity and surface elevation measurements were made for the waves in the region directly above the bed. Video observations of material movement under the action of the waves were made for conditions identical to those for the water particle velocity measurements. Solitary waves were used in all cases. For the case of breaking waves, the tank was tilted to its maximum slope of 0.020 in order to obtain a plunging breaker. A summary of the different wave cases is shown in Table 4.1.

Table 4.1. Wave Conditions and Observation Locations.

Type of Wave	h_h (cm)	x_h/L L=1.5m	H/h_h (H/h)	Observation locations Velocities	Videos
Breaking Solitary	13.8	0.29	1.06	h = 13.8, 13.1, 12.5 (cm)	At and after breaking
Breaking Solitary	11.8	0.29	1.01	h = 11.8 (cm)	At and after breaking
Breaking Solitary	10.1	0.29	0.98	h = 10.1 (cm)	At and after breaking
Breaking Solitary	7.9	0.29	0.96	h = 7.9, 7.1, 6.5 (cm)	At and after breaking
Breaking Solitary	12.5	0.72	-----	h = 13.8 (cm)	Before breaking
Breaking Solitary	10.1	1.52	-----	h = 13.8 (cm)	Before breaking
Solitary	-----	-----	(0.18)	h = 26.0 (cm), x/L = 0.05, 0.48, 0.91	None

The reader is referred to Appendix B for a detailed list of the experimental runs performed in this investigation. For purposes of clarity, the definition sketch presented in Chapter 1 is repeated in Figure 4.1.

4.1 SOLITARY WAVE CHARACTERISTICS

The waves used in this study were photographed through the glass side walls of the tank at the same stations as those used in the experiments. These photographs are

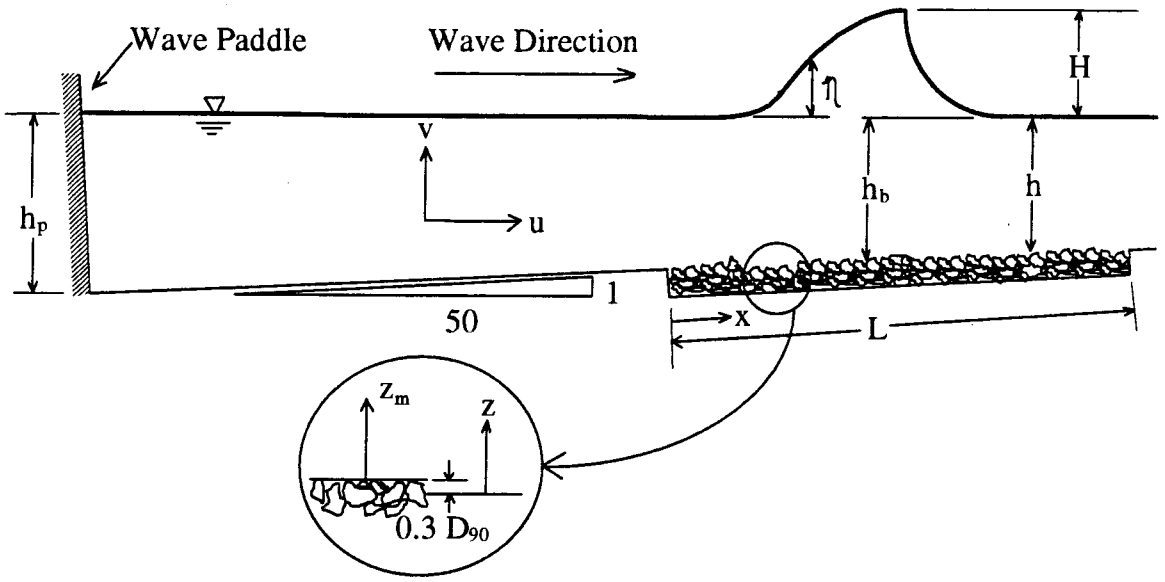

FIG. 4.1. Schematic of Wave Tank.

presented in Figures 4.2 through 4.6. The waves are propagating from the left of the picture towards the right. The cross marks near the center of the photograph represent x/L, the location of the water particle velocity measurements and the centerline of video observations of the rock bed (L, the length of the test section is 1.5 m).

Figure 4.2 shows the breaking wave with the largest depth at breaking, h_b = 13.8 cm, at three stations along the test section. The wave height and water depth for this wave were adjusted to make use of the maximum amount of freeboard at the wave plate and concurrently obtain wave breaking at a fixed location x/L = 0.29 in the test section. The wave was considered to be breaking when the slope of the leading edge of the wave at the crest just became vertical. This position was determined visually during the passage of several identical waves and confirmed with the use of a video camera. Figures 4.3 ,4.4 and 4.5 show breaking waves with successively smaller depths at breaking, h_b = 11.8 cm, 10.1 cm, and 7.9 cm respectively. The amplitude and depth of these waves were also adjusted to obtain breaking at the station of x/L = 0.29.

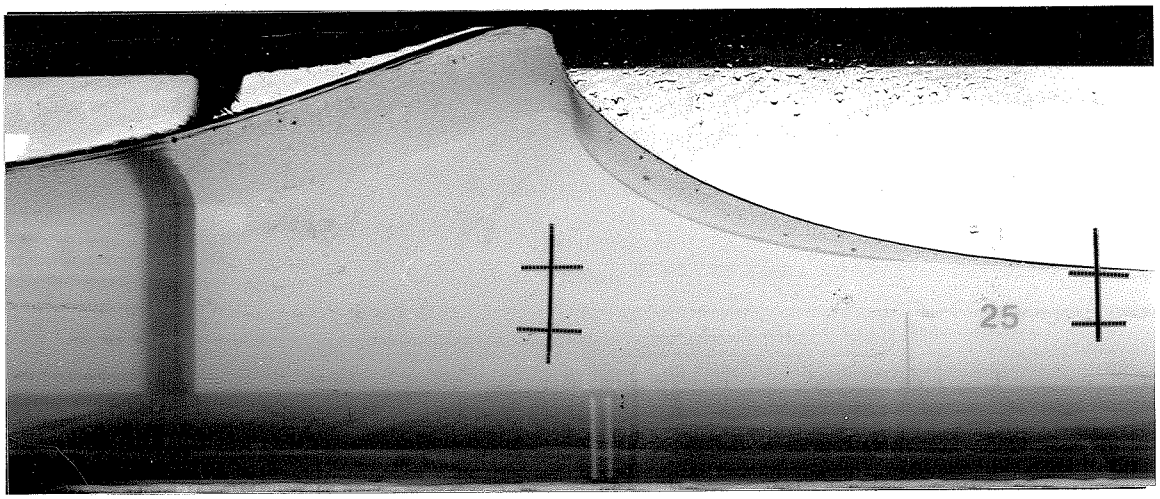

(a) $h/h_b = 1.00$, $x/L = 0.29$

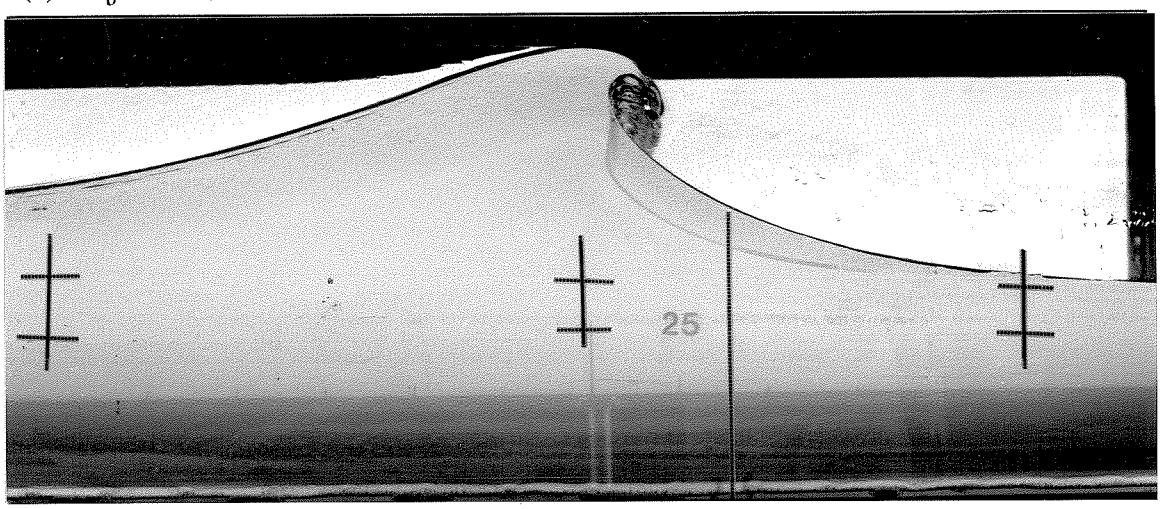

(b) $h/h_b = 0.95$, $x/L = 0.53$

(c) $h/h_b = 0.91$, $x/L = 0.73$

FIG. 4.2. $(H/h)_b = 1.06$, $h_b = 13.8$ cm
Photographs of Breaking Solitary Waves.

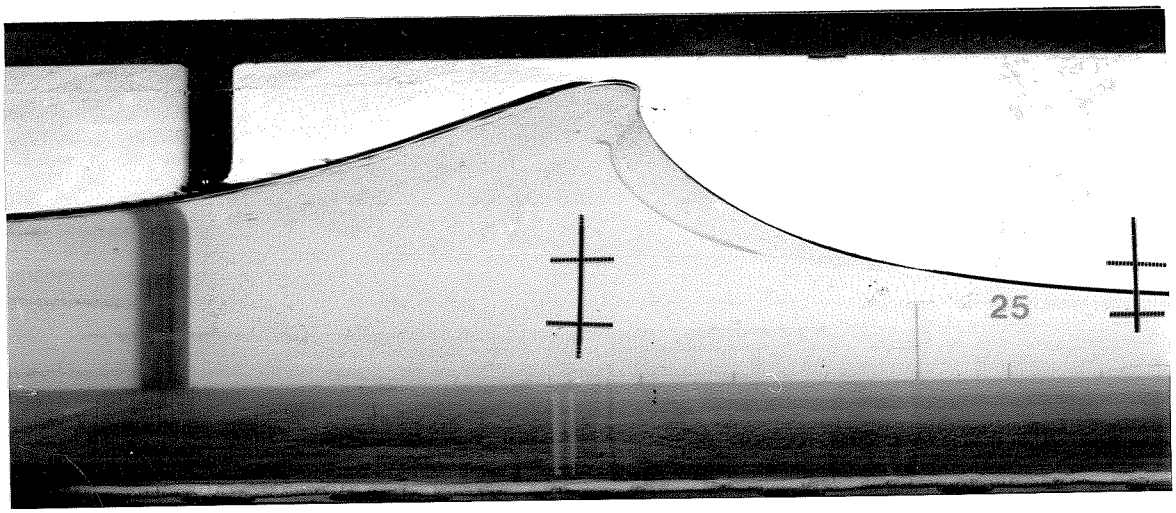

(a) $h/h_b = 1.00$, $x/L = 0.29$

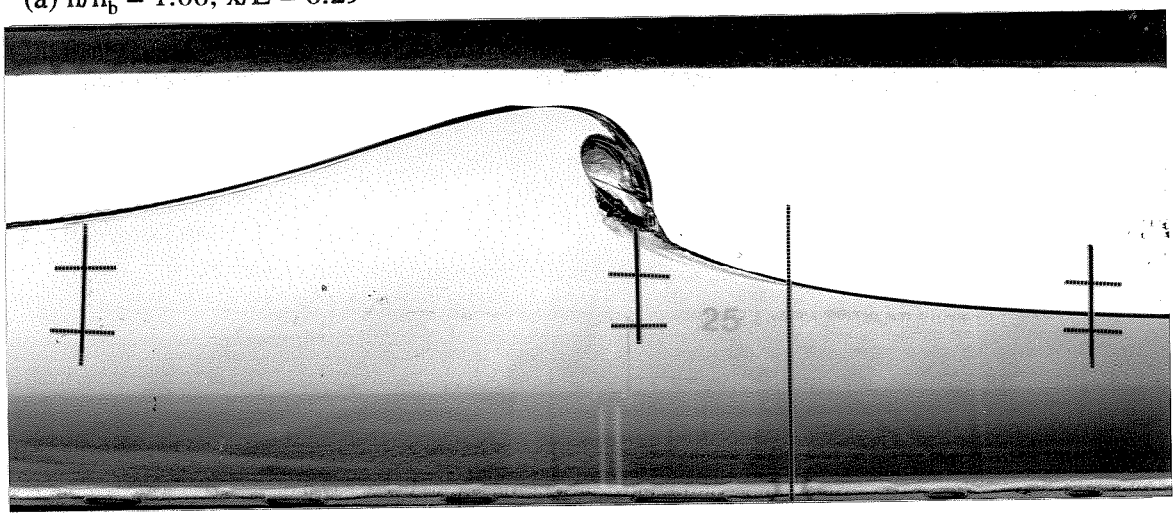

(b) $h/h_b = 0.94$, $x/L = 0.53$

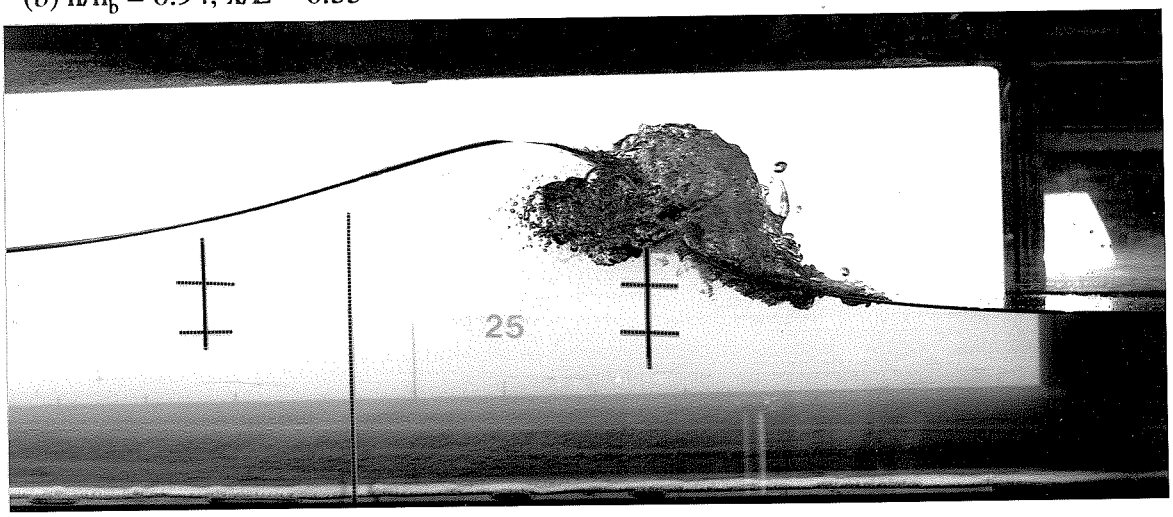

(c) $h/h_b = 0.89$, $x/L = 0.73$

FIG. 4.3. $(H/h)_b = 1.01$, $h_b = 11.8$ cm
Photographs of Breaking Solitary Waves.

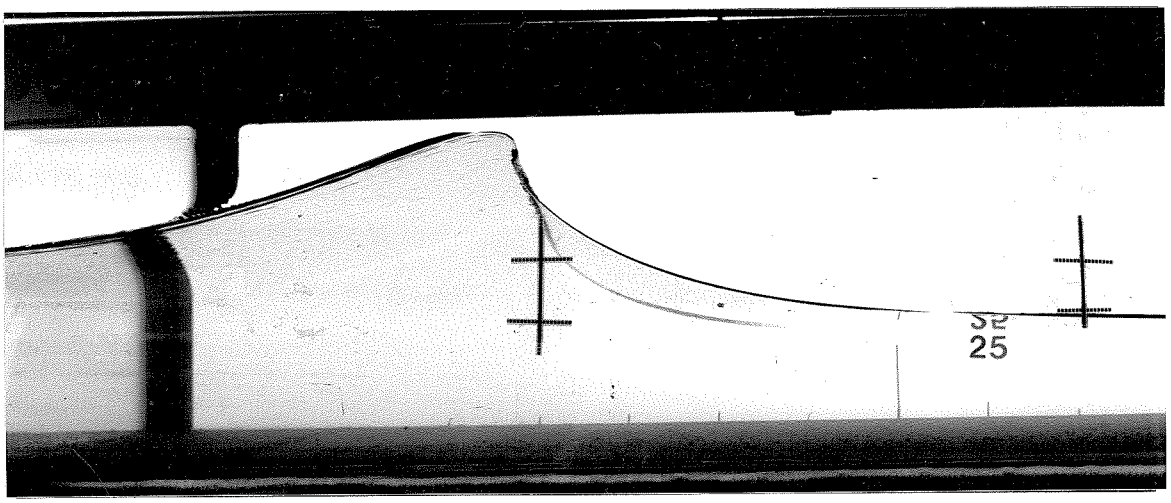

(a) $h/h_b = 1.00$, $x/L = 0.29$

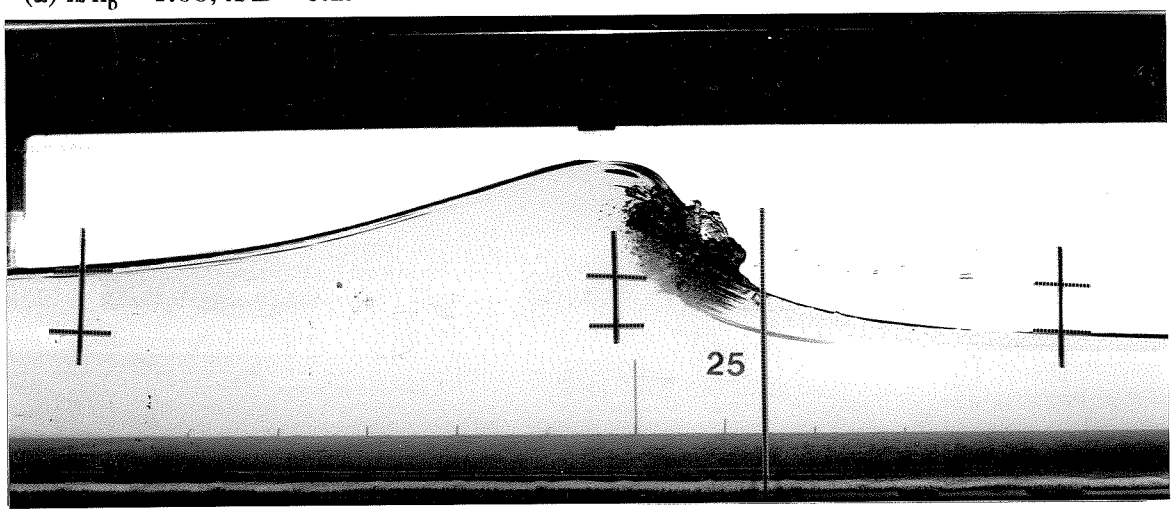

(b) $h/h_b = 0.93$, $x/L = 0.53$

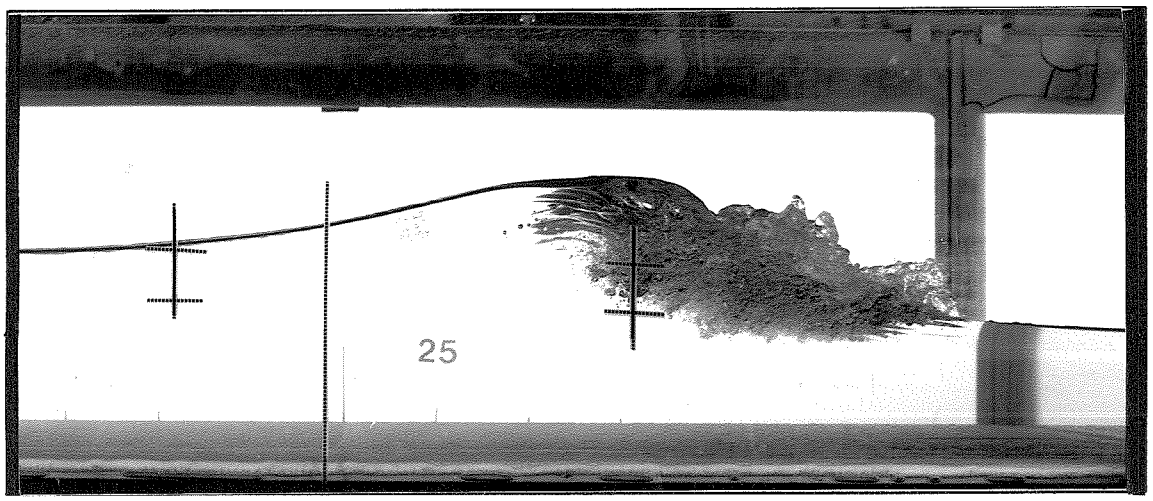

(c) $h/h_b = 0.87$, $x/L = 0.73$

FIG. 4.4. $(H/h)_b = 0.98$, $h_b = 10.1$ cm
Photographs of Breaking Solitary Waves.

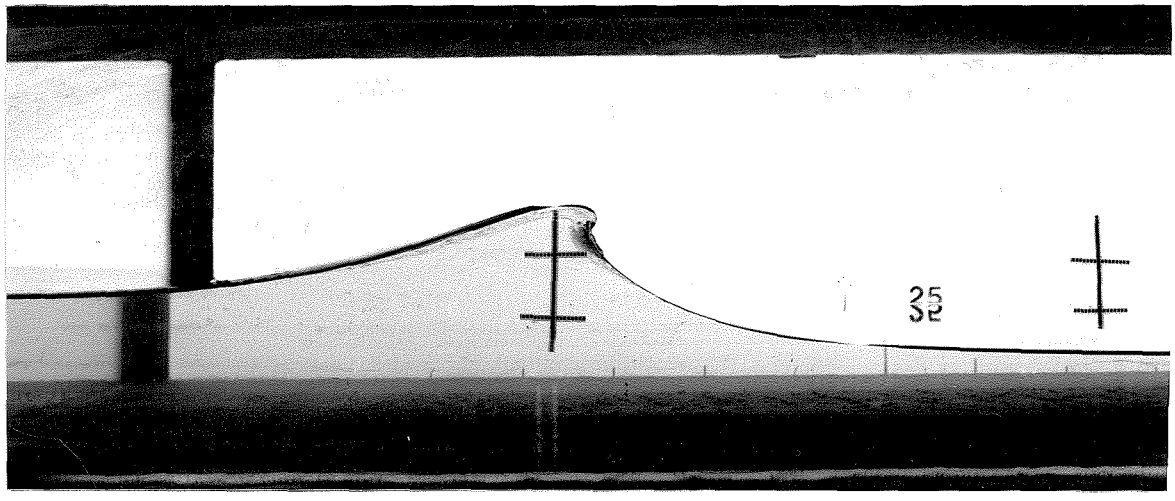

(a) $h/h_b = 1.00$, $x/L = 0.29$

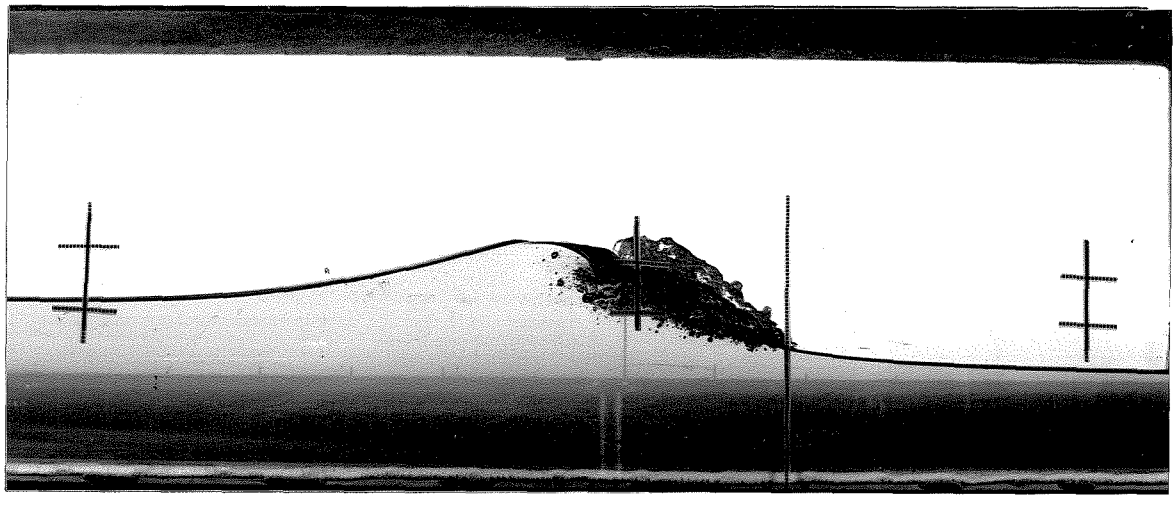

(b) $h/h_b = 0.90$, $x/L = 0.53$

(c) $h/h_b = 0.82$, $x/L = 0.73$

FIG. 4.5. $(H/h)_b = 0.96$, $h_b = 7.9$ cm
Photographs of Breaking Solitary Waves.

(a) $h/h_b = 1.08$, $H/h_b = 0.95$

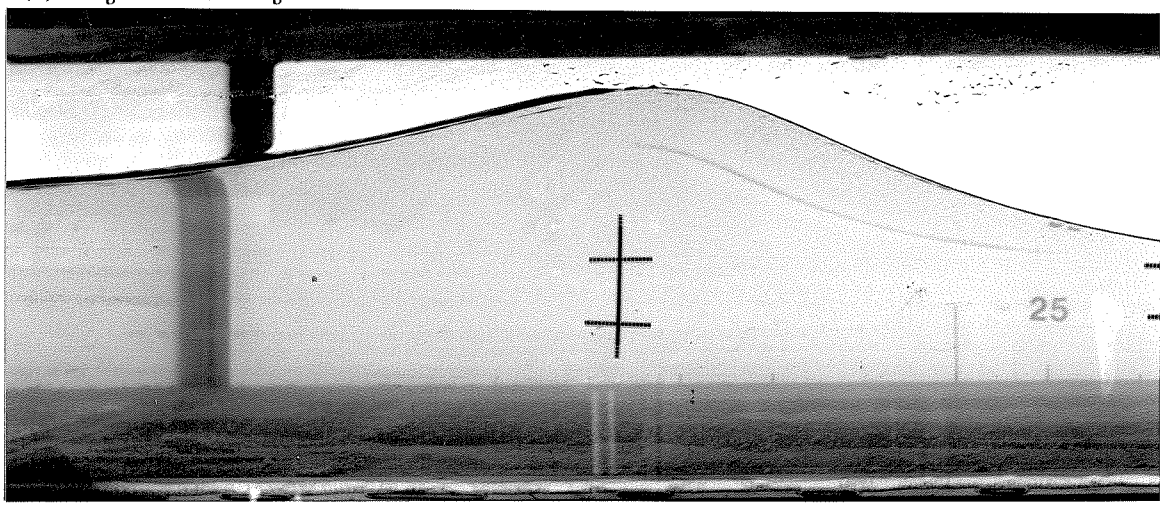

(b) $h/h_b = 1.37$, $H/h_b = 0.69$

FIG. 4.6. h = 13.8 cm, x/L = 0.29
Photographs of Shoaling Solitary Waves.

Figures 4.2 through 4.5 clearly show the development of the plunging breaking wave. At breaking, the wave appears quite asymmetric with the leading portion of the wave steepening to the vertical at the crest and the trailing portion with a higher, more gently sloping water surface elevation. From this initial point of breaking, the plunging breaker forms a jet at the crest (Figure 4.2(b)). This jet is propelled forward until it impinges upon the leading portion of the wave (Figure 4.3(b)). After impingement, an aerated overturning region forms on the front face of the wave and the overall height of the propagating wave is reduced (Figures 4.4(c) and 4.5(c)). Eventually, the turbulence

on the front face of the wave penetrates to the bottom by a series of three-dimensional oblique vortices as noted by Nadoaka (1988). These experiments investigated the effects of wave breaking up to and including the overturning region, but did not extend as far as the vortex generation region.

Reducing h_b, the depth at breaking, compresses the vertical and horizontal length scales of the experiment. This has the effect of changing the relative size of the material in the bed with respect to the wave and also changes the relative progression with distance of the wave breaking process. In the same longitudinal distance, a wave with smaller breaking depth will be further along in the breaking process compared to a wave propagating in a greater depth of water. The progression in the breaking process is expressed here by the quantity h/h_b. For example the wave in Figure 4.3(c) at station x/L = 0.73 is in a similar stage of breaking, $h/h_b = 0.89$, as the wave breaking at a shallower depth in Figure 4.5(b) at station x/L = 0.53, $h/h_b = 0.90$.

In order to investigate the importance of the breaking process in the measured velocities and particle movement under waves, two waves were generated in the same depth, h_b=13.8, at station x/L = 0.29 as the largest breaking wave. These waves had smaller amplitudes than the breaking wave and thus broke further shoreward. For the purposes of this study, these waves will be referred to as shoaling waves. The larger of the two shoaling waves and consequently the one closer to breaking, is shown in Figure 4.6(a). It exhibits the asymmetry of a steepening front face and more gradually sloping trailing portion seen in a wave near breaking. However, the crest region has not yet developed the discontinuous slope characteristic of a breaking wave. The smaller amplitude wave in Figure 4.6(b) is even further away from its breaking depth. Here the main feature of the shoaling wave is the higher water surface elevation on the trailing face of the wave with respect to the front face.

The objective of generating the shoaling waves was to compare their effects on water particle velocities and material movement with the effects seen for breaking waves. The maximum water particle velocities in the shoaling waves were matched with those observed in two of the breaking waves at an elevation of 5.18 cm above the rock bed, an elevation near the bed, but where boundary layer effects should be minimal. Figure 4.7 shows the method used to determine the generation conditions for the shoaling waves. The ratios of wave height to water depth at the wave plate appear on the abscissa. The ordinate shows the maximum horizontal and vertical water particle velocities normalized by the local shallow water wave speed at the point of observation. Water particle velocities were measured by the LDV at an elevation of z = 5.18 cm in a water depth, h, set at 13.8 cm at station x/L = 0.29 for a series of solitary waves of different amplitudes. The maximum horizontal velocities, occurring under the wave crest, were fitted with a second order polynomial curve. The shoaling wave characteristics were then determined

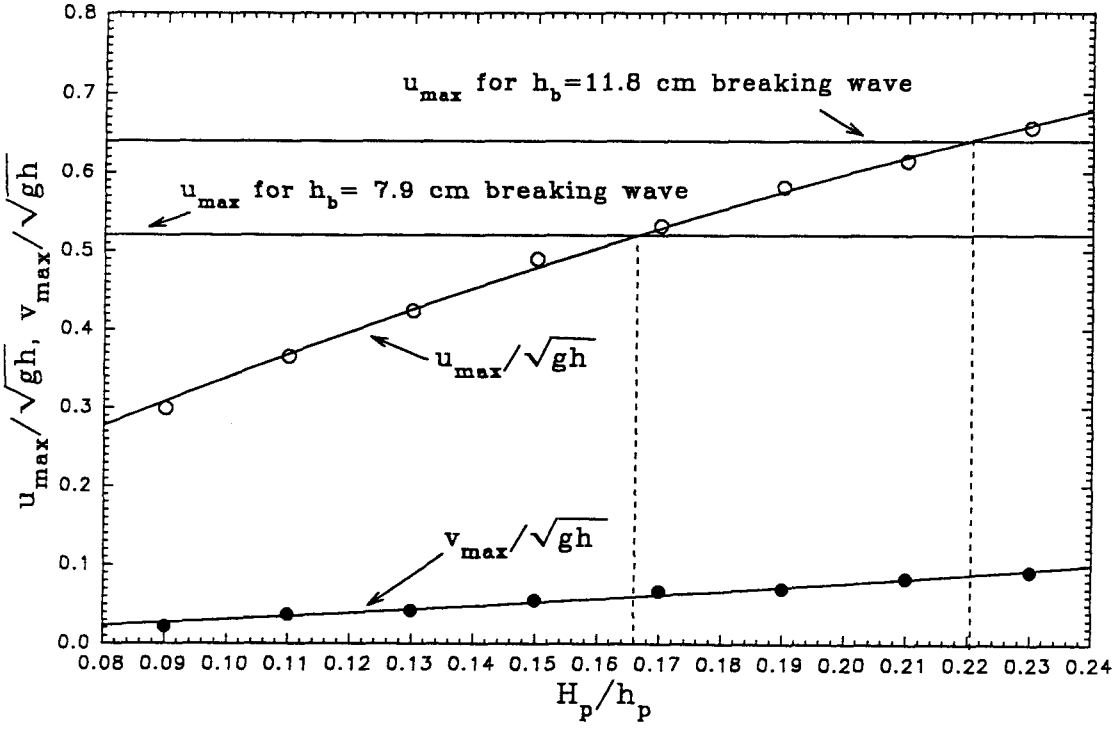

FIG. 4.7. Determination of Non-breaking Wave Heights Corresponding to Breaking Wave Velocities, z/h = 0.36, h = 13.8 cm, x/L = 0.29.

by matching conditions at the wave plate with the observed velocities in the breaking waves at the same location. For example, a shoaling wave with a relative height of 0.166 at the wave plate yields the same maximum horizontal velocity as the wave breaking at x/L = 0.29 with a depth of 7.9 cm. The results were subsequently confirmed with LDV measurements.

This study included observations of a solitary wave propagating in the tank with slope = 0.0 meters/meter. This wave was used for purposes of comparison with breaking and shoaling waves and to study the growth of the boundary layer in the rock filled test section with no material movement. Since this wave had a very gradual variation in water surface elevation, a photograph is not useful. Figure 4.8 shows a water surface elevation time history for the solitary wave. The abscissa (or time axis) has been normalized by the ratio of the local shallow water wave celerity to the local water depth, h = 26.0 cm. The

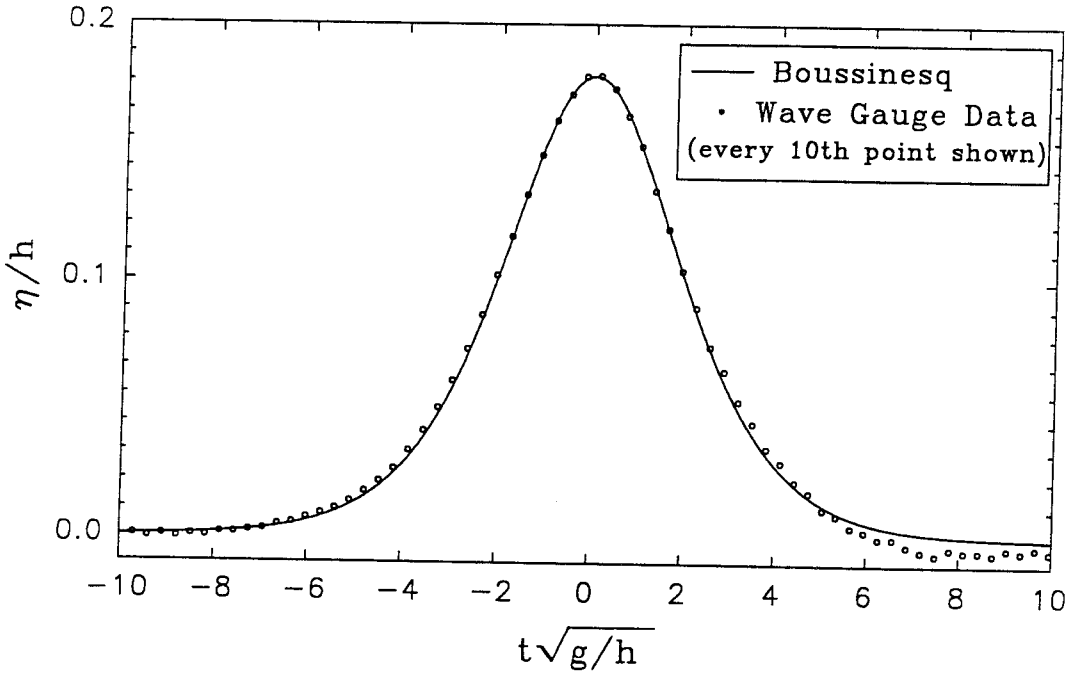

FIG. 4.8. Wave Gauge Record for Solitary Wave over Rock Bed, h = 26.0 cm.

water surface elevation above the still water level is normalized by the local water depth on the ordinate. The time $t\sqrt{g/h} = 0.0$ coincides with the passage of the wave crest at the observation location. For clarity, every tenth point of the wave gauge record has been plotted against the second order theory of Boussinesq (1872), with elevation η such that

$$\eta = H\left[\operatorname{sech}\sqrt{\frac{3}{4}\frac{H}{h}}\frac{X}{h}\right]^2 \qquad \text{where}\,(X = x - ct) \tag{4.1}$$

Here c is the celerity of the wave at the measurement location.

The data fall within ± 2 percent of Boussinesq's theory except in the trailing region of the wave. The oscillation in this region is attributed to several causes. First, as shown in section 2.2.2, the motion of the wave plate did not identically coincide with the input trajectory. Secondly, the motion of the wave plate is programmed to match plate movement with water particle velocities in the generated wave. However, while the plate is fixed in a vertical position, in a solitary wave the horizontal velocities vary to second order in the vertical direction (Equation 1.3). Thus, the plate motion could not duplicate the water particle velocity variation with depth. Thirdly, during early experiments, the solitary wave was affected at generation by the presence of the false bottom. During the solitary wave experiments with a level tank, the cavity underneath the false bottom was not sufficiently isolated from the reservoir behind the wave plate, causing a net difference in hydrostatic pressure between the upper and lower surfaces of the glass panels. The above conditions resulted in a slight distortion of the solitary wave at generation. At the observation locations this distortion caused oscillations in the trailing edge of the wave amplitude record. The false bottom panel deflections were subsequently reduced by the addition of a seal at the end of the false bottom panel at the wave plate as described in section 2.1.2. However, the oscillations in the trailing edge of the solitary wave do not

affect the results of this investigation which is concerned primarily with phenomena near the crest of the wave.

During the course of these experiments, wave gauge measurements were made concurrently with velocity and video observations. Figure 4.9 presents wave gauge records at the station x/L=0.29 for the seven waves used in this study. As before, the time $t\sqrt{g/h} = 0.0$ coincides with the passage of the maximum of the wave crest at the location observed. In Figure 4.9, frames (a) through (d) show that the normalized water surface elevation time-histories for the plunging breaking waves appear similar. The wave height to depth ratios at breaking range from 1.06 for the largest wave to 0.96 for the smallest wave. This is consistent with the findings of Saeki et al. (1971) and Skjelbreia (1987) for plunging breaking waves. In addition to the steep leading edge, the breaking wave exhibits a very gradually sloped or shelf-like region on its trailing edge. This shelf is attributable primarily to a reflection from the bottom boundary slope as the wave propagates toward breaking. The steepening of the wave and the formation of the trailing shelf can be observed in frames (e) and (f) for the shoaling waves as they approach breaking. Frame (g) repeats the wave gauge record for the solitary wave propagating at zero slope, primarily to emphasize the symmetric shape of this wave when contrasted with the breaking and shoaling waves.

It is noted that at and after wave breaking, the existence of the jet and of air entrainment at the crest of the wave greatly reduce the accuracy of a resistance type wire wave gauge. Wave gauge records were used in this study primarily to confirm the generation of a wave of consistent wave height and to observe general features of the water surface elevation during breaking, especially at observation locations shoreward of x/L = 0.29. The wave height to depth ratio obtained by the wave gauges at breaking was confirmed by observing the height of the water mark on the tank side wall at wave passage.

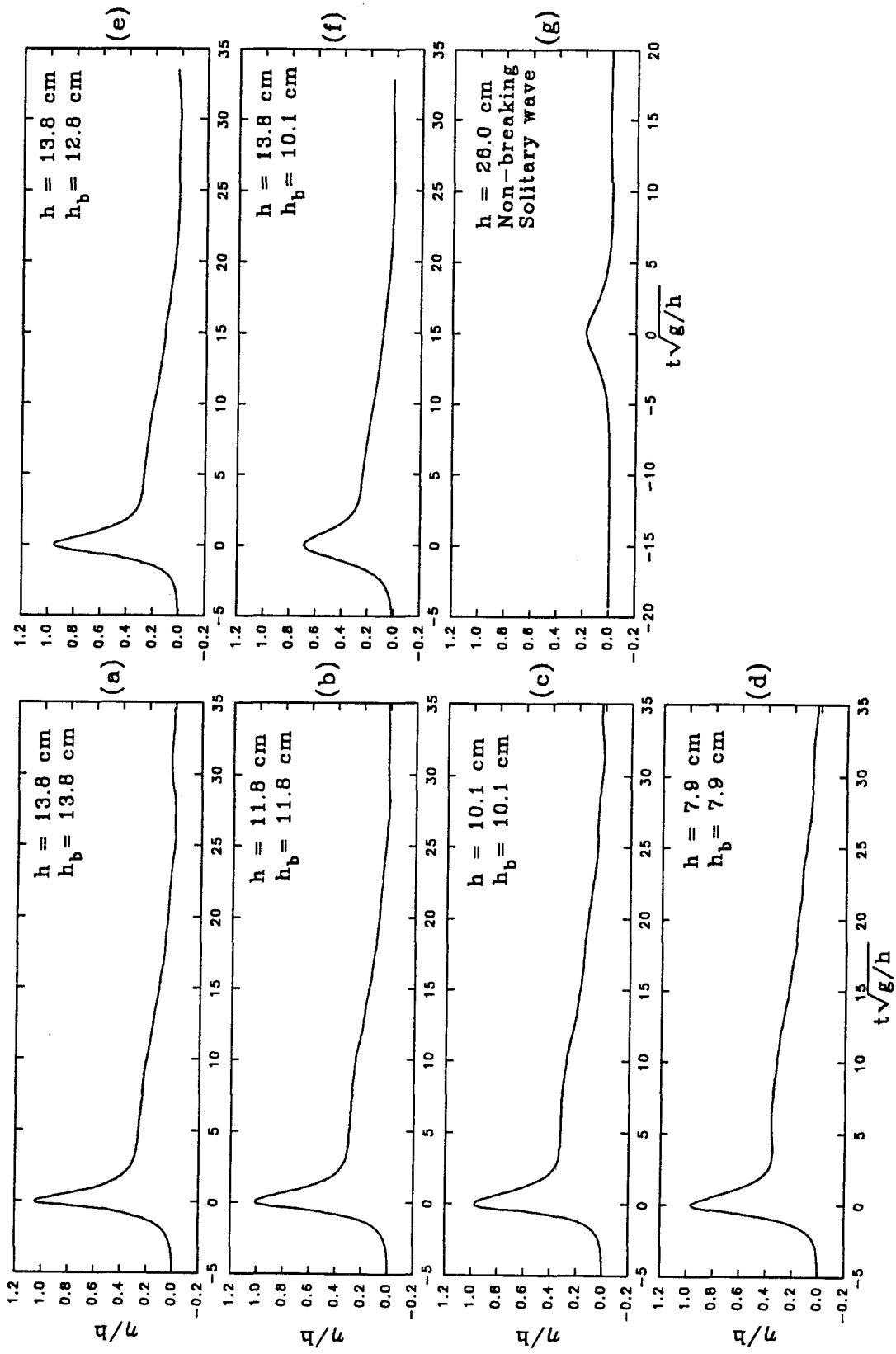

FIG. 4.9. Typical Wave Gauge Records at x/L = 0.29.

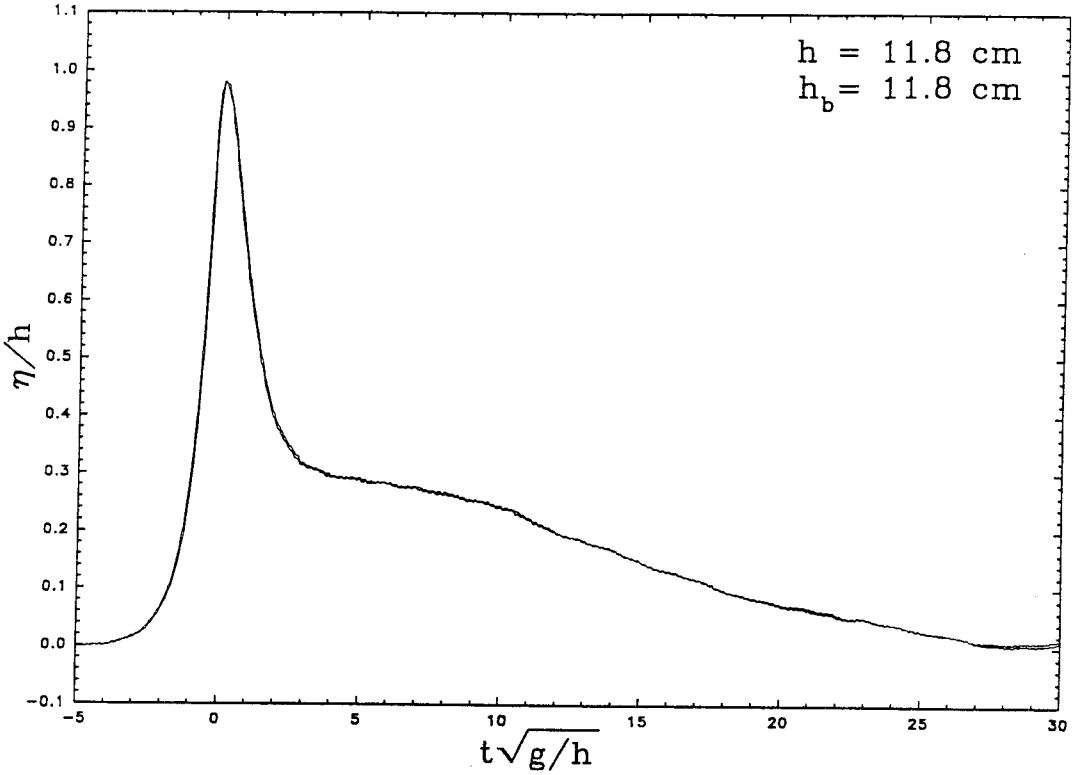

FIG 4.10. Comparison of Wave Gauge Records from Two Runs under Identical Conditions.

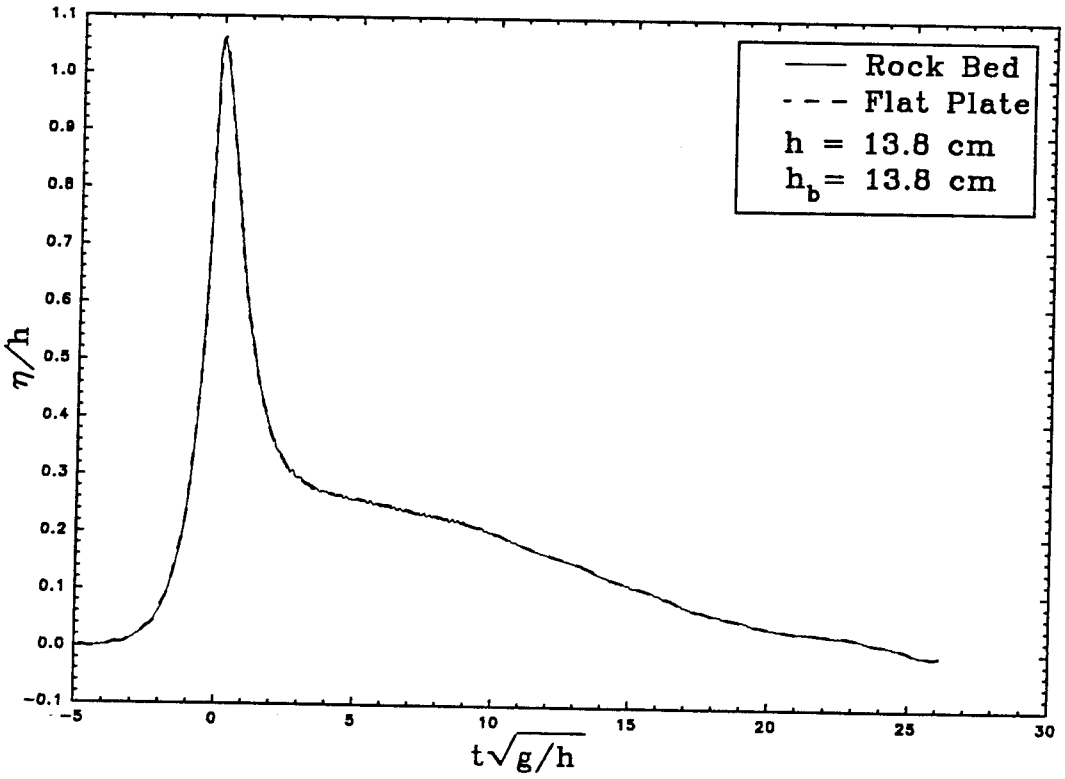

FIG. 4.11. Comparison of Wave Gauge Records over Rock Bed and Flat Plate, x/L = 0.29.

Figure 4.10 shows the water surface elevation time histories for two different experimental runs under the same wave conditions. The records are quite close. There is some variation near the crest of the wave of the exact time and shape of the maximum wave height. The onset of breaking is a very unsteady process so that the wave does not break at exactly the same location each time. If sufficient time is allowed for motion in the tank to dissipate, however, the breaking location does not vary greatly. In general, the wave gauge records from different runs agree to within ± 1.5 percent.

In Figure 4.11, it is seen that the water surface elevation time history is not affected by the presence of the rock bed. The wave gauge records shown in Figure 4.11 were recorded at the location x/L = 0.29. Due to the short length of the test section, the breaking location and the shape of the wave did not vary between the two cases.

4.2 WATER PARTICLE VELOCITIES

The water particle velocities in this study were measured using the two-dimensional Laser Doppler Velocimeter described in section 2.5. Figure 4.12 shows a typical velocity time-history at an elevation z = 0.48 cm above the rock bed for the smallest breaking wave, i.e., h_b = 7.9 cm, at breaking. As before, unless otherwise indicated, for the velocity data, the time t = 0.0 always occurs at the time of passage of the wave crest over the observation location. The velocities were sampled at a rate of 200 Hz. As shown in the inset, this sampling rate resulted in some velocity fluctuations being well defined and others defined only by a few points.

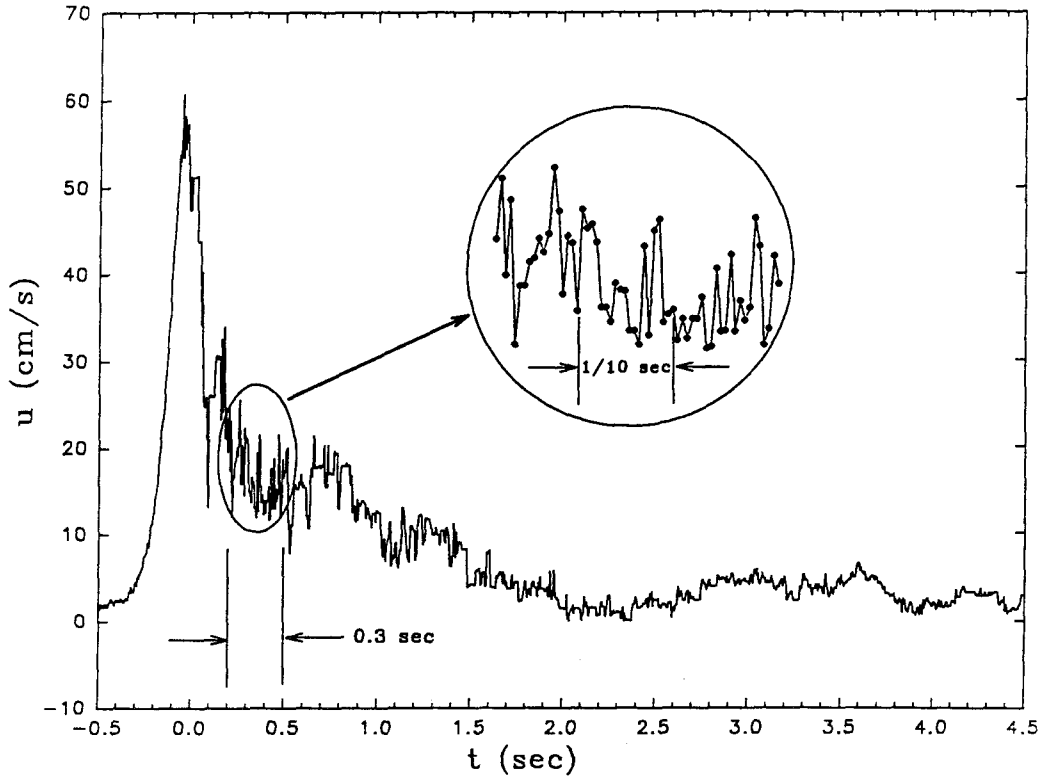

FIG. 4.12. Typical Horizontal Velocity Time History
h_b = 7.9 cm, h/h_b = 1.0, z/h = 0.061.

Figures 4.13 and 4.14 show the variation of the observed horizontal and vertical velocity time histories with elevation for a breaking wave over the rock bed at station x/L = 0.29. It should be recalled that in this location the front face of the wave first becomes vertical at the crest. In each frame, the velocity, normalized by the wave celerity at the observation location, is plotted on the ordinate and the normalized time is given on the abscissa. In Figure 4.13, several changes in the velocity time-history occur as the bed is approached. At the highest elevation, the velocity curve is fairly smooth with small fluctuations occurring after wave crest passage in the trailing portion of the wave. As the bed is approached, the maximum horizontal velocity is reduced by as much as 30 percent and the turbulence becomes more pronounced. The onset of turbulence also occurs earlier during the passage of the wave. For relative elevations less than z/h = 0.05 in this case of this particular wave, the turbulence is evident even before the passage of the crest. This implies that the turbulence is generated and starts to propagate up into the flow before the

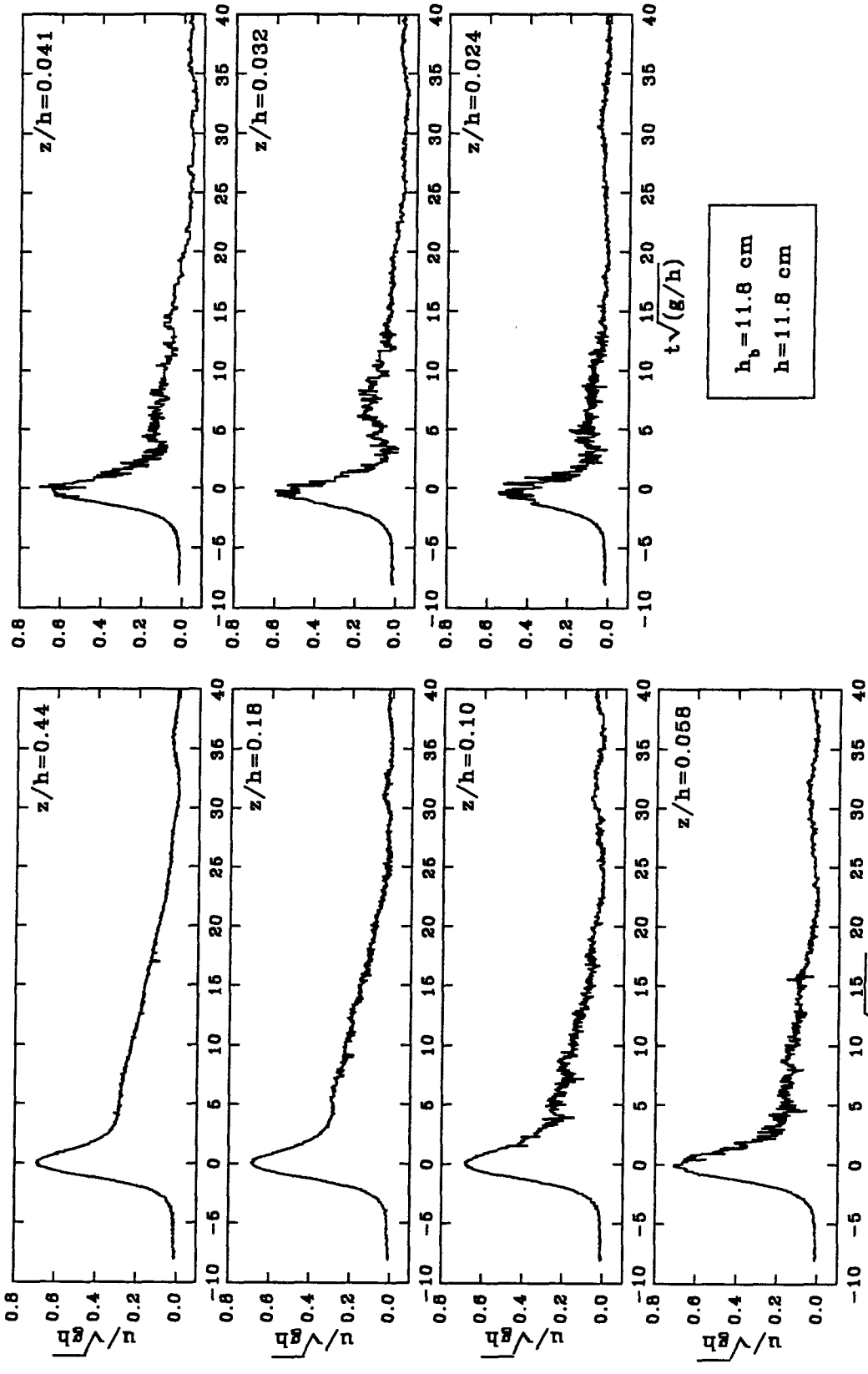

FIG. 4.13. Horizontal Velocity Time-Histories at Seven Elevations Above the Rock Bed, h_b = 11.8 cm, x/L = 0.29.

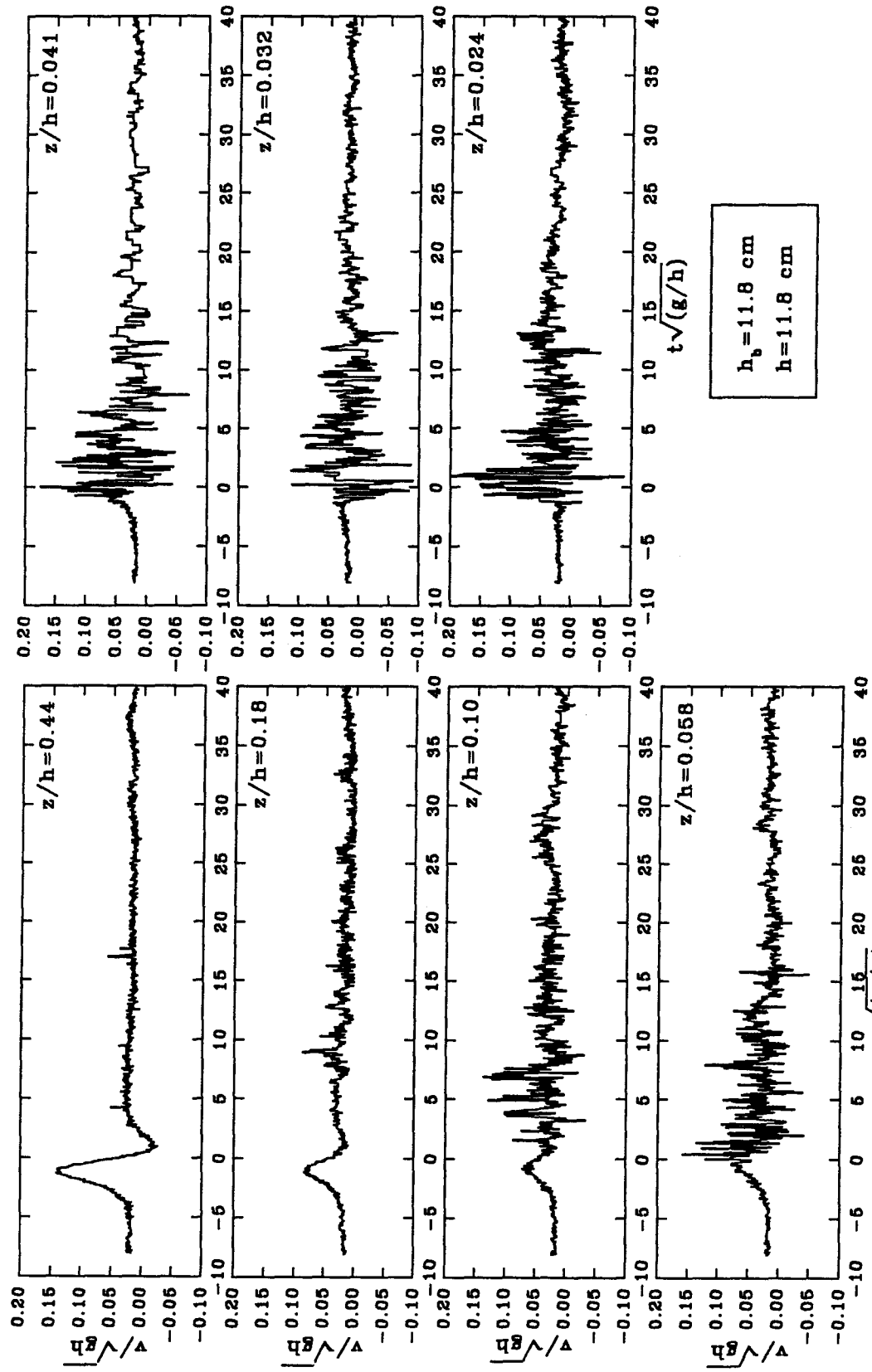

FIG. 4.14. Vertical Velocity Time-Histories at Seven Elevations Above the Rock Bed, h_b = 11.8 cm, x/L = 0.29.

actual breaking part of the waves passes the measuring location. The magnitude and characteristics of the turbulence will be discussed later. Another feature of the velocity time histories as they approach the rock bed is that the "shelf" on the trailing part of the wave is greatly reduced at the lower elevations. At z/h = 0.024 for example, the mean shape of the velocity curve is almost symmetric. The net effect of the lessening of the shelf height is to increase the rate of mean flow deceleration on the back face of the wave.

In Figure 4.14, the observed vertical velocities, although only one-fifth of the magnitude of the horizontal velocities, show the same type of variation with elevation. In this case the magnitude of the mean vertical velocity is quickly overshadowed by the turbulent fluctuations so that at the relative height z/h = 0.041 the mean signal is barely distinguishable. As with the horizontal velocities, the onset of turbulence occurs earlier in the wave as the bed is approached. At elevations close to the bed, the magnitudes of the maximum vertical velocity fluctuations are of the same order of magnitude as the free stream vertical velocities. This emphasizes that the rock boundary is in fact a permeable boundary and vertical velocities are not constrained to be small in its proximity. From the vertical velocity time histories near the bottom, however, there does not appear to be any noticeable net flow into the bed during the passage of the wave at the observation locations.

Figures 4.15 and 4.16 present the observed velocity variations with depth for the same wave at same station as Figures 4.13 and 4.14 , with a flat anodized aluminum plate in place of the rock bed. These observations reveal the effect of the rock bed on the water particle velocities quite well. Though some fluctuations occur in the trailing portion of the wave near the bed, they are very small in magnitude. In Figure 4.15, the maximum horizontal velocity changes less than ten percent throughout the depth. The lessening of the shelf region in the trailing part of the wave occurs here also, but is not as pronounced

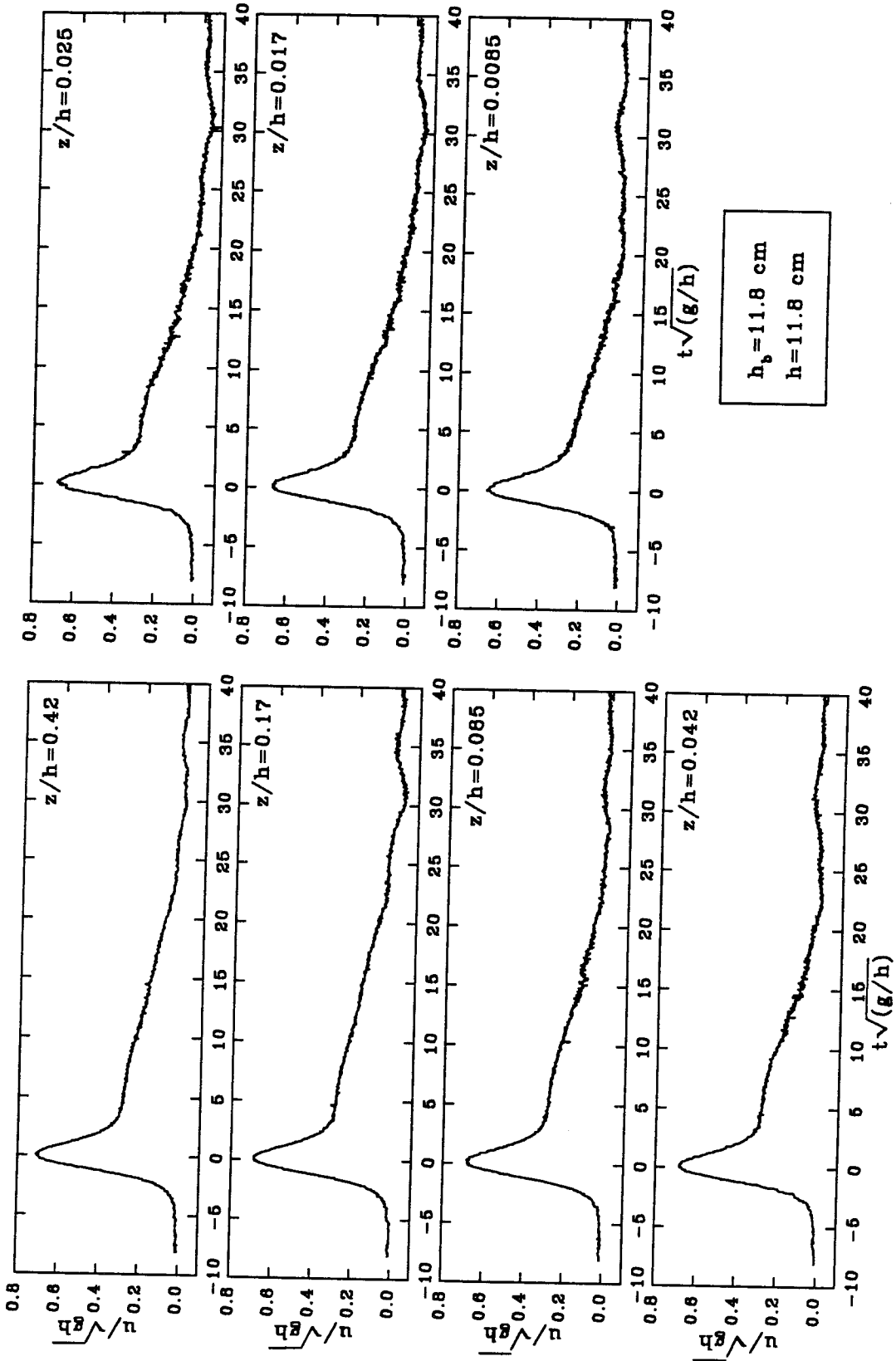

FIG. 4.15. Horizontal Velocity Time-Histories at Seven Elevations Above the Flat Plate, h_b = 11.8 cm, x/L = 0.29.

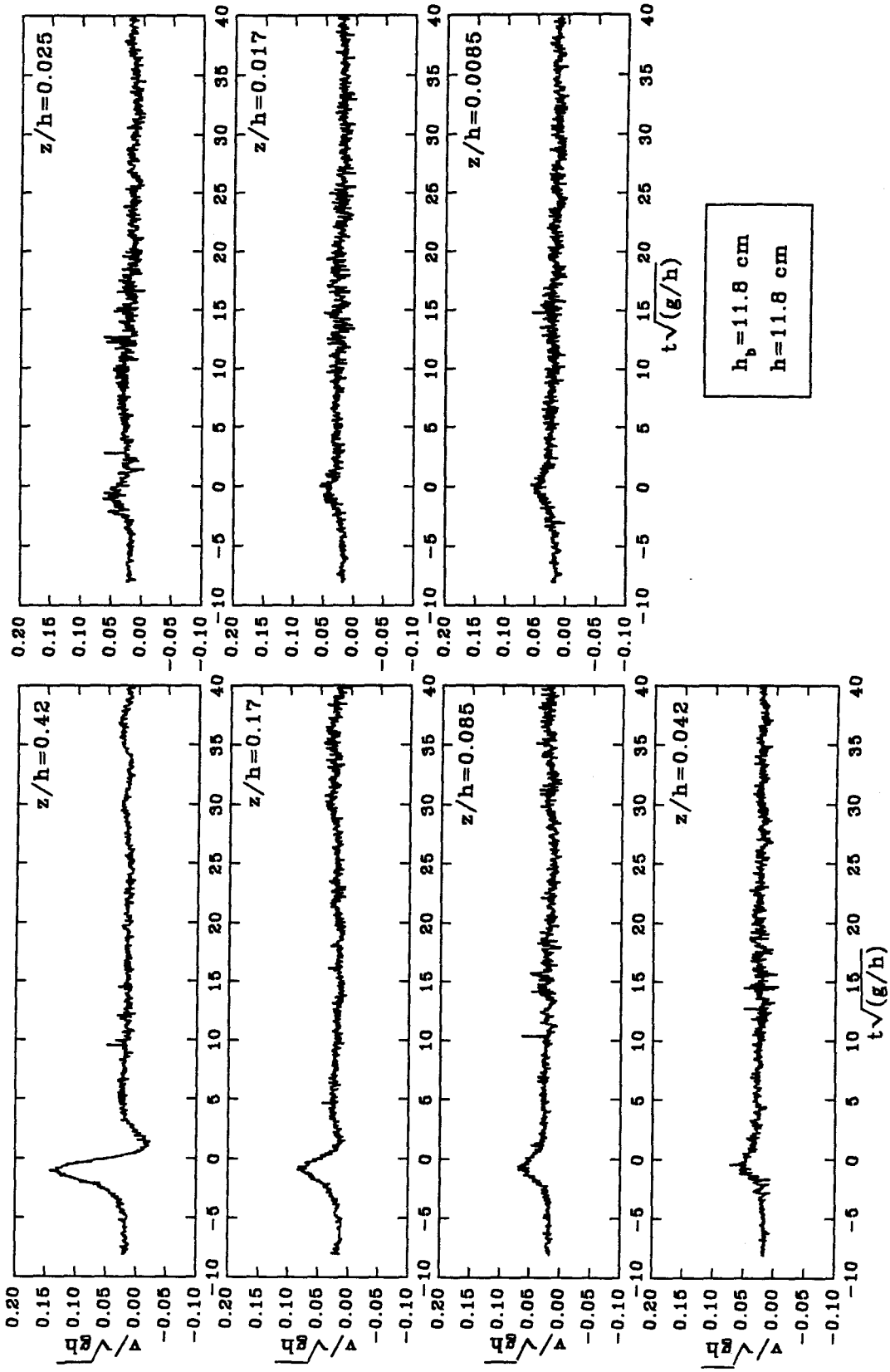

FIG. 4.16. Vertical Velocity Time-Histories at Seven Elevations Above the Flat Plate, h_b = 11.8 cm, x/L = 0.29.

as in the case of the wave over the rock bed. In Figure 4.16, the vertical velocities show a small increase in turbulence as the flat plate is approached, however the main observed effect, as expected, is the reduction of the maximum vertical velocity at elevations approaching the solid boundary.

It is noted that the relative elevations over the rock bed and over the flat plate are not identical because of the difference between the top level of the rock bed and the level taken to be z = 0.0. As mentioned before in section 2.3.3.2, the level of the bottom for the rock bed was taken to be equal to $0.3D_{90}$. This resulted in a net difference of 0.18 cm between observations taken over the rock bed and those taken over the flat plate at the same nominal height.

4.2.1 Mean Velocities under Breaking and Non-Breaking Waves

Since solitary breaking waves are by nature an unsteady process, it is not possible to obtain mean velocities by the time averaging methods conventionally used in steady flows. Conceivably, the experiments could be repeated a large number of times and an ensemble average taken with respect to the stages of the wave during its passage. This type of procedure has been used by Sleath (1988), Jensen (1989), and others in a water tunnel with a sinusoidally varying flow over a fixed boundary. The observed water particle velocities in those studies were averaged at each given phase for 50 cycles or more to obtain the mean velocity time-histories. For the purposes of these experiments, the long time interval needed for resetting the mobile particle bed and the subsequent wear on the particles made this type of averaging method impractical for obtaining mean velocities over a range of elevations. The number of different waves and locations observed in this study also made numerous repetitions difficult. As will be discussed later, many repetitions of single run were already necessary for obtaining overhead video images

of particle movement so it was not deemed feasible to repeat laser runs in the same manner.

Mean velocities for this study were obtained by performing a Fast Fourier Transform, FFT, algorithm on the velocity data, filtering the signals in the frequency domain, and performing a reverse FFT back to the time domain. Typical power spectra for a single wave at several elevations are shown in Figure 4.17. The spectra shown are for normalized horizontal velocities in the largest breaking wave, (h_b = 13.8 cm), at several elevations above the rock bed. At the highest elevation, z/h = 0.37, 90 percent of the power in the signal is found at frequencies less than 26 radians per second. At successively lower elevations in the flow, the higher frequency oscillations make increasingly greater contributions to the signal until at z/h = 0.02 only 52 percent of the power is below 26 radians per second. Since the spectra do not show a definite minimum or a bimodal distribution, the criterion for distinguishing mean and turbulent components is not clearly defined.

The cutoff point for the frequency filter was determined by observing many power spectra and testing the effect of a number of different cutoff frequencies. Figure 4.18 shows the criterion used in this investigation for filtering the velocity data. The cutoff frequency was set at the smallest value possible without observably decreasing the amplitude or affecting the overall shape of the time-history for the mean signal at the highest measured elevation. Since the mean velocity at this level was easy to distinguish visually, a comparison with the filtered data was readily obtainable. As seen in Figure 4.18, the cutoff in this case occurred when the power spectrum of the normalized velocity time-histories first crossed a level near $S(\omega) = 0.001$. All of the cutoffs occurred close to this same power level. For the highest observed elevation, the power at higher frequencies was always less than this value. Figure 4.18 also shows that the cutoff power was kept the same for both horizontal and vertical velocities over the rock bed and the flat

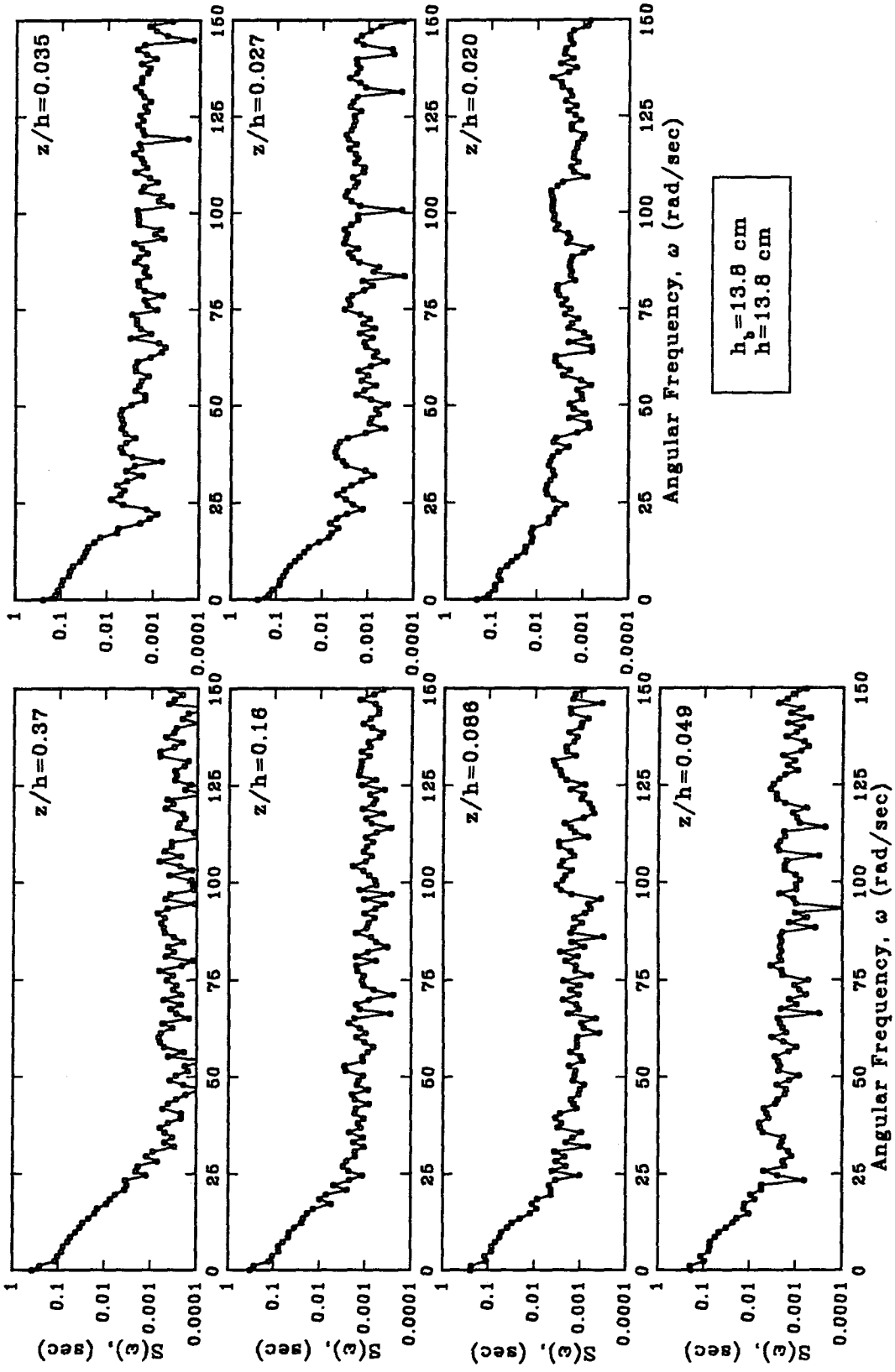

FIG. 4.17. Power Spectra for Horizontal Velocities above the Rock Bed, h_b = 11.8 cm, x/L = 0.29.

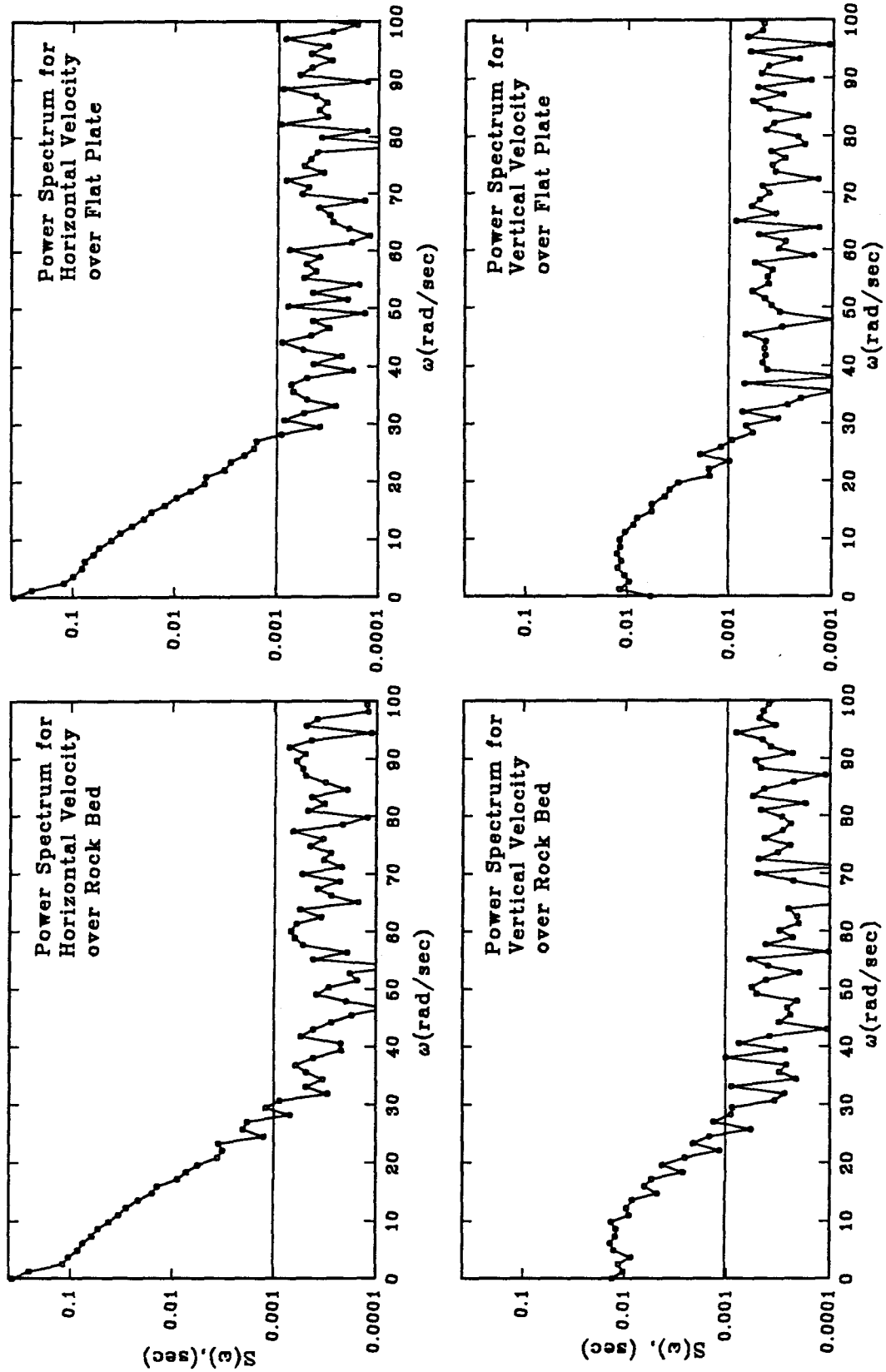

FIG. 4.18. Determination of Cutoff Frequency for Separation of Mean and Turbulent Velocities, $H/h_b = 1.06$, $z/h = 0.37$.

plate. It was deemed necessary to use the same filter for all cases in a given wave in order to define a consistent separation frequency between mean and turbulent motion. This is especially important for defining the interaction between the turbulent horizontal and vertical velocity terms. Each wave was evaluated similarly to obtain its specific frequency cutoff. The filter itself was maintained at a value of unity until the cutoff point and then decreased linearly to zero over the space of four data points in order to minimize "ringing" in the filtered signal.

The cutoff frequencies obtained using this method displayed a systematic variation with the characteristics of the breaking and shoaling waves. Figure 4.19(a) shows that as the ratio of wave height to depth at breaking, H/h_b, increased, the value of the cutoff frequency steadily decreased. This can be explained by the fact that the waves with a larger H/h_b have less of their signal contained in the gradually sloping shelf region in the trailing portion of the wave. Fewer high frequency components are thus required to make

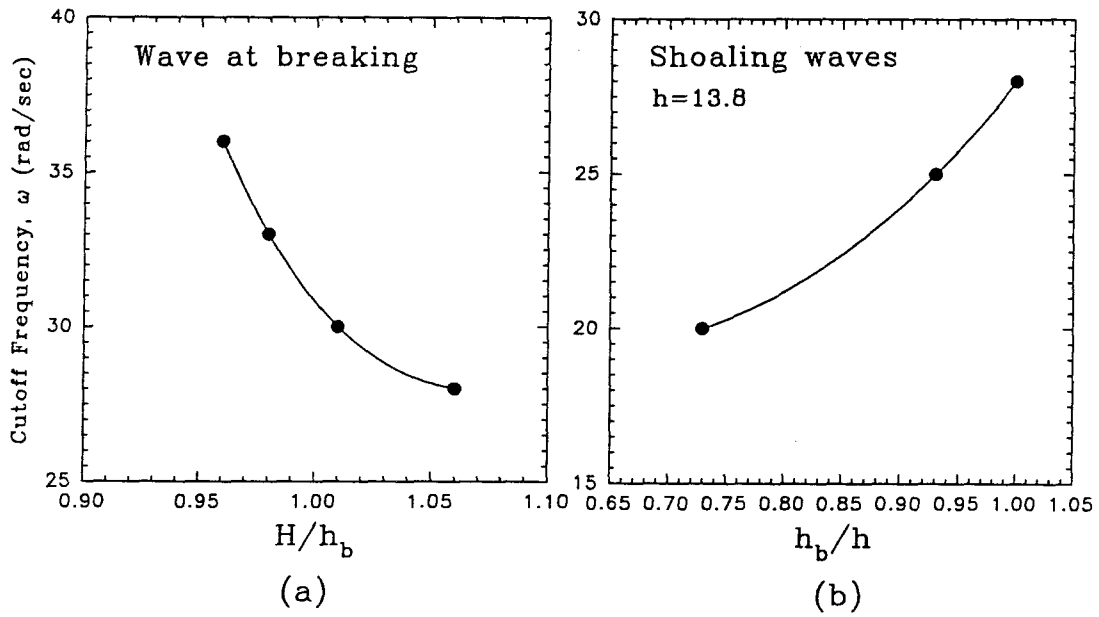

FIG. 4.19. Variation of Filter Cutoff Frequencies with Wave Characteristics.

up the mean velocity signal. This trend is also seen in Figure 4.19(b) for shoaling waves approaching breaking. The waves with a smaller h_b/h are further away from breaking and thus closer to their original solitary wave profile. Thus the mean velocities of these waves are composed primarily of the lower frequency components typical of solitary waves.

Typical mean horizontal and vertical velocities are presented in Figures 4.20 and 4.21. These velocities were obtained by filtering the total velocity records presented earlier in Figures 4.13 through 4.16. Velocities over the rock bed appear as a heavy line, while flat plate velocities at the same relative elevation are shown with a thin line.

Figure 4.20 shows that the mean velocities over the rock bed and the flat plate are nearly identical at elevations away from the bottom boundary. This observation is consistent with the similarity in wave amplitudes measured over the rock bed and flat plate. At the level $z/h = 0.10$ differences in the trailing region are observed. The value of the mean velocity in the shelf region for the case of the rock is only 80 percent of that for the plate. The effect of the rock becomes increasingly pronounced at lower elevations in the flow until at the lowest elevation, $z/h = 0.024$, the magnitudes of both the maximum mean horizontal velocity and the mean velocities in the trailing portion of the wave over the rock bed fall considerably below those for the plate. The maximum mean horizontal velocity over the rock is 70 percent of the mean velocity over the plate and appears shifted in time so that it occurs before the actual passage of the wave crest. The magnitudes of the mean velocities in the trailing shelf for the rock bed are less than one-third of those seen over the flat plate.

The main feature of the mean vertical velocities over the rock bed is that they do not decrease significantly in magnitude at elevations close to the bottom boundary. Figure 4.21 shows that the portion of the mean vertical velocity that varies to first order with

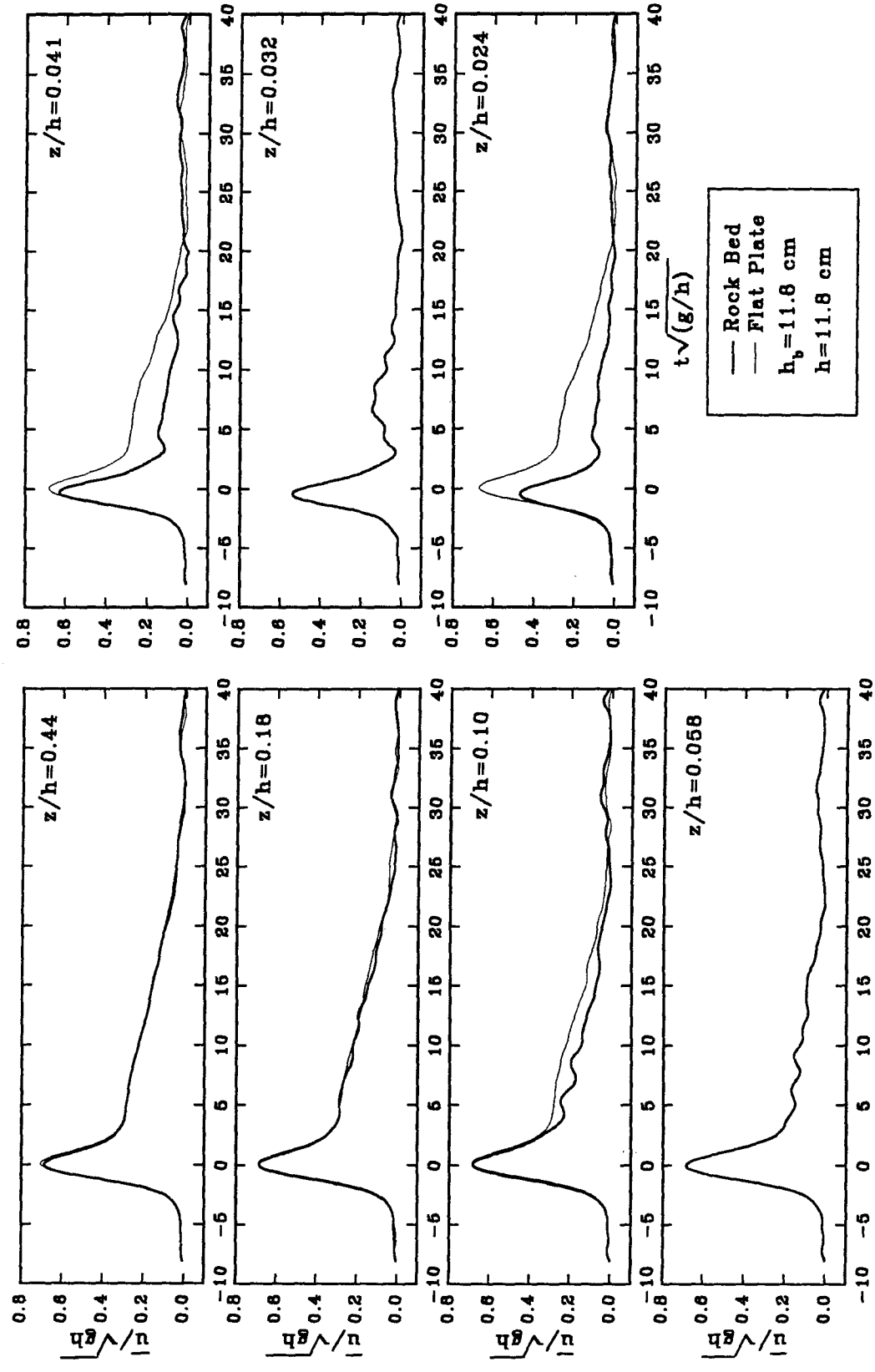

FIG. 4.20. Filtered Horizontal Velocities Above the Bottom Boundary, h_b = 11.8 cm, x/L = 0.29.

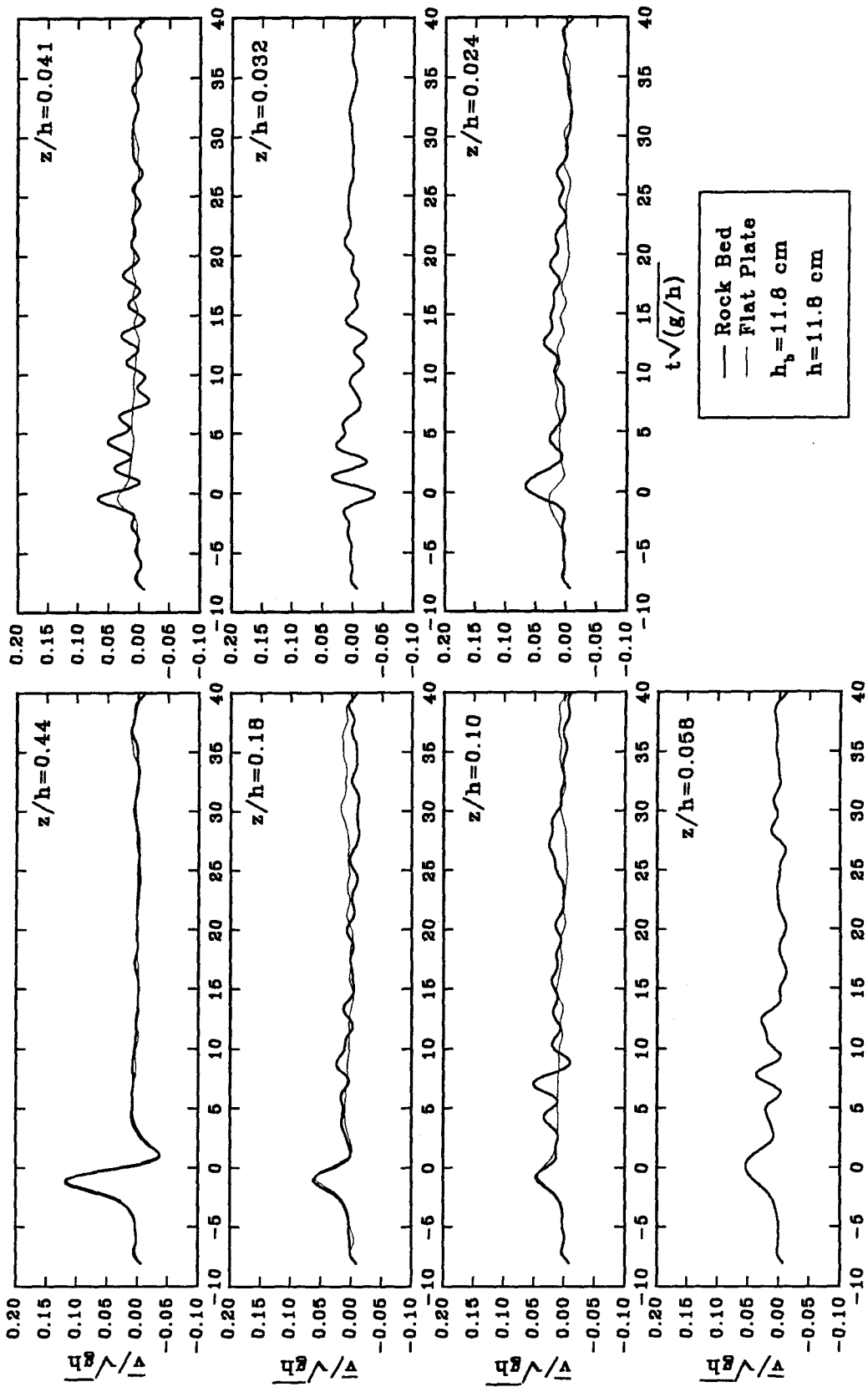

FIG. 4.21. Filtered Vertical Velocities Above the Bottom Boundary, h_b = 11.8 cm, x/L = 0.29.

$\partial\eta/\partial t$, the first derivative of the water surface elevation (Equation 1.4), decreases similarly for the rock bed and for the flat plate down to the relative elevation z/h = 0.10. Below this elevation, the mean vertical velocity under the flat plate continues to decrease. The magnitude of the mean vertical velocity, however, actually increases at lower elevations from the value computed at z/h = 0.10. This phenomenon is attributable to the fact that the bottom boundary is not solid and permits flow around the local topography of the rocks. The rapid fluctuations in the mean vertical velocities near the bottom occur at lower frequencies than the one determined as the cutoff for turbulence in the horizontal and vertical signals. As mentioned previously, the use of the same cutoff frequency for horizontal and vertical velocity components was considered necessary in order to establish a consistent criterion for turbulence in both directions.

Figure 4.22 shows mean velocity records from the four breaking waves at one elevation, z = 5.18 cm. At this elevation, the influence of the rock bed on the flow velocities is negligible. The differences in the velocity time histories of the waves are a result of the different depths at breaking, or equivalently, the different length scales of the experiments. The differences in the maximum mean horizontal and vertical velocities result because the elevation z = 5.18 cm is at a relatively higher point in the flow, z/h = 0.65, for the smallest wave than for the largest wave where z/h = 0.38. As a result of the different relative elevations from the bottom boundary, the horizontal velocities are about 4 percent less and the vertical velocities are 40 percent less for the largest wave than for the smallest wave. If the maximum mean velocities were compared at the same relative elevation, it is expected that the differences between them would be quite small. Unless otherwise noted, all future comparisons of data between waves will be made at the same relative elevation.

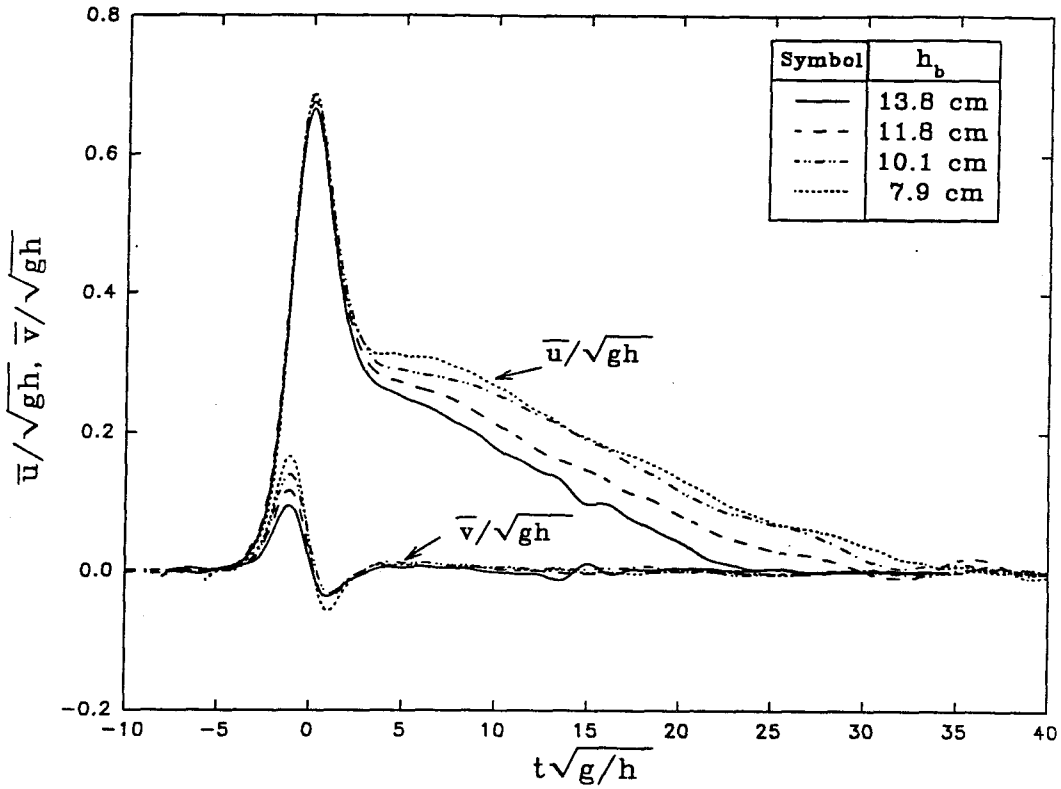

FIG. 4.22. Comparison of Mean Velocities for Four Different Waves at Breaking, z = 5.18 cm.

Another observable difference in Figure 4.22 is the shape and magnitude of the velocities associated with the shelf region in the trailing portion of the wave. Although some of the differences in magnitude could be attributed to different relative heights of observation, the principal difference is the result of the different horizontal length scales between waves. The depth at breaking of the smallest wave is less than three-fifths that of the largest wave. This means that, given a constant slope, the horizontal length scale has also been expanded by five-thirds for the smallest wave with respect to the largest. It should be recalled that the shelf behind the breaking wave is primarily attributed to the interaction between the wave and the slope of the bottom. Taking into account the scale of the wave, the smallest wave actually propagates up the slope for a distance 1.75 times that of the largest wave, observed at the same distance from the wave generator. Consequently, its trailing region velocities are affected to a greater extent by the bottom

slope. This length scale effect may also play a role in the different heights to depth ratio at breaking, H/h_b, of the four breaking waves.

The following series of velocity profiles are presented in order to observe the variation of mean velocities with depth and to investigate the growth and characteristics of the bottom boundary layer. For these profiles mean velocity magnitudes for a given time, $\bar{u}/\sqrt{gh}$, are shown on the abscissa. The relative elevation of each data point from the bottom, z/h, is plotted on the ordinate with a logarithmic axis to emphasize the velocity variations near the bottom boundary. Figure 4.23 shows a typical data set used to plot a velocity profile for wave propagation over a rock bed. It should be recalled that the focal volume for the LDV has a cross tank length of about 1.3 cm. Because of this, near the bed, each measured velocity represents a spatial average of the flow around two or three particles. As shown in Figure 4.23, the mean velocity data remained consistent between experiments, even at elevations quite close to the bed. In later figures, when multiple observations were made at the same elevation, the data points were averaged to obtain a single value for the mean velocity.

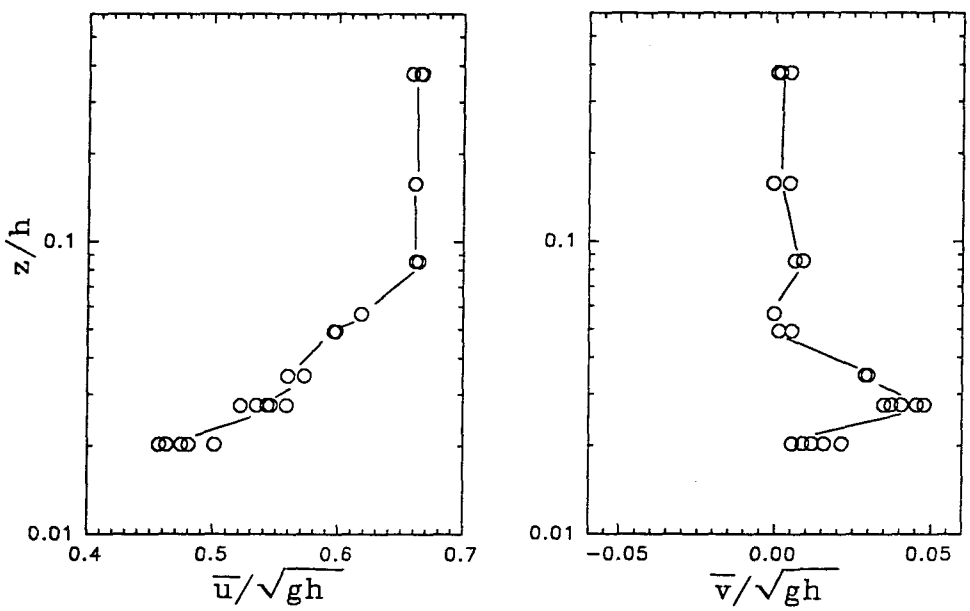

FIG. 4.23. Typical Data Set for Determination of Velocity Profiles, $(H/h)_b = 1.06$, $h_b = 13.8$ cm, $h/h_b = 1.0$, $t\sqrt{g/h} = 0.0$.

Figures 4.24 and 4.25 show velocity profile variations with time for the solitary wave propagating in a level tank over a bed of material and also over a flat plate. For these figures, Figure 4.8 is reproduced in frame (a) in order to show the shape of the wave as it passes above the measurement location. Figure 4.24 shows the variation with time of mean horizontal and vertical velocities in the solitary wave with H/h = 0.18 at a location approximately halfway across the test section, (x/L = 0.48).

It should first be noted that the magnitudes of the horizontal velocities over the rock and over the flat plate agree almost exactly at the higher measurement elevations. The mean horizontal velocities reach a maximum at $t\sqrt{g/h} = 0.0$ and decrease as the wave passes. At the higher elevations the vertical velocities over the rock and the flat plate also agree closely. As expected from Equation 1.4, they start out slightly positive before the passage of the crest, are very close to zero at the passage of the wave crest and become negative after $t\sqrt{g/h} = 0.0$. Also as expected, the vertical velocities decrease markedly with depth so that below z/h = 0.1 the variation of the velocities with wave crest passage is not really noticeable.

There is, however, a noticeable difference between velocity measurements over the rock bed and the flat plate at relative elevations below 0.02. The thickness of the boundary layer is defined here as the elevation where the horizontal velocity profile first departs from the relatively constant velocities occurring at higher elevations. At the time of wave crest passage, the thickness of the boundary layer for the rock is near z/h = 0.02, or about twice that of the boundary layer over the flat plate. As the wave continues to move over the measurement location, the boundary layer thickness continues to increase even though the mean horizontal velocity is decreasing. At $t\sqrt{g/h}$ =2.5 the thickness of both boundary layers is about twice their value at $t\sqrt{g/h} = 0.0$. Though there are not large differences between rock bed and flat plate measurements, the vertical velocity profiles in each case begin to show deviations from the higher elevation values at the same

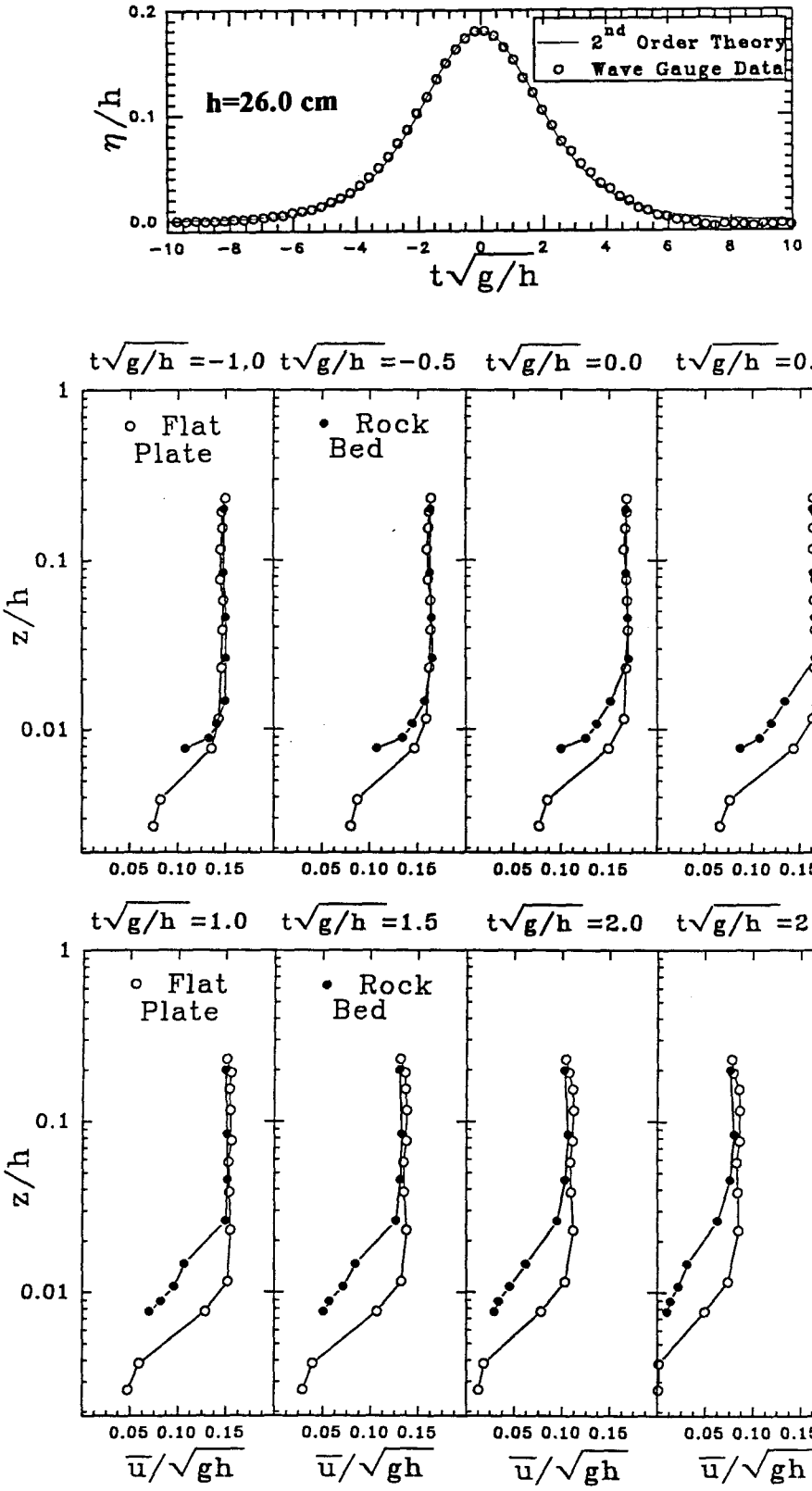

FIG. 4.24. Variation of Mean Velocities, Slope = 0.0, H/h = 0.18, x/L = 0.48.

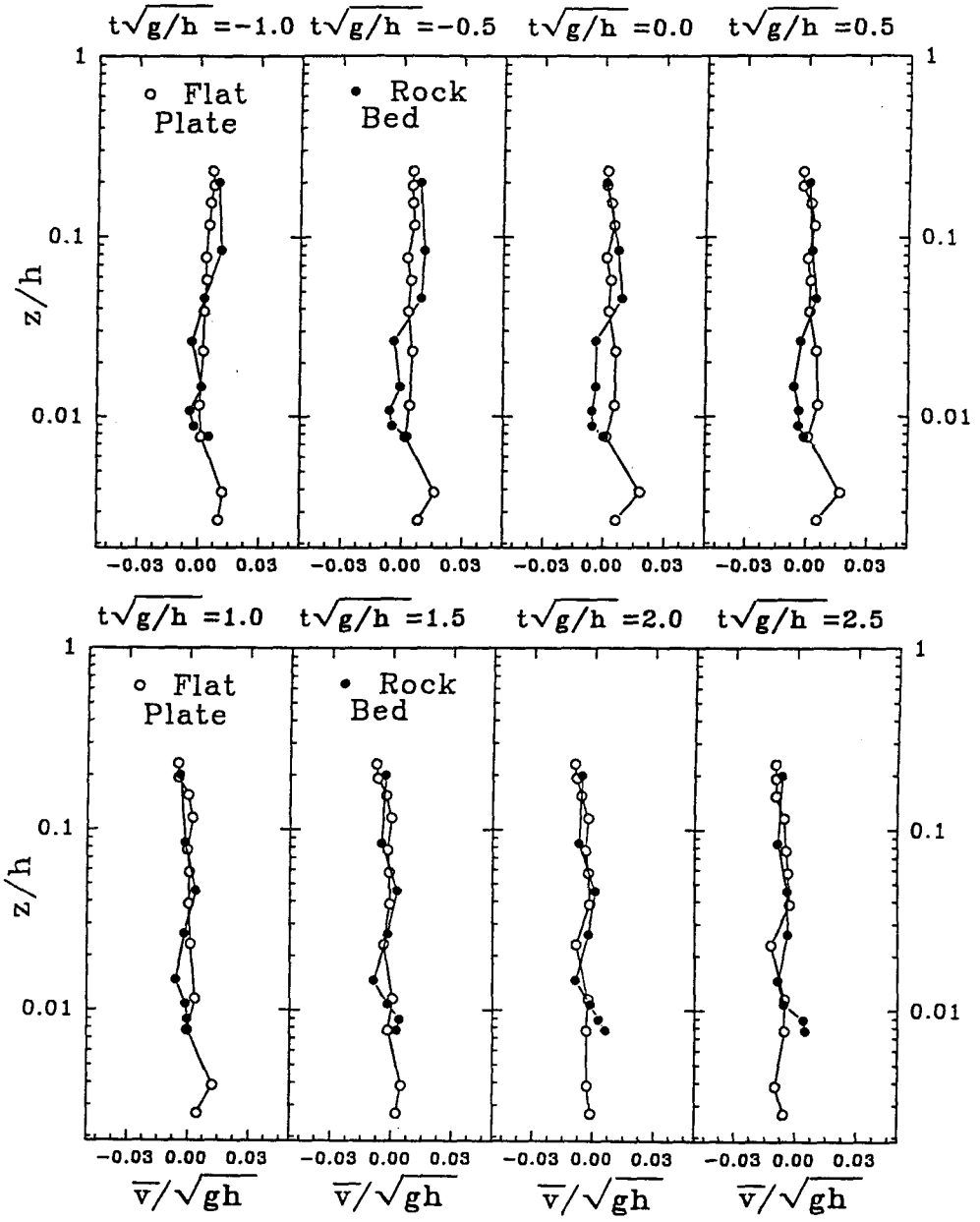

(c)

FIG. 4.24. Variation of Mean Velocities, Slope = 0.0, H/h = 0.18, x/L =- 0.48.

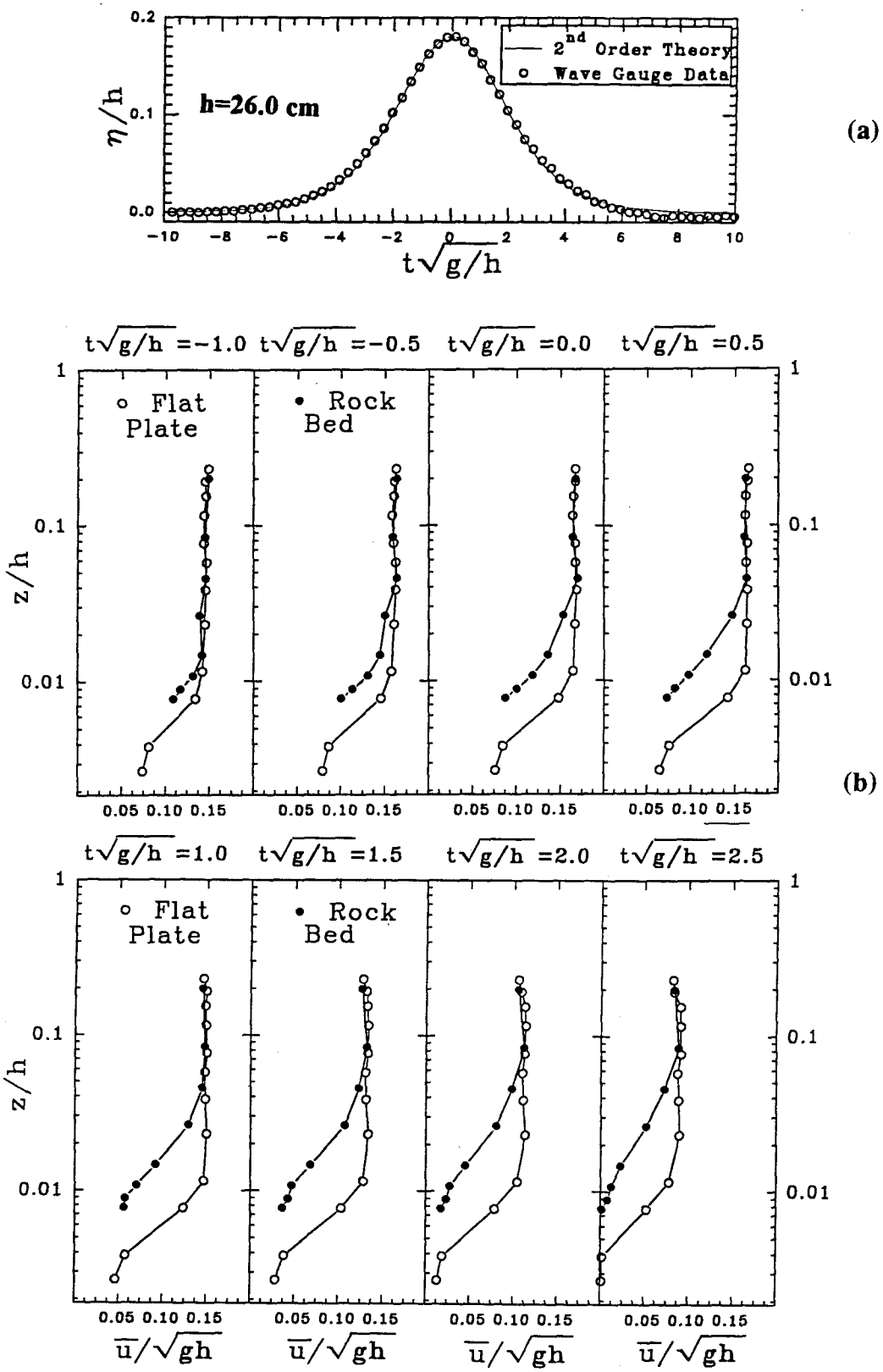

FIG. 4.25. Variation of Mean Velocities, Slope = 0.0, H/h = 0.18, x/L = 0.91.

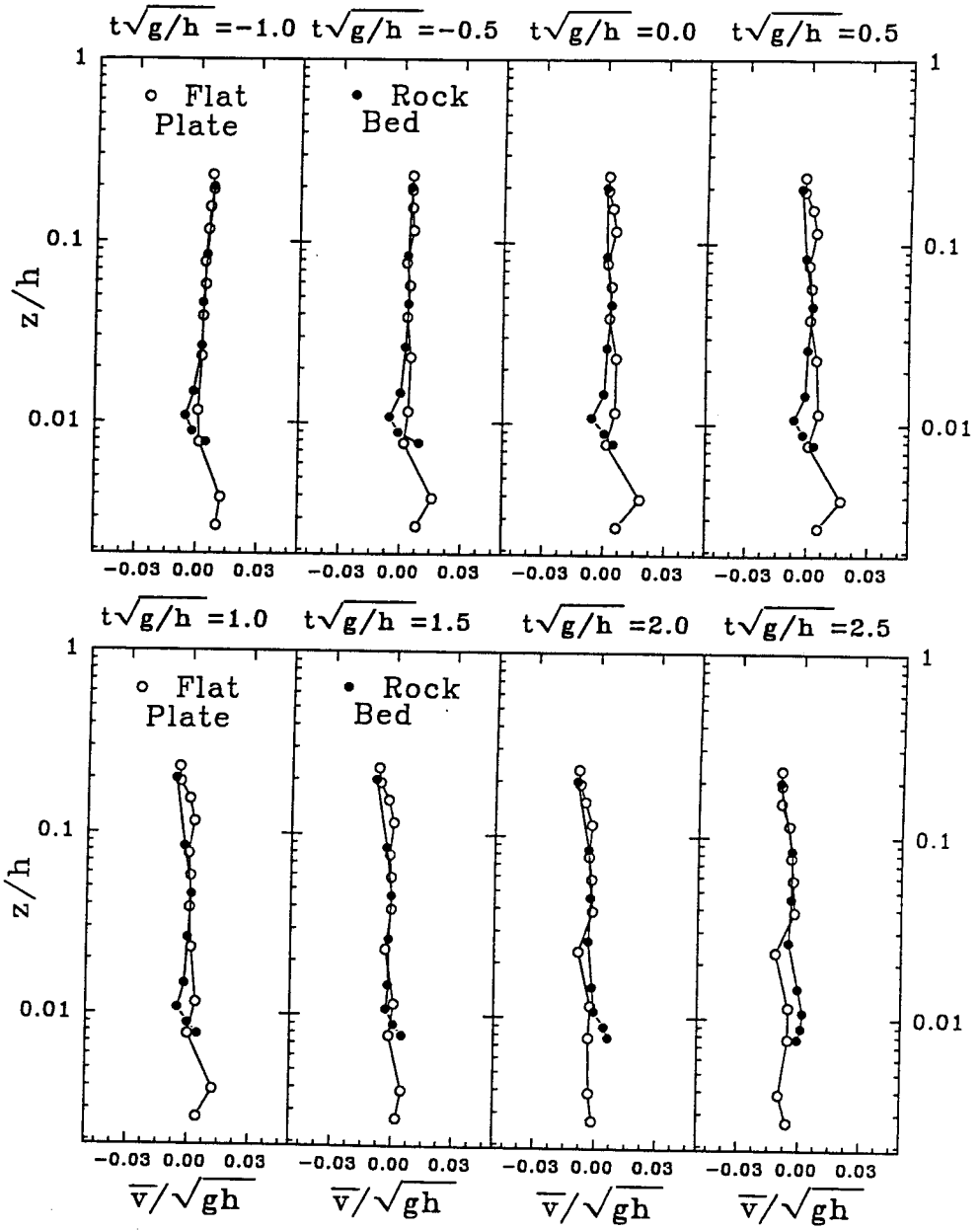

(c)

FIG. 4.25. Variation of Mean Velocities, Slope = 0.0, H/h = 0.18, x/L = 0.91.

relative distances from the boundary as the horizontal velocity profiles. In addition, significant vertical velocities occur within the boundary layer when the higher elevation velocities are small, implying that they result from the mechanics of the flow near the bottom boundary.

Figure 4.25 shows the variation with time of the mean velocities under the solitary wave at a location further shoreward in the test section, at x/L = 0.91. When compared with Figure 4.24 , the flat plate velocities are practically unchanged. The thickness of the boundary layer over the rock bed, however, has increased. At $t\sqrt{g/h} = 0.0$ the top of the boundary layer occurs between z/h = 0.03 and z/h = 0.04. Both the horizontal and the vertical velocity profiles show marked changes in curvature at this elevation. Other than the growth of the boundary layer with distance along the rock bed, the general features of the solitary wave velocity profiles are similar in Figures 4.24 and 4.25.

The mean velocities measured for the solitary wave over the rock bed at locations x/L = 0.48 and x/L = 0.91 were compared to the velocities computed by the second and third order theories of Boussinesq (1878) and Grimshaw (1971) respectively, for a wave of amplitude H/h = 0.18. As mentioned in Chapter 1, these theories neglect frictional effects at the bottom boundary. The velocities are compared at two times during the passage of the wave in Figure 4.26. Figure 4.26(a) shows the theoretical and measured values at time $t\sqrt{g/h} = 0.0$. At the relative elevations shown, the variation with depth of the theoretical horizontal velocities is negligible and the vertical velocities are defined to be zero. The measured mean velocities outside the boundary layer are well within the range of the theoretical values. In Figure 4.26(b), the third order theory of Grimshaw shows the variation with depth of the vertical velocity. Again, outside the boundary layer the measured velocities agree with theoretical values.

As discussed in section 1.3, for steady flows and sinusoidally oscillating flows where accelerations near the bottom are small, the velocity distribution near the bottom can be taken to be logarithmic. Figure 4.26 shows values for the shear velocity calculated using the velocity defect law:

$$\frac{u-u_0}{u_*}=\frac{1}{k}\ln\left(\frac{y}{y_0}\right) \tag{4.2}$$

where u_* is the shear velocity, u_o and y_o are the velocity and elevation at the top of the boundary layer, u and y are measured data and k is the von Karman constant (assumed = 0.4). This method of calculation was used because it makes no prior assumptions about the equivalent sand grain roughness, k_s, on the bottom boundary. When the grain roughness, k_s, is known the shear velocity, u_*, may be calculated using the law of the wall

$$\frac{u}{u_*}=8.5+5.75\log_{10}\frac{z}{k_s} \tag{4.2a}$$

The first indication that the solitary wave does not conform to steady state assumptions comes from comparing the calculated shear velocity values for the flat plate and the rock bed. The value of u_* for the plate should be lower than the values for the rock bed since the roughness of the plate is considerably smaller than the rock roughness. Instead, the calculated shear velocity for the plate is higher than that at both rock bed locations. Over the length of the rock bed, the shear velocity is not constant but decreases with distance along the test section. Additionally, the maximum shear velocity does not occur at the same time as the maximum mean velocity. As seen in Figure 4.26(b), the velocity profiles continue to steepen even though the mean horizontal velocity has decreased. These conditions indicate that as the wave passes the measurement location, the boundary layer does not have sufficient time to adjust to the changing velocities.

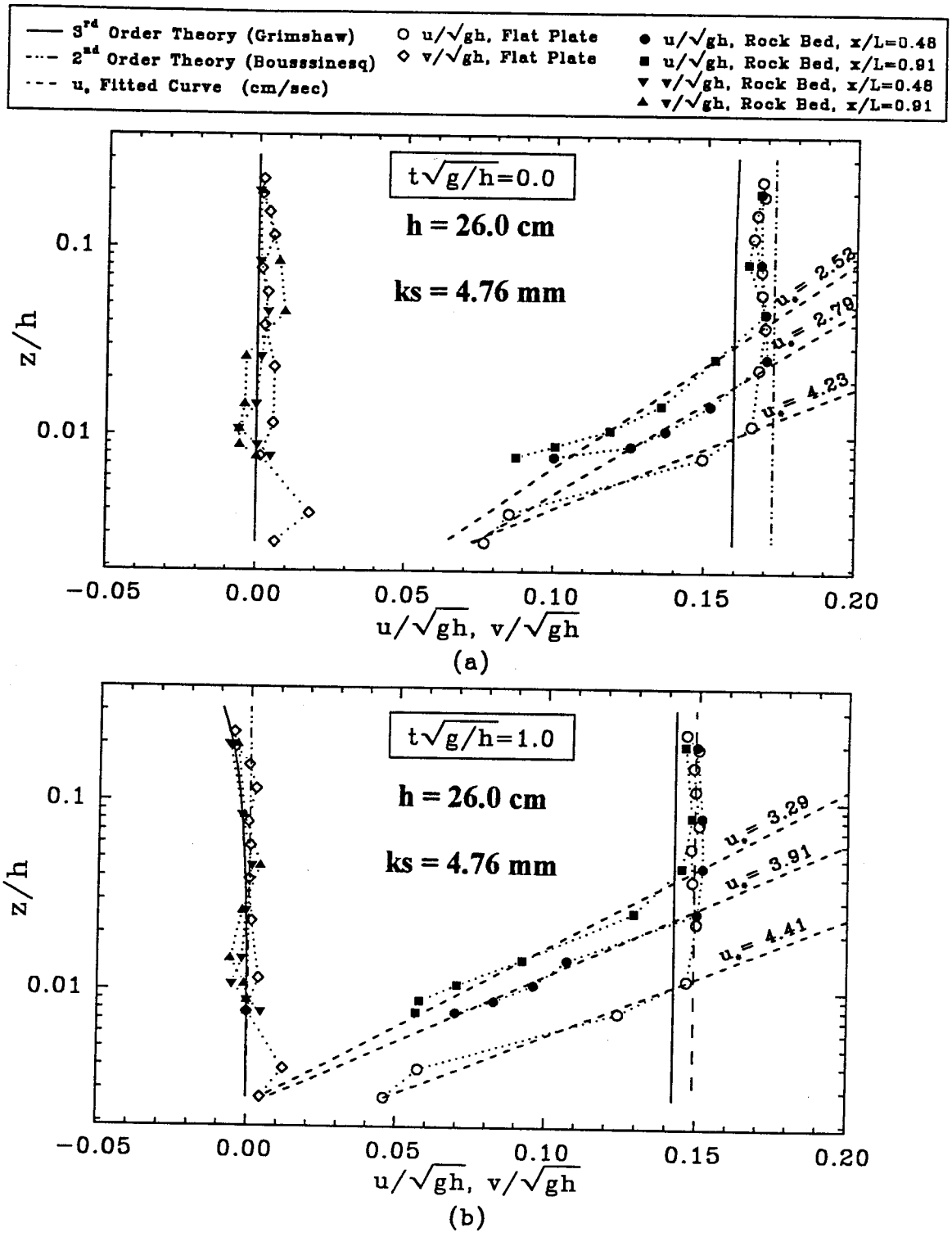

FIG 4.26. Comparison of Observed and Predicted Velocity Profiles for Solitary Wave, Slope = 0.0, H/h = 0.18.

Hence the slope of the mean velocity profile is not an accurate measure of the shear on the bottom at any one given time.

Table 4.2 shows a comparison between the values of u_*, shown in Figure 4.26 for the solitary wave, and values computed for a steady flow at depth h = 26 cm with a bottom roughness of 4.76 mm. The steady flow shear velocities use the Nikuradse sand grain roughness curves as presented by Brownlie (1981) based on the mean velocity away from the boundary, and equation 4.2a.. In addition, values for u_* obtained by Jonsson (1976) and Kamphuis (1975) for a sinusoidal flow in a water tunnel are included. These values are based on a maximum water particle excursion to roughness ratio, a/k_s. While the u_* values computed for the solitary wave over the rock fall near the corresponding values for the sinusoidal water tunnel experiments, it is not clear what criteria should be used to assign a shear velocity to the flow in the solitary wave using mean velocity profiles.

Table 4.2. Comparison of Solitary Wave Shear Velocities (cm/s) with Steady Flow and Oscillatory Flow Values. H/h = 0.18 at x/L = 0.48, k_s = 4.76 mm, h=26 cm.

	Solitary Wave		Law of the Wall		Equivalent Steady Uniform Channel Flow		Sinusoidally Oscillating Flows	
					(u= 27cm/s)	(u= 23cm/s)	Jonsson a/k_s=35.4	Kamphuis a/k_s=14.2
	$t\sqrt{g/h}$ =0	$t\sqrt{g/h}$ =1	$t\sqrt{g/h}$ =0	$t\sqrt{g/h}$ =1	$t\sqrt{g/h}$ =0	$t\sqrt{g/h}$ =1	$t\sqrt{g/h}$ = 0	$t\sqrt{g/h}$ = 0
Rock Bed	2.79	3.91	2.87	2.31	1.73	1.46	3.57	3.25
Flat Plate	4.23	4.41			1.19	1.04	-	1.71

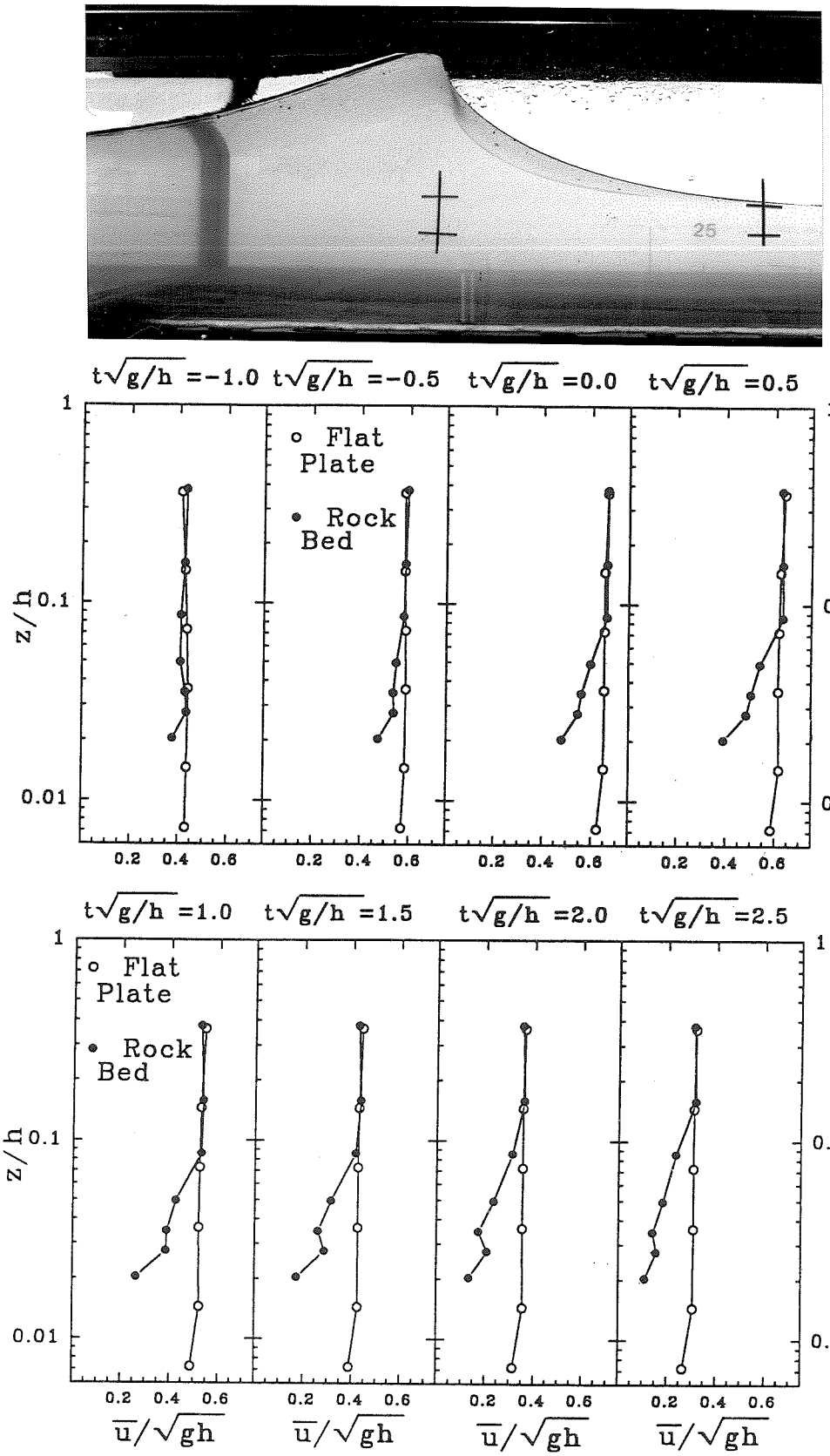

FIG. 4.27. Mean Velocities, $(H/h)_b = 1.06$, $h/h_b = 1.00$, $h_b = 13.8$ cm.

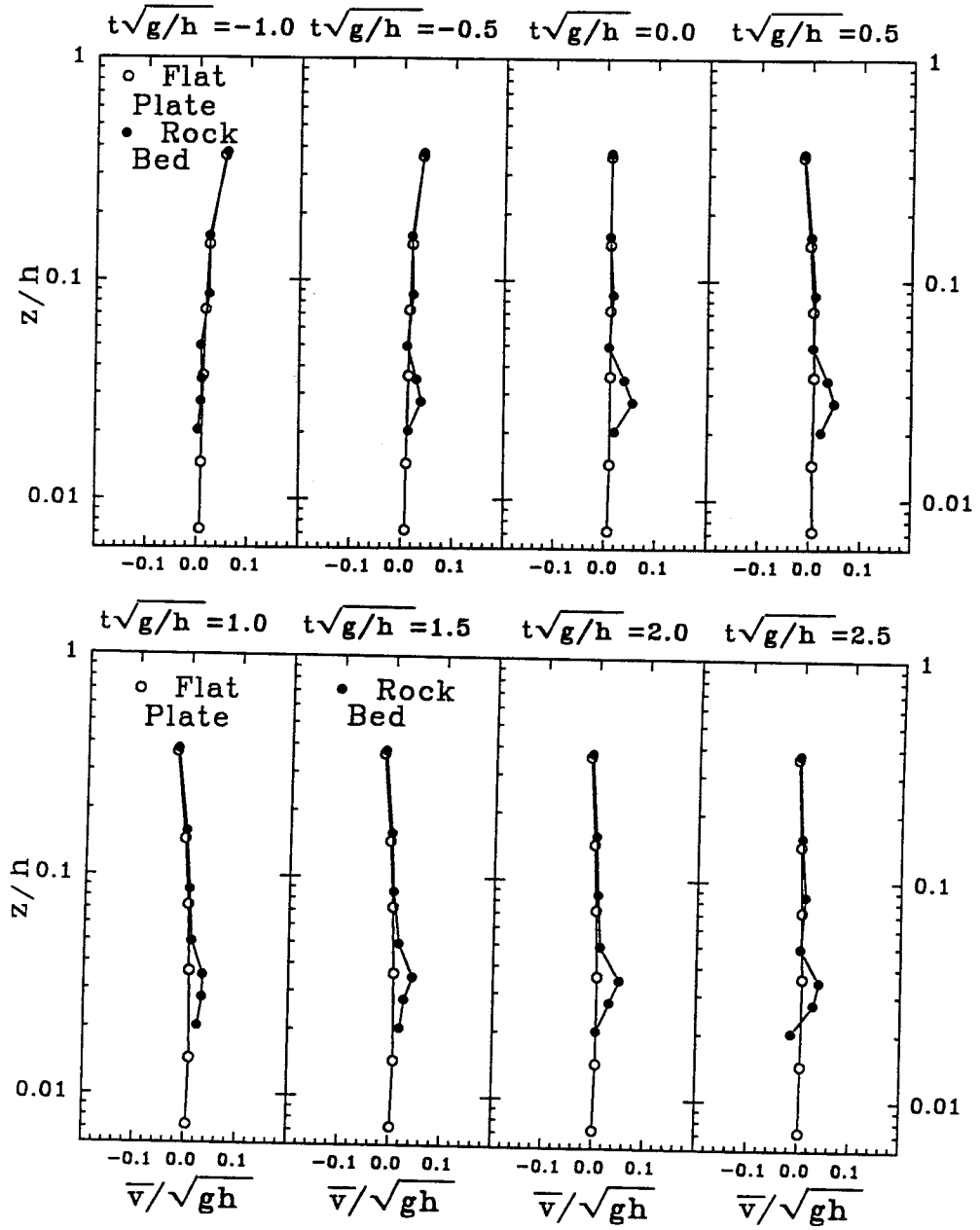

FIG. 4.27. Mean Velocities, $(H/h)_b = 1.06$, $h/h_b = 1.00$, $h_b = 13.8$ cm.

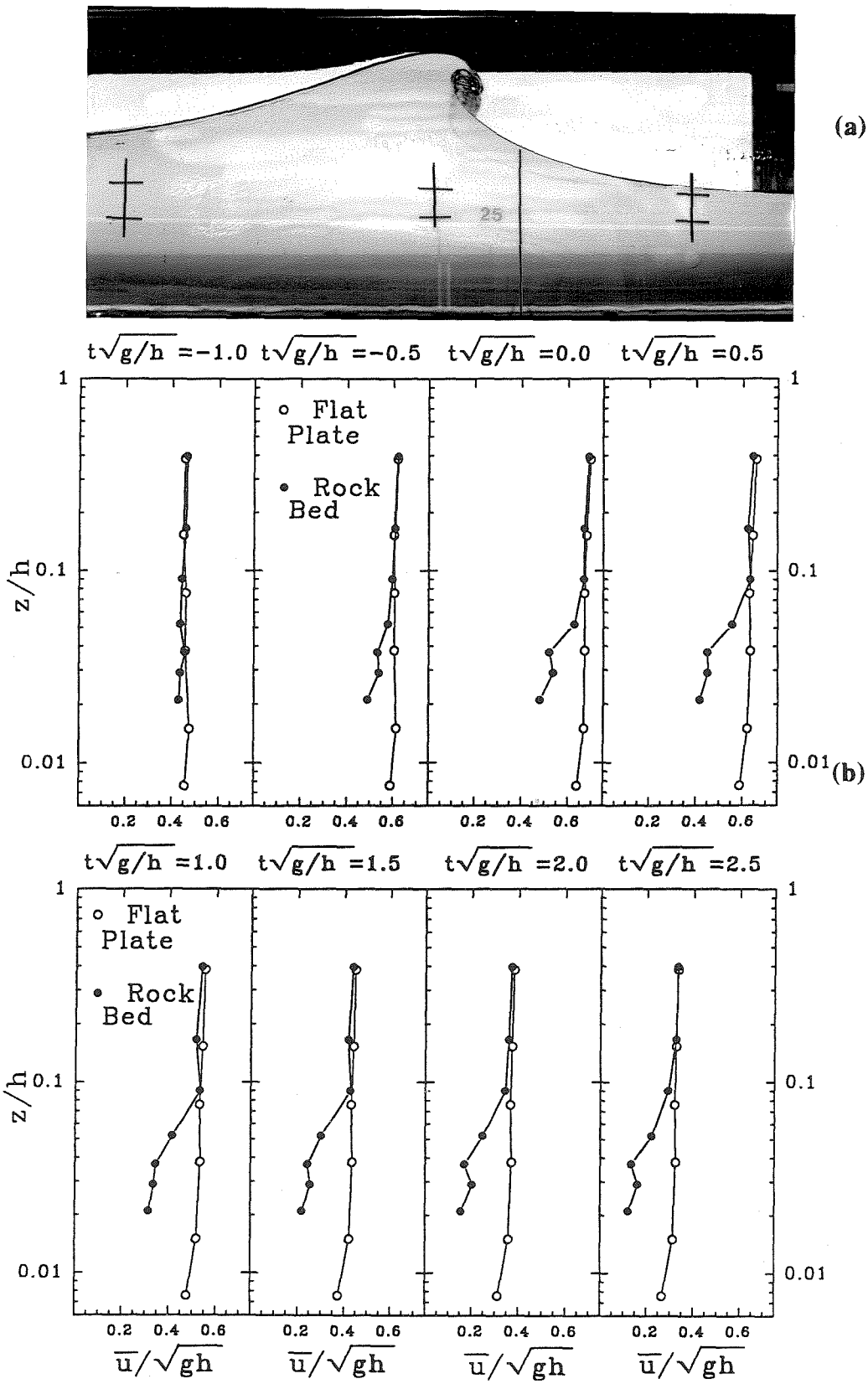

FIG. 4.28. Mean Velocities, $(H/h)_b = 1.06$, $h/h_b = 0.95$, $h_b = 13.8$ cm.

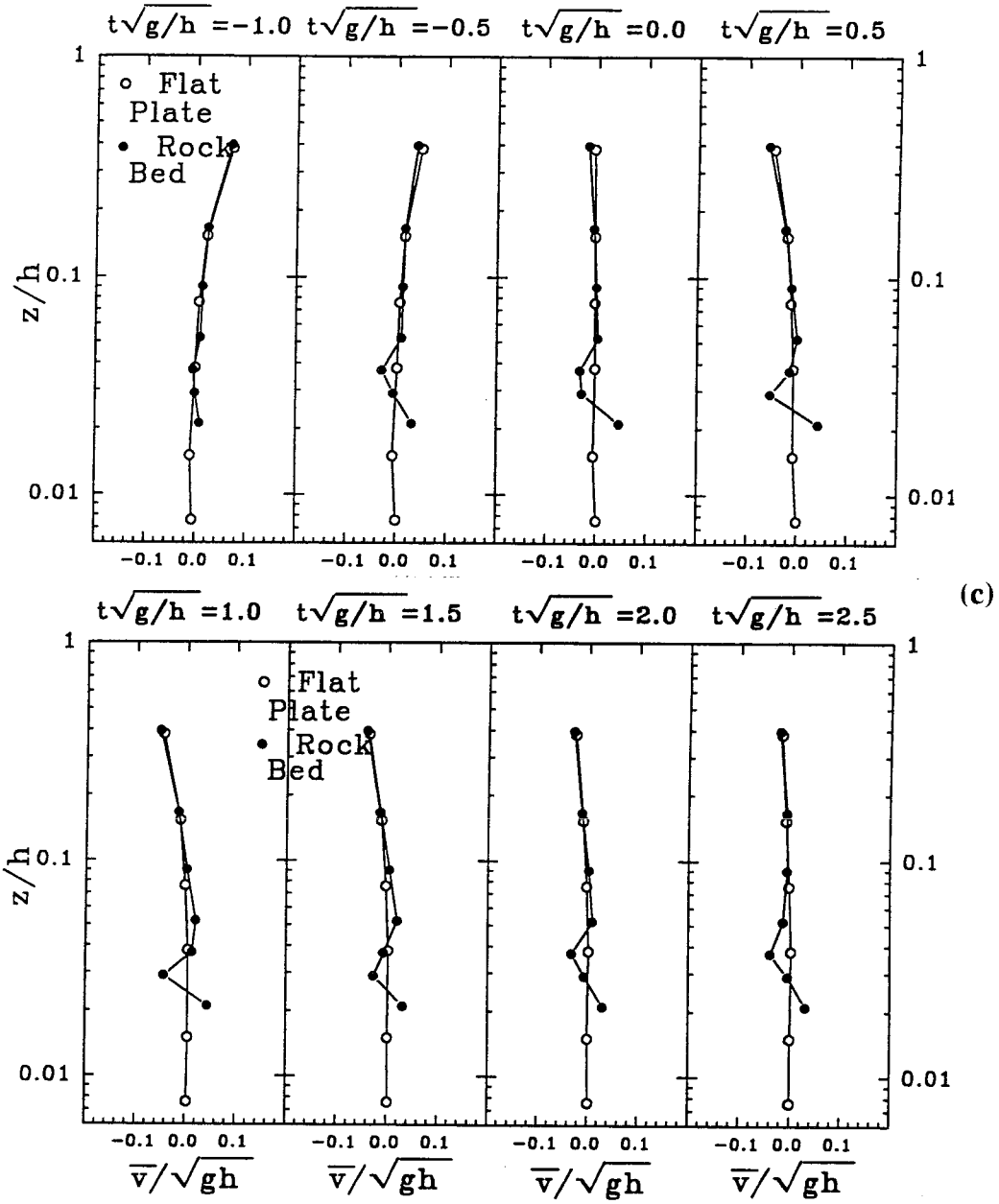

FIG. 4.28. Mean Velocities, $(H/h)_b = 1.06$, $h/h_b = 0.95$, $h_b = 13.8$ cm.

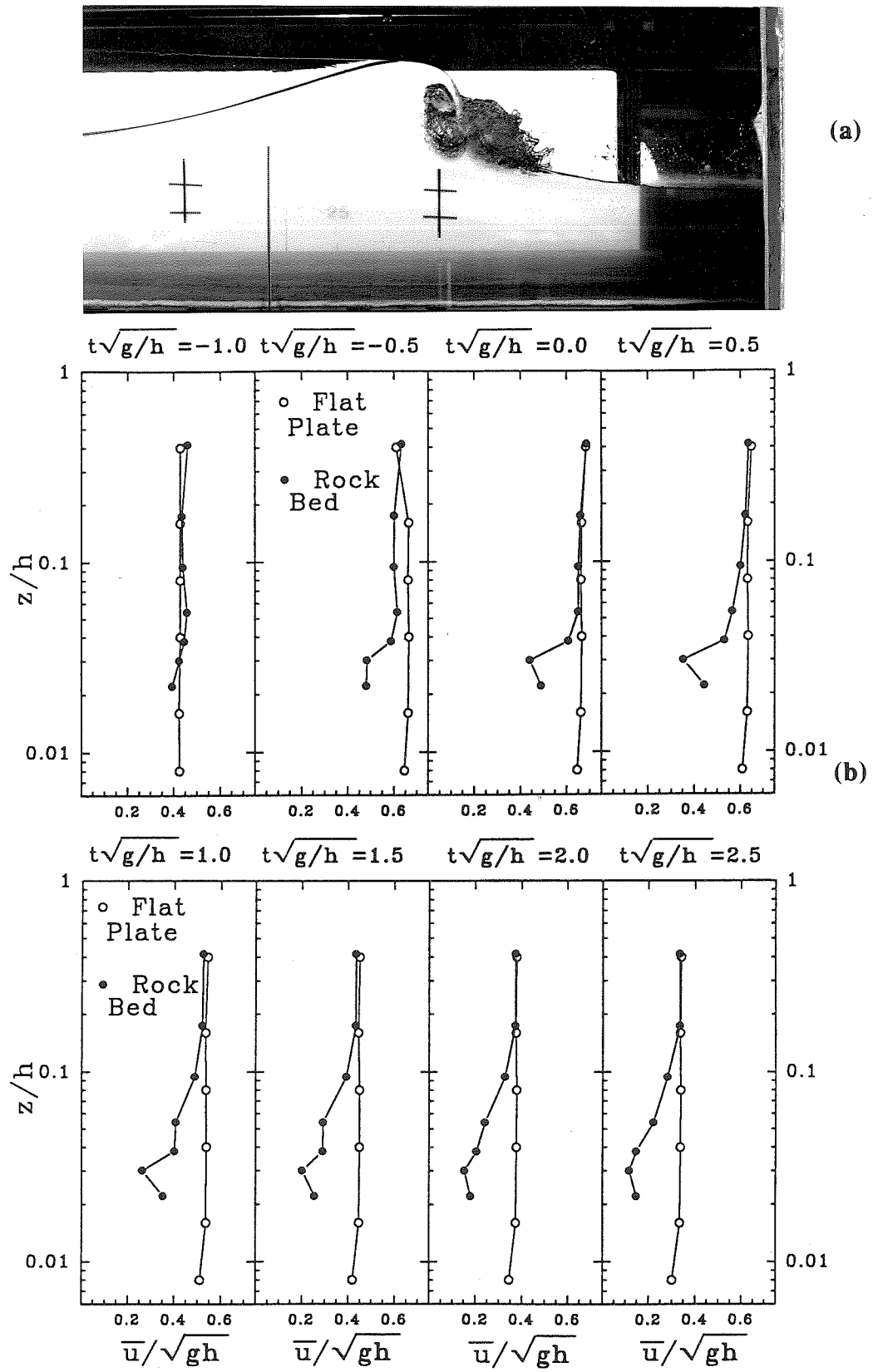

FIG. 4.29. Mean Velocities, $(H/h)_b = 1.06$, $h/h_b = 0.91$, $h_b = 13.8$ cm.

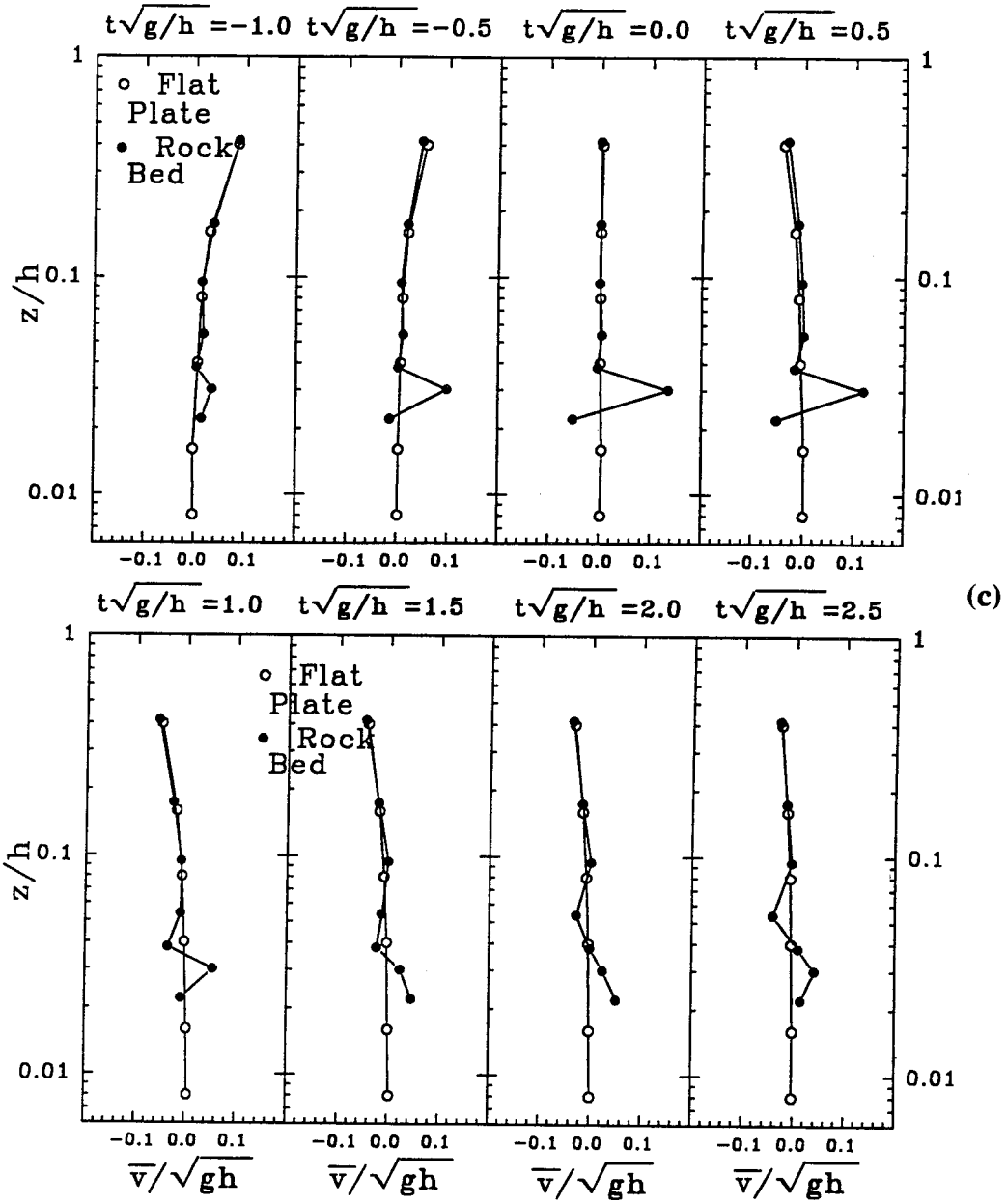

FIG. 4.29. Mean Velocities, $(H/h)_b = 1.06$, $h/h_b = 0.91$, $h_b = 13.8$ cm.

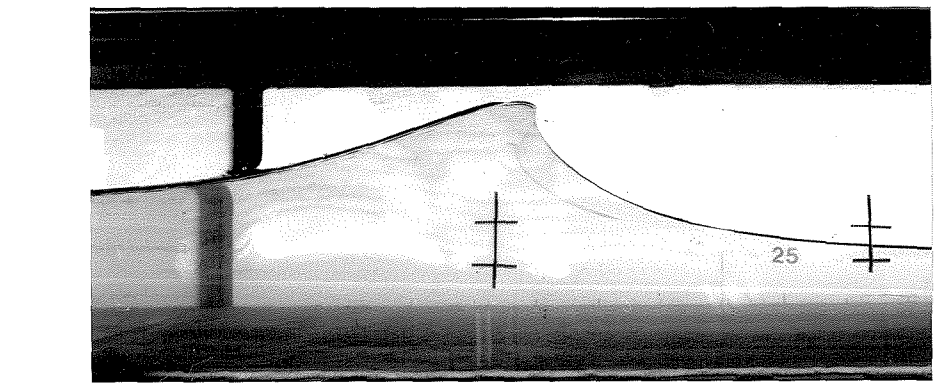

(a)

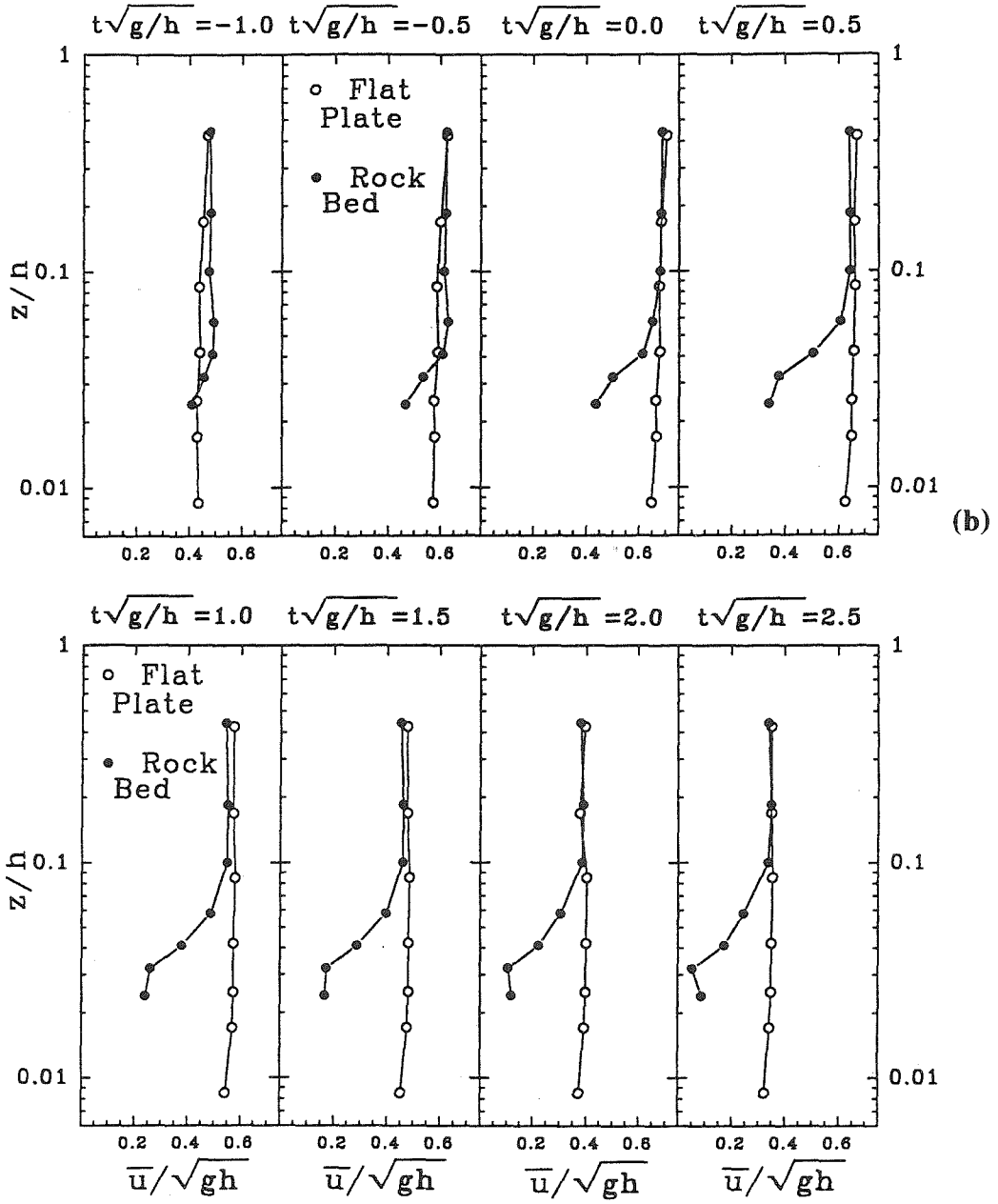

(b)

FIG. 4.30. Mean Velocities, $(H/h)_b = 1.01$, $h/h_b = 1.00$, $h_b = 11.8$ cm.

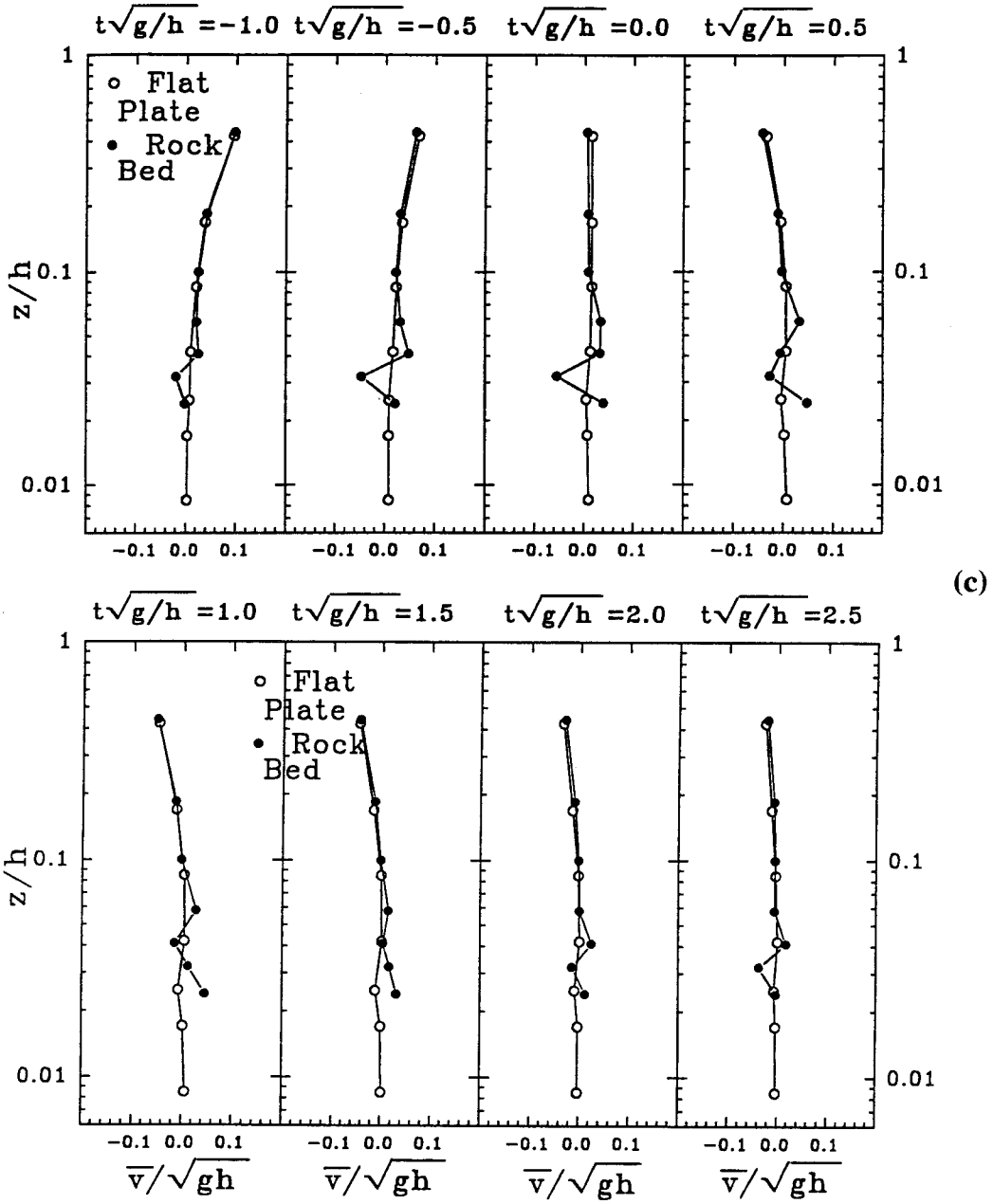

FIG. 4.30. Mean Velocities, $(H/h)_b = 1.01$, $h/h_b = 1.00$, $h_b = 11.8$ cm.

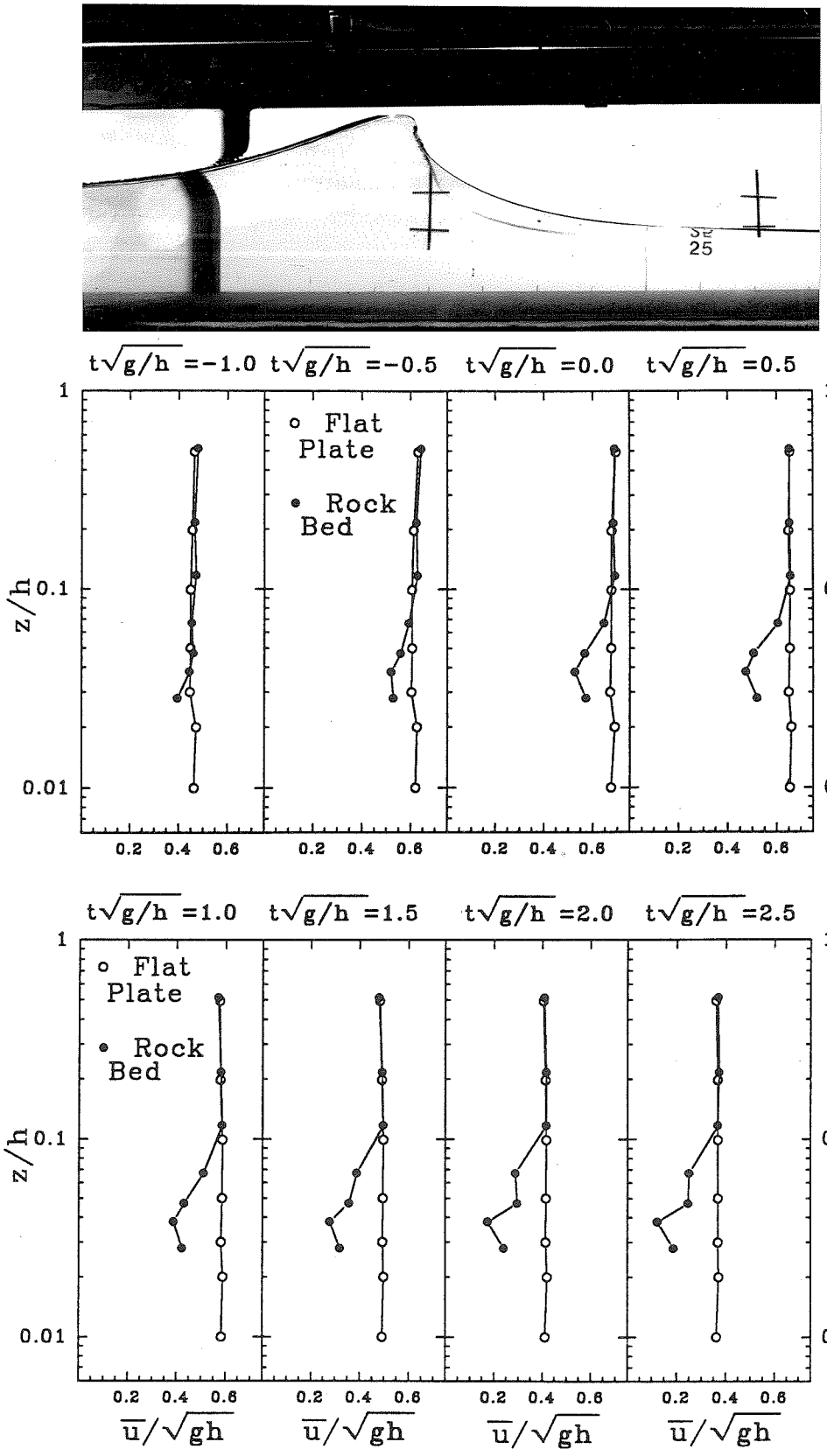

FIG. 4.31. Mean Velocities, $(H/h)_b = 0.98$, $h/h_b = 1.00$, $h_b = 10.1$ cm.

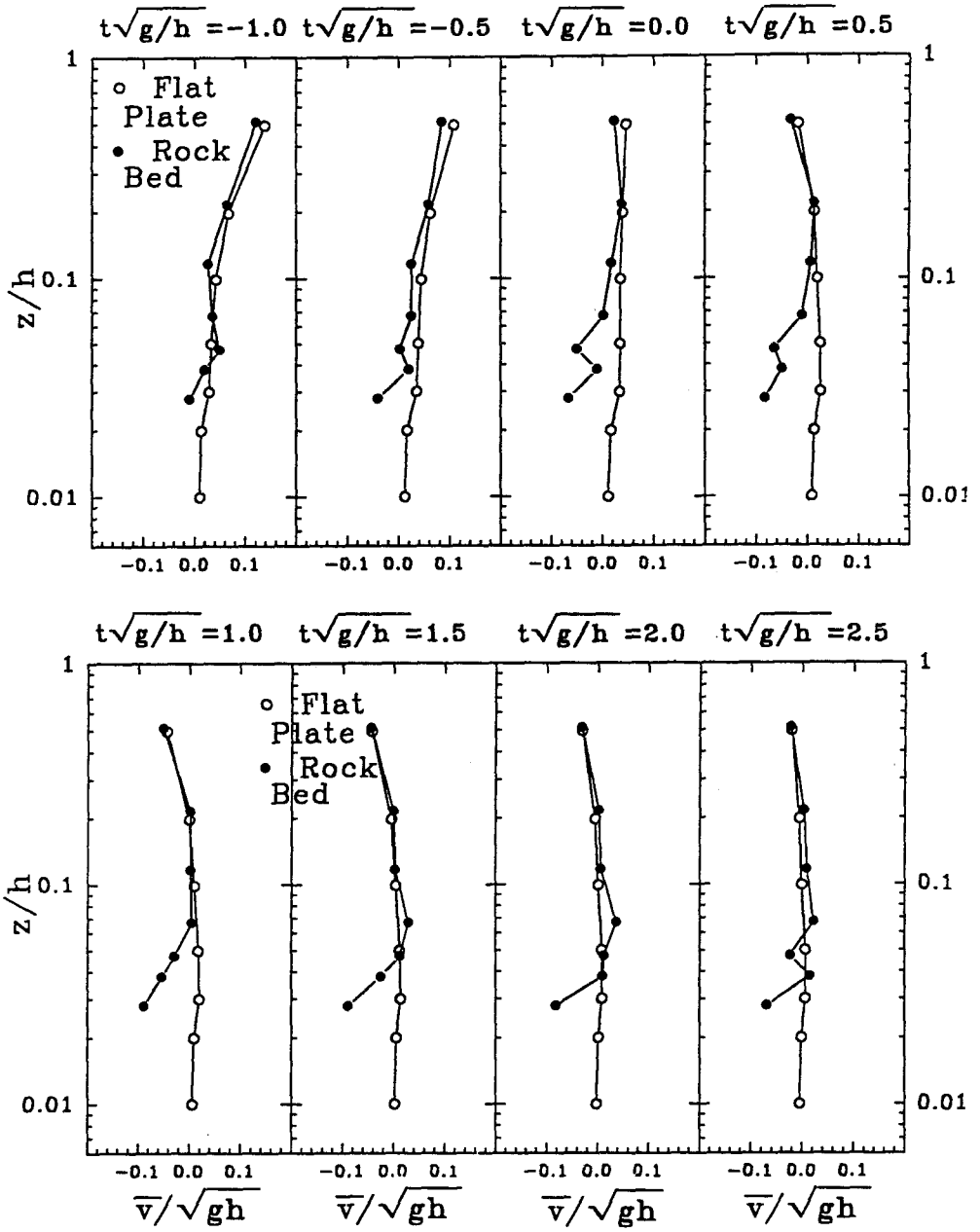

FIG. 4.31. Mean Velocities, $(H/h)_b = 0.98$, $h/h_b = 1.00$, $h_b = 10.1$ cm.

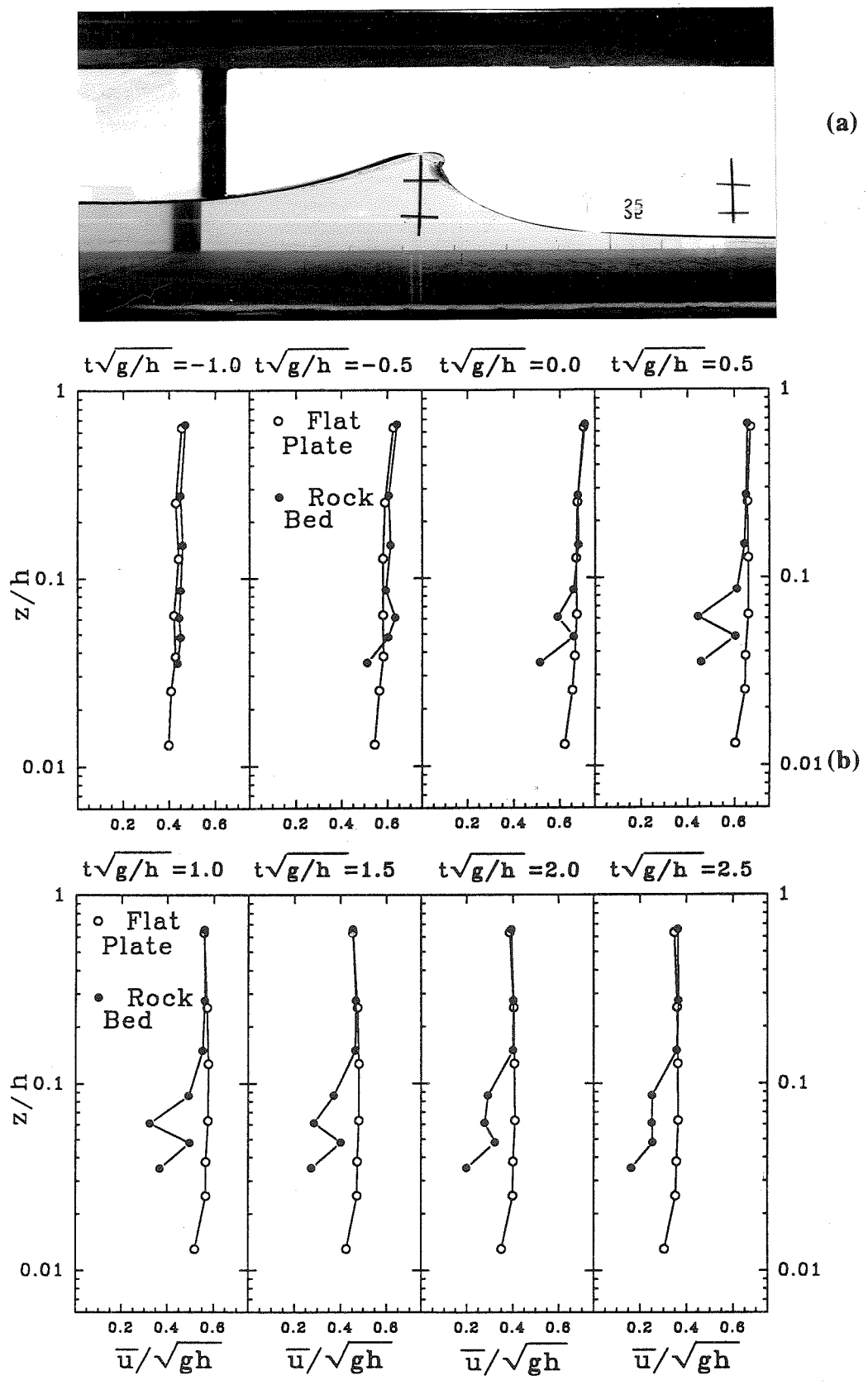

FIG. 4.32. Mean Velocities, $(H/h)_b = 0.96$, $h/h_b = 1.00$, $h_b = 7.9$ cm.

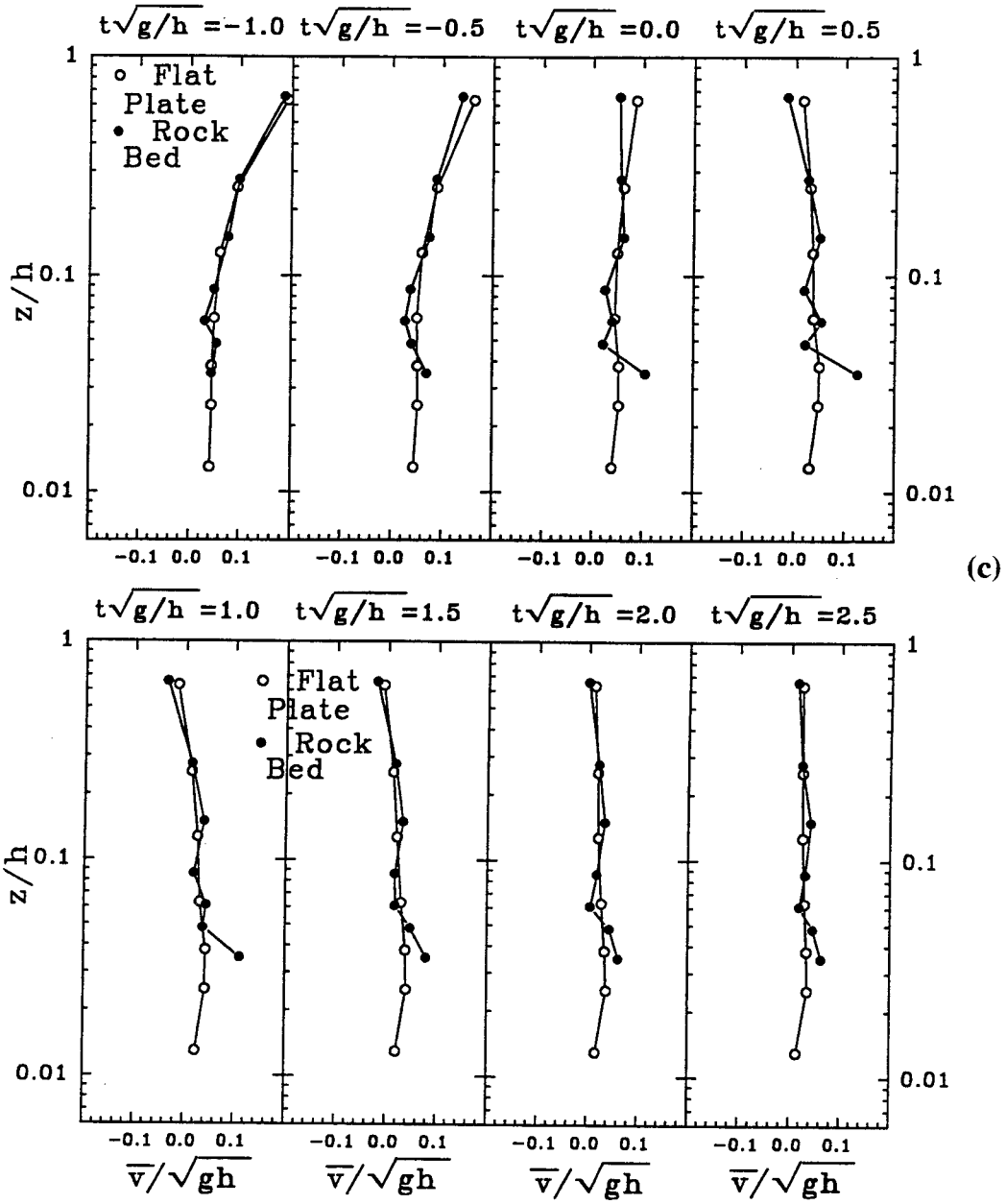

FIG. 4.32. Mean Velocities, $(H/h)_b = 0.96$, $h/h_b = 1.00$, $h_b = 7.9$ cm.

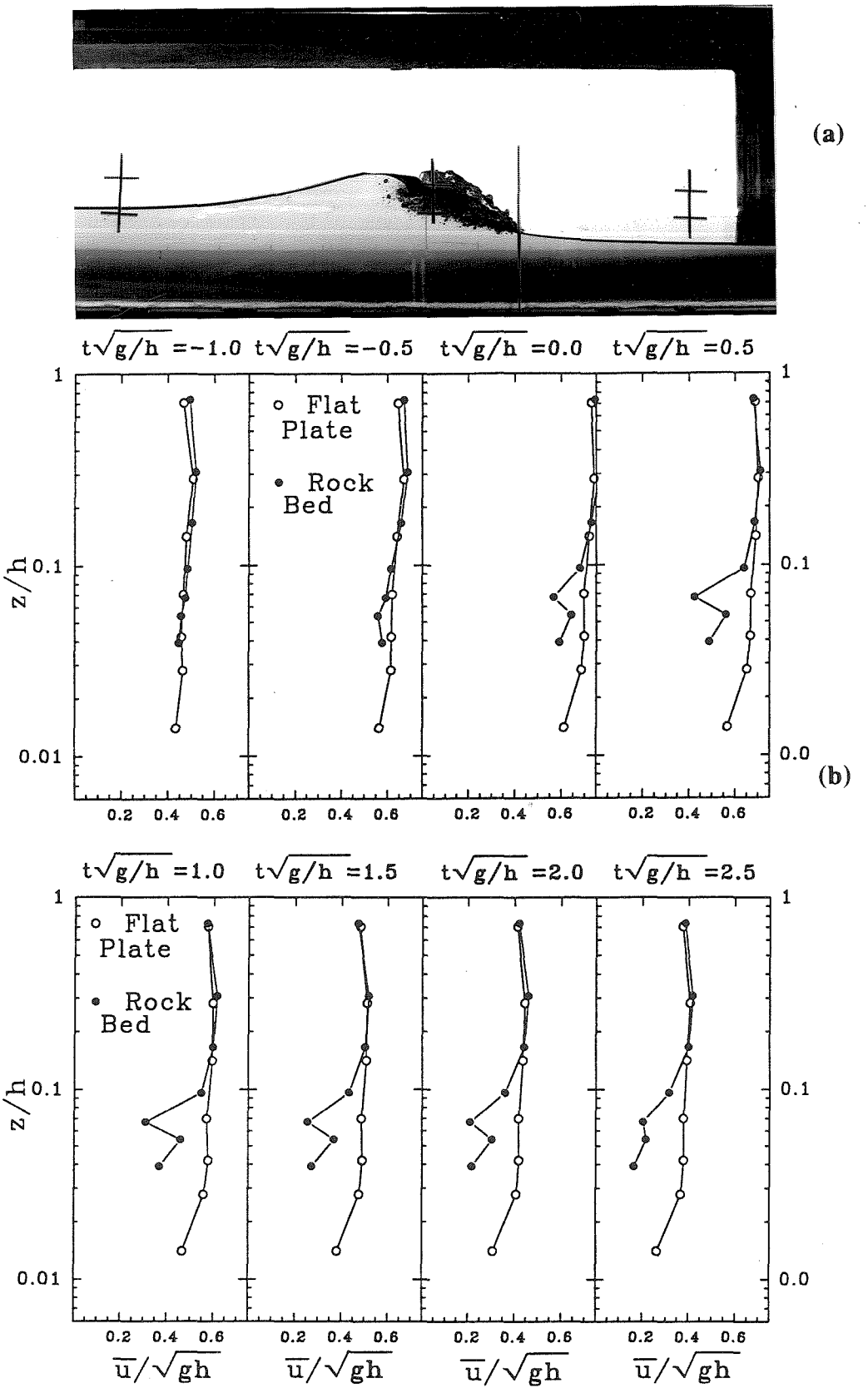

FIG. 4.33. Mean Velocities, $(H/h)_b = 0.96$, $h/h_b = 0.90$, $h_b = 7.9$ cm.

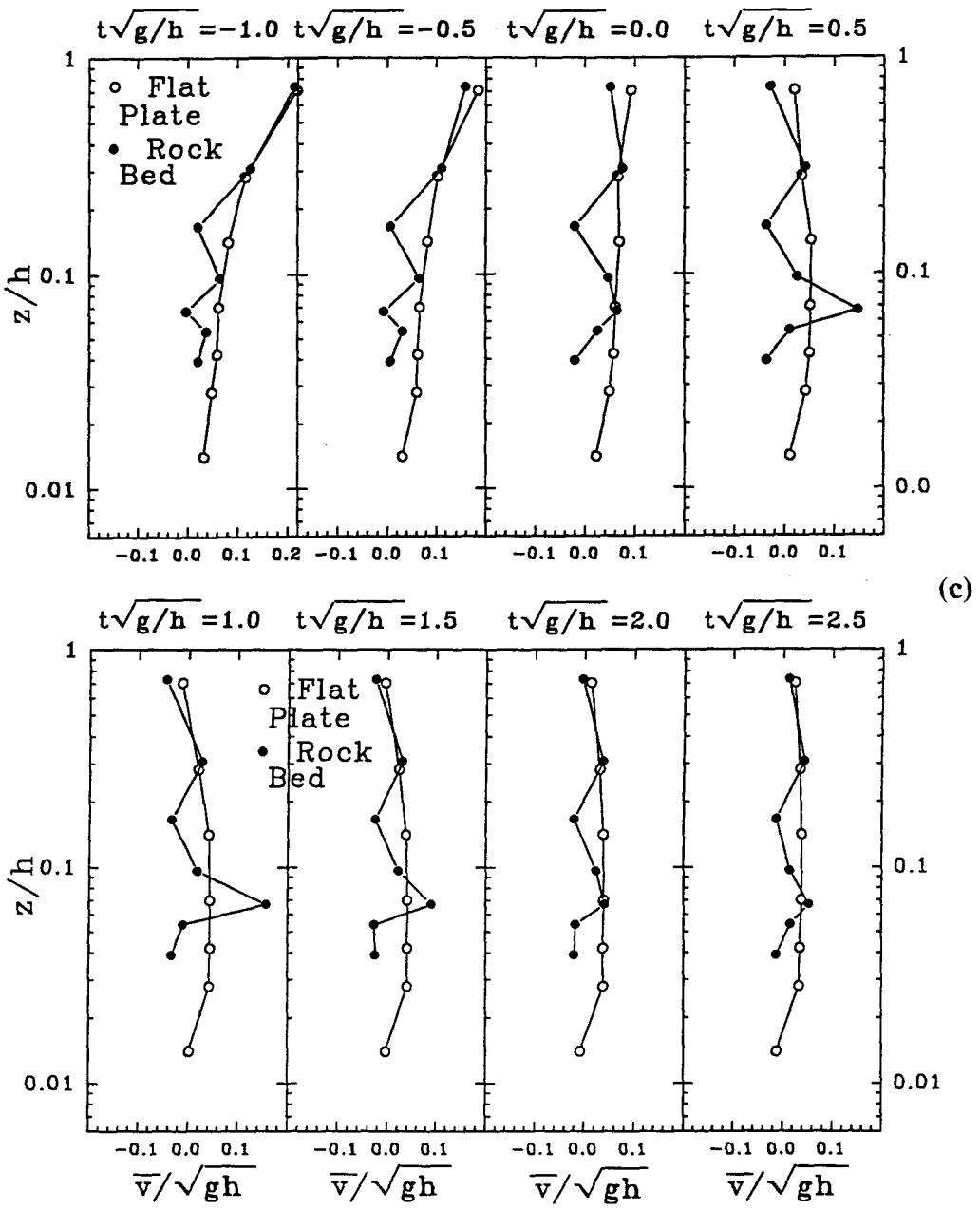

FIG. 4.33. Mean Velocities, $(H/h)_b = 0.96$, $h/h_b = 0.90$, $h_b = 7.9$ cm.

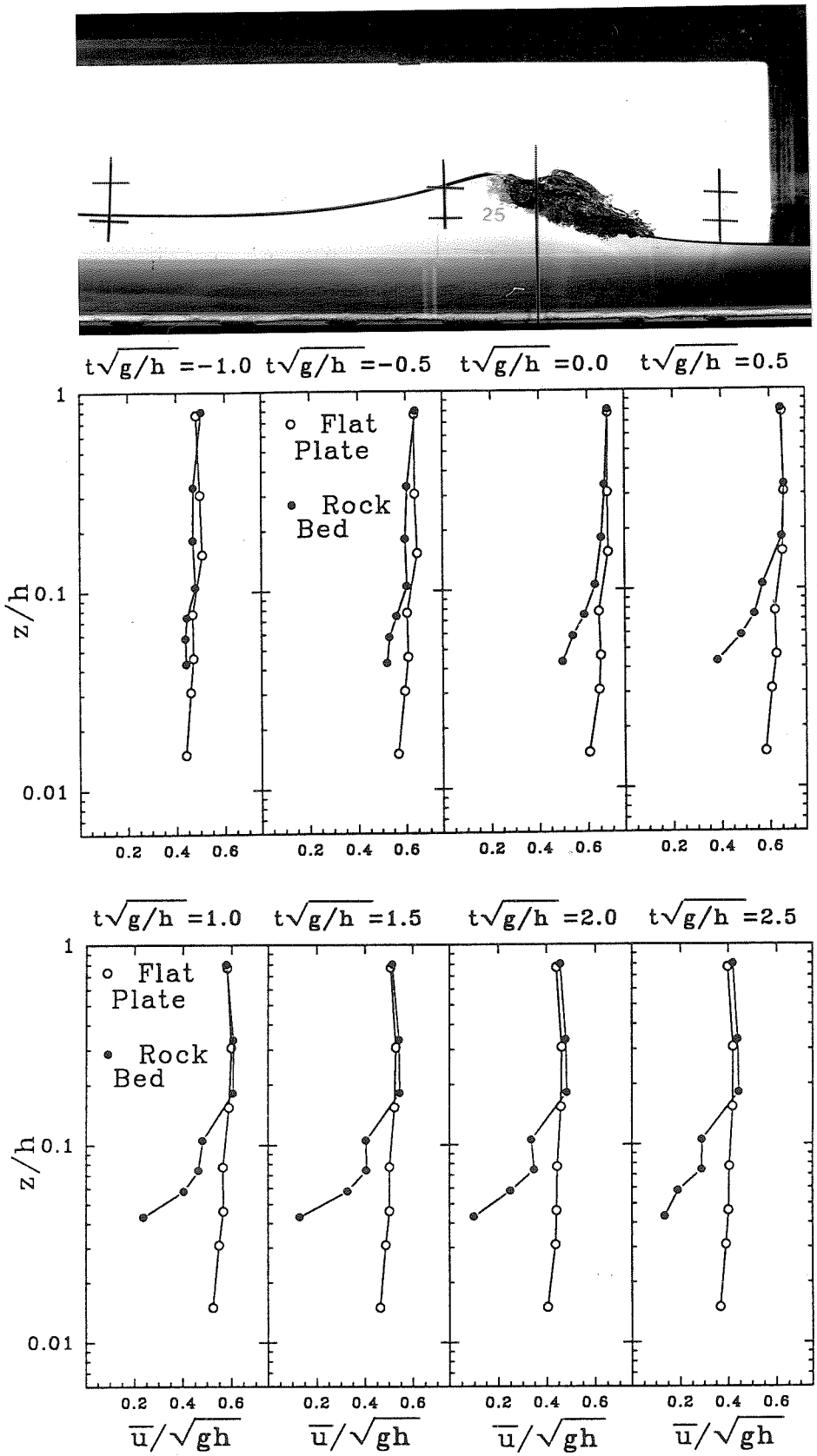

FIG. 4.34. Mean Velocities, $(H/h)_b = 0.96$, $h/h_b = 0.82$, $h_b = 7.9$ cm.

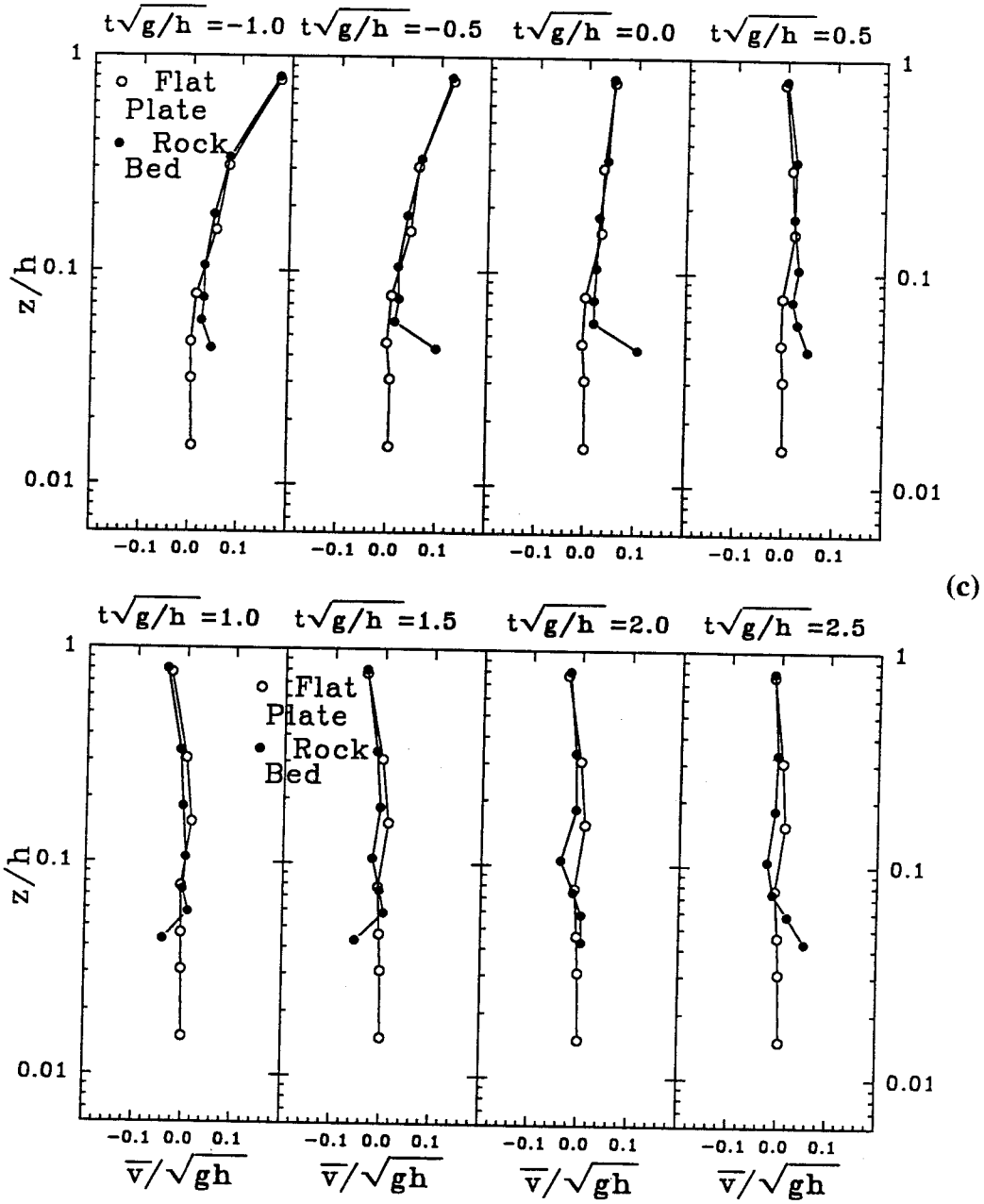

FIG. 4.34. Mean Velocities, $(H/h)_b = 0.96$, $h/h_b = 0.82$, $h_b = 7.9$ cm.

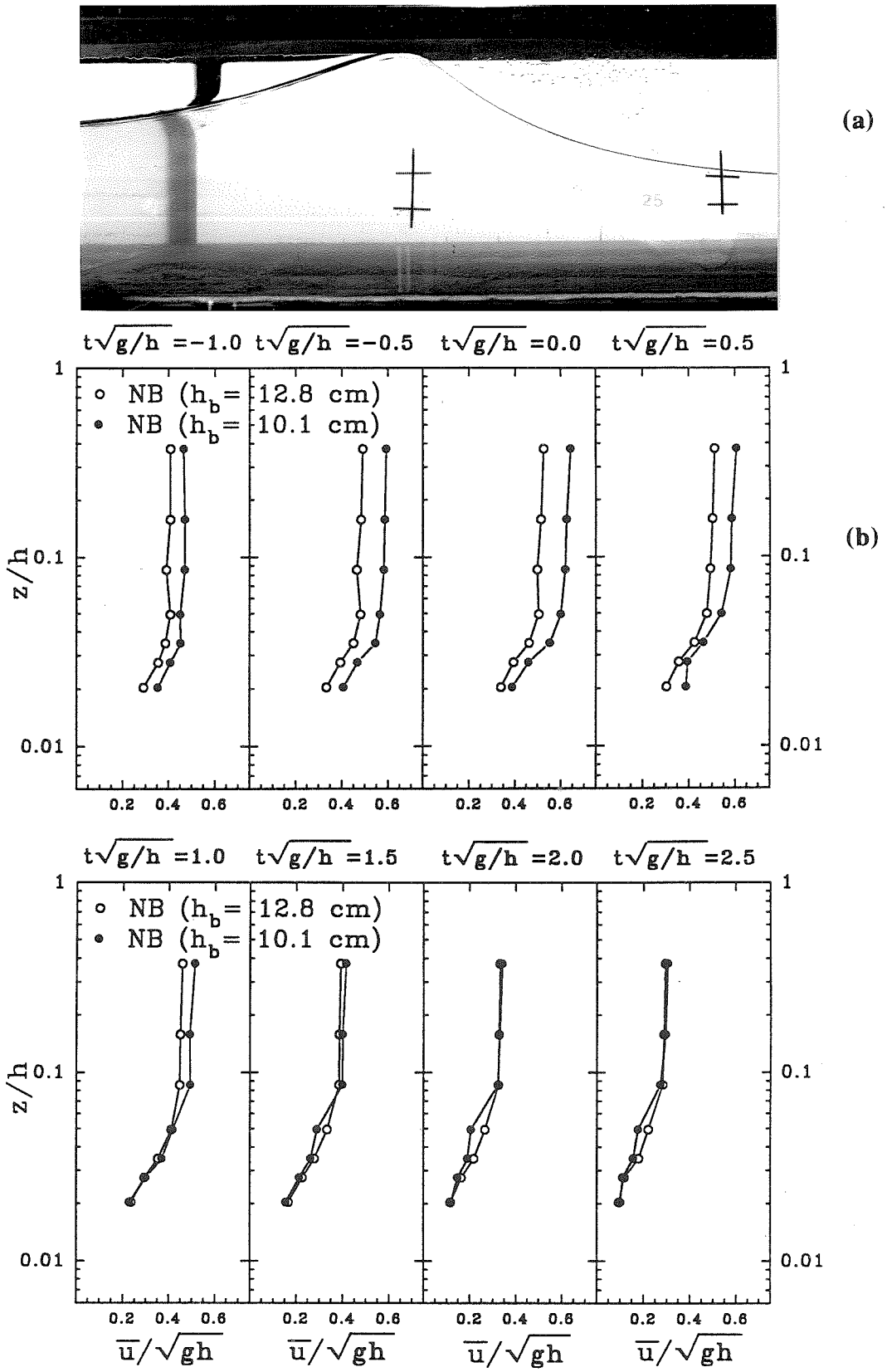

FIG. 4.35. Mean Velocities over Rock Bed, h = 13.8 cm, x/L = 0.29.

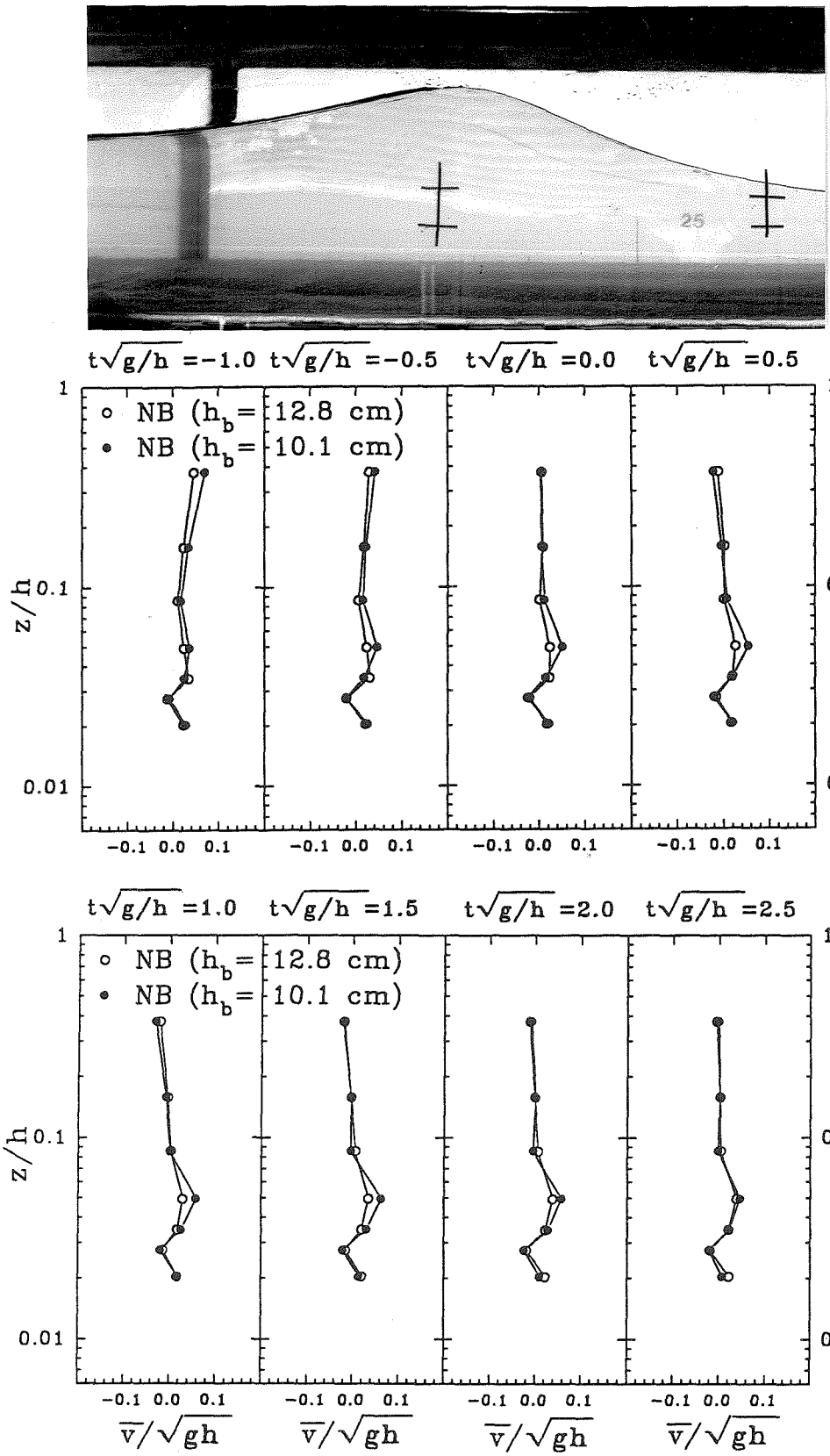

FIG. 4.35. Mean Velocities over Rock Bed, h = 13.8 cm, x/L = 0.29.

Figures 4.27 through 4.35 show the mean horizontal and vertical velocity profiles measured for the breaking and shoaling waves. A photograph of the wave at the measurement location is presented in frame (a) of each figure to show the shape of the wave at that location. Normalized time series for both the vertical and the horizontal directions show the profiles of the flow over the rock bed contrasted with the flow over the flat plate. The general flow features at the higher flow elevations are similar to those seen for the solitary waves in Figures 4.24 and 4.25 and will not be discussed here.

Near the bottom boundary, several trends are seen to persist from wave to wave and from location to location. It is again apparent that the boundary layer over the rock is significantly thicker than that over the flat plate. In addition, for each of the breaking waves near the bottom, a reversal occurs in the velocity profiles over the rock bed during the passage of the wave. In Figure 4.27 this "kink" in the curve occurs in the horizontal velocity profile for $t\sqrt{g/h}$ =1.5 near the relative elevation z/h = 0.035. Looking at the vertical velocity profile, a reversal can be seen earlier at $t\sqrt{g/h}$ = -0.5 at the level z/h = 0.028. As the wave passes, the reversal takes place further from the boundary until at $t\sqrt{g/h}$ = 1.5 it is located at z/h = 0.035 the same elevation as for the horizontal velocity profile.

This phenomenon occurs in the all the breaking wave velocity profiles. In the same measurement location, as the wave height is decreased, the relative elevation of the reversal appears further from the boundary. For example at x/L = 0.29, in the largest breaking wave, h_b = 13.8 cm (Figure 4.27),the elevation of the reversal is between z/h = 0.035 and 0 028 while for the smallest wave, h_b = 7.9 cm (Figure 4.32), it occurs between z/h = 0.06 and 0.07. As the wave travels down the test section, the height of the reversal also increases. This is especially evident in the case of the smallest wave: from a value of z/h = 0.06 to 0.07 at x/L = 0.29 (Figure 4.32), the height of the reversal has increased to z/h = 0.1 at x/L = 0.73 (Figure 4.33). The same type of reversal occurs in the shoaling

wave profiles over the rock bed (Figure 4.35), though with a smaller magnitude and a lower relative elevation than in the comparable cases with breaking waves at the same location.

From Figures 4.27 through 4.32, in the region of the velocity profile reversal, when the horizontal velocity is reduced, the magnitude of the vertical velocity tends to increase. The direction of the increase is observed to be positive, or upwards, in some cases and negative, or downwards, for others. An explanation for this effect is that, at the reversal elevation, the flow is directly affected by the local topography of the rock bed. This would correspond to the region described as the "inner layer" in section 1.3 where the bottom can no longer be considered in terms of an average roughness but must be seen as a field of individual particles. The observed reversals in the velocity profile would then correspond to eddies or undulations resulting from the flow over the individual particles. This inner layer region is quite large in the case of the smallest breaking wave and comprises more than 30 percent of the boundary layer thickness (see Figure 4.34).

The coincidence between the reversals in horizontal and vertical profiles appear to show that horizontal momentum is being exchanged with vertical momentum at the level of the reversal. In addition, because of the relatively small magnitudes of the vertical velocities, small changes in the flow are readily observed. The vertical velocity profiles show that the reversal develops over a period of time and moves upward during the wave passage, as noted above. For the smaller breaking waves, Figures 4.32 and 4.33, with a relatively large inner layer region, a second reversal is seen at an elevation below the first. This is consistent with the generation and growth of an eddy structure at the level of the particle bed.

Figure 4.36 shows the variation of the region of strong influence of the bed roughness elements, or inner layer, with distance along the test section for the different

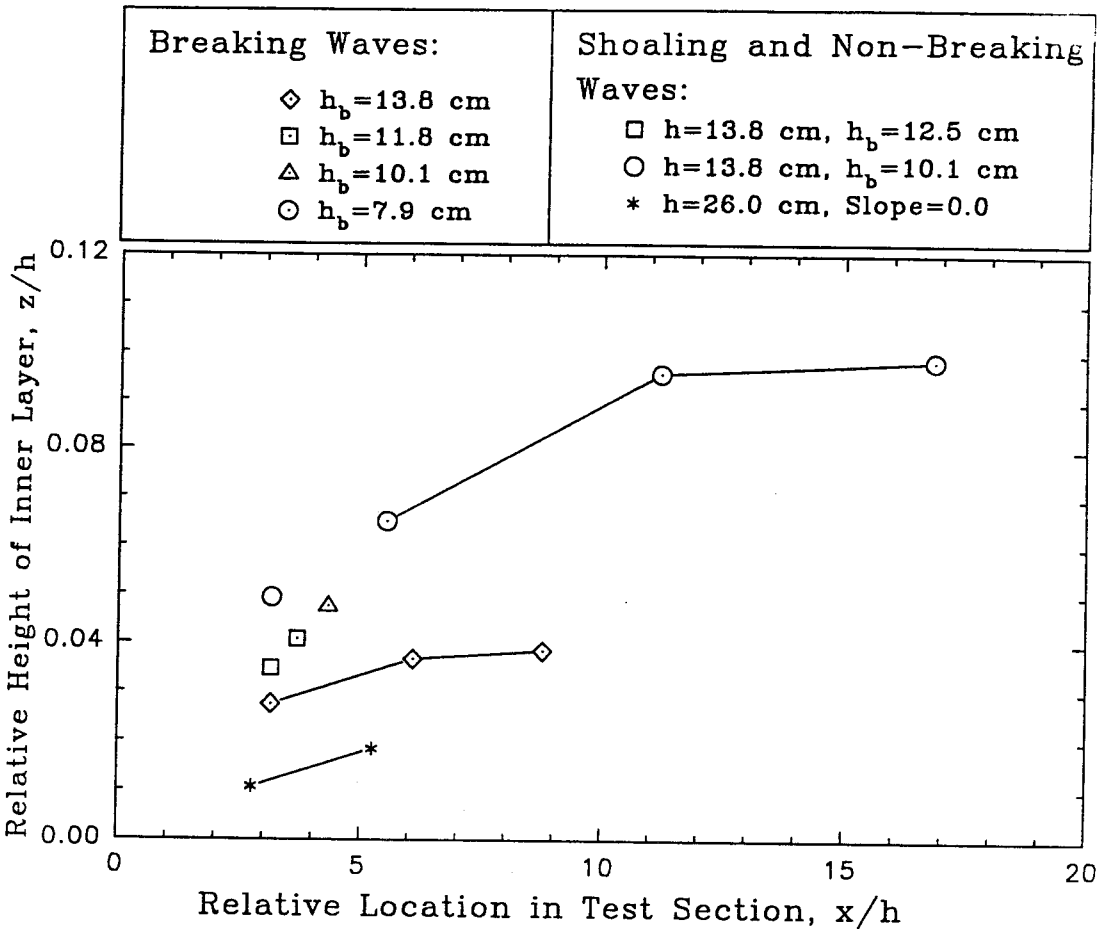

FIG. 4.36. Observed Range of Influence of Rock Bed for Different Wave Cases.

wave cases. The height of the inner layer was taken at the highest reversal elevation of the vertical velocity profile. Distance across the test section was normalized by the local still water depth. As a given wave travels along the rock bed, the region of influence of the bed material, or inner layer, increases. The growth rate of the inner layer appears to increase with decreasing wave height. This may be attributed to the fact that as the length scale of the experiment is changed by reducing h_b, the size of the rock increases with respect to the scale of the wave and thus exerts a greater influence on the flow.

4.2.2 Turbulence Intensities under Breaking and Non-Breaking Waves

The magnitudes of the root mean square of the turbulent fluctuations u' and v', in the horizontal and vertical directions respectively, are presented in Figures 4.37 and 4.38. These graphs show the variation with relative elevation of u' and v' for the different wave cases at a single measurement location, x/L = 0.29. The root mean square, or r.m.s., values for u' and v' were averaged over the entire period of the wave passage and, as such, are only general descriptors of the turbulence at a given elevation for a given wave. After first subtracting a background level associated with the measurement error of the LDV, the r.m.s. turbulent velocities in each wave have been normalized by the value of the maximum mean horizontal velocity away from the boundary layer in that wave. The measurement error associated with the Laser Doppler system is derived in Appendix C.

Comparing Figures 4.37 and 4.38, it is seen that the magnitudes of the horizontal and vertical velocity fluctuations in a given wave are of the same order. From the relative elevation z/h = 0.4, the turbulence values appear to form three groups. For the waves passing over a flat plate, the r.m.s. turbulence values are of similar magnitudes at each elevation and range from zero outside the boundary layer to a maximum of 0.8 percent of the maximum horizontal velocity at elevation z/h = 0.007. The turbulent velocities in the breaking and shoaling waves over the rock bed also vary similarly with elevation. They show a much greater increase as one approaches the bottom boundary, reaching values between 1.8 and 2.6 percent of the maximum horizontal velocity for r.m.s. u' and between 1.7 and 2.8 percent for r.m.s. v'. The turbulent velocity fluctuations for the solitary wave on the level rock bed reach values between 3 and 4 percent at the lowest observed elevations, but do not appear to follow the same pattern of variation with depth as the breaking wave velocities.

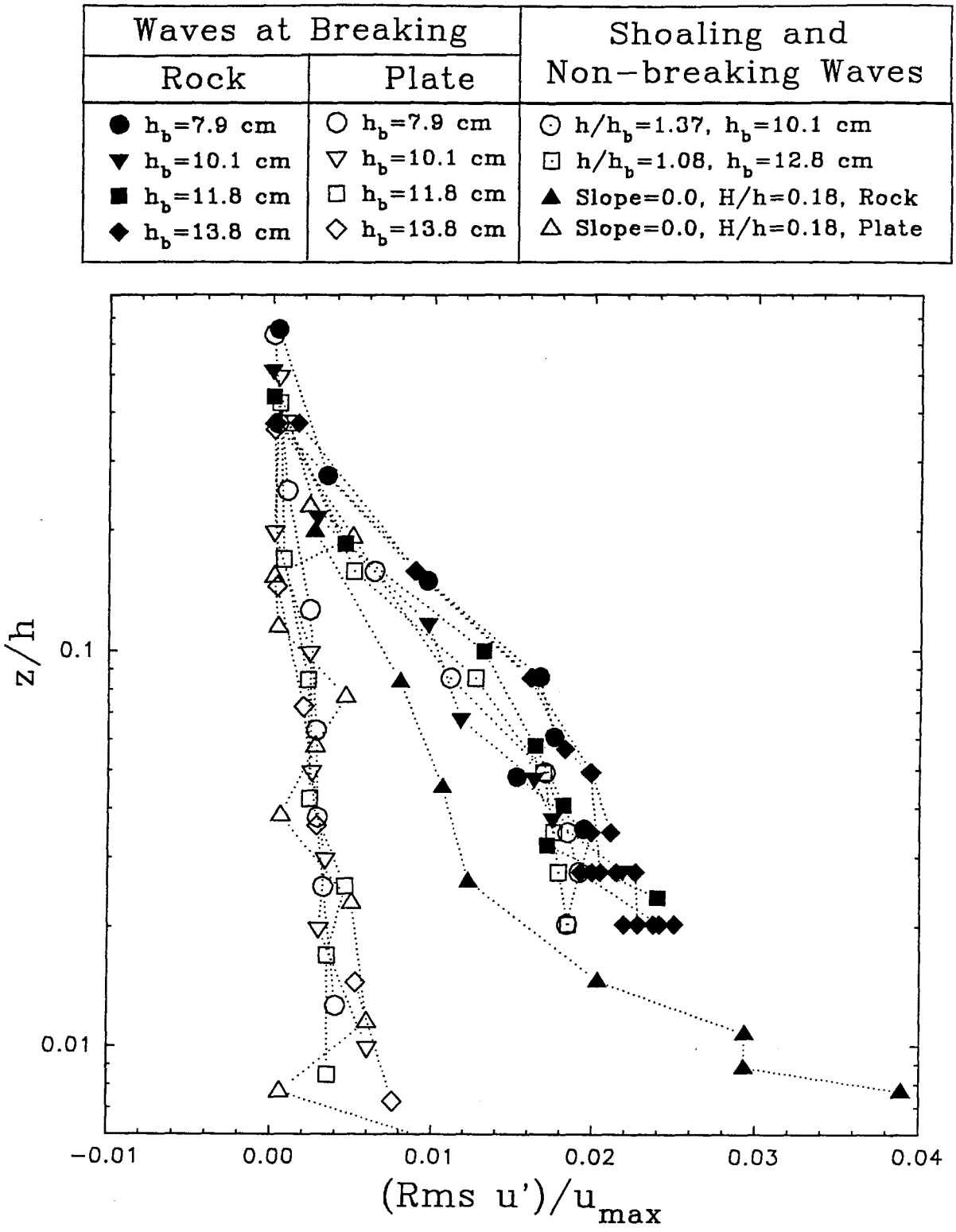

FIG. 4.37. Variation of Root Mean Square Horizontal Turbulence with Depth for Different Wave Cases at x/L = 0.29.

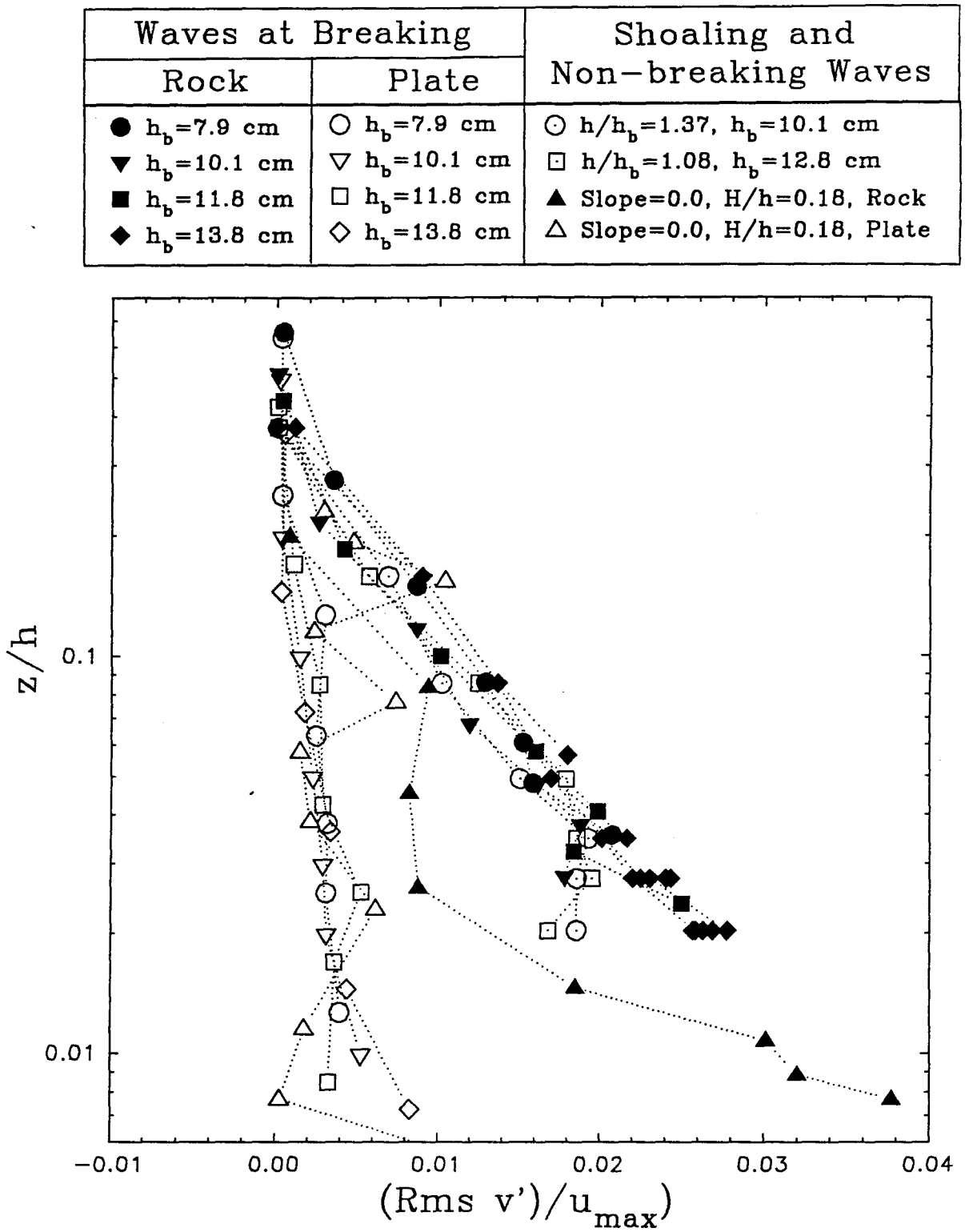

FIG. 4.38. Variation of Root Mean Square Vertical Turbulence with Depth for Different Wave Cases at x/L = 0.29.

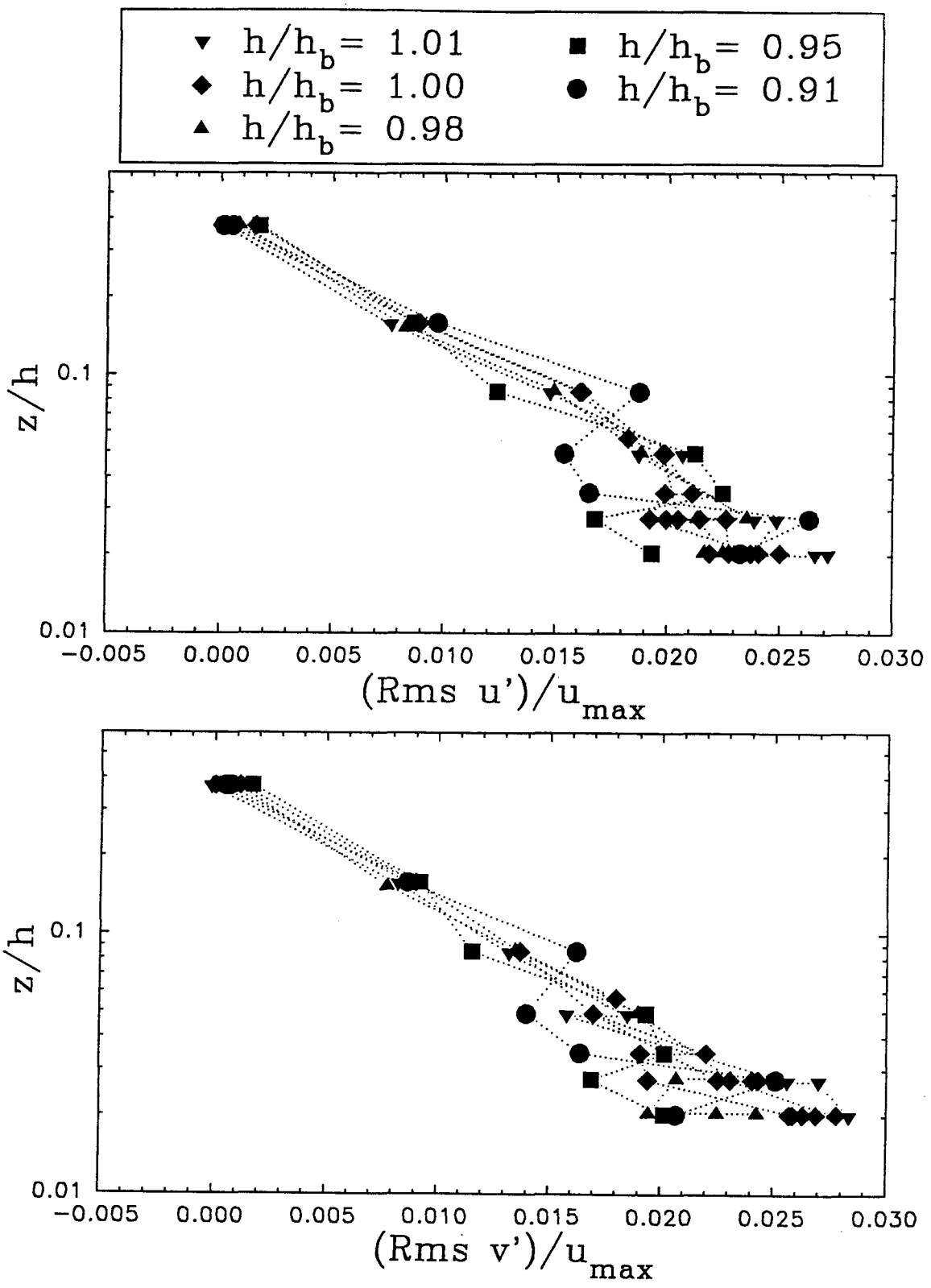

FIG. 4.39. Variation of Root Mean Square Turbulence with Measurement Location over Rock Bed, h_b = 13.8 cm.

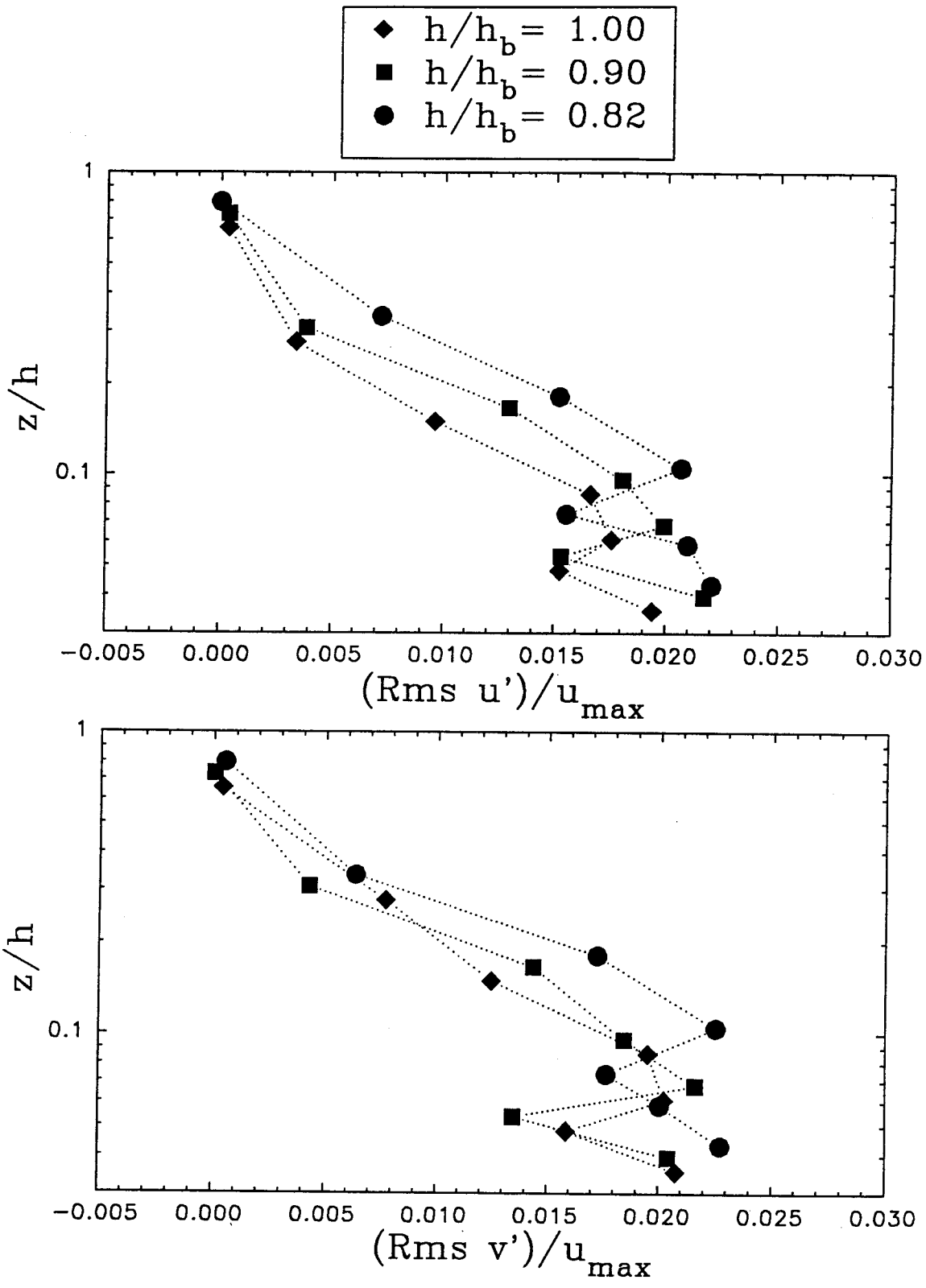

FIG. 4.40. Variation of Root Mean Square Turbulence with Measurement Location over Rock Bed, h_b = 7.9 cm.

Since the normalized values of r.m.s. u' and v' for the different breaking waves vary by as much as 50 percent at any given relative elevation, the root mean square turbulence at a particular elevation does not appear to be directly proportional to the maximum horizontal velocity in the wave. Though in general, the turbulence values increase with decreasing z/h, it is not clear from the data whether this increase is proportional to the logarithm of the z/h. It is also noted that at the lower observation elevations, the range of variation of the turbulence data between different waves appears to increase.

The increase in the range of variation of r.m.s. u' and v' at lower depths is also evident in Figures 4.39 and 4.40. Figure 4.39 shows the variation with relative depth ofthe largest breaking wave, h_b = 13.8 cm, at five locations along the rock bed. While the turbulence values for all five locations are within 30 percent of each other above z/h = 0.1, they are twice as large and vary by more than 45 percent at z/h = 0.02. These figures also show that for a given wave at a single location, instead of increasing uniformly with depth, the turbulence intensities appear to fluctuate at elevations near the bed. The relative elevation at which this intensity first appears to fluctuate in magnitude rises with increasing distance along the test section. This can be seen in Figure 4.41 for the wave with breaking depth, h_b = 7.9 cm. At location x/L = 0.29, both the root mean square horizontal and vertical turbulent velocities begin to fluctuate near z/h = 0.07.

Further along the rock bed at x/L = 0.73, the fluctuation becomes apparent near z/h = 0.1. The fluctuations in r.m.s. values for u' and v' are further evidence that the individual particle geometry affects the flow characteristics at elevations very close to the rock bed. In order to clarify the structure of the turbulence generated by the breaking and non-breaking solitary waves, autocorrelations were computed for the u' and v' values in each wave. Figure 4.41 shows a series of autocorrelation curves for the horizontal turbulence data near the rock bed in the largest wave of h_b = 13.8 cm at x/L = 0.29. The curves at z/h = 0.049 and z/h = 0.027 show a definite periodicity with a peak positive

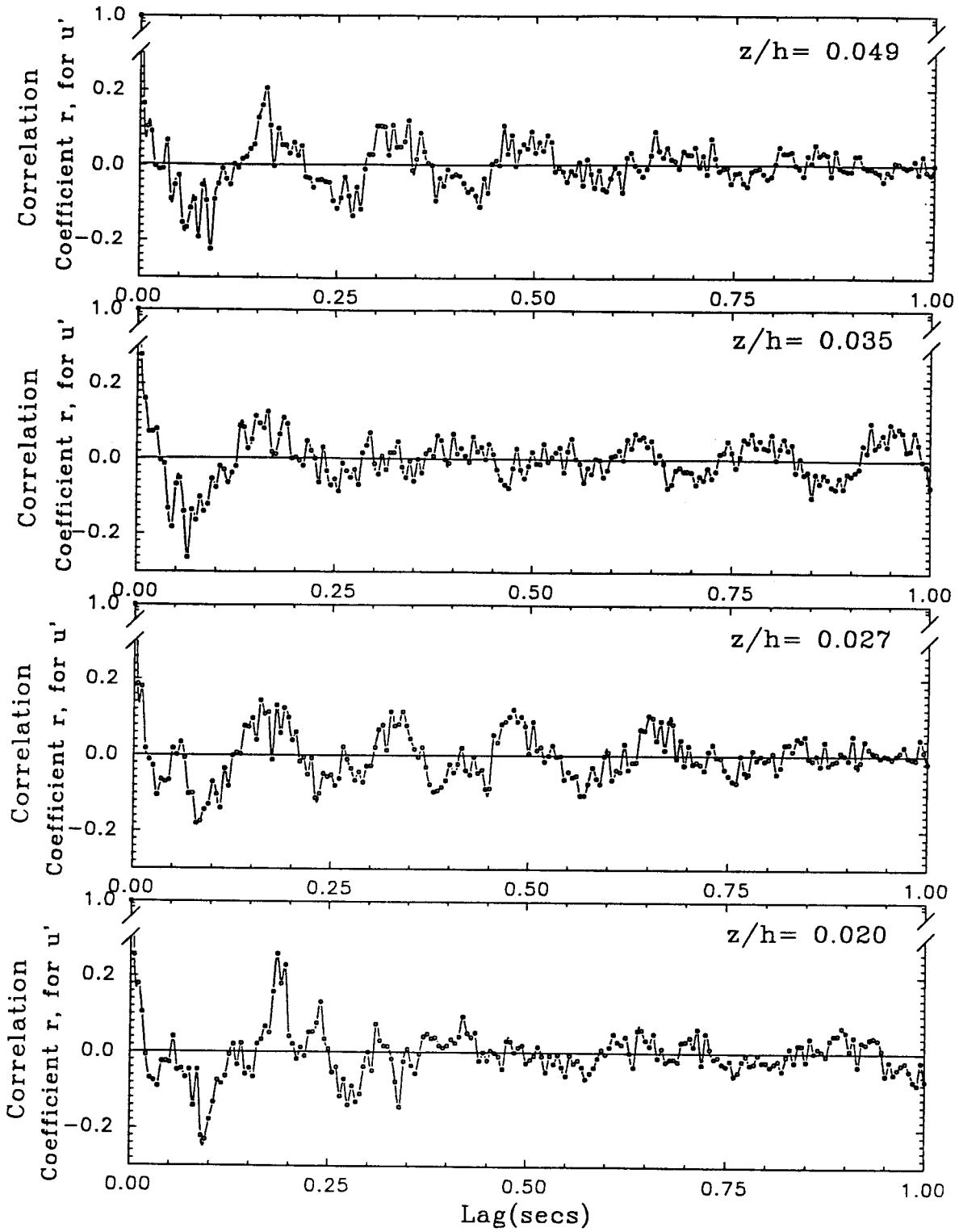

FIG. 4.41. Typical Autocorrelation Curves at x/L = 0.29, h_b = 13.8 cm.

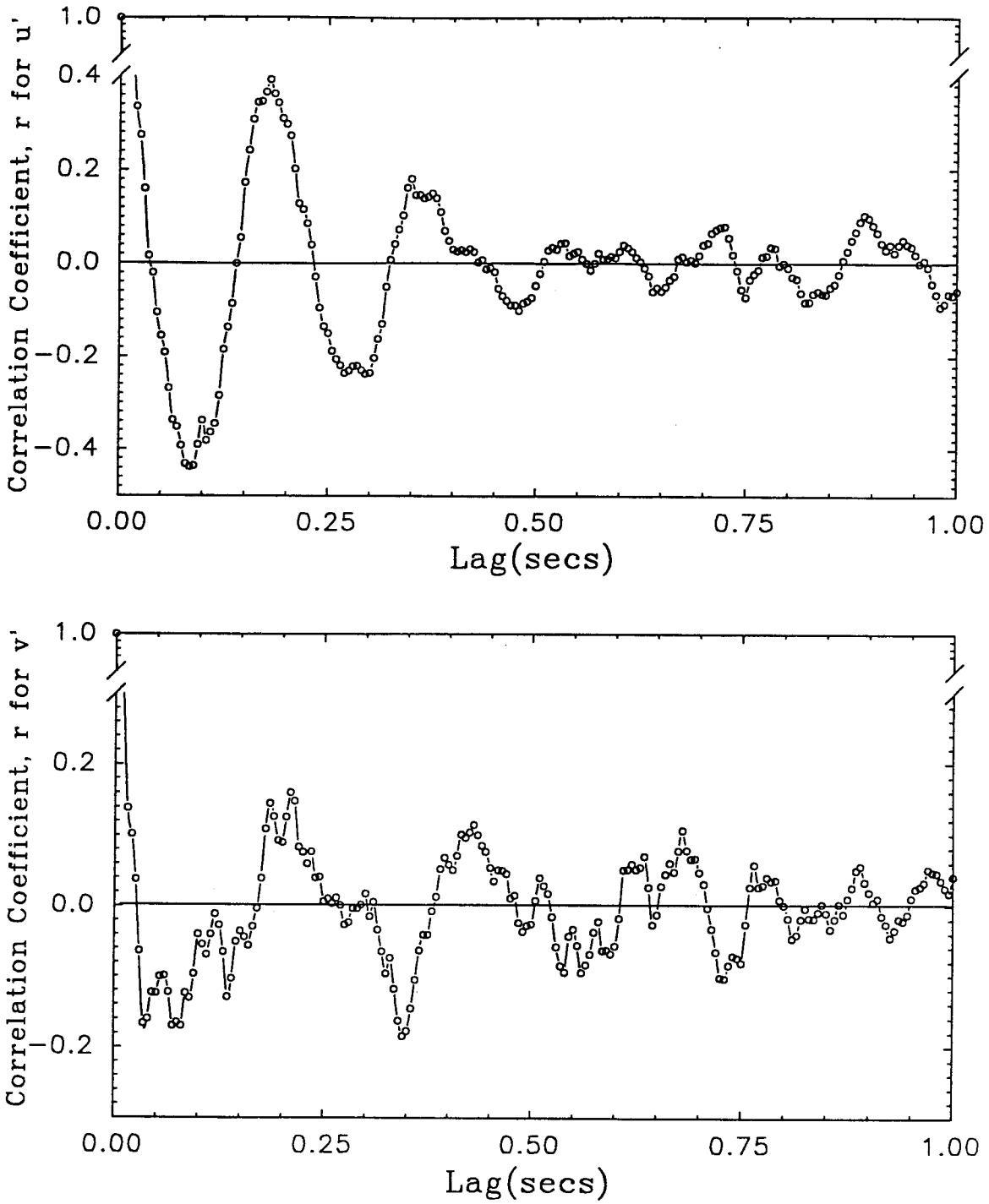

FIG. 4.42. Comparison of Horizontal and Vertical Autocorrelation, x/L = 0.73, h_b = 13.8 cm, z/h = 0.022.

correlation of near 0.2 at a lag of 0.15 seconds at the first elevation and 0.17 seconds for the second one. The periodicity is not as marked for z/h = 0.035 and z/h = 0.020, but a local maximum in the correlation coefficient also occurs near 0.17 and 0.19 seconds respectively. The periodicities in the autocorrelation curves may indicate the circulation frequencies of the vortices shed from individual particles.

It is difficult to assign a typical length scale to the vortex motion. For example, the circulation may be considered to be a function of the maximum water particle velocity away from the boundary layer. For the wave in Figure 4.41, the product of this velocity, 77 cm/sec, and the frequency of the vortex yields a length scale of 11.5 cm. The autocorrelations, however, are computed using the entire turbulent velocity time-history. Hence, if the circulation is a function of the local water particle velocity, a more appropriate choice might be the mean velocity of the flow at the measurement location averaged over the passage of the wave. Use of this velocity of 19 cm/s yields a length scale of 3.2 cm. Because of the uncertainty of assigning a typical velocity to the turbulence data, this discussion only addresses periodicity trends.

Figure 4.42 shows a comparison of the autocorrelations in the horizontal and vertical directions at location x/L = 0.73 for the largest wave. For this particular elevation, the horizontal turbulence records shows an especially strong periodicity at multiples of 0.18 seconds. The autocorrelation of the vertical turbulence at this level is not as regular in its variation and has a longer typical time lag of 0.22 seconds.

Table 4.3 shows a summary of the time lags of the first discernible positive correlation peak for all the observed wave cases. These lag times describe the size and shape of the turbulent eddies near the bottom. The lag times do not show any consistent trends with depth, but are generally longer in the horizontal direction than in the vertical and tend to decrease with decreasing depth at breaking.

4.2.3 Determination of Turbulent Shear at Bottom Boundary

The magnitudes of the Reynolds stresses for the breaking and non-breaking waves were computed from the product of the horizontal and vertical turbulent velocities. Figure 4.43 shows a typical set of time-histories of the product u'v' at seven elevations in the largest breaking wave, h_b= 13.8 cm. As expected from the values of u' and v' shown above, the magnitude of u'v' increases at elevations approaching the bottom boundary. In addition, on the average, the excursion of u'v' appears to be in the negative direction. From Equation 1.8 this indicates that there is a positive turbulent shear at the lower elevations of the flow.

Table 4.3. Typical Periodicities in Horizontal and Vertical Turbulence Time-Histories.

			u' Periodicities (sec)			
h (cm)	h_b (cm)	z (cm) x/L	0.5	0.3	0.2	0.1
13.8	13.8	0.29	0.15	0.17	0.17	0.19
		0.53	0.15	0.18	0.17	0.18
		0.73	-	0.15	0.15	0.17
11.8	11.8	0.29	0.13	0.13	0.15	0.06
10.1	10.1	0.29	0.11	0.08	0.14	0.17
7.9	7.9	0.29	0.14	0.13	0.13	0.12
		0.53	0.14	0.12	0.14	0.08
		0.73	-	0.14	0.15	0.13
13.8	13.8	0.29	0.21	0.23	0.23	-
13.8	10.1	0.29	-	0.22	-	0.18
			v' Periodicities (sec)			
h (cm)	h_b (cm)	z (cm) x/L	0.5	0.3	0.2	0.1
13.8	13.8	0.29	0.13	0.13	0.14	0.17
		0.53	0.15	0.15	0.15	0.15
		0.73	-	0.15	0.16	0.17
11.8	11.8	0.29	0.14	0.14	0.10	0.13
10.1	10.1	0.29	0.10	0.12	0.14	0.17
7.9	7.9	0.29	0.10	0.11	0.09	0.08
		0.53	0.12	0.14	0.13	0.14
		0.73	-	0.15	0.13	0.15
13.8	13.8	0.29	0.21	-	0.24	0.19
13.8	10.1	0.29	0.17	0.22	0.18	0.15

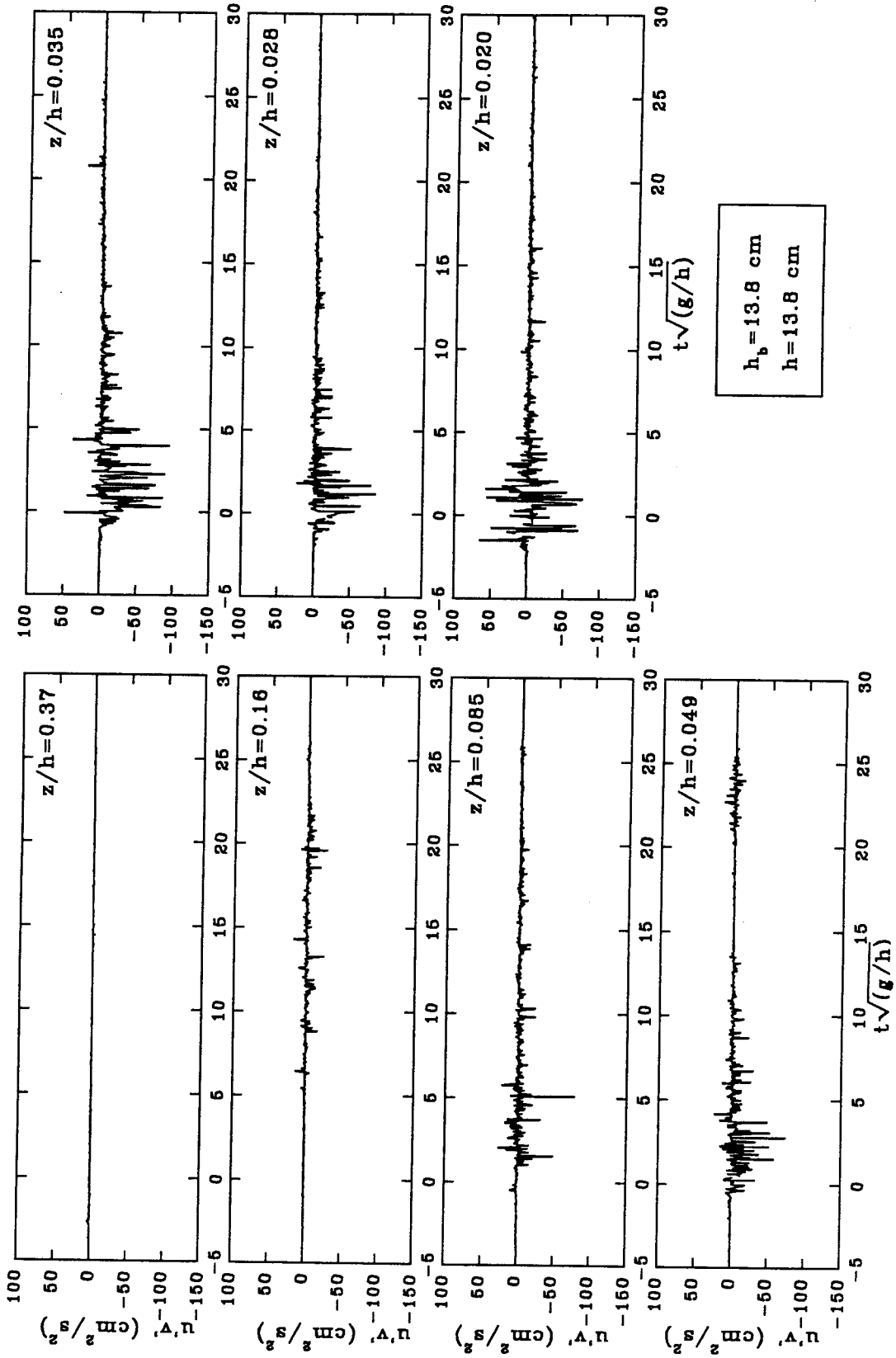

FIG. 4.43. Typical Time Histories for u'v' at Seven Elevations in a Breaking Wave, h_b = 13.8 cm, x/L = 0.29.

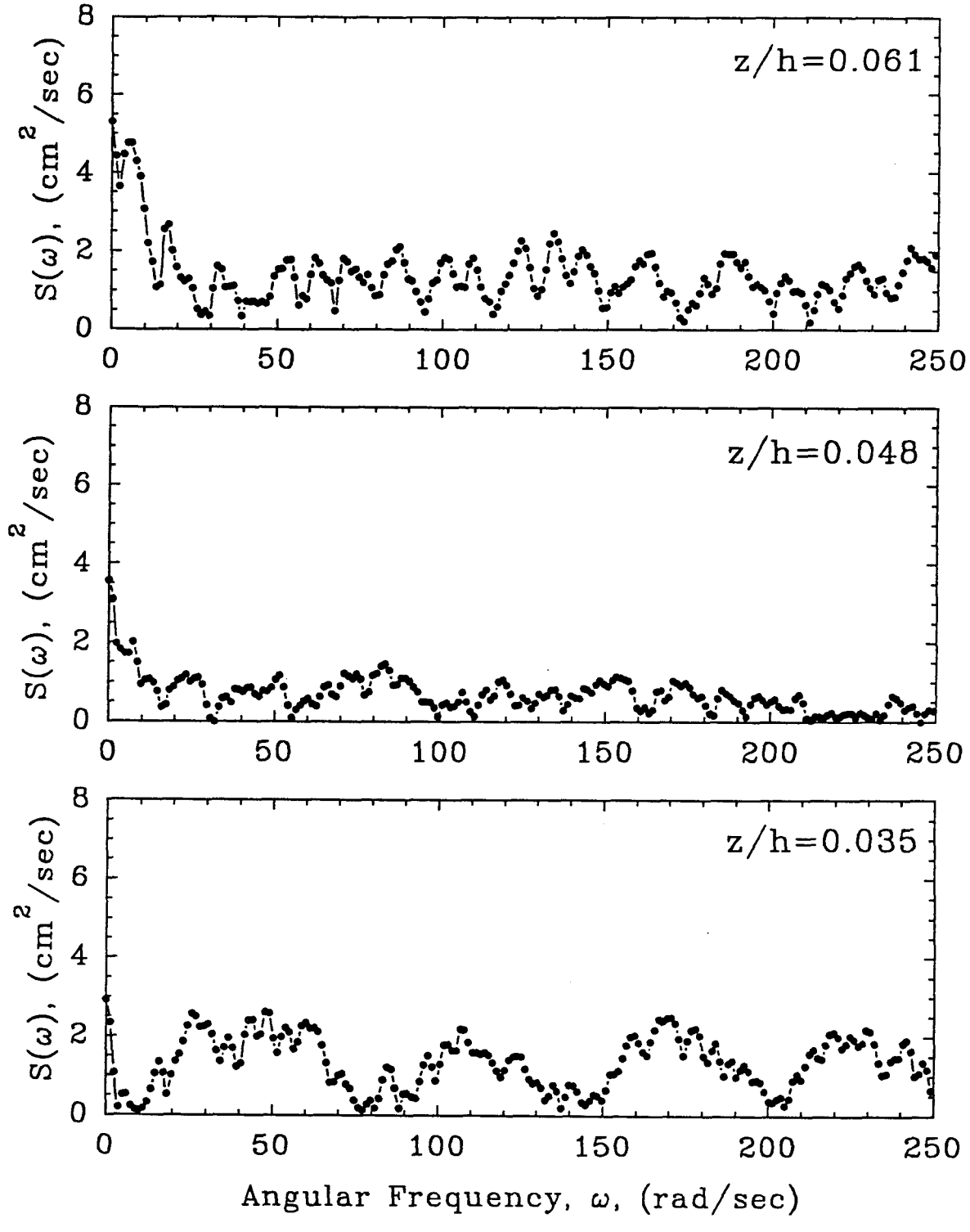

FIG. 4.44. Power Spectra of Typical u'v' Time Histories, x/L = 0.29, h_b = 7.9 cm.

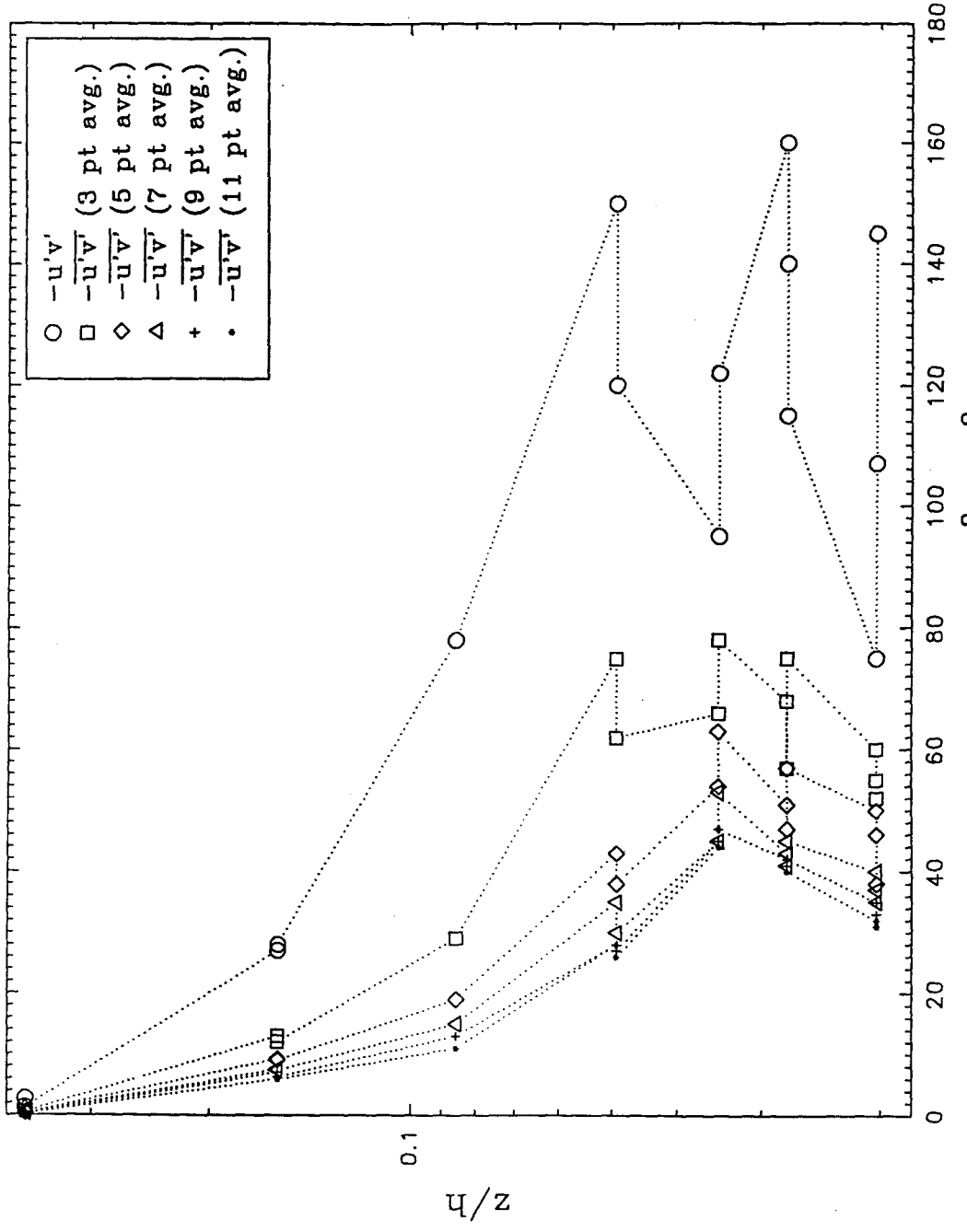

FIG. 4.45. Averaging Criterion for Determining Mean Shear, h_b = 13.8 cm, x/L = 0.29.

The evaluation of the turbulent shear requires the formation of a time average for the u'v' data. Typical power spectra of the u'v' time histories are shown in Figure 4.44. These spectra were calculated for the smallest wave, h_b = 7.9 cm , at x/L = 0.29. The shapes of the spectra vary considerably with elevation and show no consistent dominant frequency that could be used to average the u'v' data. It is noted that both the periodicities and the total power contained in the spectra change with elevation. Spectral analysis did not yield a criterion for time averaging the u'v' data.

Figure 4.45 shows the method used to determine the interval for time averaging. Starting with a data set in which many readings were taken at each elevation, the u'v' time series were averaged over successively longer intervals. The value of the maximum shear divided by the density of water, $\tau_{max}/\rho = -\overline{u'v'}_{max}$, was determined from the data for each averaging interval and plotted against relative elevation from the bed. As the averaging interval increases, the values for the maximum mean shear from repeated experiments at the same elevation start to converge. It was reasoned that for a long enough averaging interval, the value of the mean shear in identical experiments will be nearly identical. If the averaging interval is lengthened further, the mean shear values remain identical but are reduced in magnitude, and information is lost about the shape of the shear curve and the value of the maximum turbulent shear.

Starting at the right of Figure 4.45, the unaveraged u'v' data shows up to ±30 percent variation in magnitude at any given elevation. As the number of data points in the time average increases, the values of different measurements at the same elevation get closer together until, at an averaging interval of 0.045 seconds, or 9 points, the experiments fall very nearly on one curve. Individual readings at any elevation vary by less than ± 3 percent from the average. At the slightly larger interval of 0.055 seconds, the entire shear profile is seen to be shifting to the left. The averaging interval was taken as 0.045 seconds (9 points) for all the u'v' time-histories in this study.

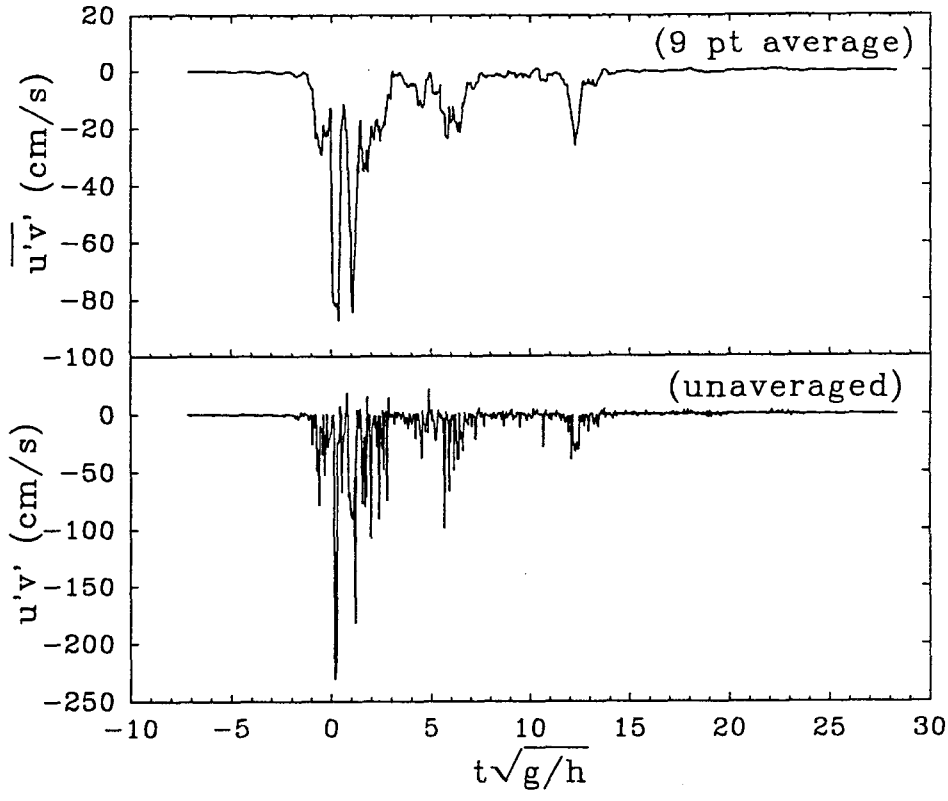

FIG. 4.46. Comparison of Typical u'v' and $\overline{u'v'}$ Time Histories, h_b = 13.8 cm, x/L = 0.73, z/h = 0.030.

The result of taking the time average of a typical u'v' time history is shown in Figure 4.46. The use of this interval reduces the peak value for the shear by 33 percent. The averaging interval is short enough that fluctuations in the shear values are still quite evident and yet the peak shear values are readily identifiable. It is also seen in Figure 4.46 that the maximum shear occurs near $t\sqrt{g/h} = 0.0$, the time at which the wave crest passes over the measurement location. The variation of $-\overline{u'v'}$ with water particle velocities suggests that it is a much better measure of the shear in the wave than the slope of the velocity profile. It should be noted that, as discussed in section 1.2.2, the magnitude of the mean momentum transport is not necessarily negligible. This mean momentum transport, $\bar{u}\,\bar{v}$, is addressed in section 4.2.5

The maximum shear values calculated for the different waves in this study, at location x/L = 0.29, are plotted against relative elevation in Figure 4.47. As should be

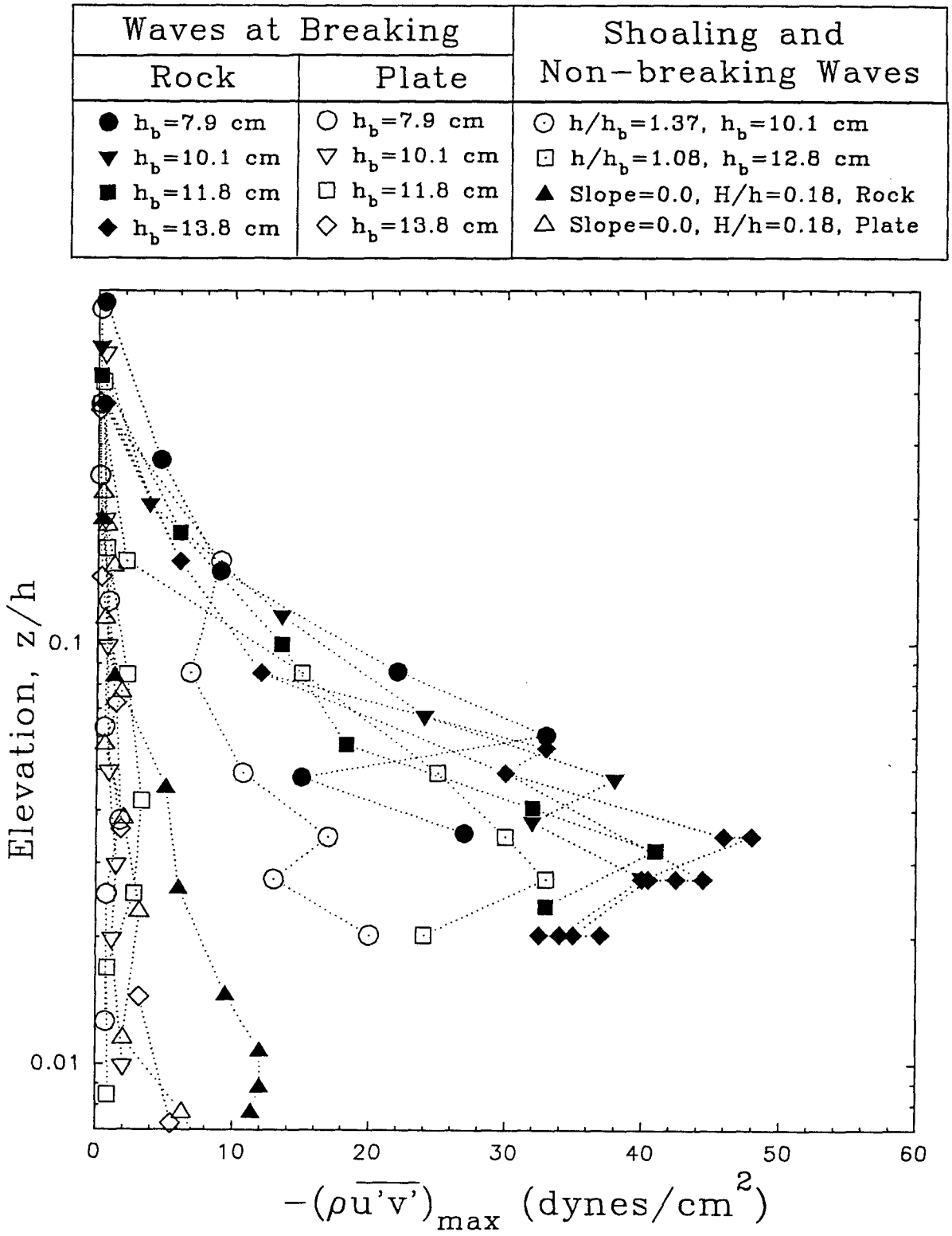

FIG. 4.47. Variation of Maximum Turbulent Shear for Different Waves, x/L = 0.29.

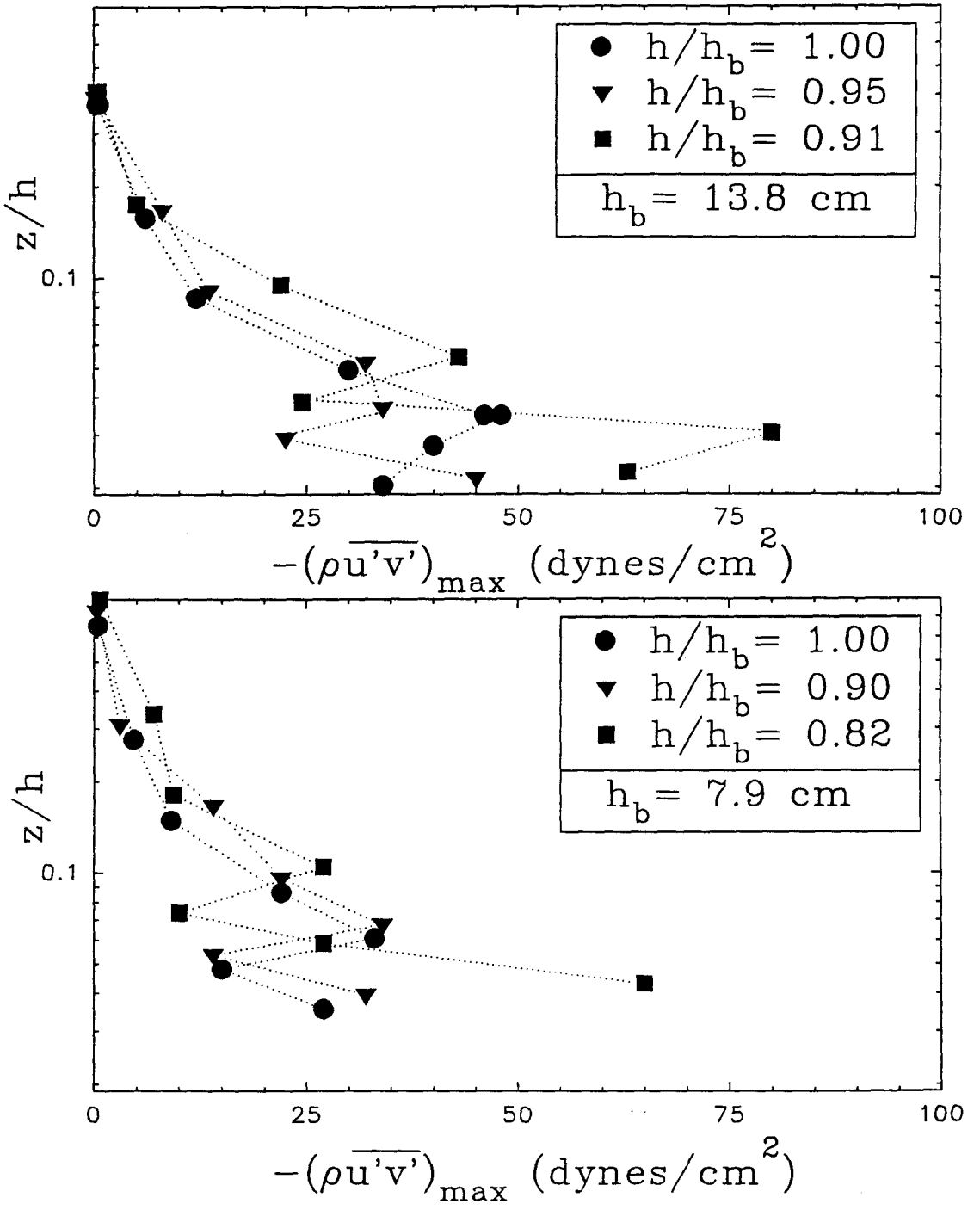

FIG. 4.48. Variation of Turbulent Shear with Location over the Rock Bed.

expected, the $\rho\overline{u'v'}_{max}$ values fall into the same groups as the values of the root mean square horizontal and vertical turbulent velocities. The shear values for the flat plate experiments show only a slight increase with depth, the values for the breaking and shoaling waves increase markedly approaching the rock bed and the shear values for the solitary wave fall in an intermediate region between the two.

The primary feature of the maximum shear curves for the rock bed experiments is that, in each case, the shear increases approaching the boundary down to a certain elevation and then begins to fluctuate in magnitude. As with the mean velocity profiles, the relative elevation at which this fluctuation begins is greater for waves with a smaller breaking depth. In addition, the elevation of the fluctuations in a breaking wave is greater than in the pre-breaking or shoaling wave with the same maximum horizontal water particle velocities.

Figure 4.48 shows that as the wave propagates along the rock bed, the elevation of the onset of fluctuations increases. This is the case for both the largest breaking wave with h_b = 13.8 cm and the smallest breaking wave with h_b = 7.9 cm. For the smallest wave at x/L = 0.29, the inner layer height is z/h = 0.06, while at x/L = 0.73 the height is near z/h = 0.1. The magnitude of the fluctuations at the lower elevations appear to increase with distance along the rock bed.

If the height where shear fluctuations begin is taken to indicate the extent of the inner layer where individual particles affect the flow, then a convenient location to evaluate the maximum shear in the wave may be at the top of this inner layer. At this elevation, the time averages in Equation 1.5 are still applicable. At elevations closer to the bed, it is not clear that the mean flux of turbulent momentum is an adequate descriptor of the flow mechanics. Accordingly, the value for the maximum shear under a wave at a given location was taken at the height of the first reversal in the magnitude of the shear.

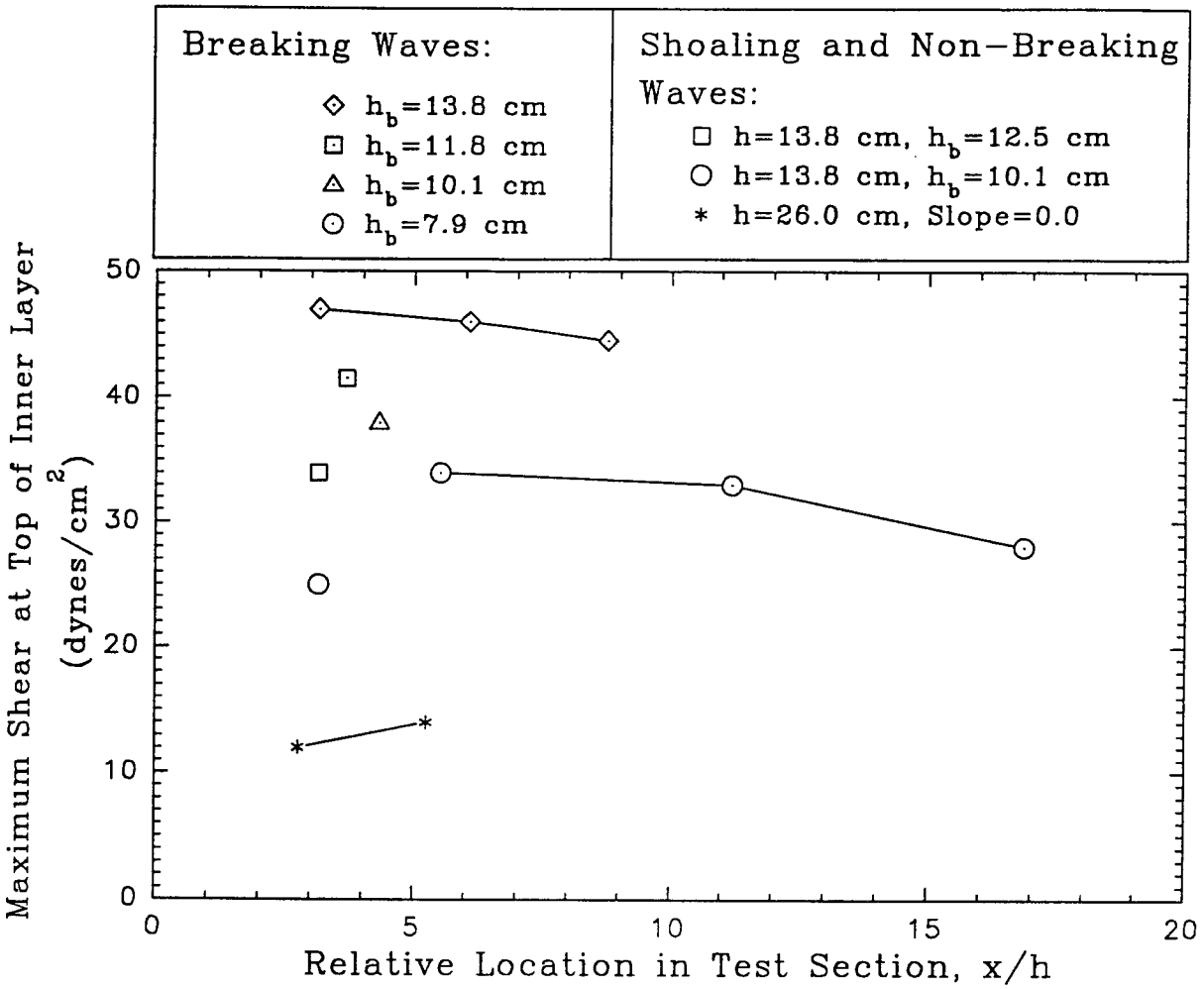

FIG. 4.49. Summary of Maximum Turbulent Shear Values at the Top of the Inner Boundary Layer over the Rock Bed.

Figure 4.49 shows the computed maximum shear values for the different wave cases. On the ordinate, the calculated values for maximum shear just above the inner boundary layer are plotted against the location along the test section normalized by the local depth at the measurement location. It is noted that the determination of the shear relies on the value at a single elevation where the shear is varying rapidly. Since data are available only for a limited number of elevations, the computed shear value represents a lower limit for the maximum shear at the top of the inner boundary layer. The maximum shear at the precise elevation of the inner and outer boundary layer interfaces is probably somewhat larger in magnitude.

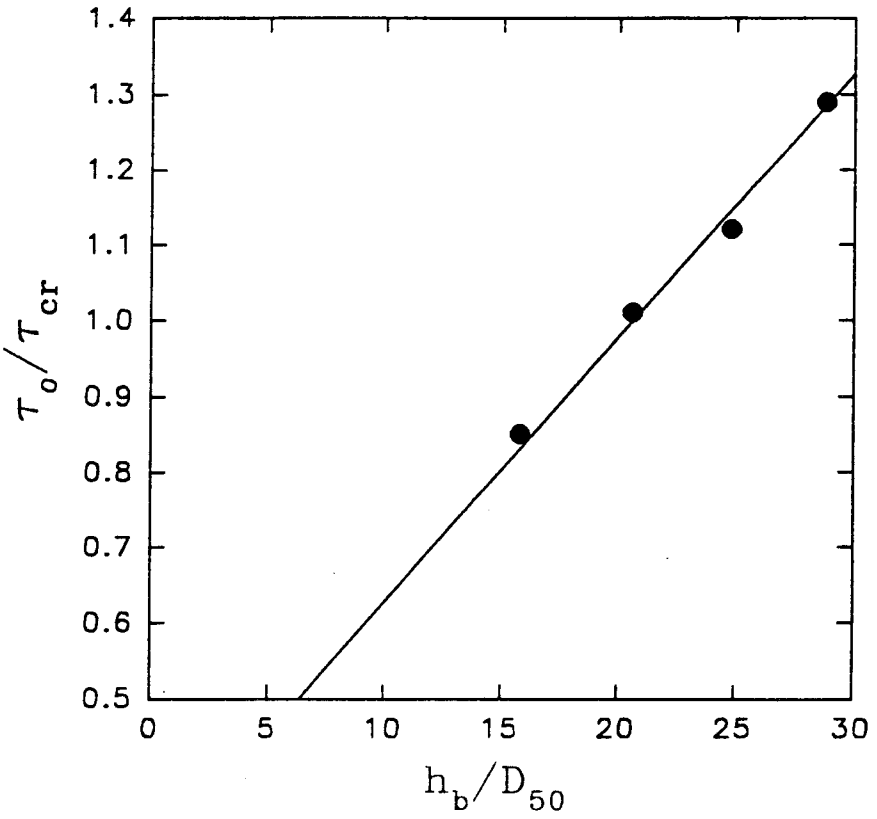

FIG. 4.50. Variation of Dimensionless Shear with the Ratio of Depth at Breaking to Mean Particle Diameter.

The shear values appear to show a slight decrease with distance along the bed as seen in the breaking waves shown with dotted symbols. The shear values for the shoaling waves, shown with hollow symbols, are significantly lower than for the analogous breaking waves. As the depth at breaking is reduced, the value of the maximum shear is also reduced. This variation is summarized in Figure 4.50. The shear values on the ordinate have been normalized by the critical shear stress calculated for a particle of mean diameter D_{50} = 4.76 mm from the Shields diagram as presented by Vanoni (1964). In this instance the critical shear parameter, θ, was determined to be 0.055 yielding a τ_{cr} of 37.2 dynes/cm^2 (ρ_s = 2.49). The depth at breaking, normalized by mean particle diameter, is plotted on the abscissa. The computed values for τ_o range from 0.92 to 1.27 times the value of the steady state critical shear, τ_{cr}.

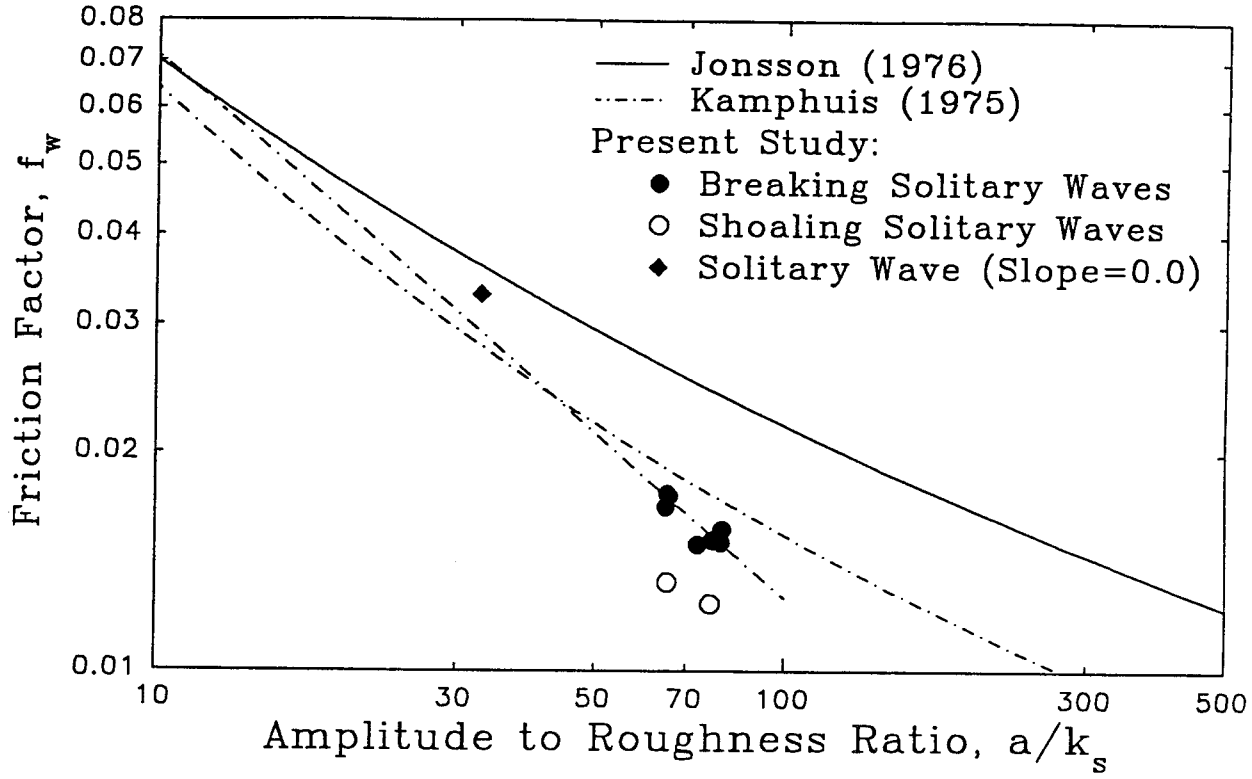

FIG. 4.51. Comparison of Maximum Friction Factors with the Ratio of the Amplitude of Maximum Water Particle Excursion to Grain Roughness in Sinusoidally Oscillating Flows.

Recall that the wave friction factor, f_w, as used in work by Jonsson, Kamphuis, and others is defined as

$$f_w = \frac{\tau_0}{\frac{1}{2}\rho\,(\bar{u}_{max})^2} \tag{4.3}$$

where τ_0 is the bottom shear stress, ρ, the density of water, and $\bar{u}_{max}$, the maximum free stream velocity. Using the calculated values for maximum shear, wave friction factors were determined for the each of the waves in this study. These friction factors are plotted against the ratio of maximum water particle excursion to bed roughness, a/k_s. For sinusoidal oscillations in a water tunnel, the value of a is taken to be the amplitude of motion over one-half cycle of the signal. For the purposes of this study, the amplitude of motion was assumed to be the integral of the mean horizontal velocity over the entire

period of passage of the solitary wave. The value of the mean grain size, D_{50} = 4.76 mm, was used for k_s.

Figure 4.51 shows that, except for the case of the solitary wave over the flat rock bed, the friction factors determined for the breaking waves fall below Jonsson's suggested curve (1976) and are closer to values observed by Kamphuis (1976). The friction factors for the shoaling waves are over 20 percent smaller than both the breaking wave and Kamphuis curve. It is noted that both Jonsson and Kamphuis studied flows in which the roughness elements were fixed to the bed. Allowing movement of the bed material may affect the values of the observed friction factors. Considering the many differences between breaking solitary waves in a tank and sinusoidal oscillations in a water tunnel, the friction factors calculated in this study are surprisingly close to the range of previously observed values.

4.2.4 Local Acceleration Measurements

At each measurement location, a time derivative was taken of the horizontal and vertical velocity time-histories to calculate the local accelerations $\partial u/\partial t$ and $\partial v/\partial t$ in the flow. Figures 4.52 and 4.53 show typical acceleration time-histories for several elevations in the largest breaking wave, h_b = 13.8 cm, at the point of breaking, x/L = 0.29. The acceleration values are normalized by g, the acceleration of gravity. The contribution of the mean velocity to the horizontal accelerations is visible in Figure 4.52 at elevation z/h = 0.37 This mean acceleration at this level reaches a maximum of 0.3 times g before the passage of the wave crest and becomes slightly negative afterwards. As the depth increases the observed mean acceleration also decreases until at elevations below z/h = 0.049, the acceleration due to variation in the mean velocity is greatly exceeded by the

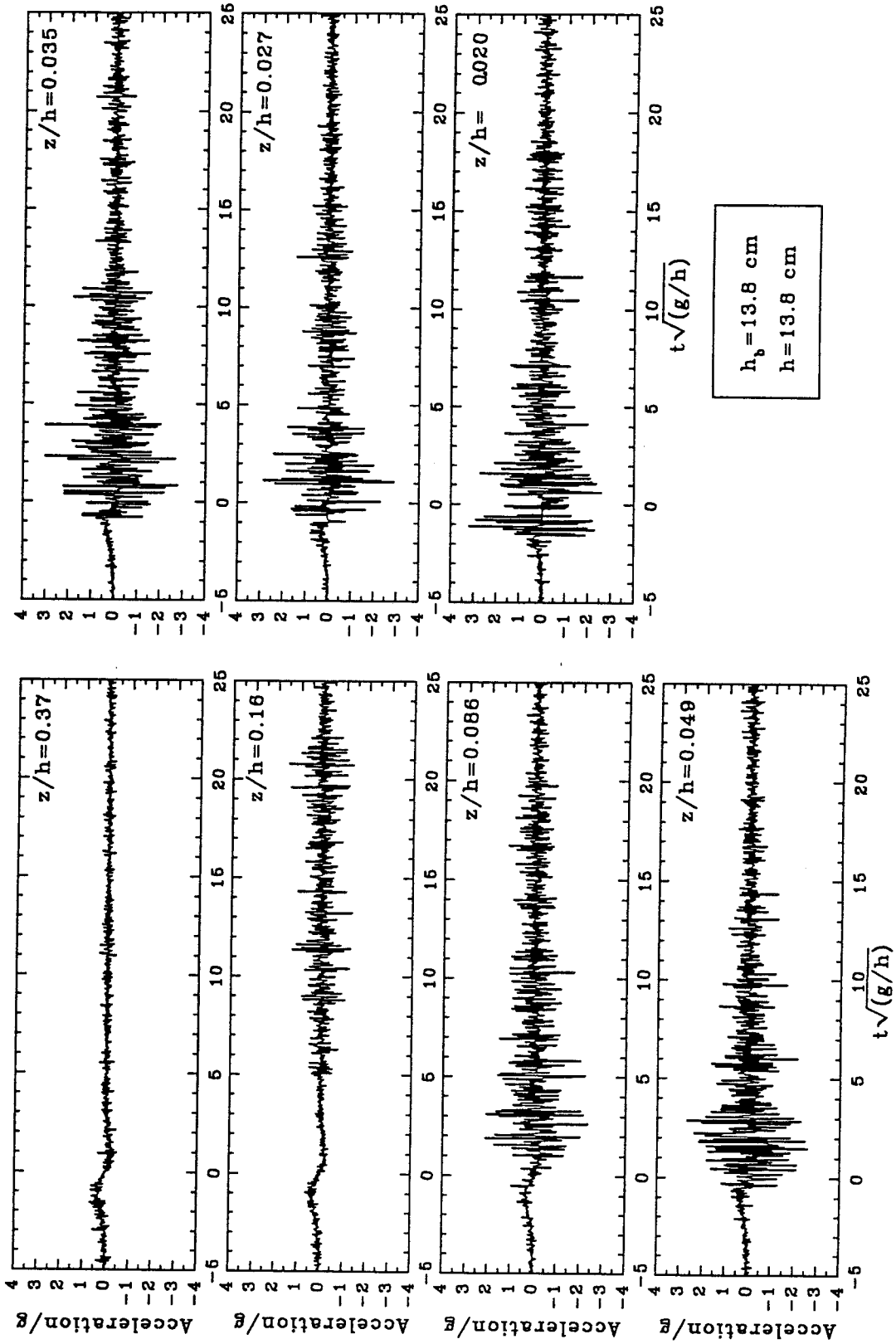

FIG. 4.52. Typical Horizontal Acceleration Time-Histories at Seven Elevations Over the Rock Bed, x/L = 0.29.

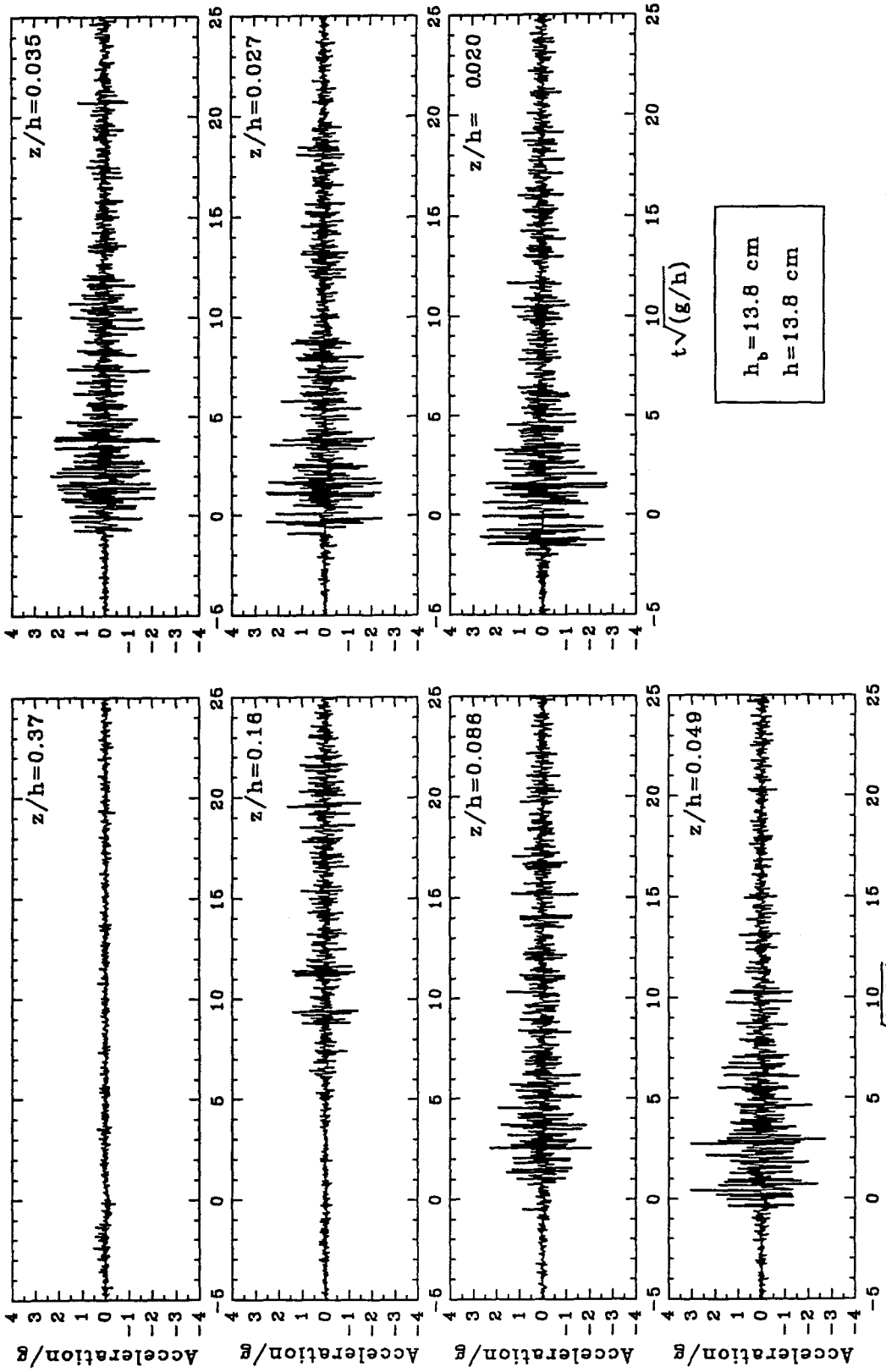

FIG. 4.53. Typical Vertical Acceleration Time-Histories at Seven Elevations Over the Rock Bed, x/L = 0.29.

turbulent velocity contributions. The accelerations caused by the turbulence reach magnitudes as high as 3g in the region following the passage of the wave crest. The magnitude of the accelerations remains high even at the lowest elevation of z/h = 0.020. Figure 4.53 shows that the magnitudes of the vertical accelerations in the flow are equal to the horizontal values. In the vertical direction, practically all the calculated acceleration is caused by the variation of the vertical turbulence, v'. As with the horizontal accelerations, the vertical accelerations remain large, often exceeding 2g even very near the rock bed.

Figure 4.54 shows the variation with relative elevation of the root mean square values of the horizontal and vertical accelerations at a single location, x/L = 0.29. The r.m.s. values are calculated over the entire passage of the wave and so give a large weight to the turbulent motion occurring after t=0. Consequently, it is expected that the variation of r.m.s. accelerations with depth will appear very much like that of the r.m.s turbulent velocities in Figures 4.37 and 4.38. From Figure 4.54 it is seen that this is indeed the case.

The magnitudes of the r.m.s. accelerations in the horizontal and vertical directions are of the same order. Figures 4.54 (a) and (b) both show the same three groups for the r.m.s. values of acceleration as were found in the r.m.s. u' and v' graphs: the measurements over the rock bed, the measurements over the flat plate and those for the solitary wave over the level rock bed. The values for the horizontal wave tank are significantly below those for the sloping bed because of the much smaller absolute velocities used in the former experiments. In Figure 4.54 (a), the contribution of the mean velocity variation to the r.m.s. horizontal acceleration at the upper elevation is less than 0.03 times g and decreases rapidly with depth. As seen in Figures 4.37 and 4.38 for r.m.s. turbulence, the accelerations over the flat plate increase slowly with depth, rising from 0.1g to values of 0.2g to 0.3g. The corresponding rock bed accelerations increase at more than twice this rate reaching values between 0.45g and 0.65g. As for the turbulent

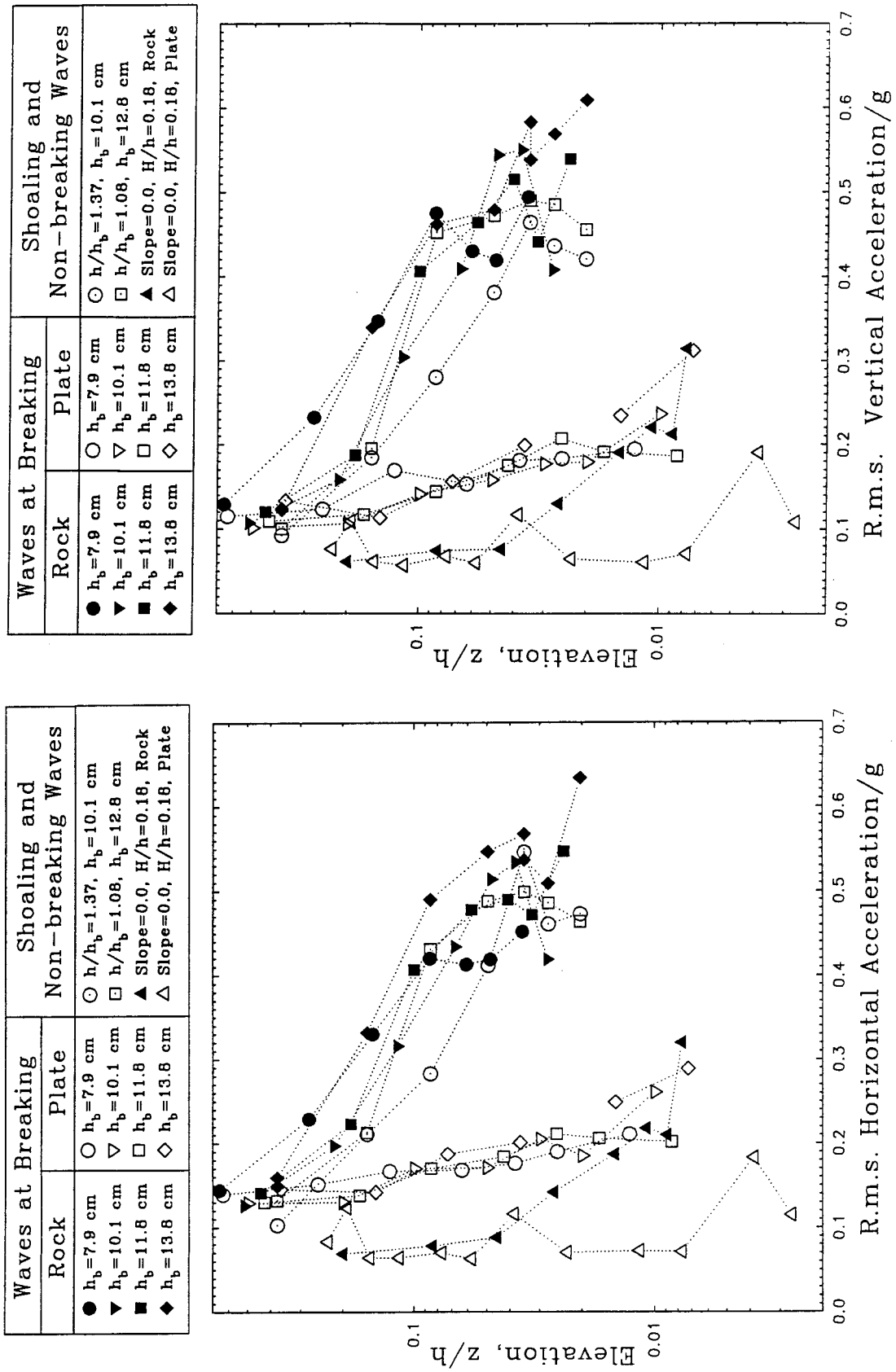

FIG. 4.54. Variation of Root Mean Square Acceleration with Relative Elevation x/L = 0.29.

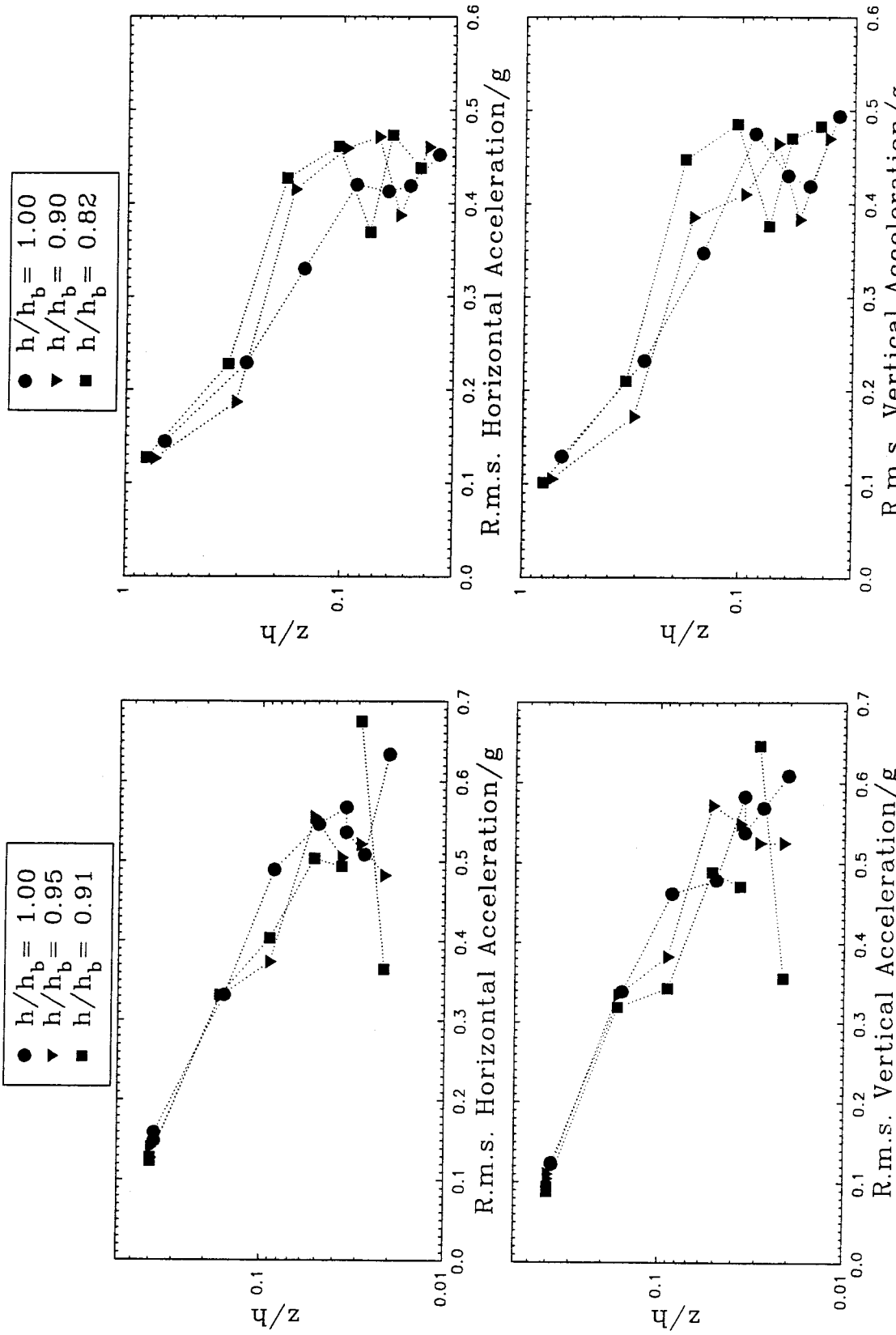

FIG. 4.55. Variation of R.M.S. Acceleration with Distance for Breaking Waves, (a) h_b = 13.8 cm, (b) h_b = 7.9 cm.

velocities, the r.m.s. accelerations increase uniformly down to a certain elevation near the bed and then begin to fluctuate in value. The elevation of the onset of the fluctuations is higher for smaller breaking wave heights and is lower for a shoaling wave than for a breaking wave with the same maximum velocity.

Figure 4.55 shows the r.m.s. acceleration values for the largest breaking wave, h_b = 13.8 cm, in Figure 4.55 (a) and values for the smallest breaking wave, h_b = 7.9 cm, in Figure 4.55 (b) for different locations along the rock bed. The figures present the same characteristics as the analogous Figures 4.39 and 4.40 for the turbulent velocities. The r.m.s. acceleration values again increase uniformly approaching the bottom and then fluctuate in value. The level of the fluctuation increases as the wave progresses along the rock bed. In addition, the magnitude of the fluctuations is greater at greater distances along the bed. This is especially evident in Figure 4.55 (a) for the wave of breaking depth h_b = 13.8 cm. At the lowest elevation, near z/h = 0.02, the variation in r.m.s. acceleration for the wave at x/L = 0.29 is ±0.04 g while at x/L = 0.73 the acceleration varies by more than ± 0.15g. As expected, the values for r.m.s acceleration support the idea that the inner layer, where particle geometry affects the flow over the bed, extends proportionately higher in the flow with decreasing depth at breaking and grows as the wave travels along the bed.

4.2.5 Convective Acceleration Measurements

As described in Chapter 1, most models for shear stress at the bottom boundary are based on simplifications of the time averaged Navier-Stokes equations. Specifically, in the x or horizontal direction:

$$\frac{\partial \bar{u}}{\partial t} + u\frac{\partial \bar{u}}{\partial x} + v\frac{\partial \bar{u}}{\partial y} = -\frac{1}{\rho}\frac{\partial \bar{p}}{\partial x} + \nu\left(\frac{\partial^2 \bar{u}}{\partial x^2} + \frac{\partial^2 \bar{u}}{\partial y^2}\right) - \frac{\partial \overline{u'^2}}{\partial x} - \frac{\partial \overline{u'v'}}{\partial y} \qquad (4.4)$$

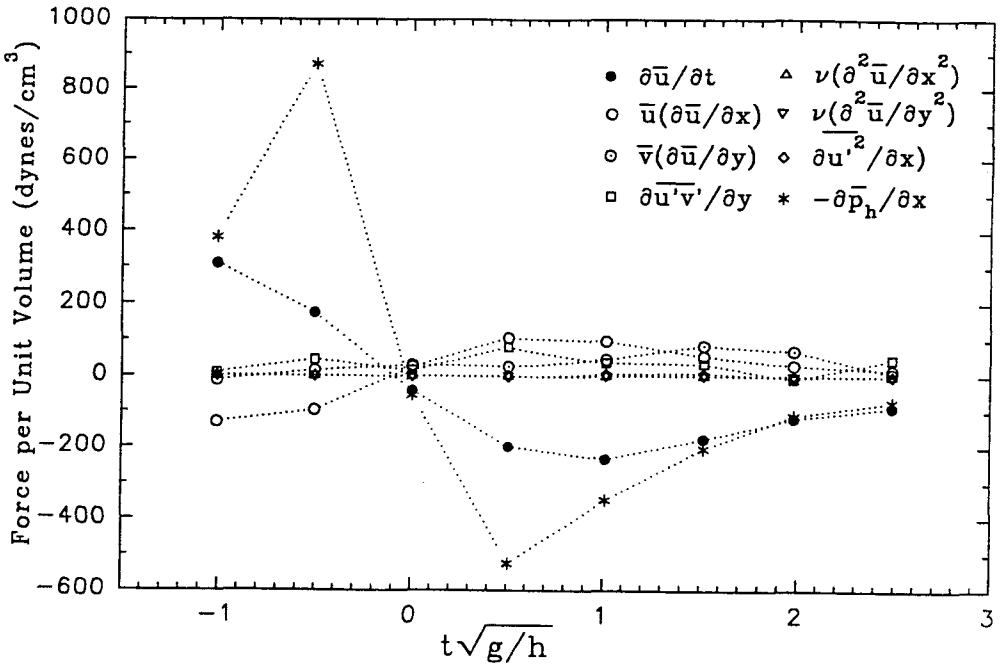

(a)

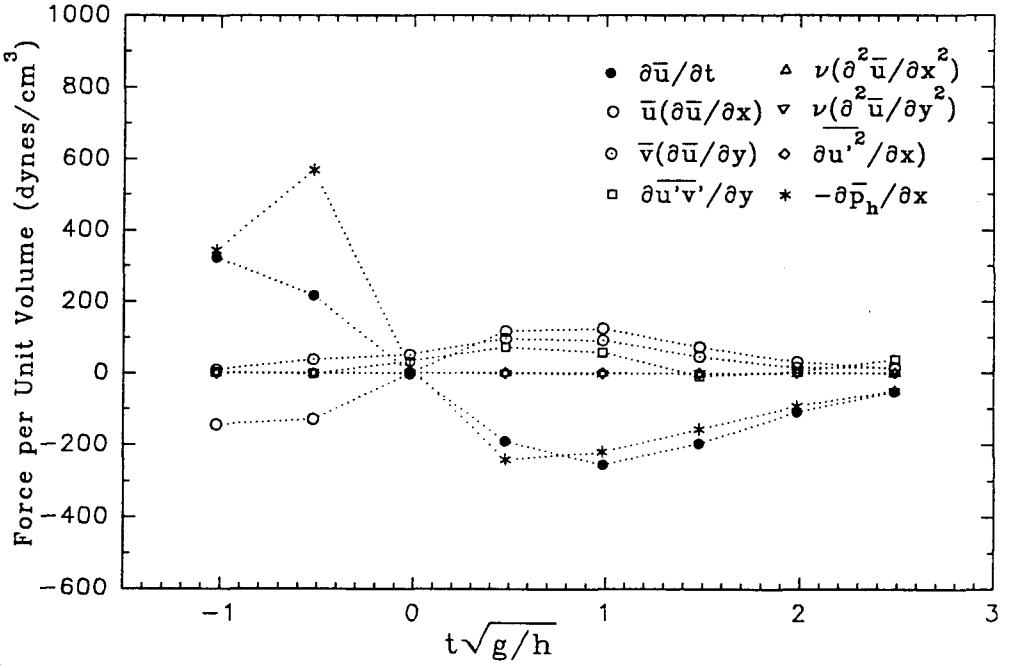

(b)

FIG. 4.56. Comparison of Terms in the Navier-Stokes Equation for Breaking Wave (a) h_b = 13.8 cm, (b) h_b = 7.9 cm at x/L = 0.29, z = 5.18 cm.

where p is the pressure and υ is the kinematic viscosity. All other terms are as previously defined. From the measured velocity data, it is possible to estimate the magnitudes of these terms for the flow under a breaking wave. Figure 4.56 shows the relative magnitudes of the terms in Equation 4.4 for several times near the passage of the wave crest under the largest breaking wave, Figure 4.56 (a), and the smallest breaking wave, Figure 4.56 (b). The location of the measurements used for these calculation was taken at 0.68 cm over the rock bed at x/L = 0.29. This elevation was within the boundary layer for both waves but above the influence of the bed material. For this analysis, it was assumed that $\frac{\partial}{\partial x} = -\frac{1}{c}\frac{\partial}{\partial t}$. Derivatives with respect to the vertical or y direction of $\bar{u}$ and $\overline{u'v'}$ were obtained by fitting a second order curve to the depth profiles at the desired elevation. This was repeated for eight different points in time near the passage of the wave crest.

It is seen from Figure 4.56 that the terms describing the convective inertia, $-\bar{u}\frac{\partial \bar{u}}{\partial x}$ and $-\bar{v}\frac{\partial \bar{u}}{\partial y}$, are of the same order of magnitude as the turbulent fluctuation force $\frac{\partial \overline{u'v'}}{\partial y}$. A table of the range of values for all the terms computed for Equation 4.4 appears below. The following discussion concerns only the convective inertia terms.

Table 4.4. Range of Values for Terms in the Navier Stokes Equation for Two Breaking Waves at Elevation z = 0.68 cm, $-1 \le t\sqrt{g/h} \le 2.5$, x/L = 0.29.

	$\frac{\partial \bar{u}}{\partial t}$	$-\bar{u}\frac{\partial \bar{u}}{\partial x}$	$-\bar{v}\frac{\partial \bar{u}}{\partial y}$	$\nu\frac{\partial^2 \bar{u}}{\partial x^2}$	$\nu\frac{\partial^2 \bar{u}}{\partial y^2}$	$\frac{\partial \overline{u'^2}}{\partial x}$	$\frac{\partial \overline{u'v'}}{\partial y}$
h_b=13.8cm	-231 to 310	-130 to 106	-12 to 84	-.003 to .001	-.5 to .4	-3.1 to 6.0	-10 to 80
h_b= 7.9cm	-254 to 323	-144 to 125	8 to 95	-.07 to .003	-1.9 to .6	-1.3 to 1.3	-9 to 72

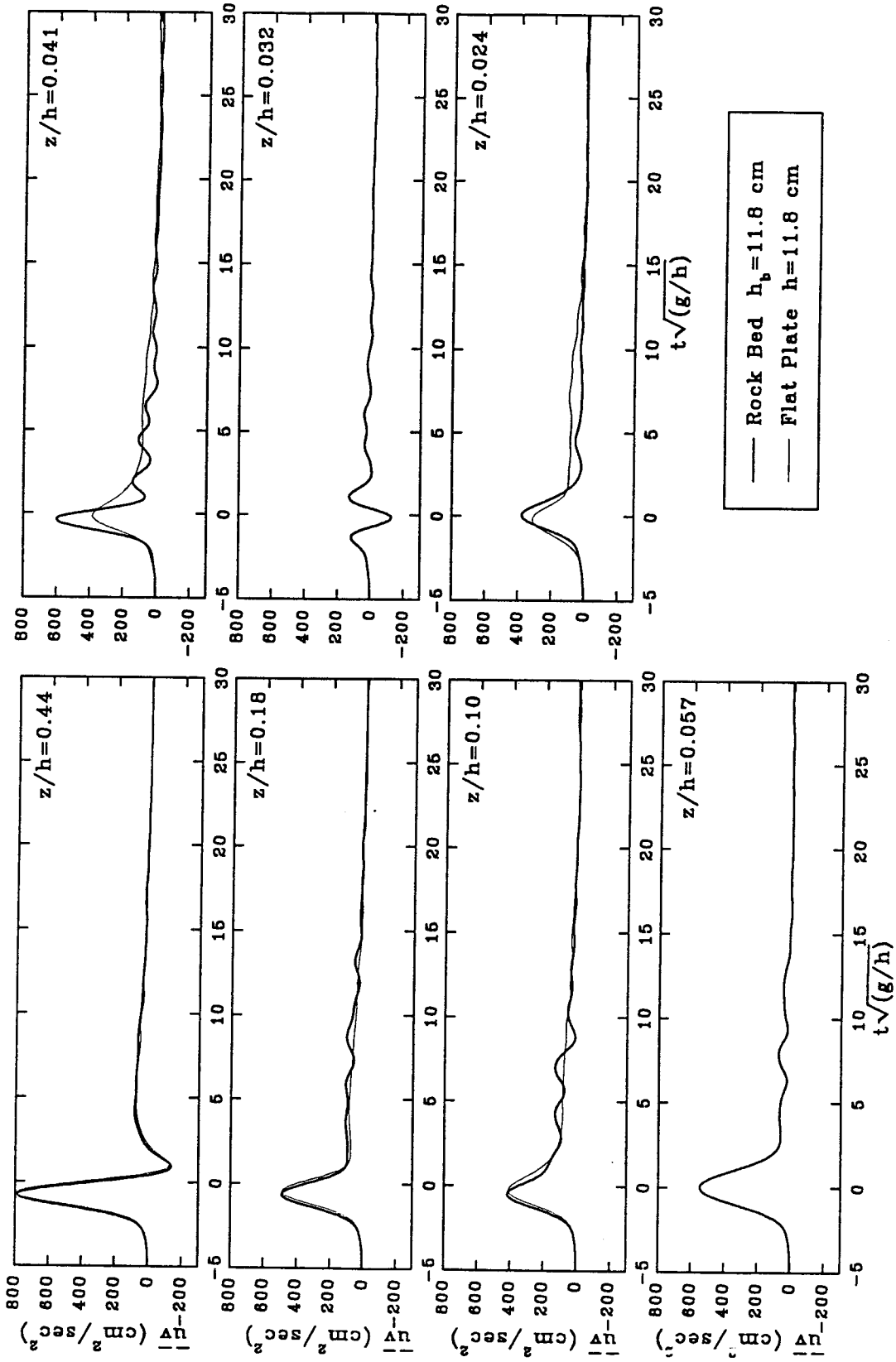

FIG. 4.57. Typical $\overline{uv}$ Time-Histories at Seven Elevations Over the Bottom Boundary, h_b = 11.8 cm, x/L = 0.29.

The terms $\bar{u}\frac{\partial \bar{u}}{\partial x}+\bar{v}\frac{\partial \bar{u}}{\partial y}$ can be expressed in the form $\frac{\partial \overline{u^2}}{\partial x}+\frac{\partial \overline{uv}}{\partial y}$ by using continuity considerations. The variation of $\bar{u}^2$ with location has not been investigated in this study. The term $\overline{uv}$, which can be viewed as measuring the flux of mean horizontal momentum in the vertical direction, is usually assumed to vanish along with the vertical velocity near the bottom boundary. In this study, however, although the vertical velocities near the rock bed are small, they are of finite magnitude.

Figure 4.57 shows that the product $\overline{uv}$ retains a finite value even in the lower elevations of the flow under a breaking wave. In this figure, the values of $\overline{uv}$ are plotted on the ordinate for several elevations under a breaking wave with h_b = 11.8 cm. Since the mean horizontal velocities are always positive, the direction of the product $\overline{uv}$ is controlled by the direction of the vertical velocities. As a result, at the lower elevations

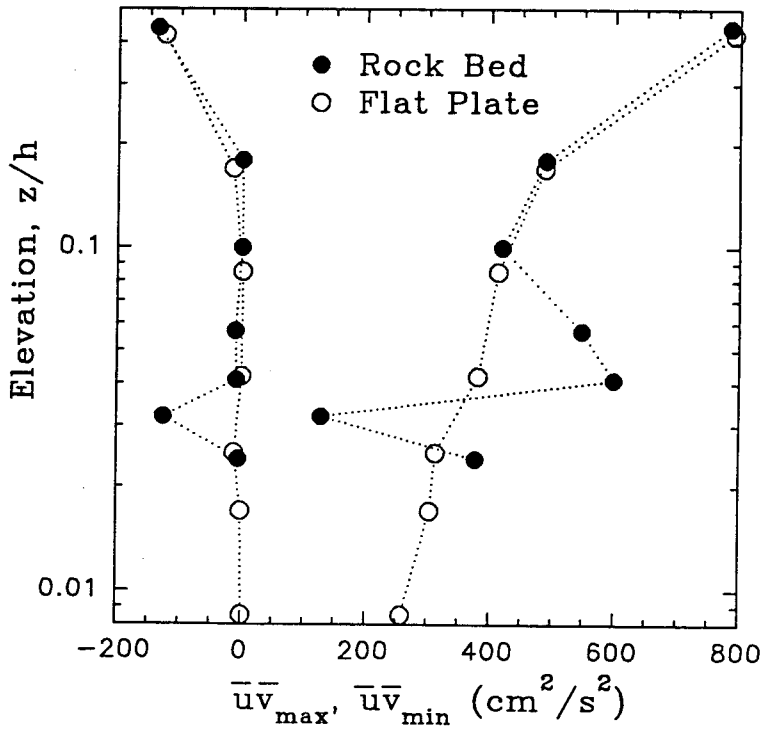

FIG. 4.58. Range of Variation for $\overline{uv}$ Values, h_b = 11.8 cm, x/L = 0.29.

the shape of the $\overline{uv}$ curve is affected increasingly by the bottom boundary. At z/h =0.032, for example, the characteristic positive peak under the wave crest is lost entirely and replaced by a negative peak.

Figure 4.58 shows a comparison of the maximum and minimum values of $\overline{uv}$ for the breaking wave of h_b = 11.8 over the flat plate and over the rock bed. For the flat plate experiments, the magnitude of $\overline{uv}$ decreases uniformly with depth. Near the bottom boundary, the minimum value goes quickly to zero. For the rock bed, though the minimum values of $\overline{uv}$ generally tend to be small near the bed, the maximum $\overline{uv}$ values begin to depart form the flat bed curve near z/h = 0.1 and show no definite trend in magnitude below that elevation.

The range of values for $\overline{uv}$ during the passage of a wave is summarized in Figure 4.59. The maximum and minimum values of $\overline{uv}$ for waves over a rock bed are plotted on the abscissa while the relative elevation of the measurement location is shown on the ordinate. It appears that the $\overline{uv}$ values tend to decrease with depth in the upper part of the flow. At elevations between z/h = 0.09 and 0.05, the magnitudes of $\overline{uv}_{max}$ in the breaking waves no longer vary uniformly and show the same type of fluctuating behavior as seen in the turbulent velocities, appearing to increase with depth. It is also seen that increases in the magnitude of $\overline{uv}_{min}$ are generally accompanied by comparable decreases in $\overline{uv}_{max}$. For the solitary wave on the level bed, with no particle movement, the value of $\overline{uv}$ remains uniformly small throughout the depth. It is also noted that the range of $\overline{uv}$ for the shoaling waves is consistently smaller at a given elevation than the range for the comparable breaking waves.

The above observations of the variation of $\overline{uv}$ with depth indicate that the term $-\overline{v}\frac{\partial \overline{u}}{\partial y}$ in the Navier-Stokes equation may only be neglected at the elevation in the

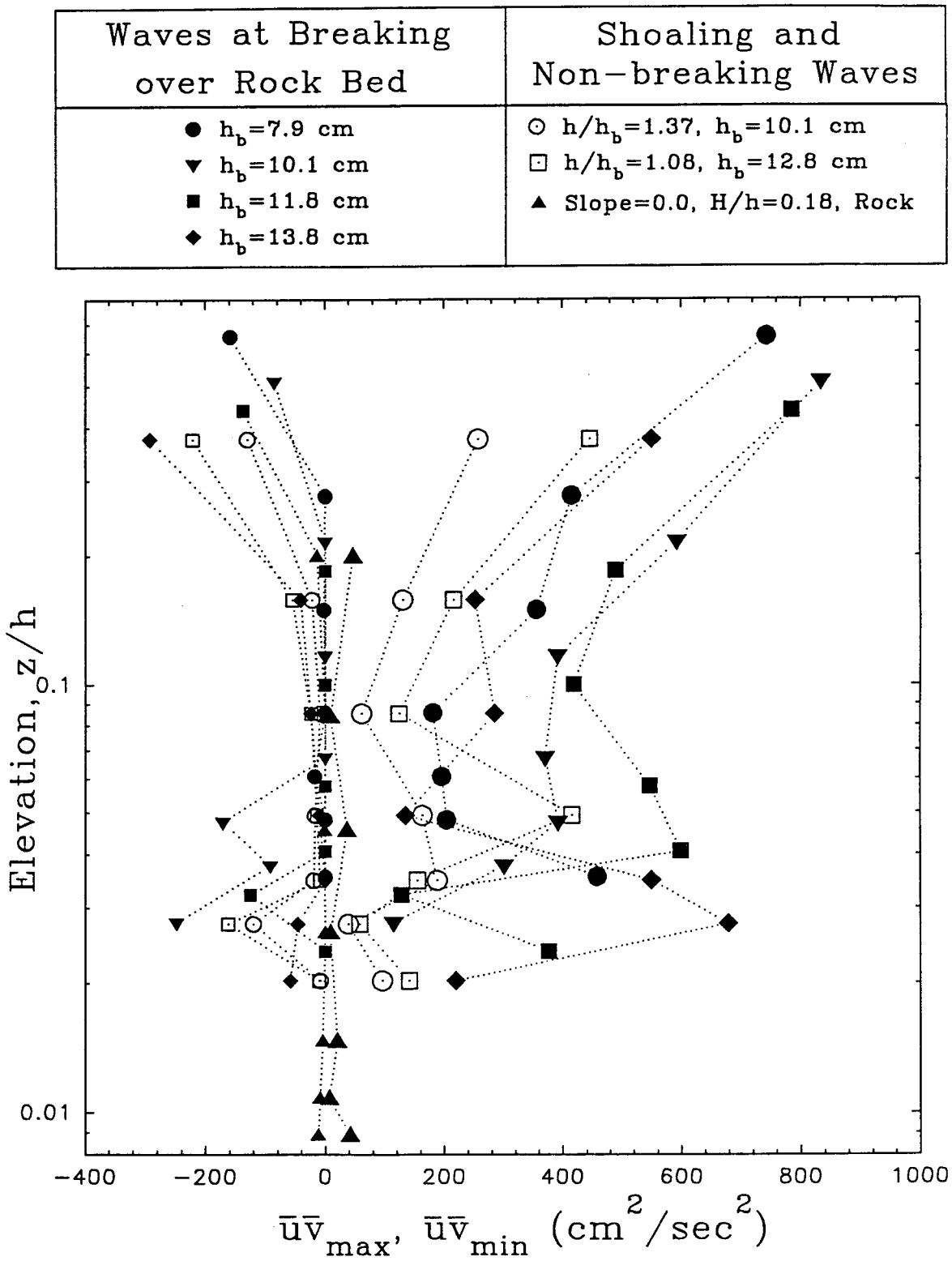

FIG. 4.59. Variation of $\overline{uv}$ with Relative Elevation for Waves Over a Rock Bed, x/L = 0.29.

boundary layer where the change of $\overline{uv}$ with depth becomes zero. At this elevation, the derivative with respect to the y or vertical direction vanishes. The value of $\overline{uv}$ at this elevation, however, does not itself vanish for flow over a rock bed. In fact, the contribution to momentum transport, $\overline{uv}+u'v'$, of the $\overline{uv}$ term is 5 to 10 times larger than the contribution of u'v' near the time of wave crest passage.

4.2.6 Forces on Particles in the Inner Boundary Layer

In order to understand the mechanics of particle movement in the breaking waves, the forces on a spherical particle of diameter D equal to D_{50} of 4.8 mm were calculated using Morison's equation. As recalled from Chapter 1, a spherical particle is expected to move from its position on a bed of identical spherical particles when the moment applied by the hydrodynamic forces exceeds the restoring moment of gravity.

$$\text{Overturning Moment,} \quad M_H = F_x \frac{\alpha_m D}{2}\cos\varphi + F_y \frac{\alpha_m D}{2}\sin\varphi \tag{4.5}$$

$$\text{Restoring Moment,} \quad M_R = W\frac{\alpha_m D}{2}\sin\varphi \tag{4.6}$$

Here, as in Chapter 1, F_x and F_y are the horizontal and vertical components of the hydraulic force, W is the submerged particle weight, φ is the contact angle of the particle to the bed (estimated to be 30 degrees), and α_m (estimated to be 0.86) is based on the particle bed geometry. The applied forces were calculated using:

$$F_x = \frac{1}{2}\rho C_D \frac{\pi D^2}{4} u^2 + \rho C_m \frac{\pi D^3}{6}\frac{du}{dt} \tag{4.7}$$

$$F_y = \frac{1}{2}\rho C_D \frac{\pi D^2}{4} v^2 + \rho C_m \frac{\pi D^3}{6}\frac{dv}{dt} + \frac{1}{2}\rho C_L \frac{\pi D^2}{4} u^2 \tag{4.8}$$

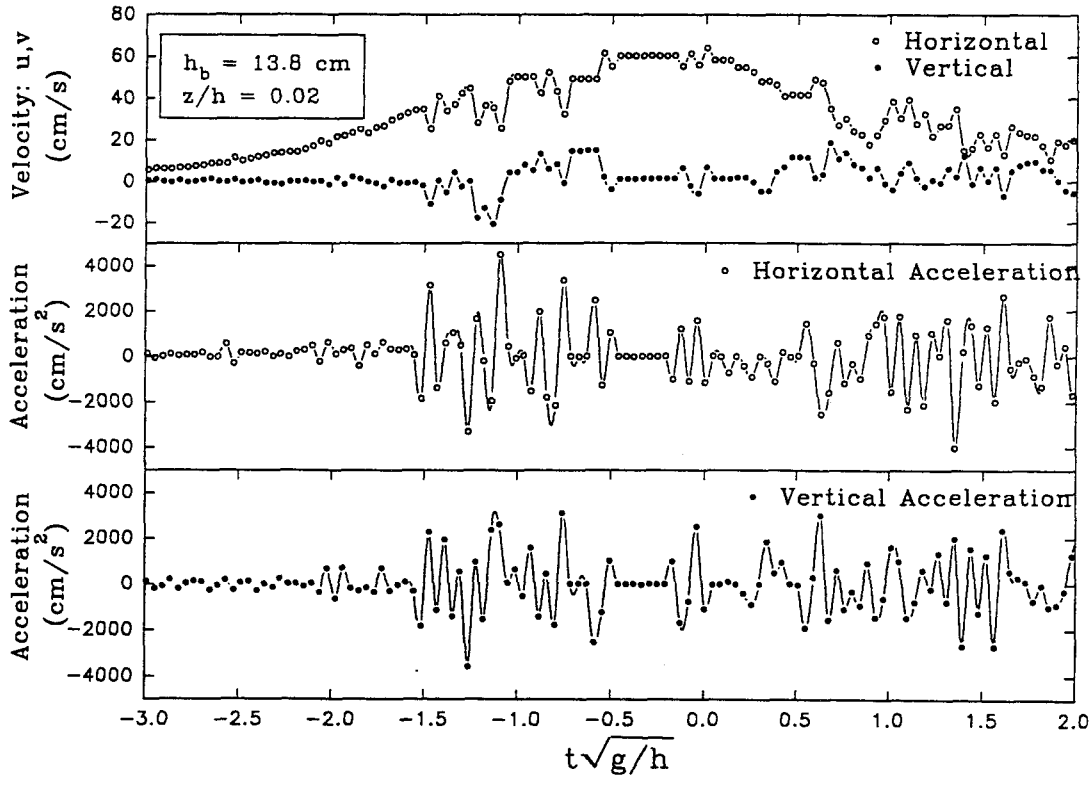

(a)

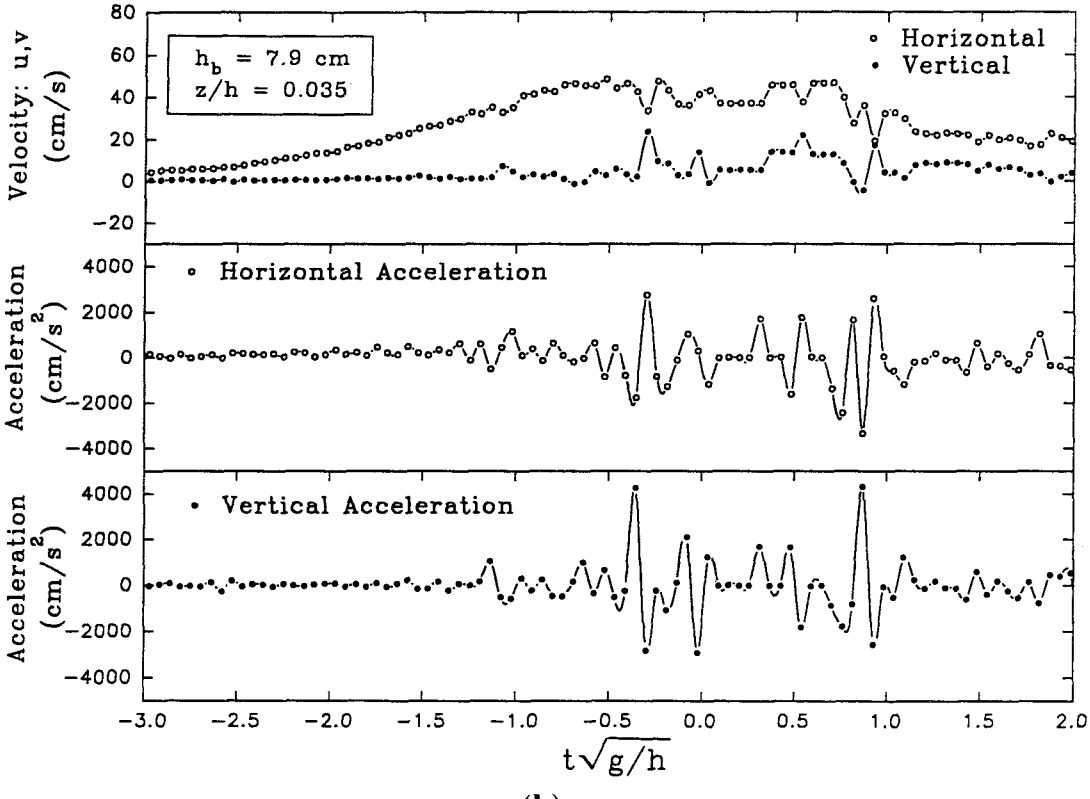

(b)

FIG. 4.60. Measured Velocities and Accelerations in Two Breaking Waves at x/L = 0.29.

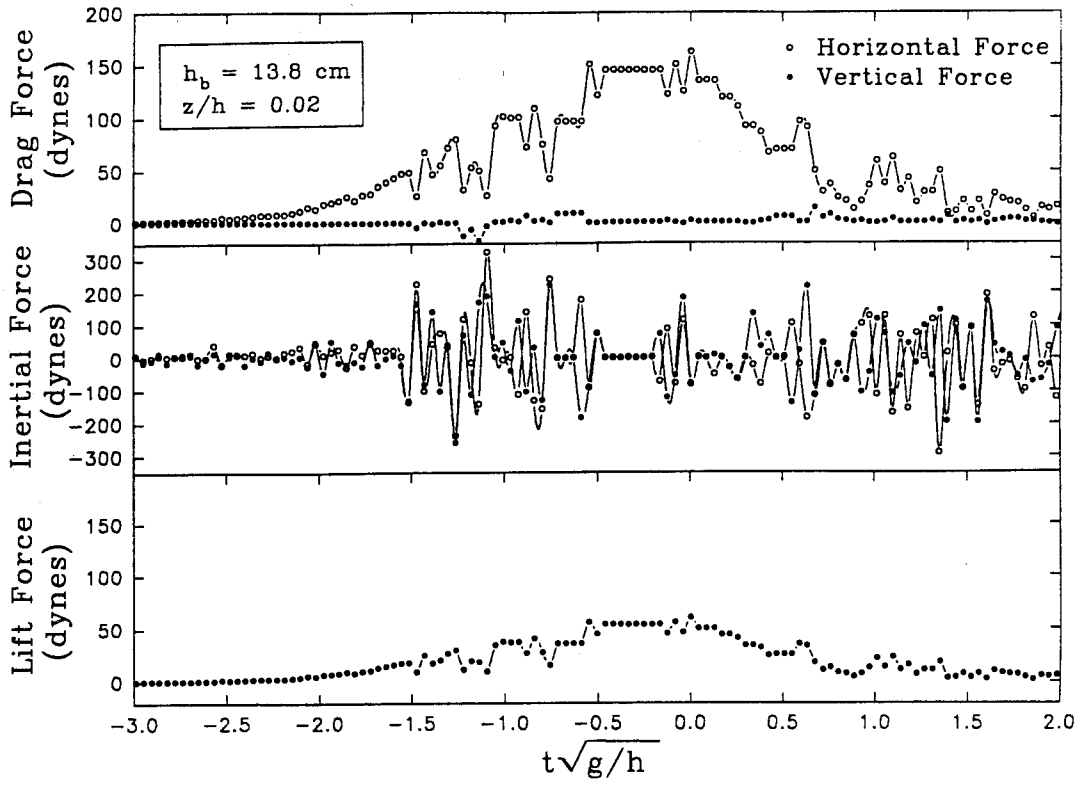

(a)

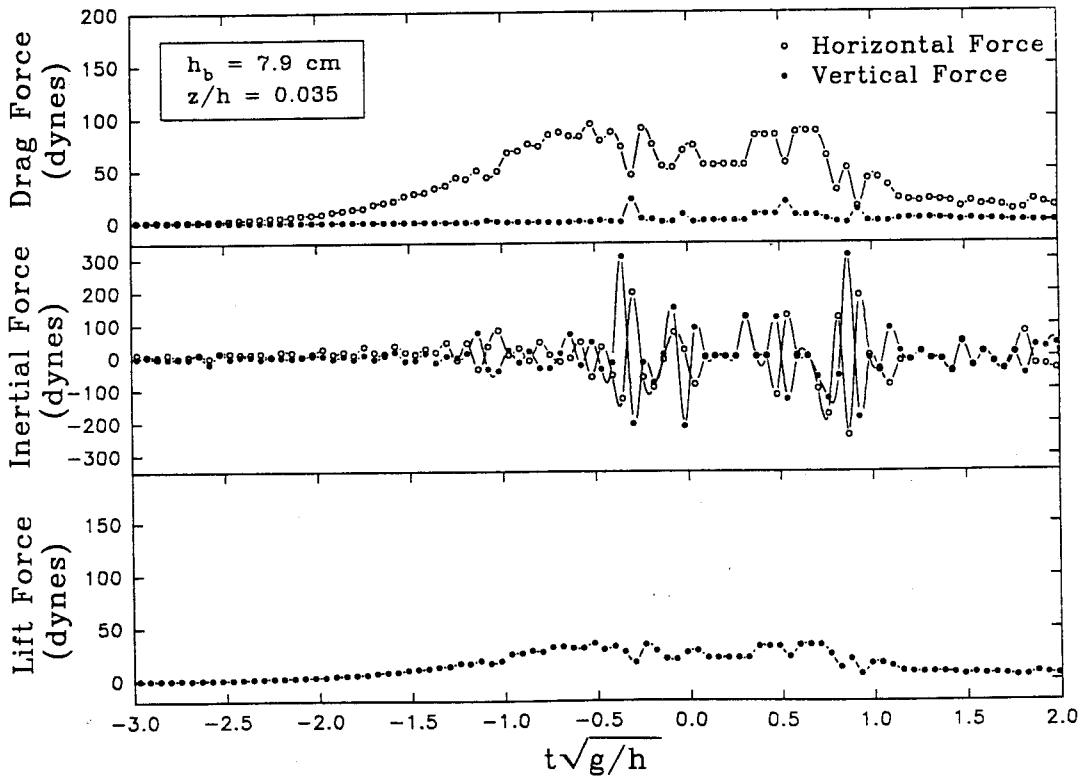

(b)

FIG. 4.61. Calculated Forces on a Sphere of Diameter 0.48 cm for Two Waves at x/L = 0.29.

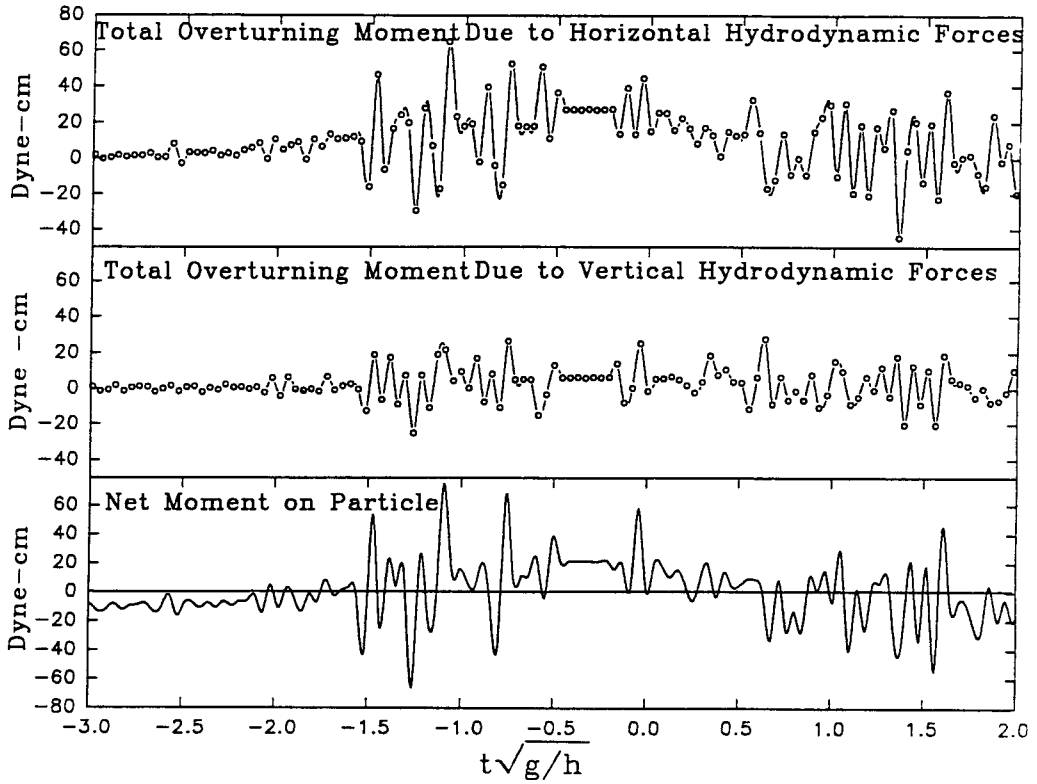

(a)

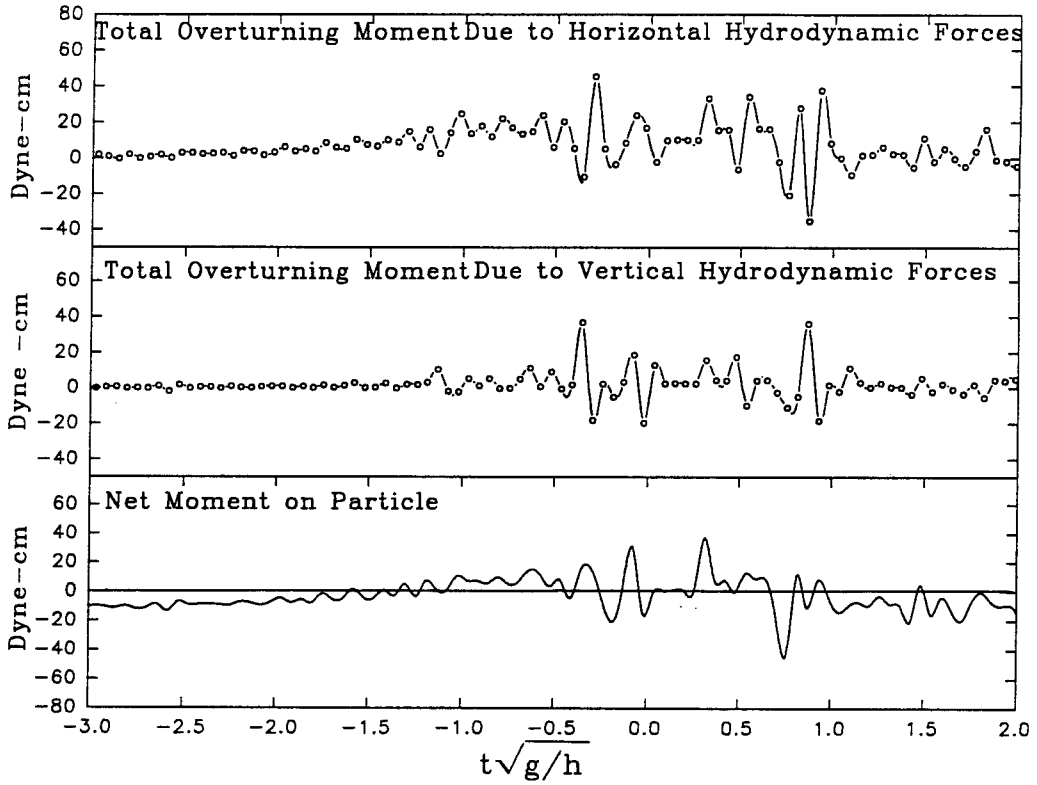

(b)

FIG. 4.62. Calculated Moments on a Sphere of Diameter 0.48 cm for Two Waves at x/L = 0.29.

The sphere weight was computed using a specific gravity of 2.49. Values for C_D, C_M and C_L were estimated based on force measurements performed with spheres in solitary waves. These measurements are documented in Petroff and Raichlen (1991), which is reproduced in Appendix A. The constants, $C_D = 0.4$, $C_M = 1.10$, and $C_L = 0.15$, were chosen for a sphere near a boundary in the presence of other spheres. The forces are assumed to act through the center of the sphere.

The time required for a sphere to rotate from an initial contact angle φ_o to an angle $\varphi = 0.$ can be expressed as:

$$t = \frac{1}{\sqrt{C_3}}\left\{ F\left[\sin\frac{\varphi_o'}{2}, \frac{\pi}{2}\right] - F\left[\sin\frac{\varphi_o'}{2}, \sin^{-1}\left(\frac{\sin\frac{\beta}{2}}{\sin\frac{\varphi_o+\beta}{2}}\right)\right]\right\}, \quad \text{for} \quad C_3 = \frac{\alpha_m D}{2I}\sqrt{F_x^{\,2} + (F_y - W)^2}$$

$$\beta = \tan^{-1}\left[\frac{F_x}{F_y - W}\right] \quad \text{and} \quad \varphi_o' = (\varphi_o + \beta) \tag{4.9}$$

Here the function F[,] refers to an elliptic integral of the first kind. A derivation of this relation is presented in Appendix D.

The instantaneous velocities and accelerations measured under two breaking waves near the time of wave crest passage for elevations near z/h = 0.03 are presented in Figure 4.60. This figure shows the horizontal and vertical velocities and accelerations plotted for a normalized time interval of $-3.0 \le t\sqrt{g/h} \le 2.0$. In Figure 4.60(a) the flow quantities are presented for the largest wave with h_b = 13.8 cm at the relative elevation z/h = 0.02 and location x/L = 0.29. Figure 4.60(b) shows the smallest wave, h_b = 7.9 cm, at elevation z/h = 0.035 and x/L = 0.29. As expected, the larger wave exhibits larger horizontal velocities and more frequent turbulent accelerations than the smaller wave.

Figure 4.61 shows the forces calculated to act on the sphere under the two waves. For both waves it is noted that the vertical drag force is negligible. As expected the drag

and lift forces computed for the larger wave are greater in magnitude than the forces for the smaller wave. Although the inertial forces for the larger wave show more large magnitude excursions, the values of the maximum inertial force is very nearly the same for the smaller breaking wave as for the larger one.

The moments acting on the sphere are summarized in Figure 4.62. The total overturning moment, as shown in this figure, is composed of forces both in the horizontal and vertical directions while the restoring moment is a function of the submerged weight of the sphere. In Figure 4.62 (a) both the drag and inertial forces play a role in creating a net positive moment on the sphere. From a non-dimensional time $t\sqrt{g/h}$ of -1.5 to 0.5, (a duration of 0.24 seconds), the net moment on the particle is on the average positive, indicating that under the conditions of this analysis, it would start to move.

In Figure 4.62 (b) the effect of the drag force is less pronounced than for the larger wave, and the major contributions to net positive moment are due to inertial forces. It is seen in both Figures 4.61 (a) and 4.61(b) that the vertical inertial force and, to some extent, the lift force contribute significantly to the overturning moment for short intervals of time. When the vertical inertial force is at a maximum at the same time that the horizontal inertial force is at a maximum, this creates a large positive excursion in net moment on the sphere. This is seen in Figure 4.62(a) for time slightly less than $t\sqrt{g/h}$ = 0.0, and for Figure 4.62(b) at times $t\sqrt{g/h}$ = -0.03, -0.1 and 0.4. The net moment on the sphere is mostly positive between $t\sqrt{g/h}$ = -1.3 and 0.7.

Though the net positive moment in these cases may be enough to initiate motion of the sphere, the relative combinations of magnitude and duration of the positive moment pulse must be correct to actually move the sphere out of its resting position. For an inital net moment of 20 dyne-cm, the time to rotate a spherical particle from $\varphi = 30°$ to the vertical is approximately 0.02 seconds. At a higher initial moment of 65 dyne-cm, this

time is reduced to 0.01 seconds. It appears that both the small long duration positive moments associated with drag forces and the large short duration moments associated with inertial forces can both remove a particle from its original position.

Though the calculations performed on an idealized sphere do not quantitatively define the motion of the bed material in these experiments, they do serve to clarify some aspects of particle motion. First, the instantaneous moment on the particle is a function of both the velocities and accelerations present in the flow. The drag force is associated with sustained gradual variations of net moment over long time intervals, while the inertial forces cause short term large magnitude variations in net moment. Thus, in a flow where the drag force is not large enough to overcome the restoring moment, the particle may still be set into motion by a large variation in inertial force.

A second consideration in the motion of the particle is the frequency of occurence of net positive moment. Figure 4.63 shows frequency distribution curves for the two sets of velocities and accelerations used in the moment calculations. The velocity curve for the larger wave appears to the right of that for the smaller wave. As an example, if the drag force required to move a particle was satisfied by velocities greater than 40 cm/s, then the velocities in the smaller wave would only exceed this value 6 percent of the time during the period of wave passage, while the larger wave would exceed the value 16 percent of the time. If the value required were greater, at 60 cm/s, the probability of achieving sufficient drag in the larger wave would still be 12 percent, while the probability for the smaller wave would be negligible. While large differences are seen between the horizontal velocities in the two waves, the variation of the acceleration is less marked. The probability of exceeding 1 g in horizontal acceleration is 10 percent for the large wave and 5 percent for the smaller one. As noted above, the temporal distribution of the inertial forces is also important in creating a net positive moment on the particle and that variation is not shown in the frequency distribution curves.

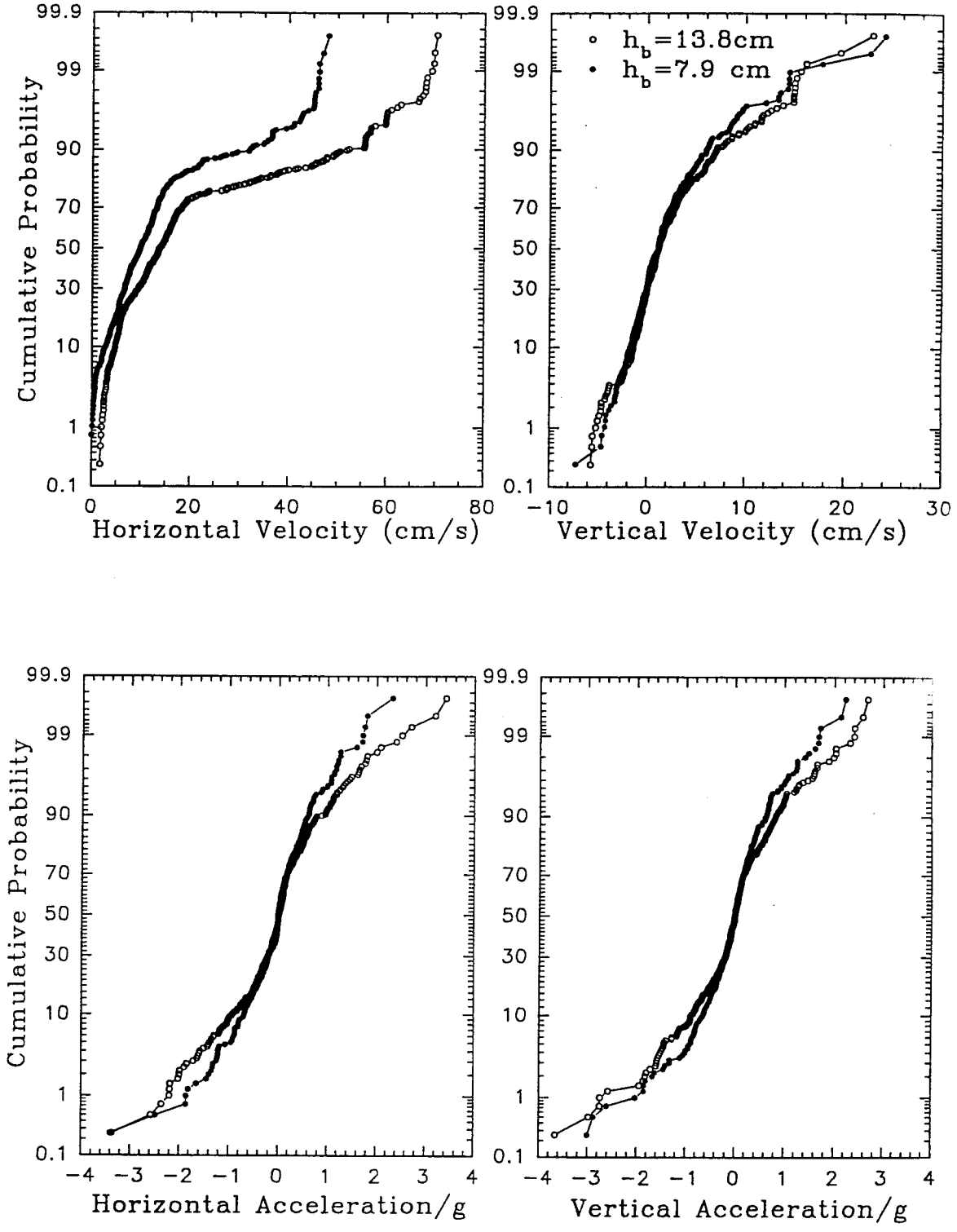

FIG 4.63. Frequency Distribution of Velocities and Acceleration Under Two Breaking Waves at x/L = 0.29, z = 1 mm.

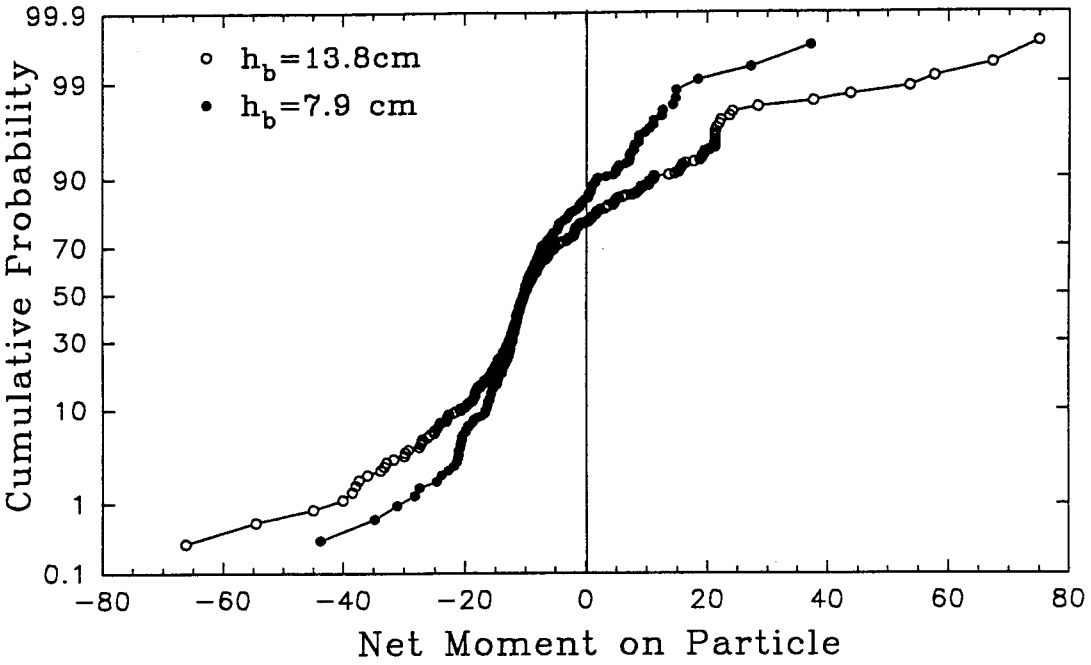

FIG. 4.64. Frequency Distribution of Net Moment on Sphere of Diameter 0.48 cm Under Two Waves, x/L = 0.29, z = 1 mm.

The frequency of occurrence of net positive moment for the case of the idealized sphere is shown in Figure 4.64. The net moment is positive about 25 percent of the time for the larger wave and 13 percent of the time for the smaller one. Although the frequency distribution curves are convenient for assigning a probability for the conditions causing movement in a particle, as was shown in Figure 4.62, the exact duration and timing of the applied forces is quite important in determining whether this movement will be sustained.

4.3 PARTICLE MOVEMENT OBSERVATIONS

4.3.1 Overhead Views

The overhead video observations before and after the passage of a given wave were compared and filtered using the methods described in Chapter 3. The resultant

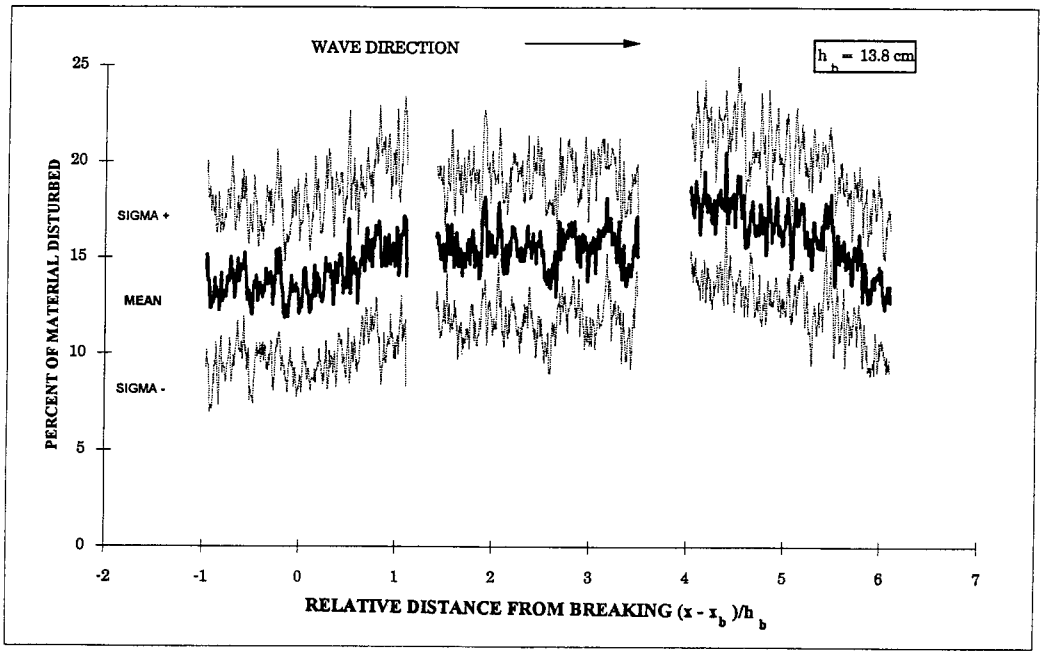

(a)

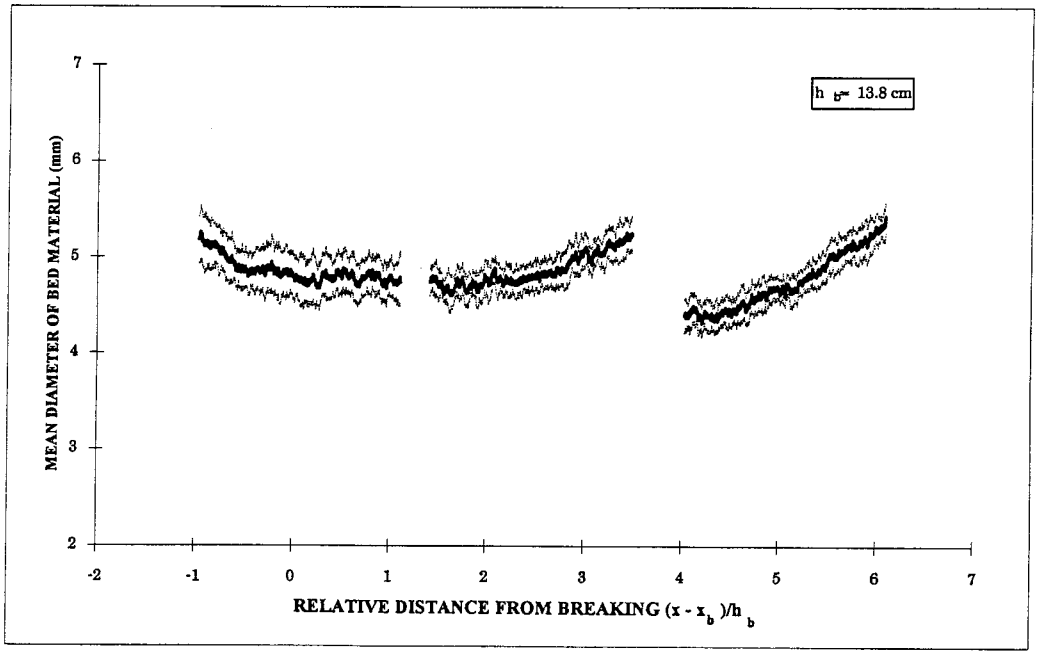

(b)

FIG. 4.65 Calculated Movement Intensities and Bed Composition for Breaking Wave with h_b = 13.8 cm at x/L = 0.29.

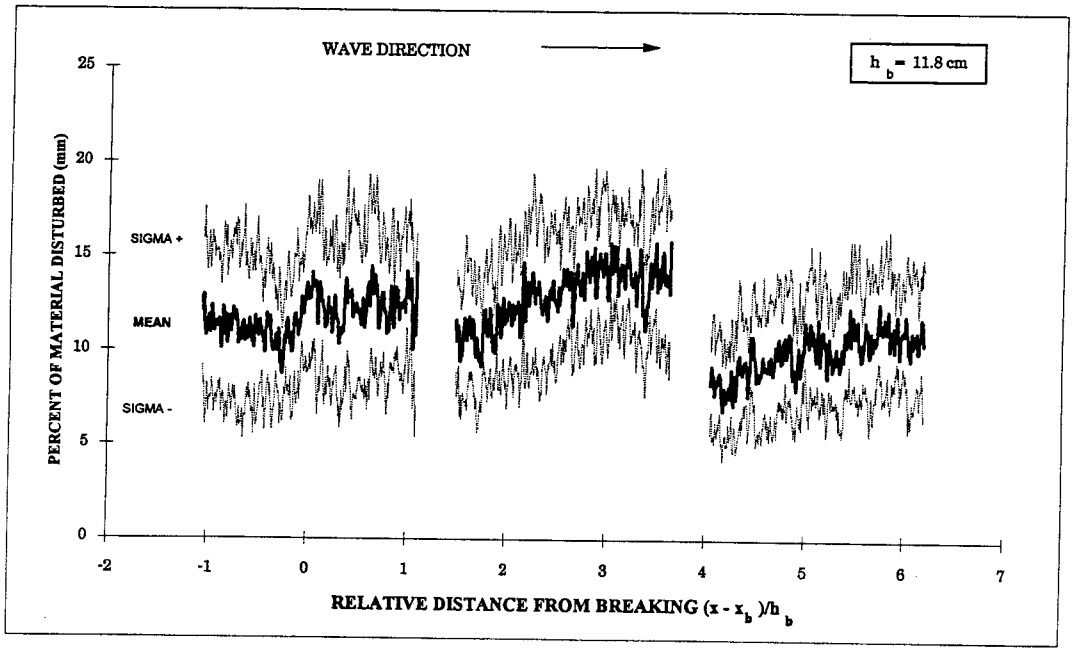

(a)

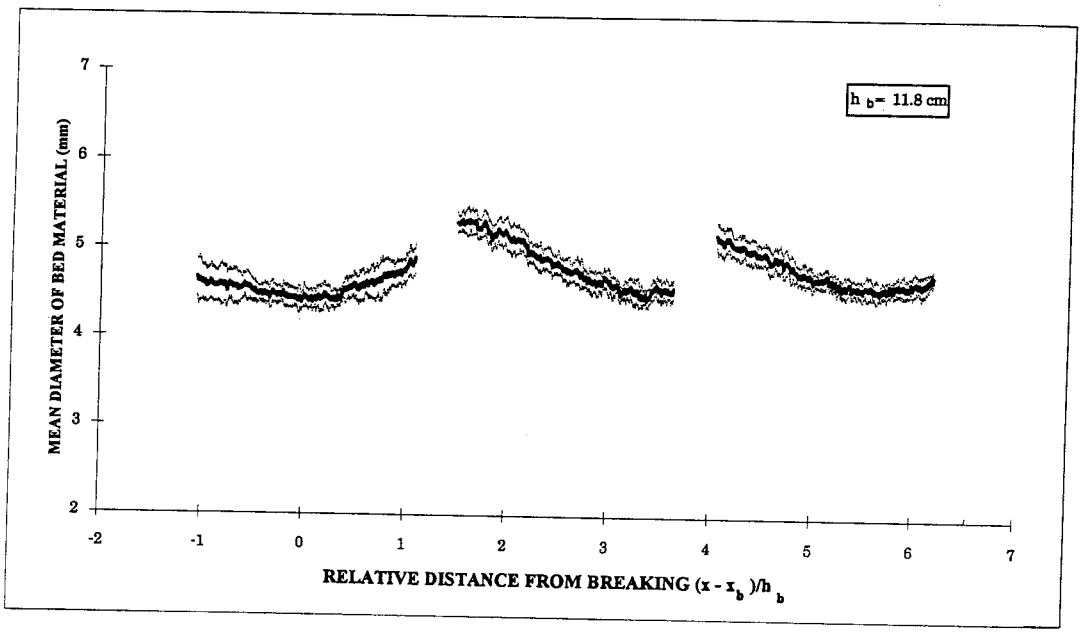

(b)

FIG. 4.66 Calculated Movement Intensities and Bed Composition for Breaking Wave with h_b = 11.8 cm at x/L = 0.29.

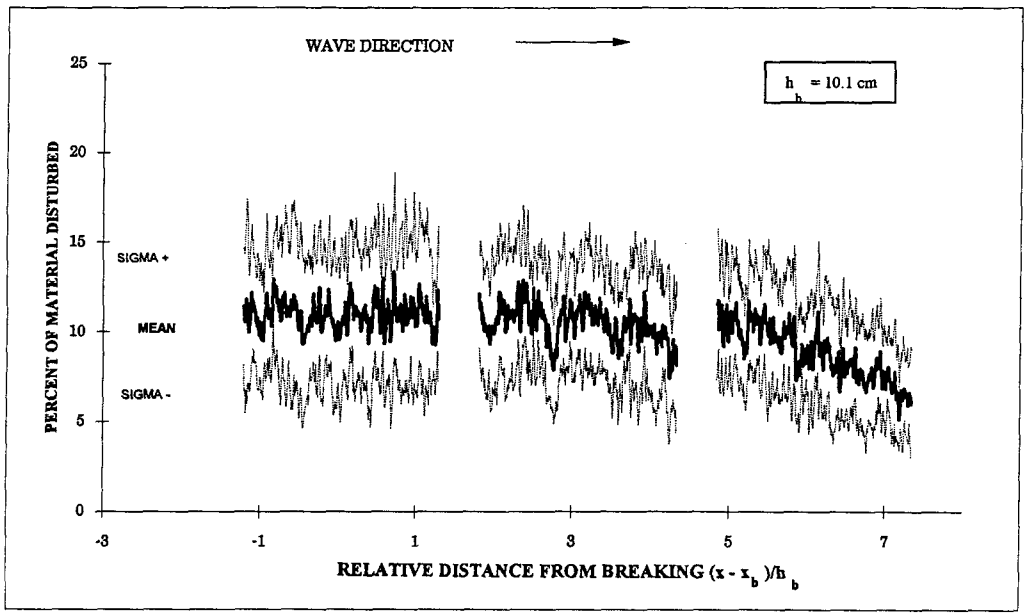

(a)

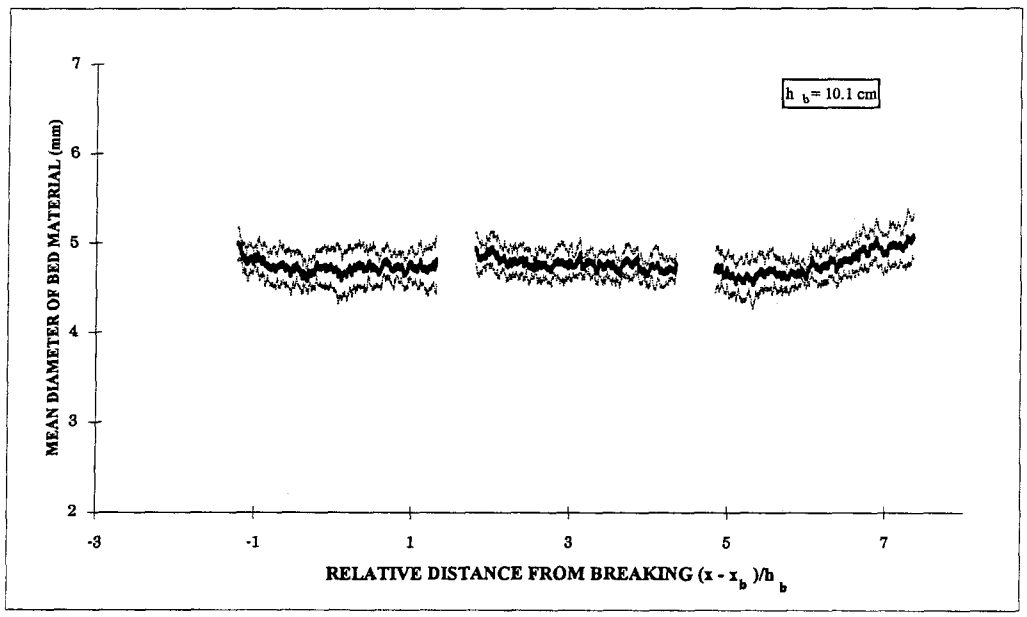

(b)

FIG. 4.67 Calculated Movement Intensities and Bed Composition for Breaking Wave with h_b = 10.1 cm at x/L = 0.29.

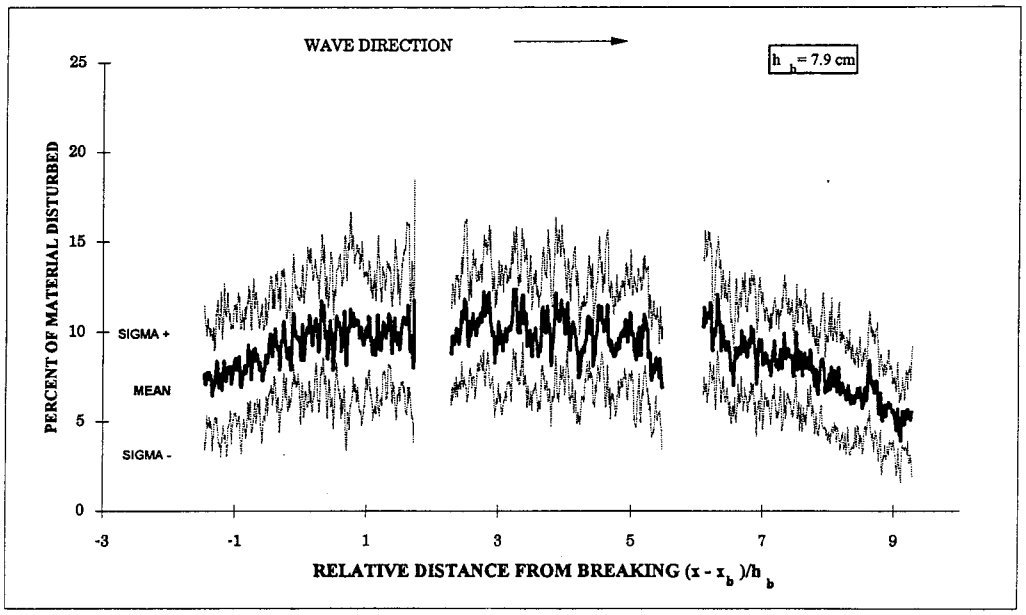

(a)

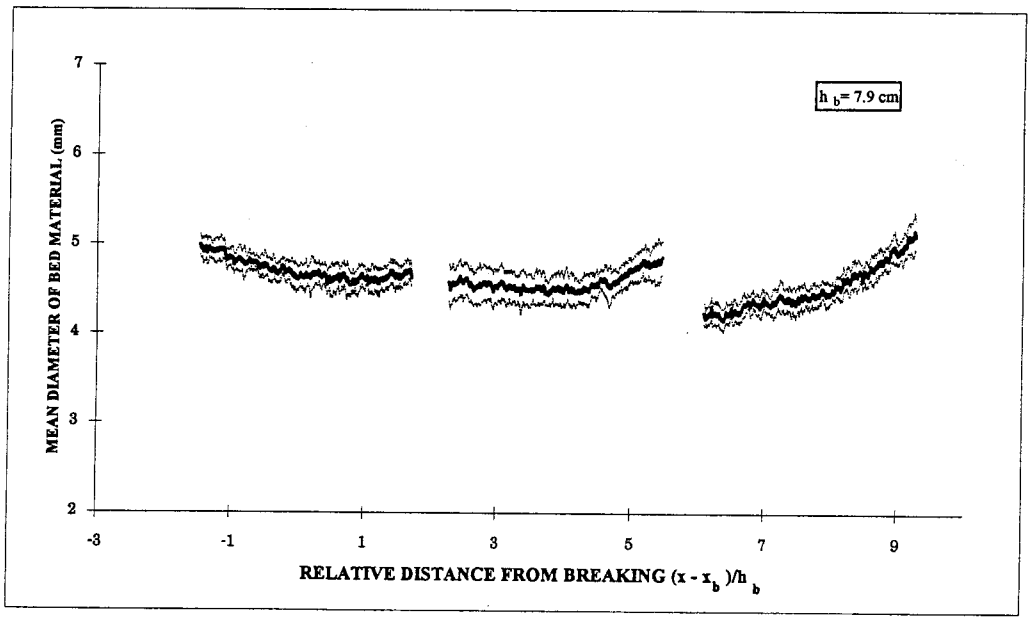

(b)

FIG. 4.68 Calculated Movement Intensities and Bed Composition for Breaking Wave with h_b = 7.9 cm at x/L = 0.29.

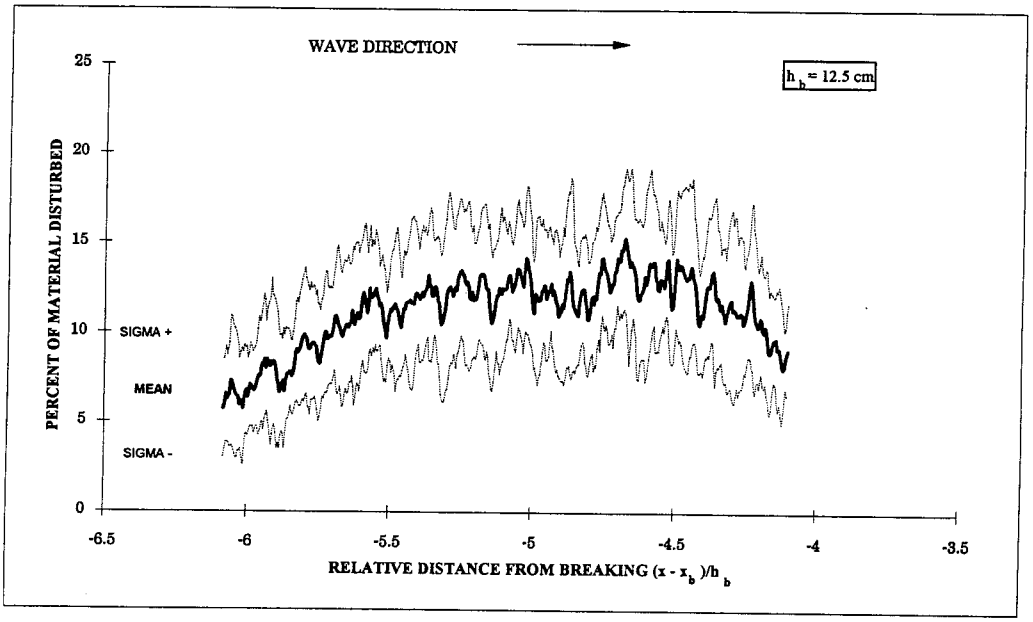

(a)

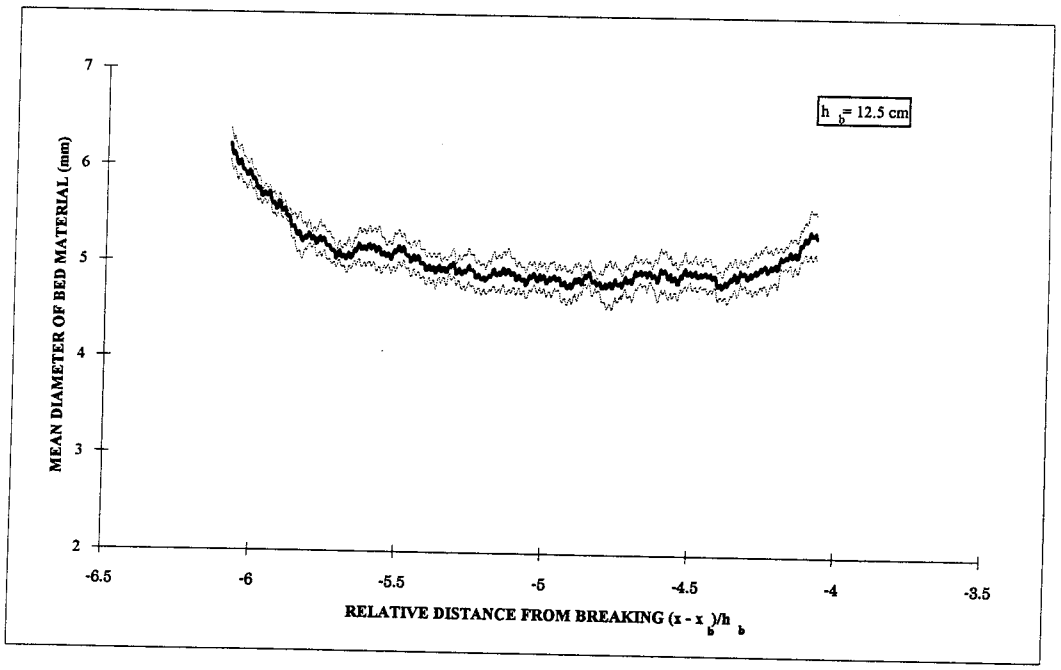

(b)

FIG. 4.69. Calculated Movement Intensities and Bed Composition for Shoaling Wave with h_b = 12.5 cm at x/L = 0.72.

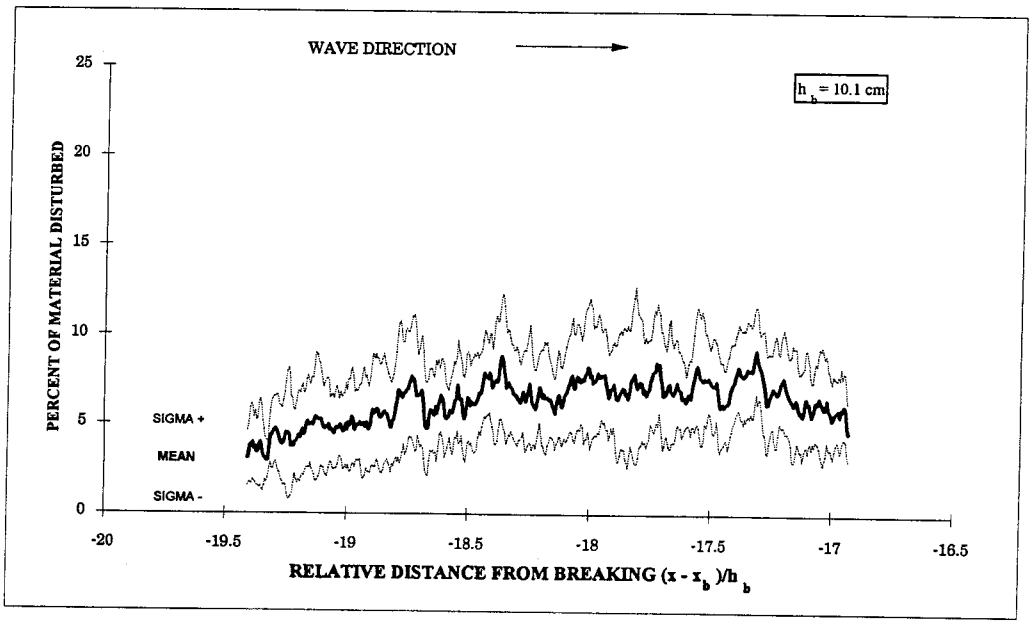

(a)

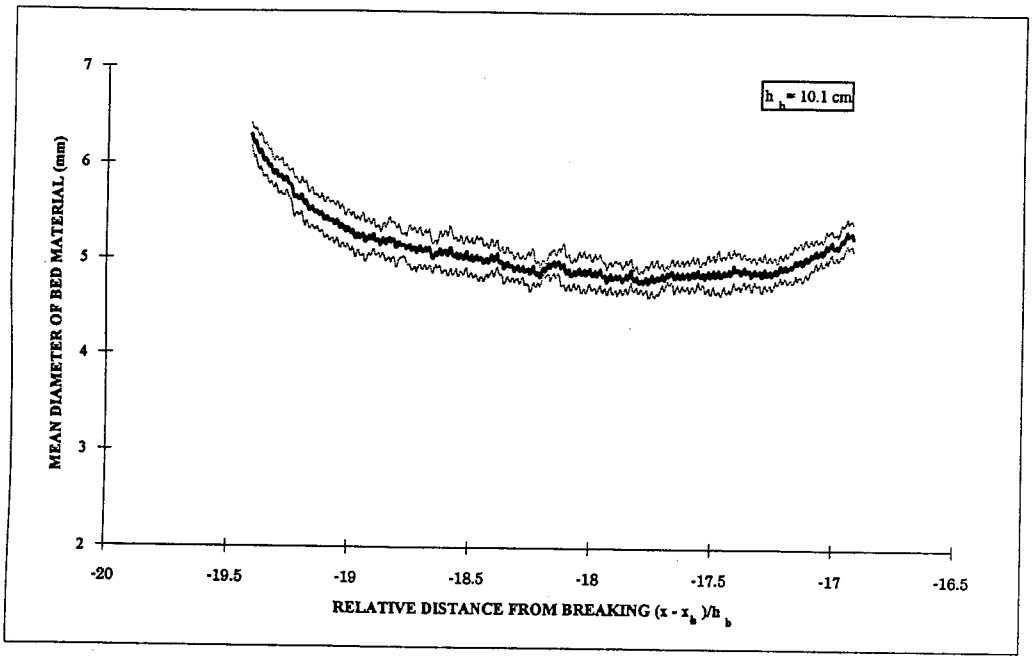

(b)

FIG. 4.70 Calculated Movement Intensities and Bed Composition for Shoaling Wave with h_b = 10.1 cm at x/L = 1.52.

movement intensities were averaged for each pixel location over at least fifteen identical experimental runs. Since the pixel locations each correspond to a particular location along the test section, the resulting average shows the variation of particle movement with longitudinal distance along the tank. Figures 4.65 through 4.70 present the movement intensities measured for the four breaking waves and the two shoaling waves.

In frame (a) of each figure, the percent by area of material disturbed is plotted on the ordinate. This disturbed area consists of both the particles removed from their original locations and the particles deposited in new locations. For the waves used in this study, it was visually estimated that approximately the same number of particles were removed as were deposited in any given location. As a result, the values shown in Figures 4.65 through 4.70 represent about twice the actual number of particles moved. Each bold trace represents the mean of the 15 to 20 experiments at that position in the test section. The lighter traces show the range of variation of the data obtained by adding and subtracting one standard deviation, σ, from the mean intensity. It was not determined whether the distribution of the intensity values was in fact Gaussian, so that these lighter traces only serve to show the variation in observed movement.

Frame (b) of Figures 4.65 to 4.70 shows the variation with location of the mean diameter of the bed before wave passage. The mean grain size was determined by using the calibration curve shown in Figure 3.3. It will be recalled that this calibration was obtained by computing the size fraction of each color of rock at a given longitudinal pixel location. As in frame (a), the bold trace represents the mean diameter at a particular location and the lighter traces show the 95 percent confidence intervals. From Figure 4.65 it is seen that the composition of the bed has a very large effect on the amount of movement seen under a given wave. As discussed in Section 2.3, it was not possible to obtain a uniform distribution of rock size at all locations in the bed. Thus areas of smaller or larger material occurred randomly along the test section and only changed gradually

with the raking process. In Figure 4.65, at location $(x-x_b)/h_b = -1.0$, the bed appears to have a mean grain size of 5 mm. At this location, the value of movement observed for the wave of breaking depth, $h_b = 13.8$ cm, is nearly 14 percent. At $(x-x_b)/h_b = 4.0$ for the grain size of 4.4 mm, the movement intensity increases to 17.5 percent. For $(x-x_b)/h_b = 6.0$, the apparent grain size is 5.4 mm and movement decreases to 13 percent. For the purposes of comparing movement results for a consistent grain size, the movement values in the following discussion were measured at a calculated mean grain size for the entire exposed bed of 4.76 mm as shown in Section 3.1.

Figure 4.71 shows the calibration curve used to calculate the actual number of particles disturbed in a given experiment from the intensity record of the disturbed area of the bed. For one run for each different wave at each of the measurement locations, a visual count was made of the total number of particles visible and the total number of particles observed to move. The total number of particles in a video frame was obtained from counting an area roughly 13 cm^2 and scaling the result to the size of the entire frame. The number of moved particles was counted from the unfiltered comparison of the rock bed before and after wave passage using the entire frame.

The percent by number of particles disturbed, calculated for the single runs, is plotted on the abscissa, with the average percent disturbed by area on the ordinate. The observation location is designated with an asterisk for $x/L = 0.29$, an "x" for $x/L = 0.53$ and a cross for $x/L = 0.73$. The data have been fitted with a least squares fit to a second order polynomial with the line constrained to pass through the origin. It appears that, given the variation of the amount of particle movement between different runs, the particle counts agree well with observations of the area of movement intensities. The percent by number of particles disturbed is noted to be uniformly larger in magnitude than the percent of the bed area disturbed. The relation between particle count and particle area will be discussed below.

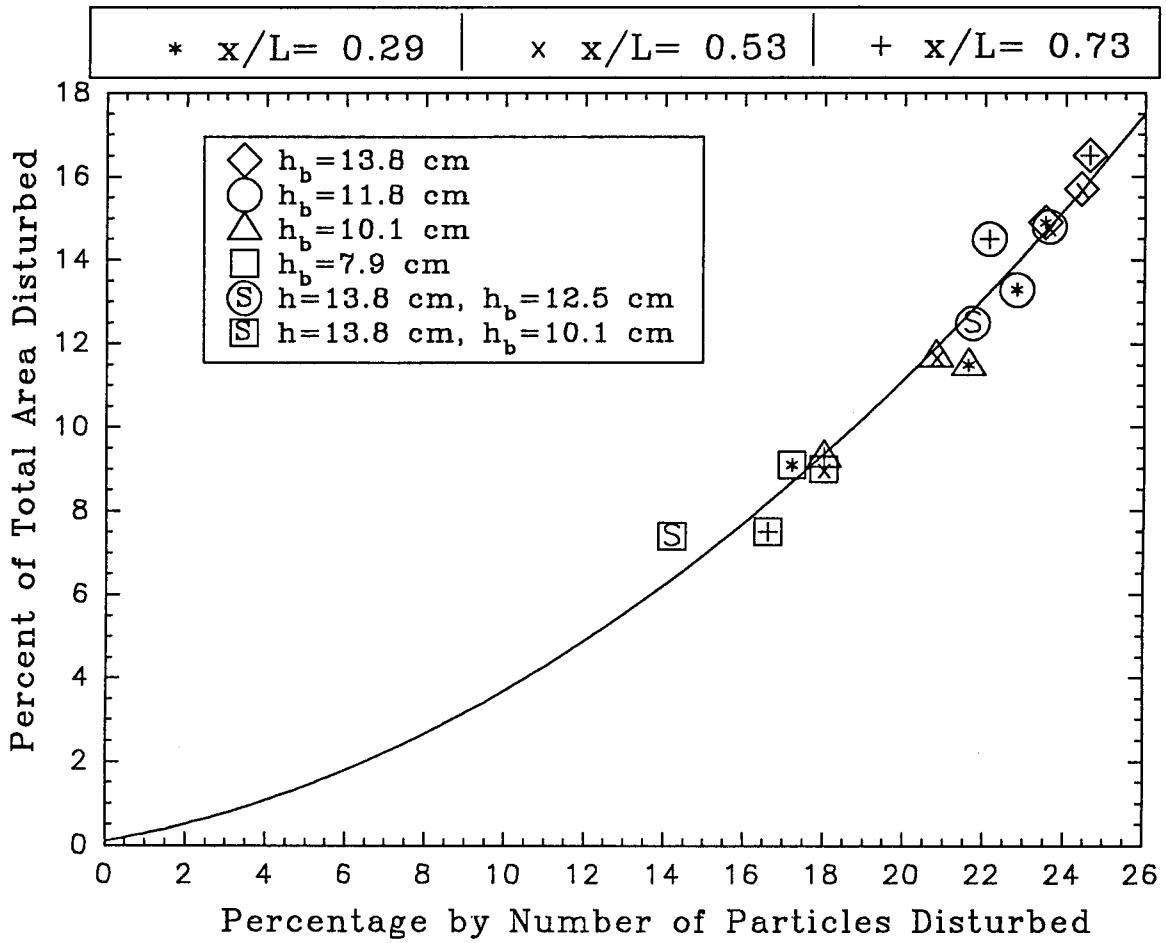

FIG. 4.71. Calibration for Number of Particles Disturbed against Area Disturbed.

Using the calibration from Figure 4.71, the percent by number of particles disturbed were calculated for the different wave cases. These values are shown in Figure 4.72 plotted on the ordinate against the relative distance of the wave from breaking on the abscissa. The error bars indicate the range of the data over plus or minus one standard deviation at a given measurement location, while the location of the symbol shows the mean value.

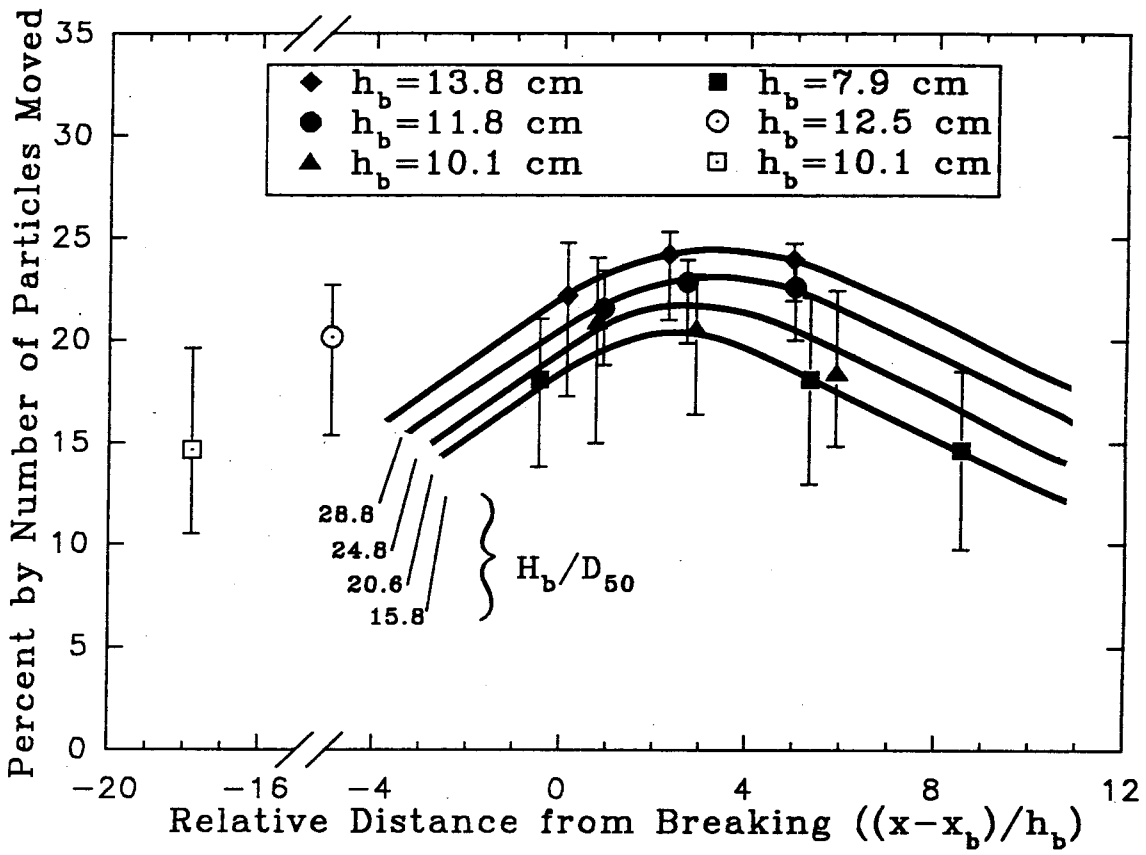

FIG. 4.72. Variation of Particle Movement with Distance From Breaking.

The movement values for the different wave cases show a maximum material movement between the breaking location, $(x-x_b)/h_b = 0$, and a distance about 5 breaking depths shoreward, $(x-x_b)/h_b = 5$. The values of movement for the shoaling waves are noticeably smaller than those for the breaking waves with the same maximum free stream velocity. In the case of the shoaling wave with $h_b = 12.5$ cm, the percent by number of particles disturbed is 10 percent less than for the breaking wave with $h_b = 11.8$ cm. For the shoaling wave observed further from breaking, $h_b = 10.1$ cm, the movement value is approximately 17 percent less than that of the breaking wave with the same maximum velocity, $h_b = 7.9$ cm.

After breaking, for distances greater than 5 breaking depths away from the onset of breaking, the percent of particles disturbed shows a decreasing trend. At this distance, as seen in the photographs at the beginning of this chapter, the wave collapses and begins

to reform as a propagating bore with a greatly reduced wave height and, consequently, smaller mean water particle velocities. The measurement of less particle movement before and after breaking support the premise that the amount of particle movement under the wave is a function of both the mean velocities and the breaking process itself.

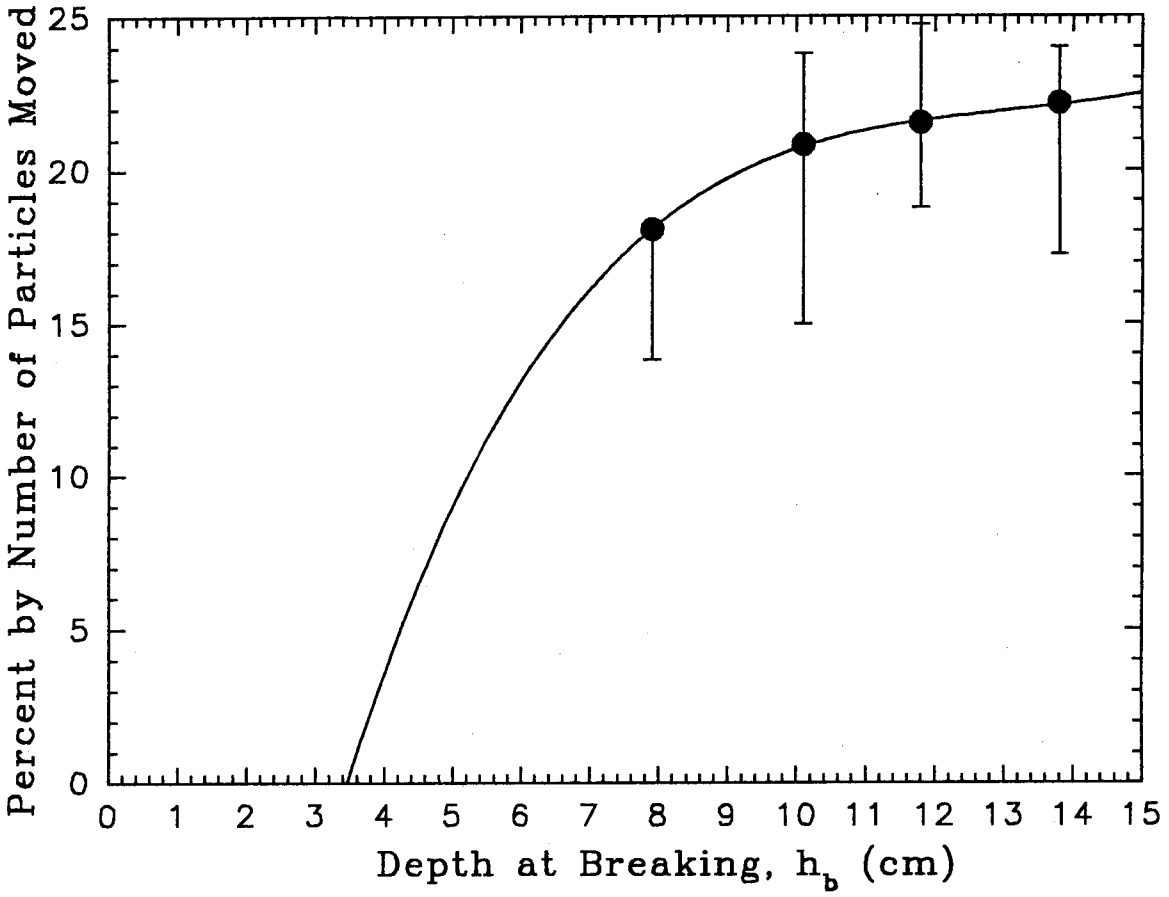

FIG. 4.73. Comparison of Particle Movement to Depth at Breaking.

From Figure 4.72, it is seen that at a given location, as the depth at breaking decreases, the amount of material movement also decreases. This relation is presented in Figure 4.73, where the percentage by number of particles moved at x/L = 0.29, the point of onset of breaking, is plotted for the four different breaking waves. The data show a relatively small increase of 6 percent in particle movement between breaking depths of 10.1 and 13.8 cm. Between breaking depths of 7.9 cm and 10.1, however, the number of

particles disturbed changes by over 13 percent. Given the changing rate of particle motion decrease, it is not reliable to predict a point of initiation of motion from these data.

Figure 4.74 summarizes the particle movement observations with respect to the turbulent shears calculated in section 4.2.3 from water particle velocity measurements. The calculated shear values have been normalized by the Shields critical shear value for a

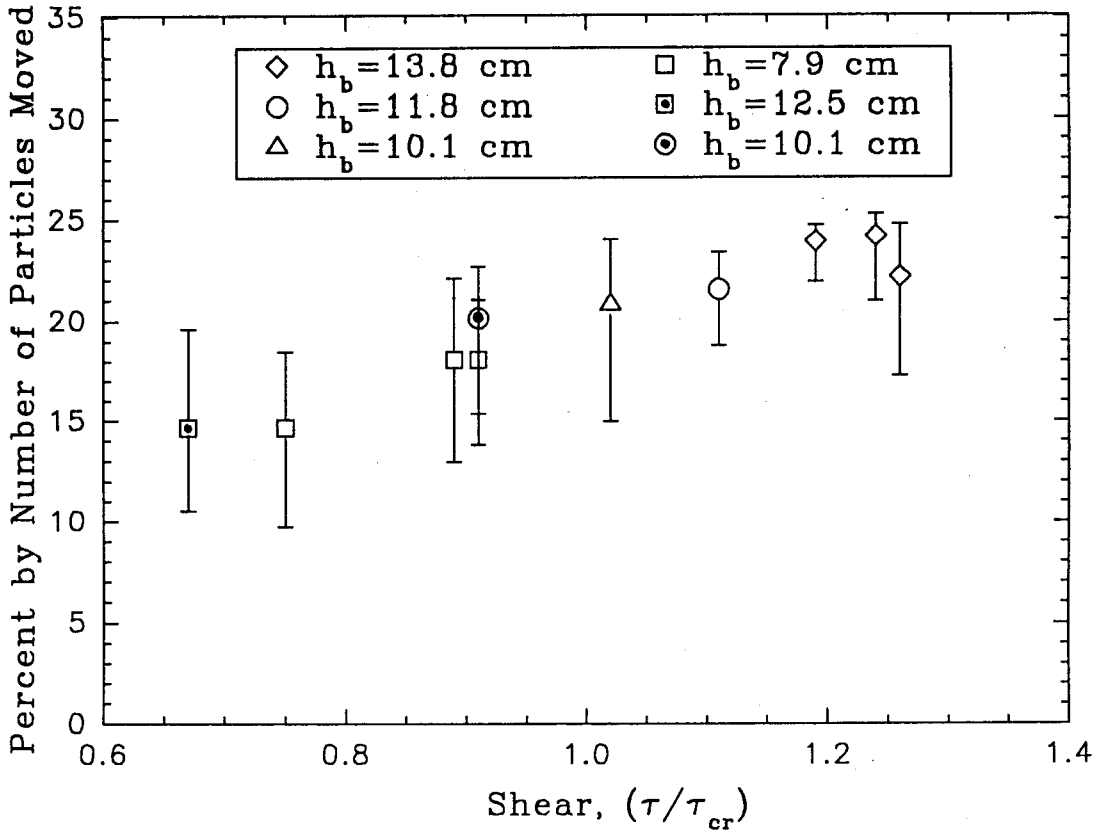

FIG. 4.74. Comparison of Particle Movement with Normalized Shear.

particle of diameter 4.76 mm, (from Vanoni (1964)). For values of τ/τ_{cr} greater than 0.9, the increase of particle movement with increasing shear appears more gradual than for shear values less than 0.9.

The determination of a shear for the zero movement level is not readily apparent using these observed values. For the solitary wave propagating over a level rock bed with

no observable movement, the calculated shear ratio is 0.46. This value is hence a lower bound for the value of the shear stress causing the initiation of motion.

In Figure 4.74 it is seen that, at the Shield's critical shear level for rock of 4.8 mm, a substantial amount of particle movement is observed. It is noted that the value obtained from the Shield's curve at this diameter is approximately equal to the value computed by Naheer (1977) for incipient motion under solitary waves. One factor that greatly influences the amount of observed particle motion, it should be recalled, is that the present study observed particle movement for an unpacked bed. As discussed in Section 1.1, the movement of particles in a bed packed by wave action is almost two orders of magnitude less than for the unpacked case. Similarly, for a steady flow where loose material has been removed by the time the flow reaches the steady state, the conditions of particle motion may be closer to those of a packed bed.

Another reason that motion is seen in the rock bed at shear levels well below the Shields critical shear stress for particles of diameter 4.8 mm has to do with the actual mean diameter of the particles in motion. Table 4.5 summarizes the observations for one experiment of the actual numbers and sizes of particles removed and deposited at the observation location of x/L = 0.29 for the wave with breaking depth of h_b = 13.8 cm. These observations were made by visually outlining the moved particles in one half of a subtracted frame and then finding those particles on the color video picture of either the bed before wave passage or the bed after wave passage.

Table 4.5. Moved Particle Size Observations, h_b = 13.8 cm, h/h_b = 1.00.

Particle Color	Removed	Deposited	Total	% by Number	D_{50}	% by Area
White	62	73	135	54.4%	3.1mm	36%
Yellow	45	40	85	34.3%	4.2mm	42%
Green	16	12	28	11.3%	5.3mm	22%

Using the assumption that the mean area occupied by a particle of arbitrary shape is proportional to the square of the mean diameter of that size fraction, the mean grain size of the moved particles can be computed to be 3.9 mm. This is substantially less than the mean grain size of the bed material in general. In order to check computation of area size fractions, the total number of disturbed particles in the bed were counted and compared with the total disturbed area. For this case, the area observed measured 520 square cm and 548 particles were disturbed by the wave passage. For a mean diameter of 3.9 mm the disturbed area is 548 x $(.39)^2$ or 84 cm. This yields an estimate for the disturbed area of 16 percent. The disturbed area calculated from the image processed frame was 14.9 percent. The closeness of these two values supports the idea that the mean diameter of the moved material is less than that of the bed as a whole.

It is noted that in Table 4.5, the count of the number of particles removed from their original location was not substantially different than the number deposited. This was taken as confirmation that the movement percentages shown herein are approximately twice the actual amount of particles moved.

Using the calculated percentage of area disturbed and a visual count of the number of particles moved, the mean diameter of the moved particles was estimated once for each wave case. Figure 4.75 shows the variation of calculated mean grain size of the removed particles with normalized shear. Here, τ_{cr} again refers to the critical shear for a particle of mean diameter = 4.76 mm from the Shields curve as presented by Vanoni (1964). It is evident that as the shear stress decreases the mean size of the particles moved also decreases. The decrease is seen to be less marked at normalized shear values less than 1.0 and is limited by the minimum size of particles available for movement.

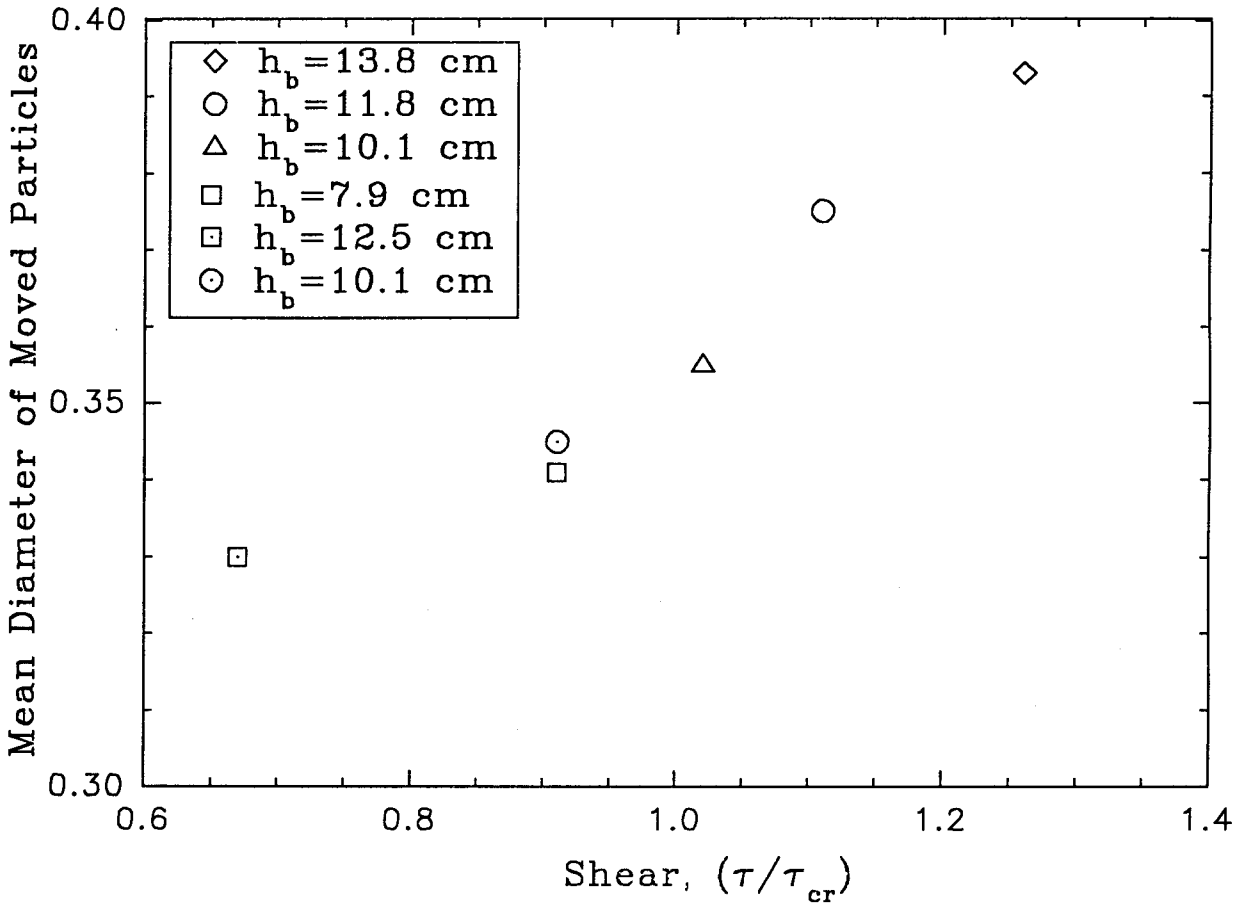

FIG. 4.75. Variation of Moved Particle Diameter with Shear.

Figure 4.76(a) shows the turbulent shear values calculated in this study plotted with the Shields curve (Vanoni (1964)) for comparison. The solid symbols show the position of the dimensionless shear values when calculated with the mean bed particle diameter of 4.8 mm and a specific gravity of 2.49. The hollow symbols use the estimated mean diameter of the moved particles to calculate the shear and bed Reynolds numbers. For both groups of data, the probability of movement (calculated at one half the observed

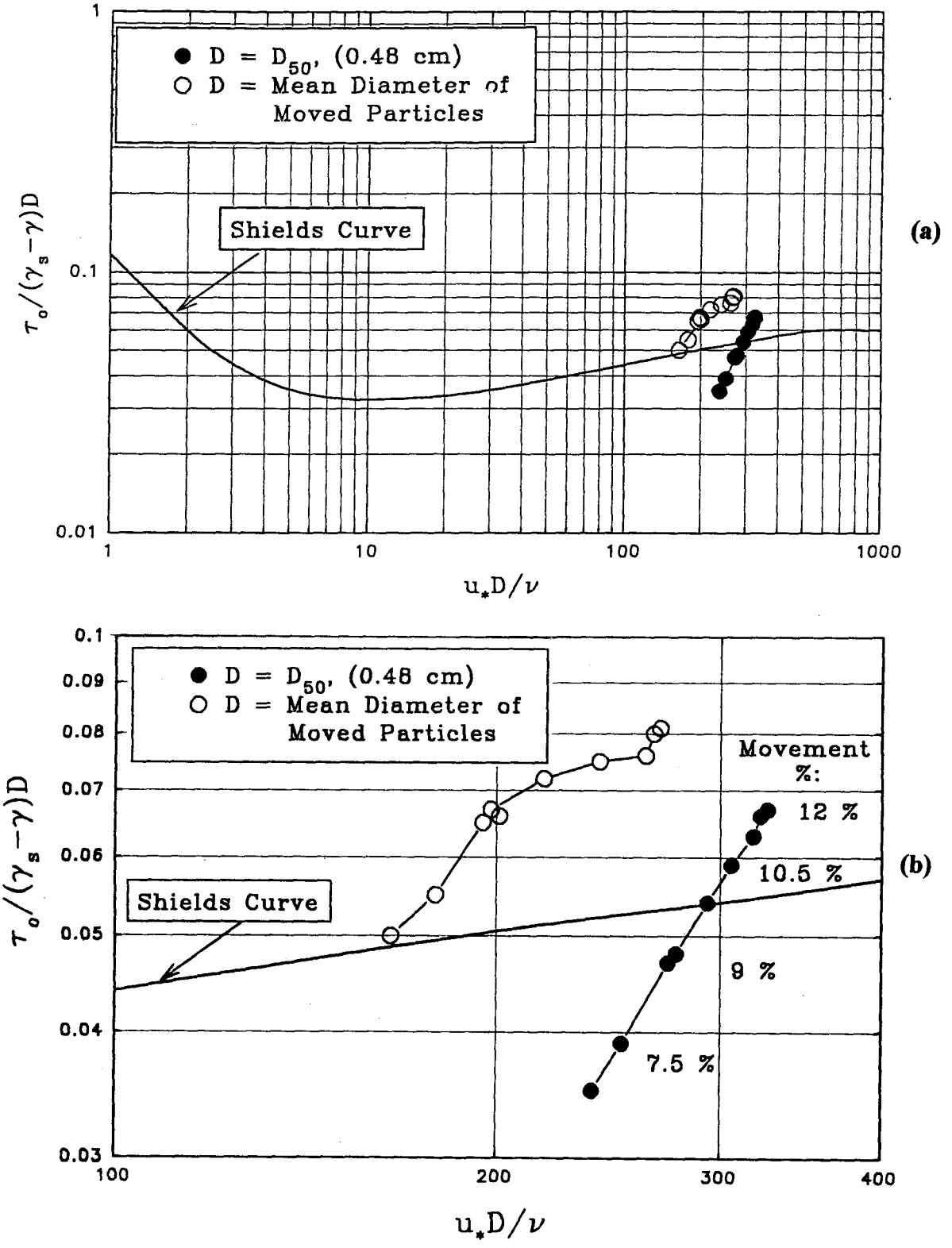

FIG. 4.76. Shields Curve Comparison.

motion) is 12 percent by number for the data point with the highest shear value and 7 percent for the lowest one, as shown in Figure 4.76(b). Since the Shields curve is based on experiments with particles of uniform diameter, the values adjusted for mean diameter are perhaps a better basis for comparison. It should be noted that the effect of the mean momentum tranfer term $\overline{uv}$ has not been included in the calculation of the shear on particles in Figure 4.76.

4.3.2 Sideview Observations

Recordings of particle movement through the sidewall of the tank were made for each wave at one or more locations. The comparison between two successive frames of the video recorder, taken about 1/30 of a second apart, permits an analysis of the particle movement under the wave as it passes over the bed. Figures 4.77 and 4.78 show a typical progression for a breaking wave with depth at breaking, h_b = 11.8 cm across the observation location centered at x/L = 0.29. The data shown are the average of three successive runs with the same wave over an unpacked bed.

In Figure 4.77 the image of the wave at each successive location has been compared to the bed before the passage of the wave. The frame comparisons show a series of snapshots in time of the cumulative particle movement during the wave passage. The location in the test section of the leading edge of the wave crest is marked with an arrow in each successive frame. The initiation of motion in the particles starts well ahead of the crest of the wave. The distance from the wave crest to the start of particle motion remains fairly uniform as the wave progresses over the bed. From the very small values at the start of motion, the percent of the total bed area disturbed increases gradually and

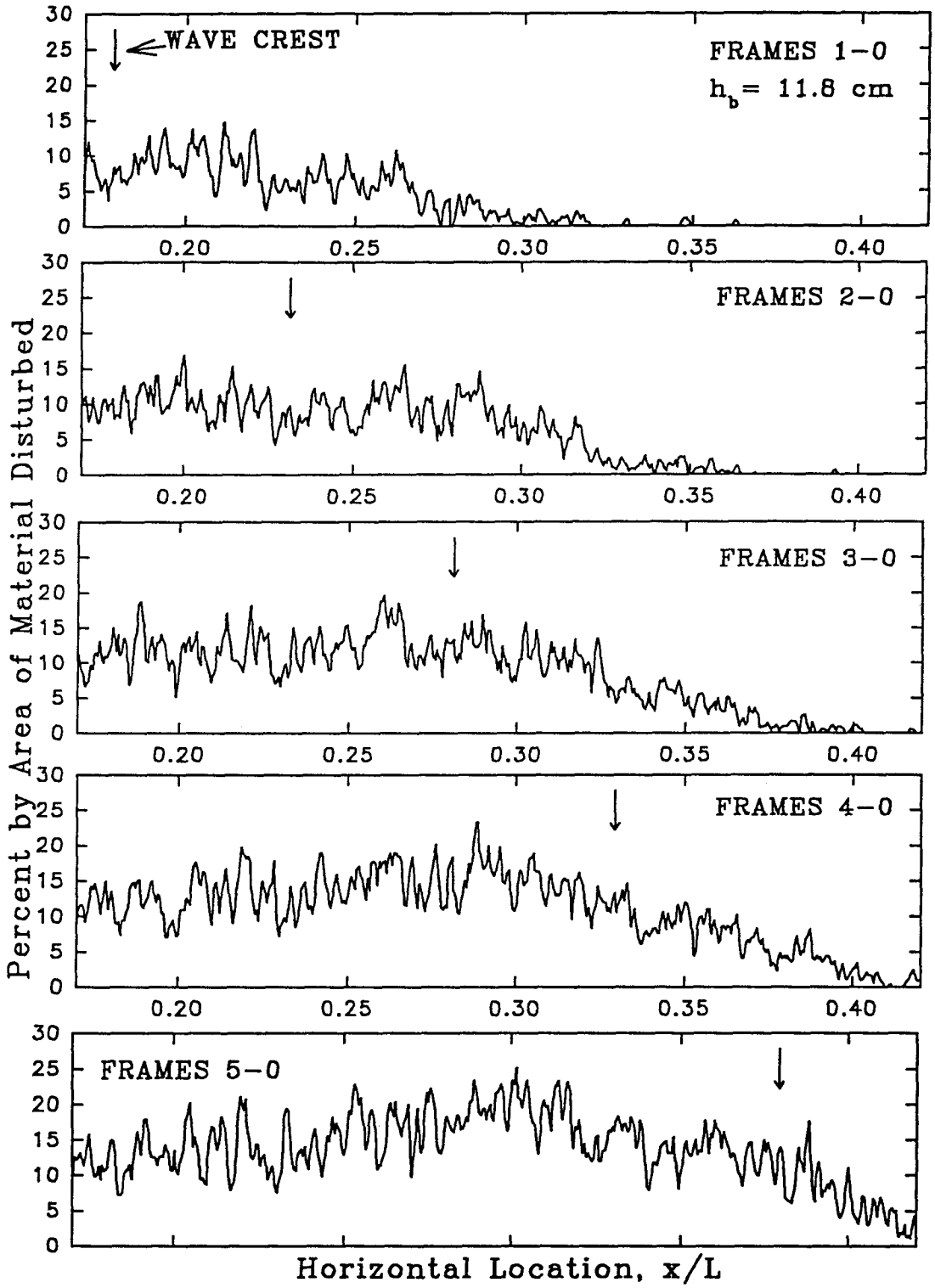

FIG. 4.77. Sideview of Cumulative Movement under Breaking Wave, h_b = 11.8 cm, x/L = 0.29.

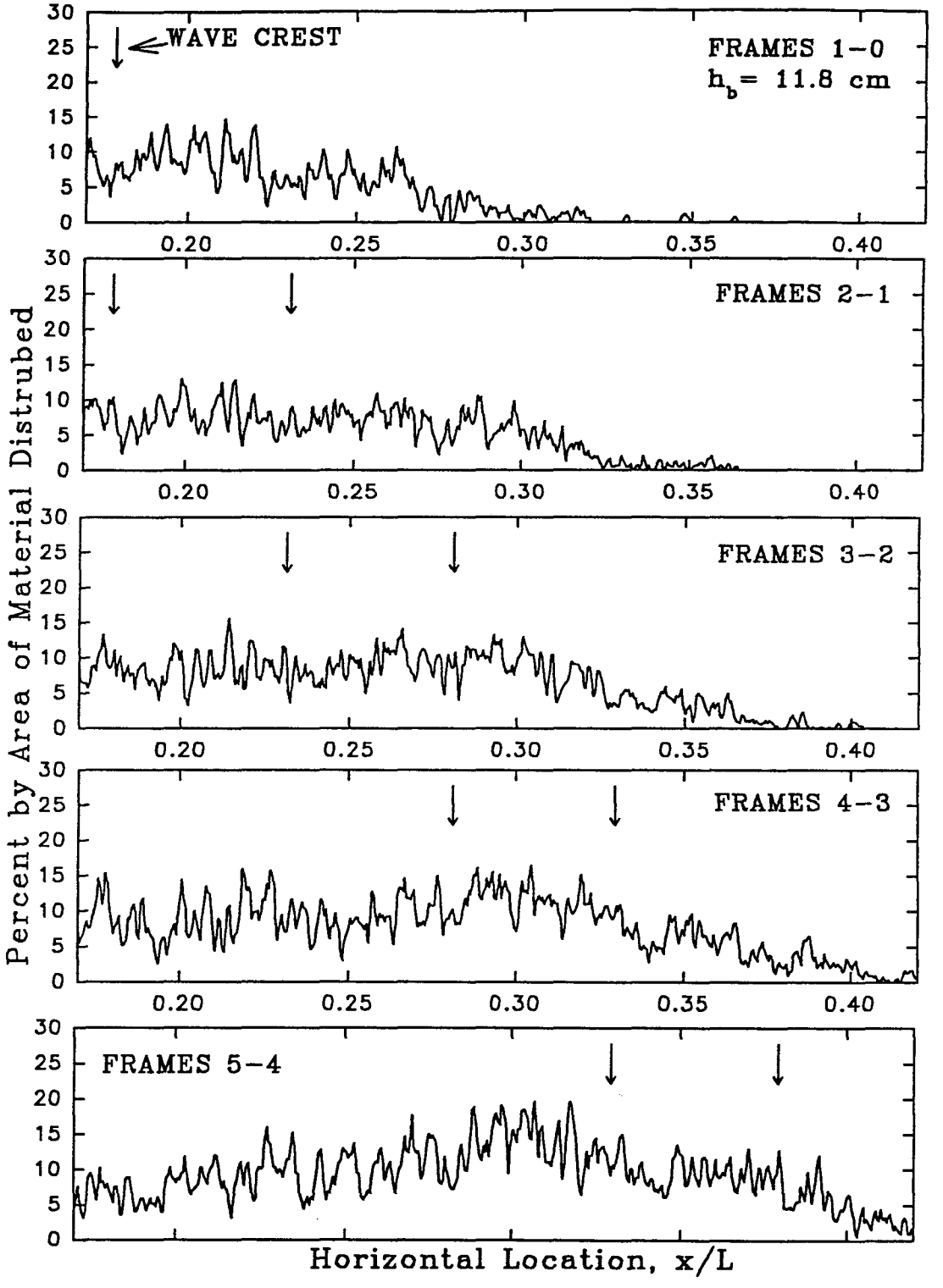

FIG. 4.78. Sideview of Incremental Movement under Breaking Wave, h_b =11.8 cm, x/L = 0.29.

reaches a maximum after the wave crest passes. In the final frame for locations less than x/L = 0.23, the particle motion appears to have reached a steady value. One explanation for the maximum seen in the particle motion behind the wave crest is that at that point particles which have been set into motion have not yet come to rest in their final locations. Alternately, since the fall velocity for 5 mm material is quite high (50 cm/sec at 20° C), particle motion may continue to occur because inertial forces from turbulent accelerations continue to be high well after the passage of the wave crest.

Figure 4.78 shows an incremental view of the motion under the wave. Each frame has been compared to the frame immediately preceding it on the video tape. The location where particle motion begins is similar to that for the cumulative case and remains at a constant distance from the wave crest. If the area under the curve is taken as a gross measure of the amount of movement at any given time, then the greatest amount of

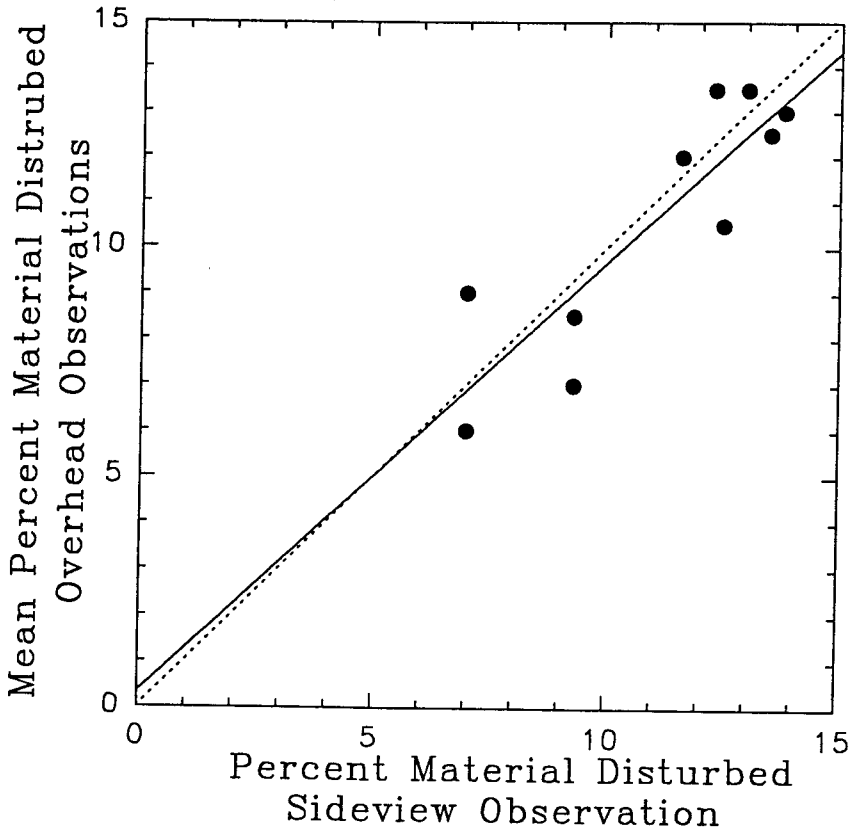

FIG. 4.79. Comparison of Overhead and Sideview Movement Values.

movement occurs in the time the wave crest travels between locations x/L =0.33 and 0.38. This supports the conclusion form Figure 4.77 that a substantial amount of motion is still occurring even after the passage of the wave crest.

In order to compare the total movement seen under the wave in a sideview and in the overhead view, the final value of percent area disturbed for the overhead and sideview observations were compared graphically in Figure 4.79. The data points cover a range of different wave cases and locations. The dotted line on the figure is the line of exact one to one correspondence of the readings. The solid is the line obtained using a least squares fit to a first order polynomial. The two data sets appear to have a very close correspondence. Since no LDV measurements were taken in the region of the sideview observations, it is not possible to tell whether the flow near the sides of the tank is substantially different from that at the center. Small differences in the flow would account for a disparity between overhead and sideview observations.

The mechanics of particle movement under two passing wavesare presented for two incremental sideview records in Figures 4.80 and 4.81. These records were made for the same waves in the same observation location, x/L = 0.29, for which instantaneous velocities and accelerations were shown in Figure 4.61. By comparing the velocity and acceleration time histories in Figure 4.61 with the observed particle movement under the wave, it is possible to deduce several characteristics of the particle motion.

Since the LDV measurements and the particle movement records are taken for different experimental runs and in different locations, the instantaneous values of the velocities and accelerations can not be compared directly to the observed particle movement. It is evident in figures 4.80 and 4.81 that the particle motion under the wave is not a steady process, but rather is characterized by bursts of movement. These bursts appear as spikes in the incremental movement records, and can often be tracked as they

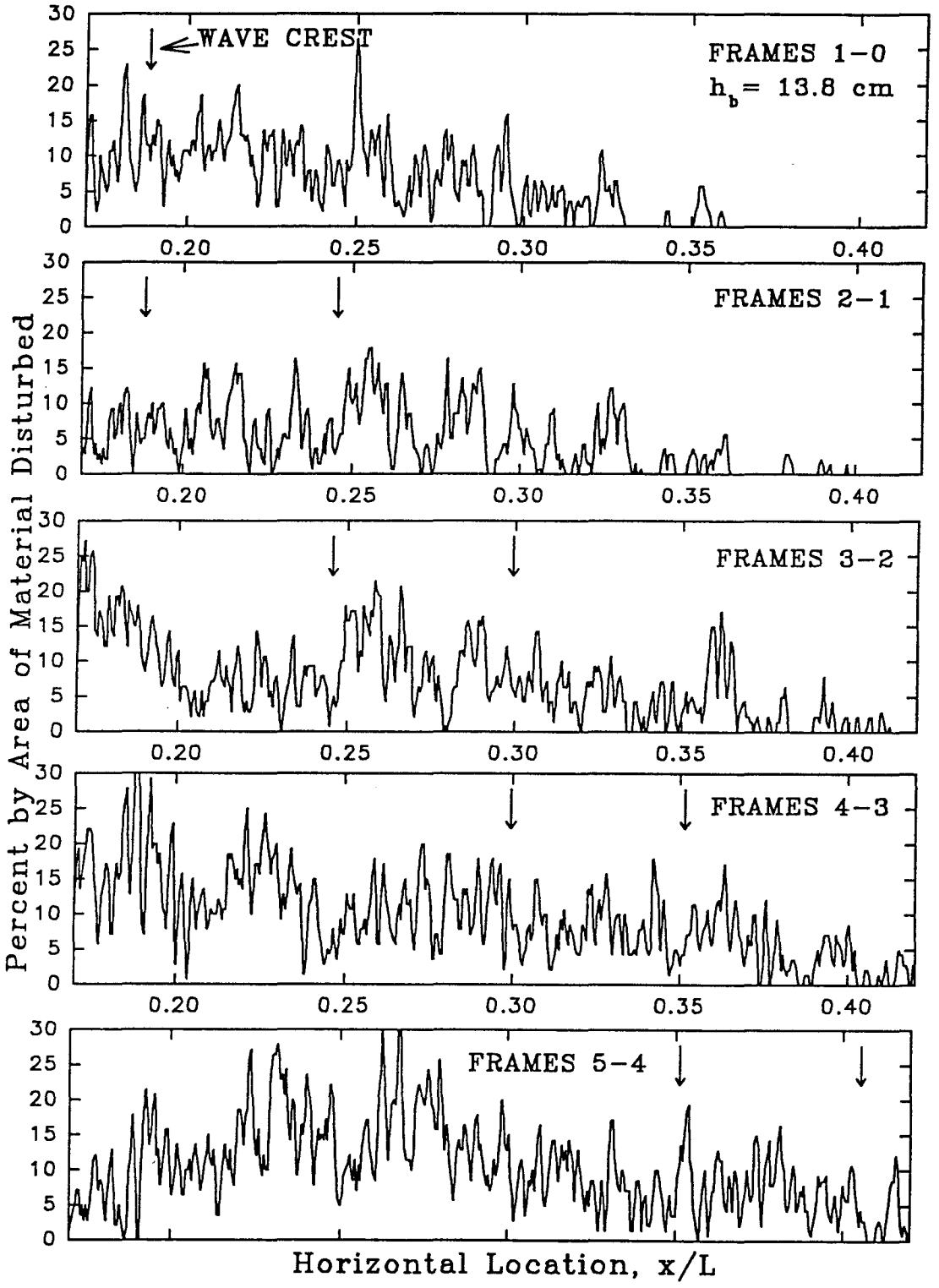

FIG. 4.80. Sideview of Incremental Movement under Breaking Wave, h_b =13.8 cm, x/L = 0.29.

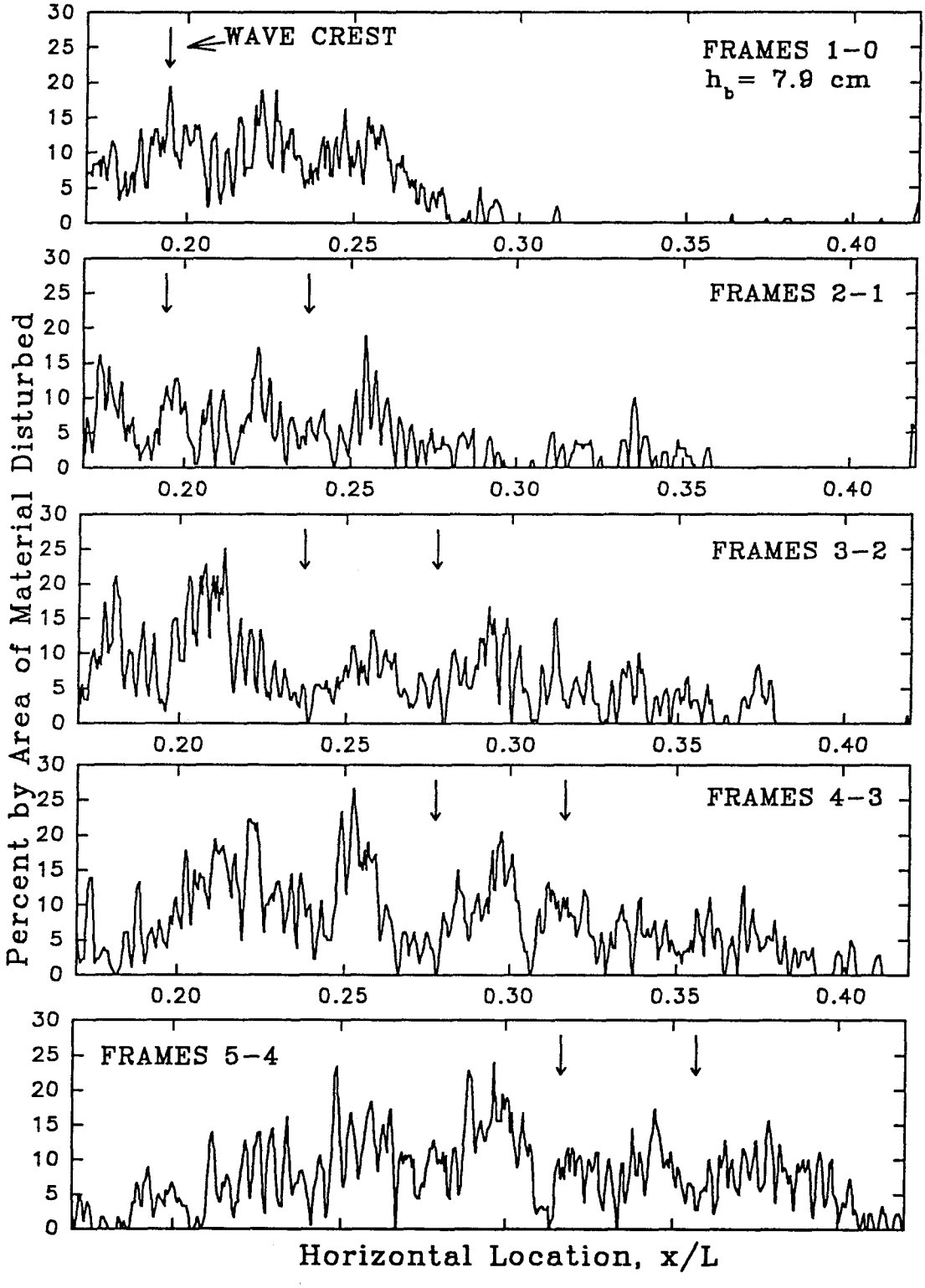

FIG. 4.81. Sideview of Incremental Movement under Breaking Wave, h_b =7.9 cm, x/L = 0.29.

pass across the bed. In Figure 4.80, for example, the peak in movement occurring at distance of approximately x/L = 0.3 behind the wave crest in frame 3-2 is visible at the same location in the frames 4-3 and 5-4. It is also evident when comparing Figures 4.80 and 4.81 that the amount and the physical extent of the motion under the large breaking wave is always greater than for the smaller one.

LDV measurements were taken at the location x/L = 0.29 for this video observation location. Figure 4.61 can be used to synchronize the velocities and accelerations in the passing wave with the observed particle movement. The normalized time periods for each incremental frame comparison are as follows:

Table 4.6. Time Intervals for Incremental Particle Movement in Figures 4.79 and 4.80.

	$t\sqrt{g/h}$				
h_b	Frame 0-1	Frame 2-1	Frame 3-2	Frame 4-3	Frame 5-4
7.9 cm	< -0.78	-0.78 to -0.41	-0.41 to -0.04	-0.04 to 0.33	0.33 to 0.71
13.8 cm	< -0.53	-0.53 to -0.25	-0.25 to 0.03	0.03 to 0.31	0.31 to 0.59

For example, in Figure 4.79, the material motion observed in frame 2-1 shows the amount of movement that has occurred under the wave for a time period $-0.53 < t\sqrt{g/h} < -0.25$.

In Figure 4.80, for frame 1-0 the particle motion begins at about x/L =0.29. The mean velocity in the wave at this time is approximately 45 cm/s. At the same distance away from the wave crest in Figure 4.81, the particle motion is already well established and the mean velocity from the velocity record is almost 60 cm/s. If the particle motion is assumed to vary slowly with longitudinal location in the tank, the point where motion is just starting, x/L = 0.33 for the wave in Figure 4.81, occurs at 48 cm/s. This implies that, in the absence of any large accelerations, the particle motion first starts when a mean velocity of about 45 cm/s is reached. Both waves do, however, show the onset of

turbulence at a distance well ahead of the wave crest and consequently particle motion seems possible ahead of the 45 cm/s mean velocity.

Figure 4.81 does indeed show a peak at x/L = 0.29 which is not connected with any subsequent general motion. In the acceleration time histories shown for Figure 4.61 (b), high accelerations occur between $t\sqrt{g/h}$ = -1.5 and -0.5. As shown by the elementary analysis in Section 4.2.6, such accelerations could cause particles to move out of place even without the existence of a very large mean velocity, if their duration is sufficient. The fact that the averaged incremental sideviews in Figure 4.78 do not show the same type of detached peaks at the leading edge of the wave supports the allegation that this type movement is the result of the turbulent accelerations or inertial force. The burst patterns of the particle motion and the continuation of motion well after passage of the wave crest also support this assertion.

It appears that both inertial and drag forces contribute to the motion of particles under waves, but are of different relative importance at different times during the passage of the wave. The influence of the inertial force is seen at the leading edge and after passage of the wave crest, while the drag force accounts for general particle motion under the crest region. As breaking wave height decreases, maximum velocities also decrease and inertial forces due to accelerations become more important for material movement.

4.4 DISCUSSION AND APPLICATION OF RESULTS

The results obtained in this study have important implications both for the design of large scale rock armor and also for the understanding of the mechanics of flow and turbulence around roughness elements in time varying flows. These implications will be

discussed by means of an example calculation for a revetment, given a particular design wave.

Consider the design of rock armor to be placed on the sloping sea bed to cover a submerged pipeline running offshore. For the purposes of this analysis let the design wave height be 6 m (18 ft) and the bottom slope be the 1 on 50 value used for the experiments in this study. The specific gravity of the rock is assumed to be 2.65. For a design wave of 6 m, the wave height with a one percent probability of occurrence is:

$$H_{1\%} = 1.67\ H = 10\ \text{m}.$$

The calculations below will be made assuming the 10 m wave height. The ratio of wave height to depth at breaking is commonly assumed to be 0.78, although for the plunging waves used in this study this ratio was closer to 1.00. For this analysis, let $(H/h)_b = 0.8$, then:

$$h_b = 12.5\ \text{m}.$$

At breaking, the maximum Froude number, $\frac{u_{max}}{\sqrt{gh}}$, which occurred at the time of wave crest passage, was approximately 0.7 in all the breaking wave experiments. Hence the assumed maximum velocity away from the bottom boundary for the 10 m design wave is:

$$u = 0.7\sqrt{9.8(12.5)} = 7.75\ \text{m/s}$$

The equivalent diameter and weight of the revetment material have been determined using four principal methods of calculation. Calculations are made using the bed shear stress, the net moment on the particle, observations of particle movement obtained by the experiments in this study, and finally the guideline from the U.S. Army

Corps of Engineers Shore Protection Manual (1977). Summaries of the calculation methods appear below.

Revetment Size Using Critical Shear:

Based on the Shields curve as presented by Vanoni (1964), general material movement begins at a Shields parameter $\theta = \frac{\tau_o}{(\gamma_s - \gamma)gd_s} = \frac{u_*^2 \rho}{(\gamma_s - \gamma)gd_s}$ with a value of 0.06 for material with a diameter greater than 7 mm. Vanoni observed negligible movement at values near $\frac{\theta_{cr}}{2}$ for 0.1 mm sand and 0 .037 mm glass beads. Accordingly the equivalent diameter of the rock armor in this analysis is based on $\theta_{cr} = 0.03$. The bed shear stress, $\tau_{o,}$ used for calculations with the Shields parameter is determined by three methods: using the law of the wall, the velocity defect law and experimental observations.

It is noted that since the wave velocities imposed upon the bed do not satisfy the normal flow assumptions of the steady flow case, an adjustment should be made to the critical shear to account for the slope of the bottom. By balancing the shear and gravitational forces along an upward slope of angle α, it can be derived that the relation between the effective shear stress on a particle and the Shields critical shear stress for that particle size is:

$$\frac{\tau_{slope\ cr}}{\tau_{cr}} = \cos\alpha + \frac{\sin\alpha}{\tan\theta}$$

For large slopes the shear stress and, consequently, the particle diameter should be adjusted accordingly. At the design problem slope, the relation yields

$\tau_{slope\ cr} = 1.03\ \tau_{cr}$.

Law of the Wall:

Using the law of the wall, equation 4.2a, $u = 8.5\, u_*$ at $z = k_s$. For the experiments in this study, at an elevation 4.76 mm (k_s) above the top of the bed, the maximum velocity at the time of wave crest passage was not significantly affected by the boundary and hence the velocity, u, was of magnitude $0.7\sqrt{gh}$ as described above. For the design problem this gives:

$$u_* = \frac{7.75\ \text{m/s}}{8.5} = 0.91\ \text{m/s}.$$

Velocity Defect Law:

In the breaking wave experiments in this study (see figures 4.27 - 4.35), at the time of wave crest passage, all of the observed mean horizontal velocities begin to show the influence of the bottom boundary at a similar elevation of z/h =0.1. For the waves at breaking, this yields a velocity defect law in the form:

$$\frac{u}{\sqrt{gh}} = \frac{2.3u_*}{k\sqrt{gh}} \log_{10}\left(\frac{z}{h}\right) + \frac{2.3u_*}{k\sqrt{gh}} + 0.7 \qquad (4.10)$$

where $\frac{2.3u_*}{k\sqrt{gh}}$ is the inverse of the slope of the velocity profile approaching the bottom on a semi-log plot. For the experiments in this study, this slope maintained an average value of $\frac{1}{2.1}$. The shear velocity at the time of wave crest passage is then

$$u_* = \frac{k\sqrt{gh}}{(2.1)(2.3)} = 0.083\sqrt{gh}.$$

The von Karman constant is assumed to be 0.4. For the design breaking depth of 12.5 m, this gives:

$$u_* = 0.083\sqrt{9.8(12.5)} = 0.92 \text{ m/s.}$$

It should be noted that the law of the wall and the velocity defect law give quite similar results in this case since they both rely on the velocity at a similar elevation.

Turbulent Shear Determined by Experiments:

It is recalled that in Figure 4.50 the shear stress calculated from the turbulent velocities near the bed is normalized by the Shields critical shear stress for a particle of diameter 4.76 mm and compared with the ratio of breaking depth to mean particle diameter (also 4.76 mm). If the data are extended with a straight line fit to the value $\tau_0/\tau_{cr} = 0.5$ this corresponds to the criterion $\theta = \theta_{cr}/2$ that is assumed for negligible rock motion. At $\tau_o/\tau_{cr} = 0.5$, Figure 4.50 shows:

$$\frac{h_b}{D_{50}} = 7$$

which yields directly that $D_{50} = 178$ cm. This includes the correction for slope effects.

It should be observed that while Vanoni (1964) found the bed was in general motion (50 percent movement) under steady flow conditions; for the wave experiments, as shown in Figure 4.76 at $\theta = \theta_{cr}$, the amount of motion observed in the bed was only seven to ten percent. The smaller amount of movement occurring under the waves may be attributed to the short duration of the maximum velocity. For the design conditions under waves, the $\theta = 1/2\theta_{cr}$ criterion may be too severe and result in the oversizing of the material.

Revetment Size using Net Moment on Armor Unit:

From Figure 4.60 it is seen that the maximum horizontal velocity very close to the particle occurs at a value of $\frac{u}{\sqrt{gh}} = 0.5$. Accordingly, the velocity close to the design rock is assumed to be:

$$u = 0.5\sqrt{9.8(12.5)} = 5.53 \text{ m/s.}$$

The moment balance is calculated both with and without the consideration of inertial forces.

Moment Calculations Neglecting Inertial Forces:

Neglecting the effects of accelerations, the net moment calculated on the particle is the result of the balance of the moment due to submerged weight with the moment due to lift and drag forces on the particle. Since these forces vary over time periods on the order of seconds, they are assumed in this calculation to exist long enough to dislodge a particle from its initial position on the bed.

Using the equations and coefficients shown in section 4.2.7:

$$\text{Drag Force, } F_x = \frac{\rho}{2} C_D u^2 \frac{\pi}{4} D^2 = \frac{1 g/cm^3}{2}(0.4)(553 cm/s)^2 \frac{\pi}{4} D^2 = 48036\, D^2$$

$$\text{Lift Force, } F_y = \frac{\rho}{2} C_L u^2 \frac{\pi}{4} D^2 = \frac{1 g/cm^3}{2}(0.15)(553 cm/s)^2 \frac{\pi}{4} D^2 = 18013\, D^2$$

$$\text{Weight, } W = \frac{(\rho_s - \rho) g \pi}{6} D^3 = \frac{1.65(981)\pi}{6} D^3 = 847\, D^3$$

The moment balance then yields the relation:

$$F_x \cos\varphi + F_y \sin\varphi = W \sin\varphi, \quad \varphi = 30^\circ + \tan^{-1}\left(\frac{1}{50}\right)$$

from which D can be solved for directly.

Moment Calculations Including Inertial Forces:

In order to include inertial effects in the problem attention must be given to the time scale used in the Froude analogy. In the experiments, accelerations in excess of 2g were observed to last for a typical time interval of 0.024 seconds at a depth h_b of 13.8 cm. In a Froude model the ratios are as follows:

$$\text{Froude No.} = \frac{v}{\sqrt{gh}}, \quad v_r = \sqrt{g_r h_r} = \sqrt{L_r}, \quad T_r = \frac{v_r}{L_r} = \sqrt{L_r}, \quad a_r = \frac{v_r}{T_r} = 1$$

where T_r and a_r are the time and acceleration ratios respectively. In the experiments at h_b = 13.8 cm, the flow Reynolds number was 1.1×10^5 while in the design problem it is more than two orders of magnitude larger at Re = 6.9×10^7. It is assumed that viscous effects are negligible in both cases so that the Froude analogy does hold. In the design problem, accelerations can then be expected to reach the value of 2g for a time period of

$$t = 0.024\sqrt{\frac{1250\text{cm}}{13.8\text{cm}}} = 0.23\,\text{s}.$$

The rock size D must then be determined using calculated forces based on u=5.33 m/s and du/dt = 2g (see equations 4.7 and 4.8) by means of the rotation time obtained in equation 4.9. This calculation gives the maximum size of material which could be moved out of its resting position by the applied forces in a time of 0.23 seconds, the duration of the forces. The initial contact angle φ_o is assumed to be $30^\circ + \tan^{-1}\left(\frac{1}{50}\right)$ in order to include the beach slope.

Referring to Appendix D, it is also possible to obtain a first order approximation for rotation time by using the equation

$$t = \sqrt{\frac{2r\varphi_o}{r\ddot{\varphi}}} = \sqrt{\frac{2\varphi_o I}{M_H - M_R}}$$

where M_H and M_R are calculated by equation 4.5 and 4.6. The first order method is referred to as Method I and the rock diameter D can be solved for directly. In the exact solution, Method II, D must be solved for by iteration.

Revetment Size using Experimental Data:

In Figure 4.73, the curve of the data may be extrapolated with a third order polynomial to the region of zero movement, yielding a depth at breaking of 3.5 cm for the material of size 4.76 mm. Although this is a large extrapolation, it is supported by the experiments with solitary waves propagating over a horizontal bed. The wave height in these experiments was 4.7 cm which would correspond to a breaking depth of 5.85 cm using the $(H/h)_b = 0.8$ criterion. Only small amounts of movement were observed for this wave supporting the idea that initiation of motion may occur near the 3.5 cm breaking depth for the 4.76 mm material used in this study. Using h_b= 3.5 cm the stable size of revetment material for the design problem is:

$$\frac{12.5\text{ m}}{.035\text{ m}}(.476\text{ cm}) = 170\text{ cm}.$$

This value is specific to the 1 on 50 slope of the experiments.

Revetment Size using U.S. Army Corps of Engineers Shore Protection Manual (1977):

Since the Shore Protection Manual (1977) equation for sizing rock revetments under wave action (equation 7-110) is designed for slopes greater than one on five, the equation for stability of channel bed revetments (equation 7-119) was used instead:

$$W = \frac{V^6 w_r w_w^3}{y(w_r - w_w)^3(\cos\theta - \sin\theta)^3}, \quad \text{where } y = \begin{cases} 15.23 \times 10^5 & \text{for embedded stone} \\ 2.06 \times 10^5 & \text{for nonembedded stone} \end{cases} \tag{4.11}$$

Here V is the velocity acting directly on the stone (ft/sec), w_r is the unit weight of the stone (pcf), w_w is the unit weight of water (pcf) and θ is the slope angle. The value of V was taken to be same as for the moment calculations with V = 5.53 m/s = 18.2 ft/s.

Table 4.7. Calculation of Stable Rock Armor Size for Design Wave.

Method of Calculation	Equivalent Rock Diameter (cm)	Weight (kg)
Critical Shear Stress		
Law of the Wall	167.3	6492
Velocity Defect Law	171.1	6945
Experiments	178.6	7899
Moment Balance		
No inertial Forces	115	2114
With Inertial Forces, Method I	25.8	24
With Inertial Forces, Method II	125	2711
Experimental Observations of Movement	170	6812
Shore Protection Manual		
Embedded Material	68 (2.25 ft)	447 (986 lbs)
Non-embedded Material	131 (4.3 ft)	3308 (7293 lbs.)

The results of particle size calculations by the above methods are summarized in Table 4.7. The critical shear stress calculations all fall approximately in the same range predicting a rock size of between 1.67 and 1.79 m with a weight between 3 and 4 metric tons. Compared to the non-embedded material estimate of the Shore Protection Manual (1977), the estimated rock size is twice as heavy. As mentioned above, the observed amount of material motion under waves was less at a given shear stress than for the equivalent steady flow case. In order to account for the reduced amount of motion under waves, it is suggested that the Shields criterion be adjusted so that $\theta = 2/3(\theta_{cr})$ for zero material motion under waves. This would result for the above calculation in a rock size of approximately 1.3 m.

It is of interest to note that the additional mean momentum transport due to convective accelerations (see section 4.2.5) does not appear to result in a significantly larger amount of material motion. Apparently, the reduction in the amount of material motion because of the transient nature of the flow has a much larger effect than the mean momentum transport caused by vertical velocities in the waves.

When calculating a particle diameter using a moment balance at the level of the particle, it is evident that the inclusion of inertial forces may indeed be an important factor. From drag and lift considerations alone, the calculated diameter for the revetment material is lower than when inertial forces are included with Method II, resulting in a 9 percent difference in diameter and a 500 kg difference in weight. The actual design rock size should be somewhat larger since the condition could occur under a wave where a large acceleration pulse occurs at the same time as a slower rise in mean velocity. This would imply that the particle would not have to be rotated fully out of its initial position by the acceleration pulse but only rotated partially: to the angle where the smaller mean velocity level would result in a sustained net positive moment on the particle. The low value of

.26 m calculated by Method I indicates that over a time of 0.23 seconds (distance of travel of center of mass = 0.26 m) the net moment on the particle changes sufficiently that a first order approximation is inadequate.

It is noted that the experimental observations of particle motion in this study require a large amount of extrapolation in order to predict the initiation of motion of a particle. Hence, while the experiments return a particle size estimate of the right order of magnitude they are not very precise. Since the objective of this study was to study flow quantities during actual particle movement and probability of particle motion under varying breaking wave conditions, it was necessary to perform experiments away from the point of initiation of motion. At low levels of movement the defining of a probability of motion would require a prohibitive number of identical experimental runs, and point measurements of flow quantities would not necessarily show the conditions necessary for particle motion.

Experimental data such as appear in Figure 4.72 do have some application to the design of rock revetments if, instead of using a criterion of zero movement, it is desired to predict the location and amount of damage which would be caused by different height storm waves in a cost benefit type analysis. By appropriately scaling the problem with the wave depth at breaking, rock diameters resulting in net particle movement in the range of 7 to 12 percent can be computed at different locations with respect to breaking. For a given rock diameter the crossshore revetment cross section may then be divided into regions of damage less than 7 percent, between 7 and 12 percent and greater than 12 percent. It is again noted that the experimental data is slope specific and would overpredict the amount of movement on slopes significantly steeper than 1 to 50.

The recommended revetment size from this analysis is in the range of 1.25 to 1.3 m which corresponds to about 1.5 metric tons. Based on experimental observations this

material size could be gradually reduced in the onshore direction. It should be noted that this estimate is in concurrence with the estimate of the Shore Protection Manual (1977) for non-embedded material. The estimate of a revetment size essentially in line with the Army Corps of Engineers method may not be surprising in that such methods are based on large amounts of empirical data and experience. The objective of this study, however, was not only to confirm and refine the prediction techniques for revetment size, but also to gain a physical understanding of the processes by which particles move under breaking waves.

The experiments in this study were designed to examine the relation between wave forces and particle movement by measuring flow quantities both in the region away from the influence of individual roughness elements and in the region immediately adjacent to the particles. Away from individual particle influence, the time averaged Navier-Stokes equations are applicable and so it is possible to measure quantities such as mean velocity, turbulent velocity and turbulent shear and relate them to particle motion. In the immediate region next to the particles, individual velocity fluctuations caused by the flow around particles and vortex shedding from particles make the concept of a time averaged turbulent shear inapplicable. Near the particles, movement must be considered in terms of the net instantaneous moment on the particle and the magnitude and duration of individual turbulent fluctuations.

When predicting particle movement from shear velocity or bed shear stress, a graphical relation such as the Shields curve, Figure 4.76 or Figure 4.74, determined by experiment is necessary to relate what is occurring at some distance away from the particles to the anticipated amount of movement. It appears that for waves, the Shields curve, which is based on steady flows overestimates the amount of particle motion occurring at a given shear stress and, as discussed above, should be modified when used with waves.

When predicting particle movement from the flow around individual roughness elements, the parameters which must be established in addition to those concerning particle shape; are the drag, lift and inertia coefficients, (C_D, C_L, and C_M), as well as the probability of occurrence and duration of individual velocity fluctuations. The coefficients in the force equations have been estimated experimentally (see Appendix A). The particle movement model presented in this study makes a great many simplifying assumptions. While it does not predict the actual amount of particles moved or their probability of motion, it does at least confirm that particles will indeed move under the flows conditions measured during actual particle movement.

CHAPTER 5

CONCLUSIONS

The conclusions presented below are divided into categories corresponding to the three main areas investigated in this study.

5.1. MEAN VELOCITY MEASUREMENTS

1. In these experiments, no appreciable change in wave height or shape was discernible between a wave passing over the flat plate and the same wave over the rock bed. The distance of passage over the rock was short enough that the wave amplitude was not affected by the changed roughness of the bottom boundary.

2. In all the observed wave cases, the mean velocities over the flat plate and the rock bed agreed well for relative elevations greater than $z/h = 0.1$. At relative elevations less than $z/h = 0.1$, however, the presence of the rock had a significant effect on the mean velocities. The presence of the rock reduced the magnitude of the mean horizontal velocities close to the bed especially after the passage of the wave crest. Vertical velocities were much more pronounced near the bed for the rock than for the flat plate.

3. The effect of changing the water depth at breaking in order to decrease the length scale of the wave with respect to the rock had an observable effect on the shape of the breaking waves and on the relative height $(H/h)_b$ of the wave at breaking. For smaller breaking depths and, consequently, relatively longer distances of travel over the sloping bottom, the waves had a smaller relative height at breaking and a more pronounced "shelf"

region trailing the wave crest. These differences in water surface elevation appear to be similar to those observed for the mean velocities.

4. The observed mean velocities in a solitary wave propagating over a horizontal bed agreed well with existing second and third order wave theories at elevations away from the influence of the bottom boundary.

5. The thickness of the bottom boundary layer over the rock bed was observed to increase with the distance traveled along the bed. The boundary layer thickness was greater and increased more in the same distance for waves with smaller breaking depths than for those with larger breaking depths. The rate of growth of the boundary layer varied inversely with the depth, h_b.

6. The mean velocity profiles over the rock bed show evidence of an inner boundary layer where the shapes of individual particles appear to have a large influence on the water particle velocities. In this inner layer, the mean velocities do not decrease uniformly approaching the rock bed but fluctuate, exhibiting large variations for small differences in elevation. The r.m.s. u' and v' profiles and the r.m.s. acceleration profiles also show similar fluctuations in the inner layer.

7. As in the case of the total boundary layer thickness, the thickness of the inner layer increases with the distance along the bed and grows more rapidly with decreasing depth at breaking, h_b.

8. The solitary waves generated in this study vary too quickly to allow time for the velocity profile to develop a quasi-steady boundary layer. The change with depth of the velocity appears to still increase after the passage of the wave crest and reaches a maximum at a later time (near $t\sqrt{g/h} = 1.0$ for the waves observed in this study).

5.2. FLUCTUATING VELOCITY MEASUREMENTS

1. The root mean square turbulent velocities, u' and v', increase approaching the bed for relative elevations less than z/h = 0.2 and appear to vary directly with the maximum mean velocity.

2. Periodicities in u' and v' are pronounced at elevations close to the bed, inside the inner layer. This appears to imply that as the wave propagates over the bed, vortices are shed from the individual rock pieces.

3. The turbulent shear stress, $\rho\overline{u'v'}$, reaches a maximum at the time of the maximum mean water particle velocity. This implies that, outside the inner layer, $\rho\overline{u'v'}$ is a good measure of the turbulent shear.

4. An order of magnitude analysis of terms in the Navier-Stokes equation shows that the value for the viscous shear is one percent that of the turbulent shear at the elevation just above the inner layer . Hence, the turbulent shear is a good measure of the total shear in this region of the flow.

5. The friction factors calculated from the maximum turbulent shear compare reasonably well with those obtained for sinusoidal flows in oscillating water tunnels.

6. Near the bottom boundary, the total vertical and horizontal accelerations are of same order of magnitude. The accelerations over the rock bed are much larger than those over the flat plate and attain peak values nearly three times the acceleration of gravity. Near the rock bed, the accelerations due to the variation of the mean velocity are less than three percent of the accelerations due to turbulent fluctuations.

7. For the waves used in this study, the convective accelerations associated with the mean velocities are of the same order of magnitude as the convective accelerations due to the fluctuating velocities and are not generally negligible. The convective accelerations decrease approaching the bottom boundary and appear to be at a minimum just above the inner layer. At elevations less than z/h = 0.1, the magnitudes of the maximum convective accelerations fluctuate and can attain values as large as the values away from the bottom boundary.

5.3 MOTION OF BED MATERIAL

1. This study shows that particle motion may be analyzed using image processed video records. The total amount of particle movement seen in sideview and overhead observations are well correlated. In addition, the sideviews allow observations of material movement during the passage of a wave.

2. Moment calculations and sideview observations imply that both drag and inertial forces are important factors in particle movement. Near the wave crest, the motion of particles is primarily due to drag. Particle motion before and after the wave crest may occur, however, if sufficient inertial forces, due to turbulent velocity fluctuations with time, are present. As the breaking wave height decreases, the maximum mean velocity under the crest also decreases and inertial forces become relatively more important for initiating particle motion.

3. The probability of occurrence and the duration of turbulent events are critical factors in determining whether or not a particle is set into motion. A particle may move if a small net positive moment is applied for a sustained amount of time (mean velocity components) or it may move under the action of a large net positive moment applied over a small time interval (turbulent velocity components). The inertial forces due

to acceleration were found in to reduce the time required for a 5 mm particle to rotate out of its initial position from 0.02 seconds to 0.01 seconds under two different observed conditions. Both drag and inertial forces are capable of initiating particle motion.

4. The amount of particle movement observed in the rock bed is significantly affected by local variations in bed composition. In general, for the experiments in this study, the number of particles removed was about the same as the number as those deposited in any given observation location.

5. The number of particles moved under a given wave reaches a maximum at and directly after breaking. At distances along the bed greater than five breaking depths from the breaking location, particle movement decreases. Particle motion is also less for waves approaching breaking than for those at or directly after breaking.

6. For wave heights where a small number of particles just begin to move, the number of particles moved increases rapidly with increasing breaking wave height. As the wave height at breaking continues to increase, the number of particles moved increases less rapidly than at the smaller breaking wave heights. This variation is also seen when comparing the number of particles moved with the normalized shear. For shear values less than τ_{cr}, the increase in number of particles moved with increasing shear is more rapid than for shear values greater than τ_{cr}.

7. The values for shear calculated in this study for unpacked well graded angular material are near those observed by Shields for uniform particles in a steady uniform flow. When the mean size of the moved particles is taken into account, the amount of particle movement observed in these experiments is consistent with the Shields critical shear criterion for initiation of general motion.

REFERENCES

Bayazit, M., 1976, Free Surface Flow in a Channel of Large Relative Roughness, *Journal of Hydraulic Research*, Vol. 14, No. 2, pp. 115-126.

Boussinesq, J., 1872, Theorie des Ondes et des Remoues qui se Propagent le Long d'un Canal Rectangulaire Horizontal, en Communiquant au Liquide Contenu dans ce Canal de Vitesses Sensiblement Pareilles de la Surface au Fond, *Journal de Mathematiques Pures et Appliquees*, 2nd series, Vol. 17, pp. 55-108.

Brownlie, W.R., 1981, A Re-examination of Nikuradse Roughness Data, *Journal of Hydraulics*, ASCE, Vol. 107, pp. 115-119.

Dean, R.G. and R.A. Dalrymple, 1991, *Water Wave Mechanics for Engineers and Scientists*, World Scientific, Singapore.

Deigaard, R., M. Bro Mikkelsen, J. Fredsoe, 1991, *Measurements of the Bed Shear Stress in a Surf Zone*, Progress Report 73, ISVA Technical University of Denmark, pp. 21-30.

Gartrell, G., Jr., 1978, *A Signal Processor for a Laser Doppler Velocimeter,* Technical Memo. 78-5, W.M. Keck Laboratory of Hydraulics and Water Resources, California Institute of Technology, Pasadena, California.

Gessler, Johannes, 1965, *The Beginning of Bedload Movement of Mixtures Investigated as Natural Armoring in Channels*, Report No. 69, Lab. of Hydraulic Research and Soil Mechanics, Swiss Federal Inst. of Technology, Zurich, translated by Edmund A. Prych, Translation T-5, W.M. Keck Laboratory of Hydraulics and Water Resources, California Institute of Technology, Pasadena, California.

Goring, D. and F. Raichlen, 1980, The Generation of Long Waves in the Laboratory, *Proceedings of the 18th Conference on Coastal Engineering*, pp. 763-783.

Grimshaw, R., 1971, The Solitary Wave in Water of Variable Depth, Part 2, *Journal of Fluid Mechanics*, Vol. 46, pp. 611-622.

Jensen, B.J., 1989, *Experimental Investigation of Turbulent Oscillatory Boundary Layers,* Series Paper 45, Institute of Hydrodynamics and Hydraulic Engineering (ISVA), Technical University of Denmark.

Jensen, B.L., B.M. Sumer, J. Fredsoe, 1989, Turbulent Oscillatory Boundary Layers at High Reynolds Numbers, *Journal of Fluid Mechanics*, Vol. 206, pp. 285-297.

Jonsson, I.G. and N.A. Carlsen, 1976, Experimental and Theoretical Investigations in an Oscillatory Turbulent Boundary Layer, *Journal of Hydraulic Res*earch, Vol. 14, No. 2, pp. 45-60.

Justesen, P., 1988, *Turbulent Wave Boundary Layers*, Series Paper 43, Inst. Hydrodynamics and Hydraulic Engineering (ISVA), Technical University of Denmark.

Kamphuis, J.W., 1974, Determination of Sand Roughness for Fixed Beds, *Journal of Hydraulic Res*earch, Vol. 12, No. 2, pp. 193-203.

Kamphuis, J.W., 1975, Friction Factors Under Oscillatory Waves, *Journal of Waterways and Harbors, Coastal Engineering Division*, ASCE, 101, 135-144.

Le Mehaute, B., 1976, *An Introduction to Hydrodynamics and Water Waves*, Springer.

Madsen, O. S. and Grant, W. D. (1975), The Threshold of Sediment Movement Under Oscillatory Waves: a Discussion, *Journal of Sedimentary Petrology*, Vol. 45, No. 1, pp. 360-361.

Nadaoka, K., S. Ueno, T. Igarashi, 1988, Sediment Suspension Due to Large Scale Eddies in the Surf Zone, *Proceedings of the 22nd International Coastal Engineering Conference*, Torremolinos, pp. 1646-1660.

Naheer, E., 1977, *Stability of Bottom Armouring under the Attack of Solitary Waves,* Report KH-R-34, W.M. Keck Laboratory of Hydraulics and Water Resources, California Institute of Technology, Pasadena, California.

Nielsen, P., 1992, *Coastal Bottom Boundary Layers and Sediment Transport*, World Scientific, Singapore.

O'Brien, M.P. and J.R. Morison, 1952, The Forces Exerted by Waves on Objects, *Transcripts of the American Geophysical Union*, Vol. 33, No. 1, Feb., pp. 32-38.

Raichlen, F., 1965, *Wave Induced Oscillations of Small Moored Vessels*, Report KH-R-10, W.M. Keck Laboratory of Hydraulics and Water Resources, California Institute of Technology, Pasadena, California.

Ramsden, J.D., 1993, Tsunamis: *Forces on a Vertical Wall Caused by Long Waves, Bores, and Surges on a Dry Bed*, Thesis dissertation, California Institute of Technology, Pasadena, California, p. 251

Rance, P.J. and N.F. Warren, 1968, The Threshold of Movement of Coarse Material in Oscillatory Flow, *Proceedings of the 11th Conference on Coastal Engineering,* London, pp. 487-491.

Raudkivi, A.J., 1990, *Loose Boundary Hydraulics*, Pergamon Press, Oxford, England.

Reidel, H.P., J.W. Kamphuis, A. Brebner, 1972, Measurement of Bed Shear Stress Under Waves, *Proceedings of the 13th Conference on Coastal Engineering*, Vancouver, Vol. 1, pp. 587-603.

Rouse, H., 1946, *Elementary Mechanics of Fluids*, John Wiley & Sons, Inc., New York, New York.

Saeki, H., S. Hanayasu, A. Ozaki, K. Takogi, The Shoaling and Runup Height of the Solitary Wave, *Coastal Engineering in Japan.*

Shields, A., 1936, Anwendung der aehnlichkeitsmechanik und der turbulenz forschung auf die geschiebebewegung, *Mitt. Preuss. Versuchsanstalt Wasserbau Schiffbau,* Berlin, 26.

Skjelbreia, J.E., 1987, *Observations of Breaking Waves on Sloping Bottoms by Use of Laser Doppler Velocimetry*, Report KH-R-48, W.M. Keck Laboratory of Hydraulics and Water Resources, California Institute of Technology, Pasadena, California.

Sleath, J.F.A., 1984, *Sea Bed Mechanics*, Wiley Interscience, New York, New York.

Sleath, J.F.A., 1987, Turbulent Oscillatory Flow Over Rough Beds, *Journal of Fluid Mechanics*, Vol. 182, pp. 369-409.

Sleath, J.F.A., 1988, Transition in Oscillatory Flow Over Rough Beds, *Journal of Waterway, Port, Coastal and Ocean Engeering.*, ASCE, Vol. 114, No. 1, pp. 18-33.

Sumer, B.M., T.S. Laursen, J. Fredsoe, 1990, *Turbulent Oscillatory Boundary Layer over a Bed with a Change in Roughness*, Progress Report #12, ISVA, Technical University of Denmark, pp. 3-16.

Sutherland, A.J., 1966, *Entrainment of Fine Sediments by Turbulent Flows*, Report KH-R-13, W.M. Keck Laboratory of Hydraulics and Water Resources, California Institute of Technology, Pasadena, California.

Svendsen, I.A., P.Å. Madsen, J.B. Hansen, 1978, Wave Characteristics in the Surf Zone, *Proceedings of the 16th Conference on Coastal Engineering*, pp. 520-539.

U.S. Army Coastal Engineering Research Center, 1977, *Shore Protection Manual,* Vol. II, Washington, D.C. pp.7-214-7-215

Vanoni, V.A., 1964, *Measurements of Critical Shear Stress for Entraining Fine Sediments in a Boundary Layer*, Report KH-R-7, W.M. Keck Laboratory of Hydraulics and Water Resources, California Institute of Technology, Pasadena, California.

Vanoni, V.A., N.H. Brooks, F. Raichlen, 1967, *A 40 meter Precision Tilting Flume,* Technical Memo. 67-3, W.M. Keck Laboratory of Hydraulics and Water Resources, California Institute of Technology, Pasadena, California.

Van Rijn, L.C., 1989, *Handbook of Sediment Transport by Currents and Waves*, Report H-461, Delft Hydraulics.

APPENDIX A

Paper by the author and Professor Fredric Raichlen published in the *"Proceedings of the American Society of Civil Engineers, Journal of Waterway, Port, Coastal and Ocean Engineering,"* No. 3, May/June, 1991, pp. 264-283.

THE EFFECT OF SHELTERING ON SPHERES IN LONG WAVES

By Catherine M. Petroff[1] (S.M.ASCE) and Fredric Raichlen[2] (F.ASCE)

ABSTRACT: The effect of sheltering and boundary proximity is examined for a sphere exposed to long nonlinear waves. Velocity field and force measurements are obtained for several configurations of spheres near a boundary. As a single sphere approaches the bottom, the maximum horizontal force due to a solitary wave is found to increase. For clearances less than two sphere diameters, this is reflected by a marked decrease in the inertial coefficient, C_M, and an increase in the drag coefficient, C_D. The reverse effect is observed for two sphere sheltering on the bottom. As the sphere-to-sphere separation decreases, the maximum horizontal force decreases and is characterized by a decrease in C_D and an increase in C_M for separations less than two sphere diameters. These observations, together with results of other sheltering experiments in this study, imply that the specific location of an object with respect to the boundary and other objects is an important factor in the observed effects of unsteady flow.

INTRODUCTION

In an effort to understand the behavior of granular materials under the influence of water waves, sediment grains are often modeled as spheres resting on an impermeable bed. The size of the material represented in this manner may vary from fine sand to large rock. Previous studies of incipient motion and fluid-sphere interactions have dealt either with a single sphere located at a plane boundary or with a bed of spheres. When proceeding from the case of a single particle or object to that of many, the question arises of how far the range of influence extends between objects. The extent to which a particle protruding above a bed can influence the wave kinematics and forces on another similar particle is important not only to the transport of sediments but also to the calculation of forces on

---

[1] Graduate Research Assistant, W.M. Keck Lab. of Hydraulics and Water Resources, California Institute of Technology, Pasadena, CA 91125

[2] Professor of Civil Engineering, W.M. Keck Lab. of Hydraulics and Water Resources, California Institute of Technology, Pasadena, CA 91125

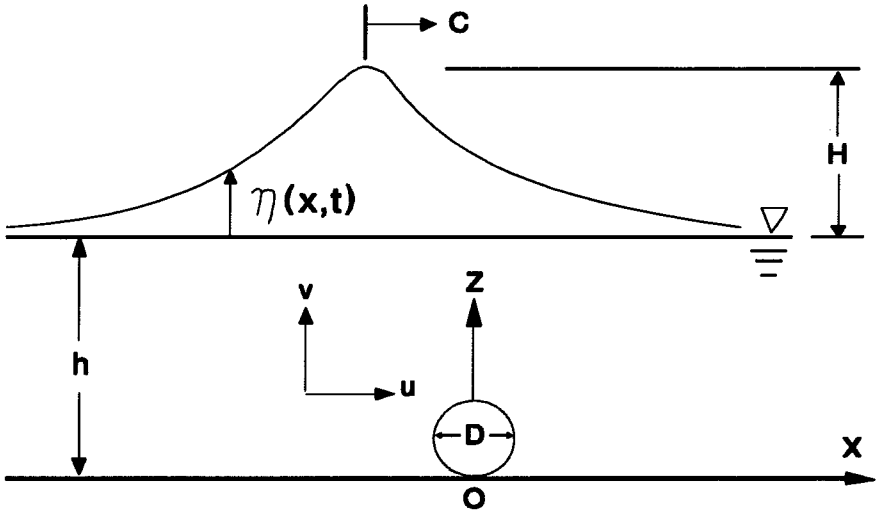

FIG. 1. Definition Sketch

structures.

This study investigated the variation of the drag, inertia, and lift force coefficients for a sphere under the action of long nonlinear waves. A definition sketch is shown in Fig. 1. Experiments were conducted with solitary and cnoidal waves. The sheltering effect was observed between two identical spheres placed, one downstream of another, on a plane tank bottom. The influences of an upstream sphere on the kinematics of the flow field and on the forces acting on the downstream sphere were studied. The effects of the close proximity of other spheres, as well as the influence of the bottom boundary and of upstream turbulence on the drag, inertia, and lift forces were also investigated.

Previous work on fluid forces on single spheres has included many experiments conducted in steady flow. Aksoy (1973), Chen and Carstens (1973), and Coleman (1977) observed fluid forces on single spheres resting on a flat bed or a bed of similar spheres at Reynold's numbers between 4 and 10^4. To simulate the behavior of wind eroded soil grains, Chepil (1961) measured the drag and lift on a sphere in a wind tunnel during separation from a porous boundary . Willetts and Murray (1981) investigated the variation of lift force on a sphere with distance from a boundary in turbulent flows with Reynold's numbers between 2.3×10^4 and 4.0×10^4.

In order to apply the results from studies on single objects to the problem of sheltering, a number of studies have measured the drag forces on pairs of objects aligned

downstream in a steady uniform flow. Lee (1979) observed that for two spheres aligned in a wind tunnel at Reynold's number near 10^4, the downstream sphere experienced an upstream thrust at separation distances of less than one half sphere diameter. The effect of the leading sphere was still visible at a separation of 2.5 diameters. Lee's experiments support earlier observations presented by Hoerner (1965) for two cylinders aligned in steady flow. It is difficult, however, to use results of steady flow experiments directly for the case of objects under waves because of the appearance of inertial forces and the characteristics of the boundary layer on the sphere in unsteady flows.

A number of researchers have conducted studies in unsteady flows to observe bed forces or forces on single objects. To address the problem of sediment motion, Eagleson et al. (1958) used spherical particles to examine waves forces and incipient motion for different bed particle geometries. Naheer (1977) investigated the fluid velocities at incipient motion for a single sphere resting on a bed of spheres for exposure to near breaking solitary waves. Rosenthal and Sleath (1985) observed lift on a sphere in oscillatory flow for gradually increasing bed clearance and Reynold's numbers up to 5,000. In experiments with periodic waves Keulegan and Carpenter (1958) correlated the variation of drag and inertial coefficients for plates and cylinders away from the boundary with the period parameter U_mT/D. Sarpkaya (1975) extended this work to cover the variation of force coefficients for spheres in sinusoidally oscillating flow in a water tunnel.

The objective of this study was to observe the effects of sheltering and boundary proximity on a sphere in unsteady flow. Results were obtained to determine the range of influence of one object on another. The understanding of the sheltering process is very important for extending results of single object experiments to a group or bed of objects.

ANALYTICAL CONSIDERATIONS

The solitary wave velocities and amplitudes observed in these experiments were compared to theoretical approximations by Boussinesq (1872) and Grimshaw (1971). Boussinesq obtained an analytical solution for the wave profile, celerity and water particle velocities accurate to the second order. Grimshaw presented a third order series expansion for these quantities. Because Grimshaw's solution better approximated our observed wave profiles and velocities, it was used to calculate the velocities and accelerations needed for estimating force coefficients. The cnoidal waves generated in these experiments were compared to the second order approximation developed by Laitone (1961).

In unsteady flows it has been observed that the in-line force on a body can be decomposed into two terms: a drag force proportional to the square of the in-line velocity, and an inertial force proportional to the fluid acceleration. This in-line force, expressed as a sum of drag and inertial forces, was formulated for a sphere by O'Brien and Morison (1952). Although only horizontal flow components are considered in this treatment, the expression, usually referred to as the Morison equation, is often presented for a spherical object (Sleath (1984)) as follows :

$$F_{inline} = \frac{1}{2}\rho\, C_D \frac{\pi D^2}{4} q|\vec{q}| + \rho\, C_M \frac{\pi D^3}{6}\frac{dq}{dt} \qquad (1)$$

where C_D is the drag coefficient, C_M the inertia coefficient, ρ the density of water, D the diameter of the sphere and q the total velocity.

Several difficulties arise in the use of the Equation 1. Since it has been demonstrated that C_D and C_M vary with time as the wave propagates past an object (Keulegan and Carpenter (1958)), one set of coefficients is insufficient to describe forces for the entire wave. McNown (1959) postulated that values of C_D and C_M vary as vortices develop in the wake of objects and hence are dependent upon the duration of the flow in any one direction. In addition, at the boundary, the object coupled with its virtual potential flow image presents different projected areas for different incident angles of the total flow velocity. Despite these considerations, the simplified equation with constant coefficients has been successful in other studies and will be used here. Since vertical velocities are small near the bottom, Equation (1) was modified to include only the horizontal components in that region:

$$F_x = \frac{1}{2}\rho\, C_D \frac{\pi D^2}{4} u|\vec{u}| + \rho\, C_M \frac{\pi D^3}{6}\frac{du}{dt} \qquad (2)$$

Away from the bottom, Equation 1 was applied.

Eagleson et al. (1958) noted that since the velocity at the top of a sphere in a flow is greater than that at the bottom, a circulation is induced around the sphere. This circulation causes a lift force on the sphere perpendicular to the direction of flow. The equation used for this study is commonly used in potential flow theory (Prandtl (1967)):

$$F_y = \frac{1}{2}\rho C_L \frac{\pi D^2}{4} u^2 \tag{3}$$

where C_L is defined as the lift coefficient.

In order to determine drag and inertia coefficients, a least squares method was employed as proposed by Dean and Aagaard (1970). The square of the error between the measured and the predicted forces was minimized with respect to C_D and C_M as shown in the following expression:

$$Err^2 = \frac{1}{N}\sum_{i=1}^{N}(F_{mi} - F_{pi})^2 \tag{4}$$

where F_m and F_p are the measured and the predicted forces, respectively, at the time increment denoted by the subscript i. F_p is defined by equation (1) or (2) as appropriate to the location of measurement. A similar approach can be used to determine the least square fit for C_L from Equation (3).

The relative magnitude of the drag force and the inertial force is important in understanding the characteristics of wave sphere interactions. Although their maxima do not occur at the same time, a convenient gauge of the size of the two terms is the ratio of their maximum values. For a sphere:

$$\frac{(dF_I)_{\max}}{(dF_D)_{\max}} = \frac{4}{3}\frac{C_M D}{C_D}\frac{\left(\frac{du}{dt}\right)_{\max}}{(u^2)_{\max}} \tag{5}$$

If either the drag or the inertia dominates this ratio, the Morison equation can be simplified. For the drag dominated case, the problem becomes one of steady flow. For the case where inertial force dominates, the problem can be treated by classical potential flow theory assuming that the influence of the body's wake on the inertial force is small.

EXPERIMENTAL EQUIPMENT AND PROCEDURES

The experiments were conducted in a 40m long precision tilting flume modified for use as a wave tank with a programmable vertical bulkhead wave generator installed at one end. The tank is 109 cm wide and 61 cm deep with a stainless steel bottom plane to

within ± 3mm and glass walls 1.3 cm thick. The tank can be tilted to a maximum slope of 2 percent using pairs of power-driven jacks both upstream and downstream of a central hinge point. For these experiments the tank was kept horizontal.

The position of the water surface was recorded with resistance gauges consisting of two parallel 0.25 mm diameter stainless steel wires tensioned on a frame and spaced 4.0 mm apart. The wave gauges were manually calibrated prior to each experiment by varying their immersion over the expected range of wave surface variation. The resolution obtained by the data acquisition system for a range of variation of 10 cm was ± 0.1 mm.

Data acquisition for these experiments was controlled by a microcomputer equipped with a 12 bit analog-to-digital converter. The converter is capable of sampling data at a maximum rate of 1 MHz and accepts a voltage range of ± 10V with a sampling accuracy of ± 2.5 mV.

A two-dimensional Laser Doppler Velocimeter (LDV) developed by Skjelbreia (1987) was used to measure water particle velocities. The laser (Helium-Neon 5 mW) , optical elements, and photodetectors are mounted to a vertically adjustable optical bench on a traveling carriage suspended from the laboratory ceiling. The LDV employs an optical arrangement in which the reference beam does not pass through the focal volume but can pass either above or below it, allowing measurements very close to either the bottom of the tank or the water surface, respectively.

Experiments were conducted 21.6 m from the mid-stroke position of the generator bulkhead with a still water depth, h = 20.4 cm for solitary wave experiments and 20.0 cm for cnoidal wave experiments. The variation of the water surface and the output from the LDV signal processor were simultaneously recorded during the wave's passage. A time interval of 20 minutes was allowed for the damping of motion between experiments. Since velocity measurements were taken at eleven vertical locations above the bottom of the tank, good wave reproducibility was essential. The experimental arrangement described above can reproduce a wave amplitude to within ± 1%.

A sphere 5.72 cm in diameter was fixed to a 0.9 mm thick sheet metal plate sealed to the bottom of the tank with the centerline of the sphere 21.6 m from the mid-stroke position of the wave plate. To investigate the influence of sheltering on the water particle velocities, a second sphere was added to the plate with various separation distances

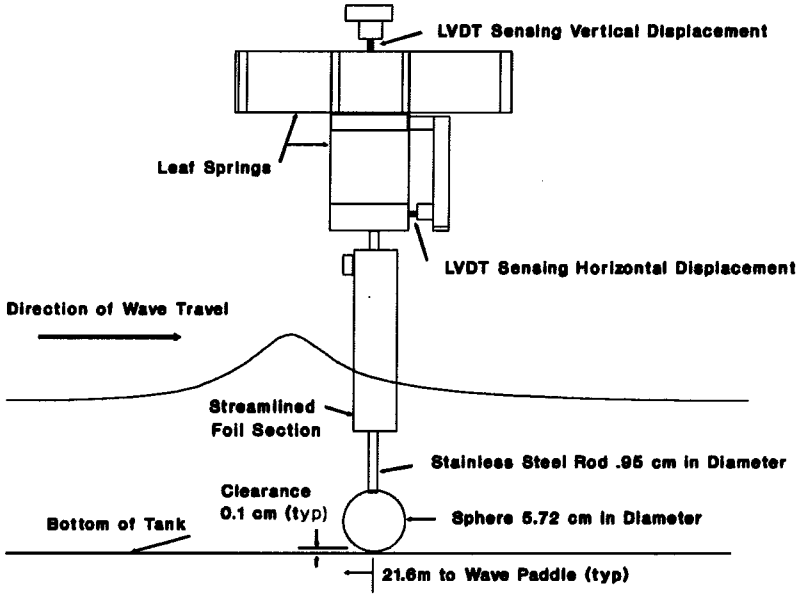

FIG. 2. Schematic of Force Transducer and Sphere

between spheres.

The forces imparted to the sphere during the passage of the solitary wave were measured using the force transducer shown schematically in Fig. 2. The transducer, developed by Goring and Raichlen (1979), consists of two sets of parallel leaf springs mounted perpendicularly to each other and firmly attached to clamping blocks so that the measurement of motions in the horizontal and vertical directions are mutually independent. As shown in Fig. 2, the motion of the springs is measured using linear variable differential transformers (LVDTs). The sphere is attached to the force transducer by means of a 0.95 cm diameter stainless steel rod partially shielded from the flow by a hollow airfoil shape mounted independently of the transducer. A second rod, referred to herein as the tare rod, identical to the sphere support rod, was used to define the net force.

Forces were applied in the vertical and horizontal directions and it was determined that the force transducer responded linearly for both positive and negative loads. Therefore, during the experiments, the force transducer was calibrated before each run only in the downward and in the downstream directions.

To determine whether force measurements would be affected by the dynamics of the force transducer, the natural frequency of the transducer was recorded for several conditions including the transducer fitted only with the tare rod, and the results are shown in Table 1.

TABLE 1. Natural Frequencies of Force Transducer Assemblies

Force Transducer with:	ν (rad/sec)
Sphere in Air	95.5
No Sphere (Tare) in Air	125.7
Sphere in Water	86.7
Tare in Water	124.4

Most of the experiments were conducted using an incident solitary wave with H/h = 0.48 with the sphere transducer combination located 21.6 m from the wave plate. After obtaining force measurements for a single sphere placed 0.1 cm from the bottom of the tank, forces were recorded for the sphere at different elevations from the boundary, for solitary waves and for two cnoidal waves of different periods. A second sphere was introduced upstream and forces were measured on the downstream sphere for different separation distances. Forces also were recorded for one sphere surrounded by six closely spaced spheres (0.32 cm clearance). In addition, measurements were made with the upstream flow disturbed by two sets of screens whose characteristics are defined in Table 2. For these experiments, the fixed spheres, or screens, rested on the bottom and the instrumented sphere was spaced 0.1 cm from the boundary.

TABLE 2. Dimensions of Screen Banks

Screen	Wire spacing (mm)	Wire width (mm)	Number of panels	Panel dimensions (cm)
A	1.3	0.5	4	15x15
B	3.2	0.6	4	17x17

PRESENTATION AND DISCUSSION OF RESULTS

The objective of early experiments was to investigate the effect of a relatively large sphere (D/h = 0.28), located at the tank bottom, on the kinematic characteristics of a solitary wave. The influence on the wave kinematics around one sphere of an identical sphere located several diameters upstream also was studied. Forces were measured for both these configurations, and for other cases, to determine the sheltering effect of one object on another. The Reynolds number of the flow relative to the sphere, based on the maximum horizontal water particle velocity, varied from 29,000 near the bottom to 32,000 at mid-depth.

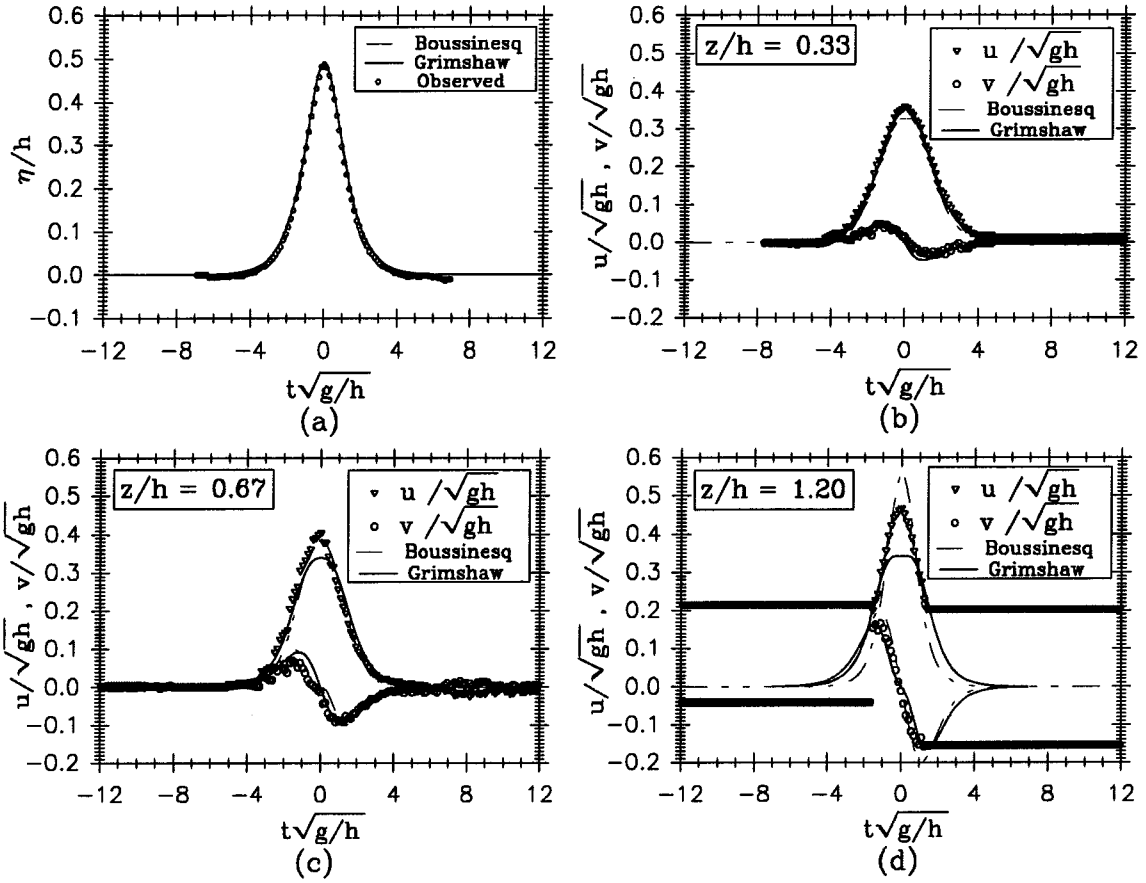

FIG. 3. Comparison of Experiments and Theory for Wave Amplitudes and Velocities in Solitary Wave, H/h = 0.48

Wave Profiles and Flow Velocities - Unobstructed Flow: As shown in Fig. 3a, the measured wave profiles agreed well with the theoretical solitary wave profile of Grimshaw (1971) and of Boussinesq (1872). The agreement of data with the Grimshaw theory is within ±1% and falls within ±2% of Boussinesq. In the trailing region of the generated wave, small water surface oscillations occur which are due to the effect of the large relative wave height on the wave generation algorithm and the vertical bulkhead generator. The effects of these oscillations on the water particle velocities and forces are not significant.

Initial experiments were conducted with the LDV for *H/h* = 0.48 without the sphere in place to establish a time history of the direction and magnitude of the water particle velocities in unobstructed flow. The vertical and horizontal components of the velocities were measured at eleven levels on the centerplane of the wave tank and compared to the theories of Boussinesq and Grimshaw as shown in Figs. 3(b), (c), and (*d*).

The ordinate is the normalized velocity and the abscissa is the normalized time. Near the bottom of the tank, at z/h = 0.33, the water particle velocities are predicted best by Grimshaw's third order theory. At z/h = 0.67, Boussinesq's theory predicts the horizontal velocity well, but it is not very accurate for the vertical velocity. In the region of the wave crest, z/h = 1.20, neither approximation agrees well with the data. In the observable range, horizontal velocities are greater than those predicted by Grimshaw's approximation near t = 0 and less than those predicted by the theory of Boussinesq in the same region. The errors in Grimshaw's approximation for this case are similar to those which occur in the Boussinesq theory near z/h = 0.33. Although higher order approximations are available for these velocities, the majority of the sphere experiments were performed in the lower region of the flow, where Grimshaw's theory appears reliable. It was, therefore, deemed appropriate to use Grimshaw's approximations for predicting velocities, accelerations, and calculating force coefficients.

Flow Velocities - One Sphere on Tank Bottom: The velocities observed at sixteen locations, denoted by A through P, around a single sphere at $t\sqrt{g/h}=0$ are compared to unobstructed flow velocities in Fig. 4(a). The length and orientation of the arrows correspond, respectively, to the magnitude and direction of the total velocities at the time of passage of the wave crest over the center of the sphere. The size of the sphere is fairly large with respect to the incident wave: D/H is about one half. The general shape of the wake is evident, and it is noted that the flow at points I, J, and K has a definite upstream component.

Velocity time histories are displayed in Figs. 4(b) and (c) at two locations along the midline of the sphere: Point D, on the sphere centerline, is 2.1 cm upstream of the sphere surface and point L is an equal distance downstream. At point D, the magnitude and direction of the horizontal and vertical components of velocity remain largely unchanged compared to the unobstructed case. This can be seen when the measured velocity is compared to that predicted by Grimshaw for a point at the center of the sphere. The distance between the two peaks represents the travel time of the wave from point D to the sphere center. After the passage of the wave, a disturbance occurs at $t\sqrt{g/h}=4$. Since the wave speed is in excess of 1.4 m/sec, this cannot be evidence of reflection from the sphere surface but may be due to the circulation around the sphere as seen at points I, J, and K. At position L, in the wake of the sphere, the horizontal motion decreases rapidly after the passage of the wave and then reverses direction. The reversal is coupled

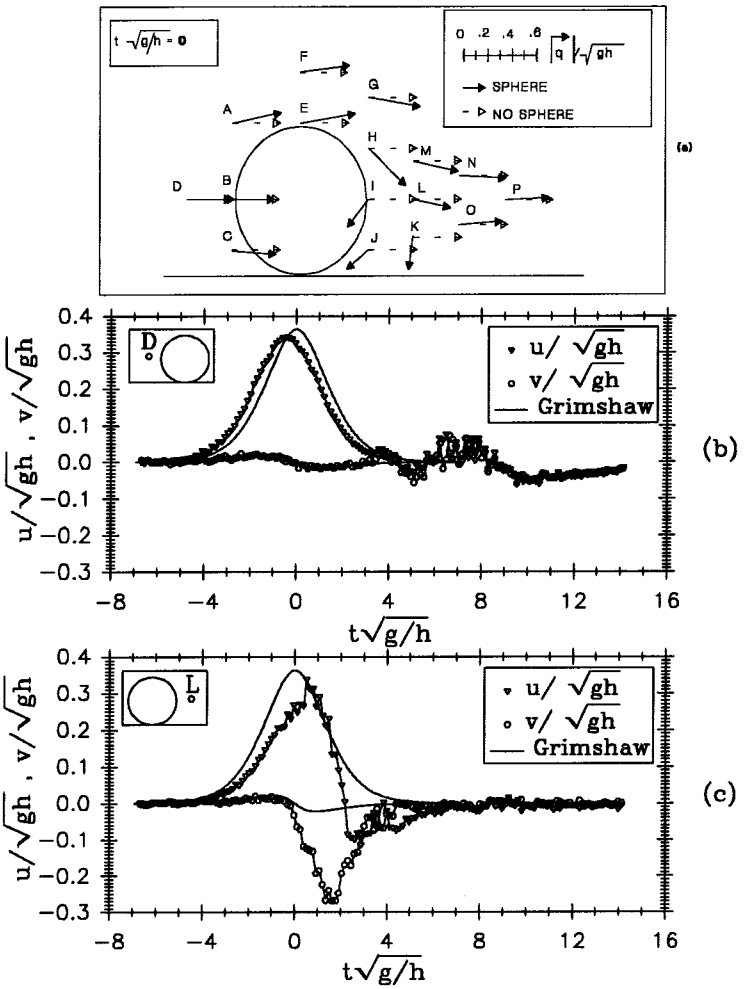

FIG. 4. Velocities around Sphere under Solitary Wave, *H/h* = 0.48, *H/D* = 1.7

with a rapid downward motion of a magnitude similar to the peak horizontal velocity. The velocity record at L is further evidence of the development of a wake as the wave sweeps past the sphere and of the subsequent return of flow to nearly undisturbed conditions at $t\sqrt{g/h} = 10$.

Flow Velocities - Two Spheres on Bottom: Fig. 5 shows the effects of the sheltering afforded by a second sphere placed with a clearance of two diameters upstream from the first. The velocity field presented in Fig. 5(a) at the time of wave crest passage over the center of the trailing sphere shows that circulation behind the leading sphere is still present. Although the flow pattern around the downstream sphere resembles that around the single sphere, it should be noted that the downward components of the

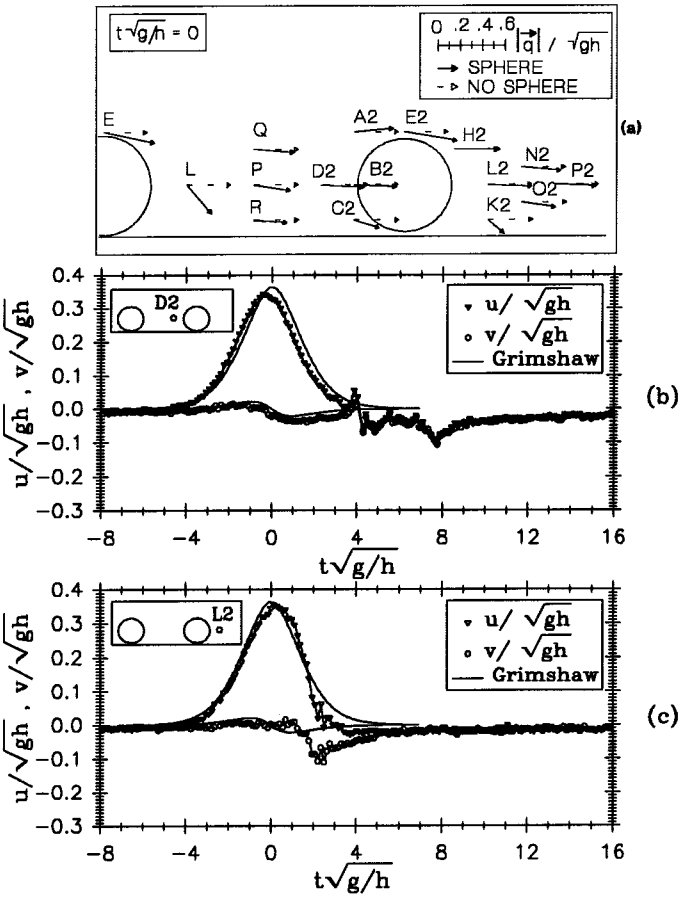

FIG. 5. Velocities around Two Spheres under Solitary Wave, *H/h* = 0.48, *H/D* = 1.7

velocities in the wake of the downstream sphere have been reduced. The reversal of the horizontal direction, seen in the case of circulation behind the single sphere, is not apparent. The variation of horizontal and vertical velocities with time is presented in Figs 5(b) and (c). In both cases the magnitude of the maximum horizontal velocity has not been substantially affected by the upstream sphere. The major difference at L2, in the wake of the downstream sphere, occurs after the passage of the wave crest. It appears, for the case of the two diameter sphere separation, the effect of the upstream sphere on the velocities around the downstream sphere is small and is limited to a decrease in the circulation in the wake region.

It was noted that the water surface profile in the case of unobstructed flow is not significantly affected by the presence of one or even two spheres. The free surface elevation plots were within $\pm 1\%$ of each other which is comparable with the variation in

reproducibility of the wave generator. As a result, with regard to the wave characteristics, the effects of scattering and diffraction do not appear to be important in this problem.

Forces on a Sphere - Effects of Sheltering: The main objective of this portion of the study was to investigate the change in forces acting on one sphere due to sheltering effects and to determine the variation of the force coefficients shown in Eqs. (1) and (3).

As with any dynamic study, it is important to establish the degree of confidence in the measured forces by comparing the spectral energy of the incident wave with the natural frequency of the force transducer. The amplitude spectra of the solitary wave and of two cnoidal waves used in the sphere experiments were obtained using the Fast Fourier Transform method. For the three cases investigated, there were essentially no contributions from frequencies greater than about 30 rad/sec. Force spectra for a sphere exposed to a solitary wave were obtained also. At 30 rad/sec, the spectral estimates for the forces acting on the sphere had decreased by nearly a factor of ten from their initial values at low frequencies. Significant components appear again near 87 and 124 rad/sec which corresponded to natural frequencies of the force transducer assembly (Table 1). The higher frequency components observed were probably due to the vibration of the transducer support and the wave tank and rails.

To reduce noise at frequencies in excess of 78.5 rad/sec, the raw force signal was filtered using both a moving average and Fast Fourier Transform (FFT). A comparison of the two results indicated that the moving average did not introduce a phase shift in the data. Although some periodicities in the filtered signal remain after the smoothing procedure, the smoothed results show good agreement between experiments and allow reliable conclusions to be drawn relative to the study objectives.

The effect of the proximity of a single sphere to the bottom is shown in Fig. 6. The sphere and force transducer were moved incrementally from a minimum clearance of 0.1 cm (F/D = 0.0175) to a maximum of 11.9 cm from the bottom (F/D = 2.08). The maximum horizontal force occurs at the smallest clearance. At a clearance of one half of the sphere diameter, the maximum force decreases by about 20% and occurs before the wave crest passes. This is due to the greater influence of inertial forces as the boundary clearance is increased. The measured horizontal force remains approximately constant for $0.47 \leq F/D \leq 2.1$. When the sphere is close to the boundary, the maximum vertical force is upward and lags the wave crest. This behavior appears to be the combined effect of a

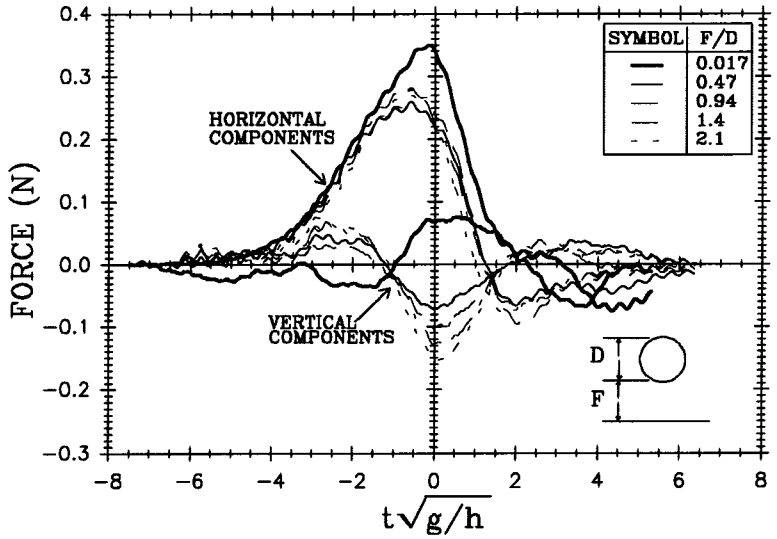

FIG. 6. Variation of Force Time Histories for Bottom Clearance Experiments

positive lift force due to the horizontal velocity and an inertial force proportional to the vertical acceleration. As the clearance increases, the maximum vertical force is directed downward.

The effect of sheltering between two identical spheres was investigated by fixing the upstream sphere and moving the downstream sphere away from it incrementally. Fig. 7 shows the forces on the downstream sphere as a function of relative clearance. The force is reduced by about 15% force on the unobstructed sphere near the tank bottom

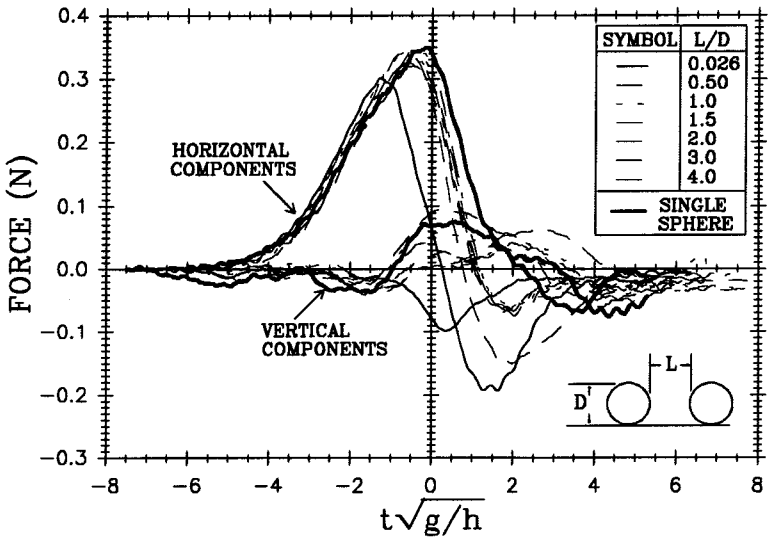

FIG. 7. Variation of Force Time Histories for Sphere Separation Experiments

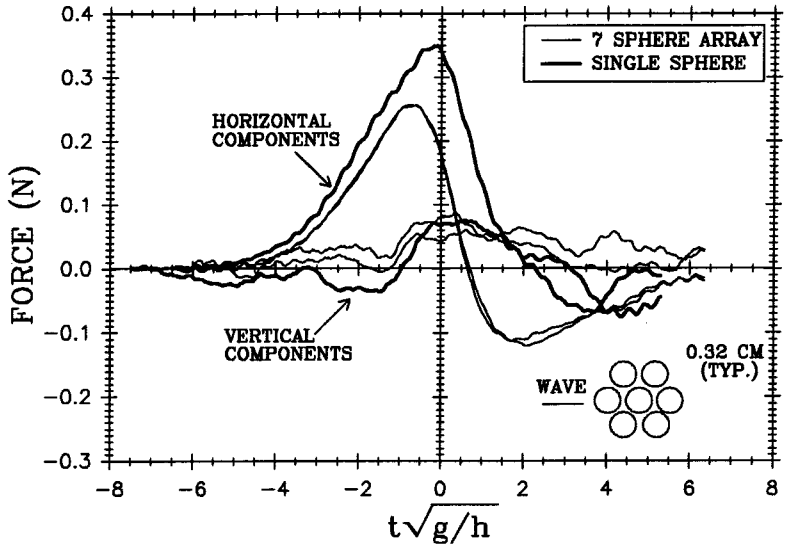

FIG. 8. Variation of Force Time Histories for Seven Sphere Experiment

(F/D = 0.017) is presented for comparison. When the relative separation is L/D = 0.026, the maximum horizontal force compared to that for the single sphere. The peak force occurs before the wave crest reaches the center of the sphere. This is probably due to the influence of the inertial force which decreases as the spacing increases. For the smallest separation (L/D = 0.026), the vertical force shows the combined effect of the negative lift on the sphere due to horizontal velocity and the inertial force component associated with the vertical acceleration. When the separation is greater than one diameter, the effects of the upstream sphere appear small.

To investigate the sheltering effect on a more realistic three-dimensional arrangement, forces were measured on a single sphere in the center of the closely packed array composed of six identical spheres. Results are presented in Fig. 8 along with those for the single sphere. There is evidence of reduced drag and increased inertial force similar to that observed for the two adjacent spheres. This causes the maximum force to occur before the wave crest has reached the sphere center and produces a relatively large maximum negative force afterwards. When compared to the single sphere, the horizontal force is reduced nearly 30%, a somewhat greater reduction than that for the sheltering associated with two spheres. It should be noted that the magnitude of the vertical force on the sphere is directed generally upward implying that the sphere surrounded by others still experiences a net upward lift.

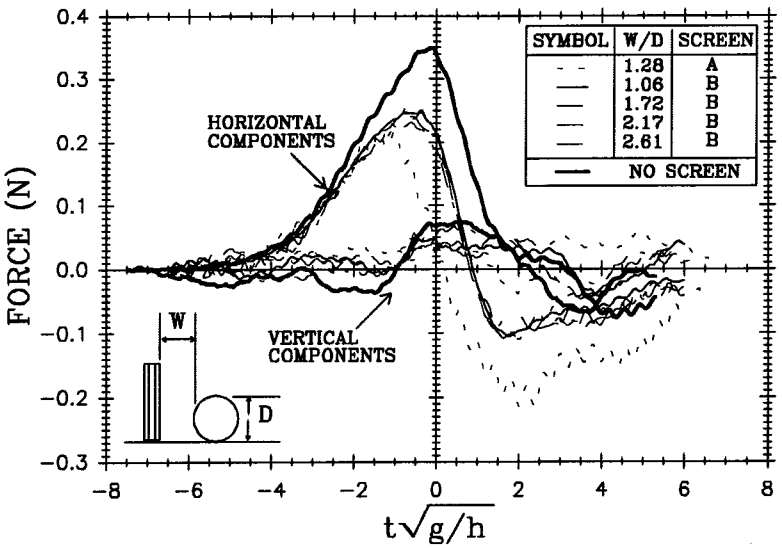

FIG. 9. Variation of Force Time Histories for Screen Experiments

A series of experiments were conducted to investigate the effects caused by sets of screens placed upstream from a sphere. The variation of the force time histories for screens A and B (see Table 2) are shown together in Fig. 9 along with the forces for the single sphere arrangement. The greatest effect is seen for the smaller wire spacing, screen A, where the maximum horizontal force is reduced by 40% compared to the single sphere. It is apparent that the reduced force results from the decrease in the contribution of the drag term compared to the inertial term in Eq. (1). It is possible that the small scale turbulence created by the fine mesh decreases the critical Reynolds number for the sphere moving the separation point on the sphere downstream and thereby reduces drag. In addition, it is observed that a significant upstream force results after the wave crest passes the sphere center.

When screen B, with the wider wire spacing, is placed upstream of the sphere, the resultant forces are very similar to the seven sphere arrangement. Inertial forces are increased somewhat less than when screen A is used. The time of the maximum force is shifted and a 30% reduction in the maximum horizontal force is realized compared to the single sphere. The vertical forces are not significantly affected by the presence of the screens. In addition, it can be seen in Fig. 9 that changing the location of the screens within the range of 1.5 - 3.0 sphere diameters seems to have little effect on the resulting forces.

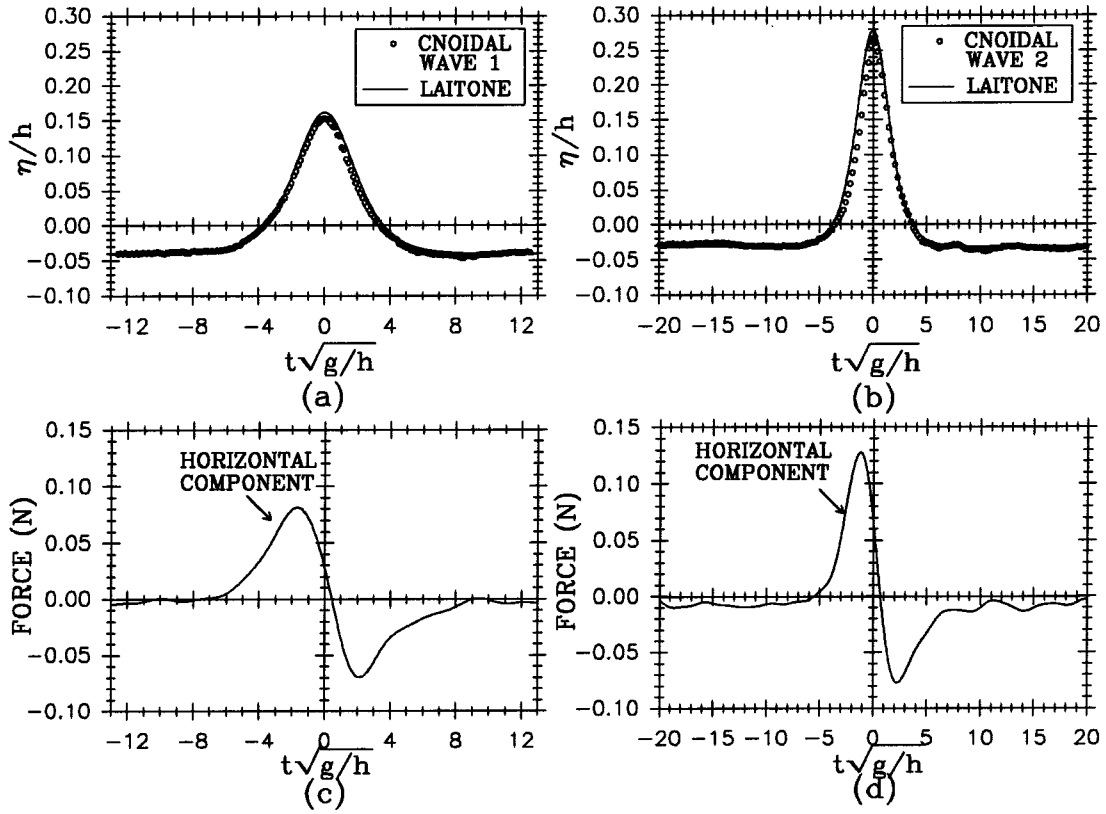

FIG. 10. Water Surface (a, b) and Force (c, d) Time Histories for Sphere in Cnoidal Waves

In order to compare the freestream forces for waves between the solitary and sinusoidal limits, a limited number of experiments were conducted to measure the forces on a sphere with a clearance of F/D = 1.56, exposed to cnoidal waves. The results for the variation of the relative wave amplitude as a function of normalized time are presented in Figs.10(a) and (b). In the first case, denoted as cnoidal wave 1, H/h = 0.2 and $T\sqrt{g/h} = 25$, while for cnoidal wave 2, H/h = 0.3 and $T\sqrt{g/h} = 40$, where T is the period of the wave. It is seen that both cases agree well with second order cnoidal wave theory as presented by Laitone (1961). Figs. 10(c) and (*d*) show the measured horizontal force time histories. Since the amplitude ratios of the cnoidal waves were not very large, it was not possible to obtain a significant vertical force component. Although both force records show a relatively large contribution of inertial force to the total force, the inertial force contribution for cnoidal wave 1 appears to be greater than that shown for cnoidal wave 2.

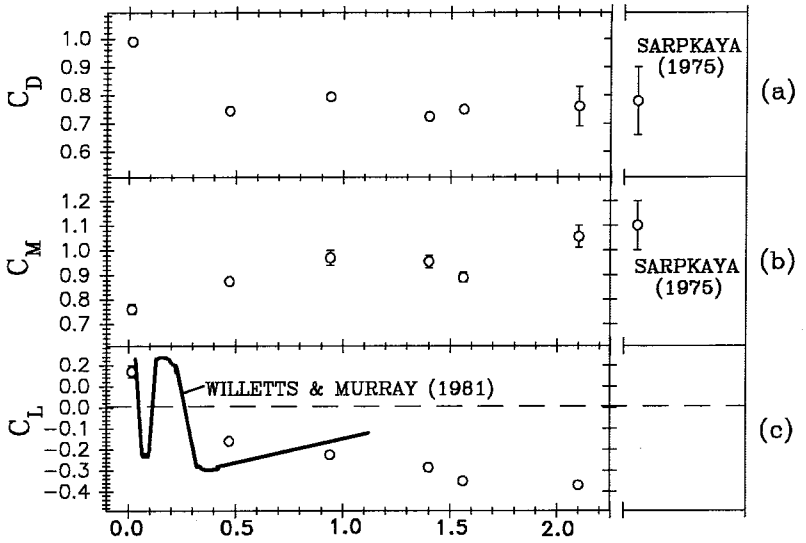

FIG. 11. Variation of Drag, Hydrodynamic Mass, and Lift Coefficients with Bottom Clearance for Solitary Waves

Using the curve fitting and least squares methods previously described, the drag and inertia coefficients in the Morison Equation: C_D, C_M and the lift coefficient, C_L, were calculated from the experiments. In Fig. 11(a), (b), and (c) the coefficients are presented as a function of the relative bottom clearance, *F/D*. Though the coefficients do not vary significantly with bottom clearance, some effects are apparent. The drag and lift coefficients are greatest when the sphere is close to the boundary and decrease with increasing clearance. Indeed as observed earlier, the direction of the vertical force changes from upward to downward as the relative clearance increases. Conversely the inertial coefficient, C_M, increases with increasing clearance. The inertial and drag coefficients for relatively large clearances compare favorably to those obtained for unsteady harmonic motion in a water tunnel by Sarpkaya (1975) shown to the right in Figs. 12(a) and (b). In addition, the values obtained for the lift coefficient, C_L, are within the range of the data of Willets and Murray (1981) for their experiments conducted in a uniform turbulent flow at a Reynolds number of 32,000.

To allow for a comparison of the drag and inertial coefficient measurements obtained with solitary waves to those of Sarpkaya (1975) in an oscillating water tunnel, Sarpkaya's data were plotted against an excursion parameter defined as $2\pi S/D$, where S is the predicted maximum horizontal water particle excursion under the wave from the median position. The total horizontal excursion for the solitary wave was calculated using the approximation developed by Munk (1951), while the excursions for the cnoidal waves

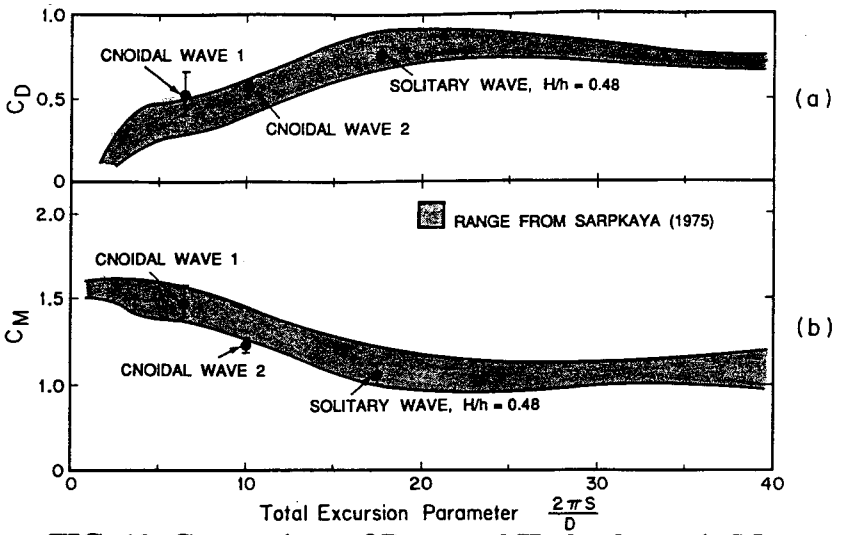

FIG. 12. Comparison of Drag and Hydrodynamic Mass Coefficients with Data of Sarpkaya (1975)

were obtained through numerical integration of the velocity time histories. The shaded region in Fig. 12 represents the envelope for Sarpkaya's data. The coefficients from the present experiments at $F/D = 2.1$ for the solitary wave and $F/D = 1.56$ for the two cnoidal waves are shown also in Fig. 12; the bars denote the range of the experimental results. Although Sarpkaya obtained his data in a constant section oscillating water tunnel and the current study used propagating periodic and non-periodic long waves, the coefficients from the two different types of experiments compare favorably.

The influence on the force coefficients of the sheltering of one sphere by another

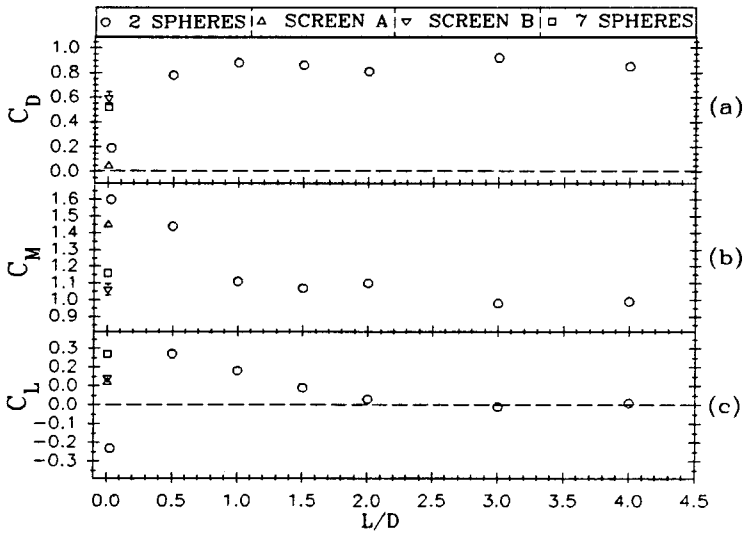

FIG. 13. Variation of Drag, Hydrodynamic Mass, and Lift Coefficients with Sphere Separation for Solitary Waves

sphere is presented in Fig. 13 as a function of the relative separation of the spheres, *L/D*. The effect of sheltering on the drag coefficient is evident in Fig. 13(a) where for *L/D* = 0.03 the drag coefficient is a factor of four smaller than that for *L/D* = 4. Figure 13(b) shows that, in contrast to the drag coefficient, the inertial coefficient is approximately 60% larger for the *L/D* = 0.03 than for *L/D* = 4. For C_L, the influence of an upstream sphere gives rise first to a downward force for the smallest separation and then an upward force at one half diameter spacing. The lift coefficient then decreases with spacing and approaches zero at *L/D* = 2. This latter effect of sheltering on C_L is supported by the velocities presented in Fig. 5 which showed a decrease in circulation in the wake of the sheltered sphere for *L/D* = 2 when compared to the single sphere experiments. The force coefficients for the experiments with the screens and the seven spheres are shown also in Fig. 13. These fall within the range of the data of the two spheres for *L/D* less than 2. (The bars shown indicate the rage of the data.) It is interesting to note that the force coefficients for the seven sphere experiment are similar to those for two spheres spaced between one quarter and one diameter apart.

The use of a single set of coefficients to predict the force-time history on a sphere is shown in Fig. 14. In the cases shown, the observed forces are compared with a computed force from Morison's Equation (Eq. 1) using the derived force coefficients and the velocities and accelerations from Grimshaw's theory (1971) for solitary waves and Laitone's theory (1961) for cnoidal waves. In Fig. 14(a), the horizontal and vertical forces on a single sphere near the bottom are shown for a solitary wave with *H*/h = 0.48. As the wave propagates into the initially still water, both C_D and C_M change with increasing velocity. This can be seen for $t\sqrt{g/h} < 0$ where the observed force is greater than that predicted by the least-square error force coefficients. After the wave crest passes, the horizontal force corresponds more closely to the predicted forces. Fig. 14(b) shows the horizontal forces on a sphere at a relative clearance from the bottom, *F/D* = 1.56, for two different cnoidal waves. The experiments correspond to the third and fifth waves in the wave train. Both the flow and the wake are well established in these instances and so the predicted values correspond well over the entire data range. Fig. 14(c) presents horizontal forces for the case of two sphere sheltering under the solitary wave. The relative separations shown are *L/D* = 0.026 and 0.50. The effect of the changing C_D and C_M is similar to that seen in Fig. 15(a). In general, it can be seen from Figure 14 that the in-line force time history is predicted fairly well using the experimentally defined coefficients.

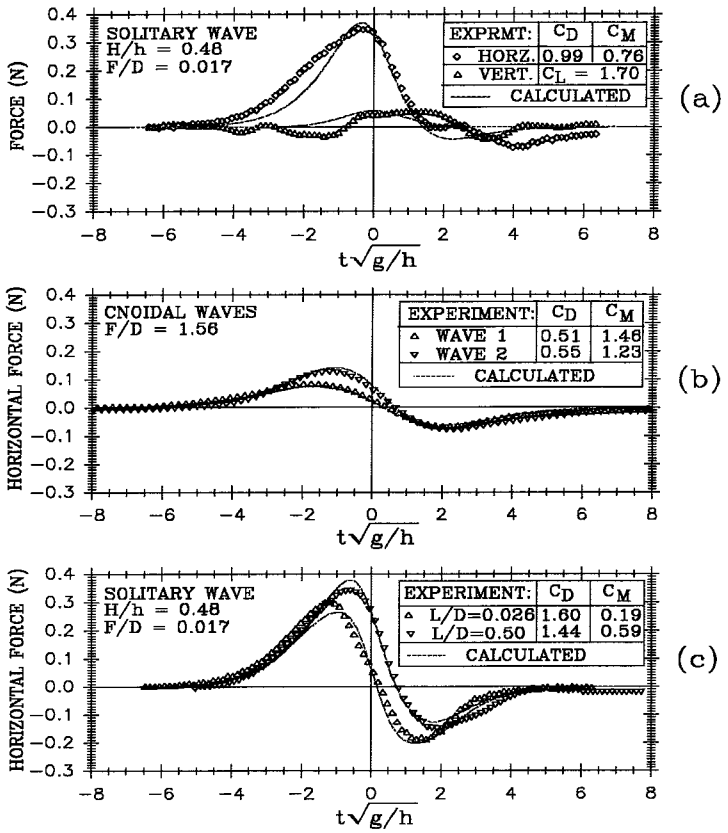

FIG. 14. Comparison of Observed and Calculated Force Time Histories, D/h = 0.28

Fig. 15 summarizes the relative importance of inertial and drag force for the various experiments. The ratio of the maximum inertial force to the maximum drag force is plotted as a function of the relative clearance from the bottom in Fig. 15(a). Though all values show a dominance of the drag force in Morison's Equation (Eq. 1), the drag is most important for the sphere nearest the bottom of the tank. As the clearance increases, the ratio approaches that calculated from the data of Sarpkaya (1975). In Fig. 15(b), the variation of the inertial to drag force ratio with sphere separation is shown for the sphere sheltered in the flow and located near the bottom. For the fine mesh screen upstream of the sphere, the force is dominated by inertial effects, and for the arrangement of seven spheres the ratio is close to unity. When the two spheres are closest the ratio is about 3.5, seven times greater than at spacings greater than one sphere diameter. As the two spheres are separated further, the ratio decreases but does not reach the limiting value of 0.33 for the single sphere. It is evident that the effect of sheltering on this ratio becomes small for spacings greater than one sphere diameter.

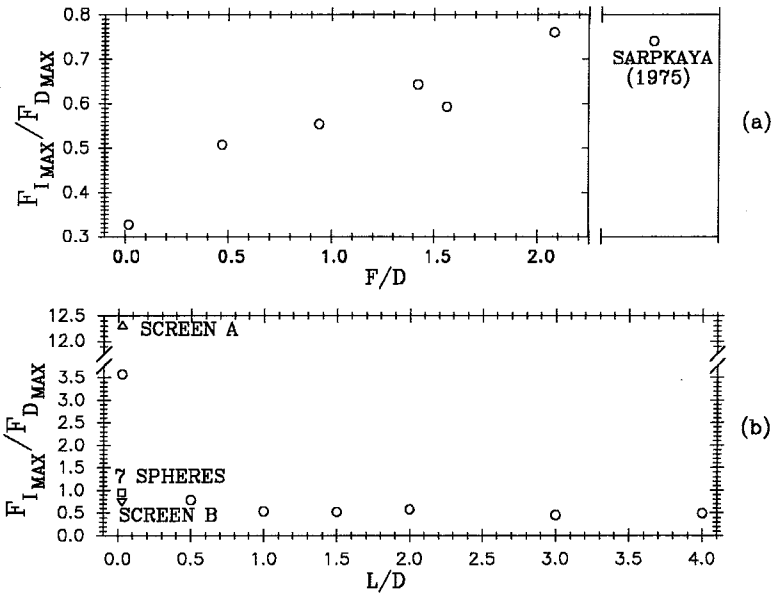

FIG. 15. Variation of Maximum Force Ratios for Sphere Experiments with: (a) Bottom Clearance; (b) Sphere Separation

CONCLUSIONS

The following major conclusions can be drawn from this study:

1. The horizontal and vertical velocities under a solitary wave in the region of z/h ≤ 0.33 are reasonably well predicted by the third order theory of Grimshaw (1971).

2. For two identical spheres on the bottom with a clearance of two diameters exposed to the solitary waves, the velocity field around the downstream sphere on the centerplane is not affected significantly by the upstream sphere.

3. The influence of the bottom on a single sphere is important only for small relative clearances. At $F/D = 0.02$ the in-line force is about 30% greater than that for $F/D = 2.1$.

4. When the relative separation between two identical spheres, one behind the other and near the bottom, is small, the in-line force is less than that at larger separations. For a large relative separation ($L/D \geq 2.0$) the effect of the upstream sphere is small.

5. For the case of a single sphere approaching a boundary, the drag coefficient increases while the inertia coefficient decreases. This is opposite to the effect observed when the two spheres near the bottom approach each other. Decreasing the sphere-to-sphere separation results in a smaller drag coefficient and a larger inertia coefficient for the

downstream sphere.

6. From an initial position in the tank at about mid-depth, the lift force on a single sphere changes direction as the sphere approaches the bottom. While the force is downward at $F/D = 0.50$, at a relative clearance of $F/D = 0.02$ the lift force is directed upward.

7. For the case of two sphere sheltering near the bottom, the lift force on the downstream sphere is downward for the smallest relative separation and it is upward for $L/D \geq 0.50$.

8. Although the solitary wave is a transient event, it appears that for the wave used in this study there is enough time for the inertial and drag forces to fully develop, i.e., the solitary wave results compare well with data obtained in this study for periodic long waves and with unsteady water tunnel data of Sarpkaya (1975) for the same relative water particle excursions.

9. This study has shown that the specific location of an object with respect to the boundary and to other objects plays an important role in the observed effects of unsteady flow. Thus, when a problem is modeled with a single sphere resting on a plane boundary or on a bed of spheres, great care must be exercised in interpreting the experimental results and applying them to the problem of initiation of motion of a bed of closely spaced particles.

ACKNOWLEDGMENTS

The authors appreciate the sponsorship of the National Science Foundation for this study under Grant No. MSM-8812187.

APPENDIX I - REFERENCES

Aksoy, S., "Fluid Force Acting on a Sphere near a Solid Boundary," *Proceedings of the 15th Congress IAHR Istanbul*, 1973, pp. 217-224.

Boussinesq, J., "Theorie des Ondes et des Remoues qui se Propagent le Long *d*'un Canal Rectangulaire Horizontal, en Communiquant au Liquide Contenu dans ce Canal de Vitesses Sensiblement Pareilles de la Surface au Fond," *Journal de Mathematiques Pures et Appliquees*, 2nd series, Vol. 17, 1872, pp. 55-108.

Chen, C. and Carstens, M. R., "Mechanics of Removal of a Spherical Particle from a Flat Bed," *Proceedings of the 15th Congress IAHR Istanbul*, 1973, pp.147-158.

Chepil, W. S., "The Use of Spheres to Measure Lift and Drag on Wind Eroded Soil Grains," *Proceedings of the Soil Science Society*, Vol. 5, 1961, pp. 343-345.

Coleman, N. L., "The Extension of the Drag Coefficient Function for a Stationary Sphere on a Boundary of Similar Spheres," *La Houille Blanche*, 1977, pp. 325-328.

Dean, R. G. and Aagaard, P. N., "Wave Forces, Data Analysis and Engineering Calculation Method," *Journal of Petroleum Technology*, Mar. 1970.

Eagleson, P. S., Dean, R. G., and Peralta, L. A., "The Mechanics of Motion of Discrete Spherical and Bottom Sediment Particles Due to Shoaling Waves," Beach Erosion Board, U. S. Department of the Army, Corps of Engineers, *Technical Memorandum No. 104*, 1958.

Goring, D. K. and Raichlen, F., "Forces on Block Bodies Accelerating in Still Fluid," *Journal of the Waterway, Port, Coastal and Ocean Division*, ASCE, Vol. 105, No. WW2, Proceeding Paper 14582, May, 1979, pp. 171-189.

Grimshaw, R., "The Solitary Wave in Water of Variable Depth," Part 2, *Journal of Fluid Mechanics*, Vol. 46, 1971, pp. 611-622.

Hoerner, S. F., *Fluid Dynamic Drag*, Hoerner Fluid Dynamics, Bricktown New Jersey, 1965.

Keulegan, G. H. and Carpenter L. H., "Forces on Cylinders and Plates in an Oscillating Fluid," *Journal of Research of the National Bureau of Standards*, Vol. 60, No. 5, Research Paper 2857, May, 1958.

Laitone, E. V., "The Second Approximation to Cnoidal and Solitary Waves," *Journal of Fluid Mechanics*, Vol. 9, 1961, pp. 430-444.

Lee, K. C., "Aerodynamic Interaction Between 2 Spheres at Reynolds Numbers around 10," *Aeronautical Quarterly*, Vol. 30, Feb., 1979, pp. 371-385.

McNown, J. S. and Keulegan, G. H., "Vortex Formation and Resistance in Periodic Motion," *Journal of the Engineering Mechanics Division*, ASCE, Vol. 85, No. EM1, Proceedings Paper 1894, Jan., 1959, pp. 1-6.

Munk, W. H., "The Solitary Wave and Its Application to Surf Problems," *Annals of the New York Academy of Science*, Vol. 51, pp. 376-424.

Naheer, E., "Stability of Bottom Armoring under the Attack of Solitary Waves," *Report No. KH-R-34*, W. M. Keck Laboratory of Hydraulic and Water Resources, California Institute of Technology, Pasadena, Calif., 1977.

O'Brien, M. P. and Morison J. R., "The Forces Exerted by Waves on Objects," *Transactions of the American Geophysical Union*, Vol. 33, No.1, Feb.,1952, pp. 32-38

Prandtl, L., *Essentials of Fluid Dynamics*, Hafner Publishing Co., New York, New York, 1967.

Rosenthal, G. N. and Sleath, J. F. A., "Measurement of Lift in Oscillating Flow," *Journal Fluid Mechanics*, Vol. 164, 1986, pp. 449-467.

Sarpkaya, T., "Forces on Cylinders and Spheres in a Sinusoidally Oscillating Fluid," *Journal of Applied Mechanics*, ASME, Mar., 1975.

Skjelbreia, J. E., "Observations of Breaking Waves on Sloping Bottoms by Use of Laser Doppler Velocimetry," *Report No. KH-R-48*, W. M. Keck Laboratory of Hydraulic and Water Resources, California Institute of Technology, Pasadena, Calif., 1987.

Sleath, J. F., *Sea Bed Mechanics*, Wiley Interscience, New York, New York, 1984.

Willetts, B. B. and Murray, C. G., "Lift Exerted on Stationary Spheres in Turbulent Flow," *Journal of Fluid Mechanics*, Vol. 105, 1981, pp. 487-505.

APPENDIX II - NOTATION

The following symbols are used in this paper:

C_D	=	drag force coefficient;
C_L	=	lift force coefficient;
C_M	=	inertial force coefficient;
c	=	wave celerity;
D	=	sphere diameter;
Err	=	error in determination of force coefficients;
F	=	clearance between bottom of sphere and bottom of tank;
F_{inline}, F_x, F_y, F_{mi}, F_{pi}, F_D, F_I	=	force acting on sphere;
g	=	acceleration of gravity;
h	=	water depth;
H	=	maximum wave amplitude;
L	=	separation distance between spheres;
q	=	total water particle velocity;
S	=	water particle excursion from mean position;
t	=	time;
T	=	wave period;
u	=	horizontal water particle velocity;
U_m	=	maximum intensity of sinusiodal current;
v	=	vertical water particle velocity;

W	=	spacing of screen bank from upstream sphere face;
x, z	=	spatial coordinates in longitudinal and vertical face;
η	=	water surface elevation;
ν	=	angular frequency; and
ρ	=	water density.

APPENDIX B
LIST OF EXPERIMENTAL RUNS

Abbreviations:

NB	=	Non-breaking Wave
B	=	Breaking Wave
H	=	Wave Height
x	=	Distance from Edge of Test Section
L	=	Length of Test Section (1.5 m)
h	=	Still Water Depth
h_b	=	Water Depth at Breaking
LDV	=	Laser Doppler Velocimeter
WG	=	Wave Gauge
z_m	=	Measured Elevation from Top of Rock Bed

Run #	Run File	Wave Type	Rock/ Plate	Tank Slope	H (cm)	x/L (cm)	h (cm)	Type of Observation
1	DIS1DAT	NB	Plate	0.00	4.4	-0.80	26.0	WG
2	DIS2DAT	NB	Plate	0.00	4.4	-0.59	26.0	WG
3	DIS3DAT	NB	Plate	0.00	4.4	-0.28	26.0	WG
4	DIS4DAT	NB	Plate	0.00	4.4	-0.02	26.0	WG
5	LDV1BASE	NB	Plate	0.00	4.7	-0.53	26.0	LDV/WG, z_m=6.0cm
6	LDV2BASE	NB	Plate	0.00	4.7	-0.53	26.0	LDV/WG, z_m=5.0cm
7	LDV3BASE	NB	Plate	0.00	4.7	-0.53	26.0	LDV/WG, z_m=4.0cm
8	LDV4BASE	NB	Plate	0.00	4.7	-0.53	26.0	LDV/WG, z_m=3.0cm
9	LDV5BASE	NB	Plate	0.00	4.7	-0.53	26.0	LDV/WG, z_m=2.0cm
10	LDV6BASE	NB	Plate	0.00	4.7	-0.53	26.0	LDV/WG, z_m=1.5cm
11	LDV7BASE	NB	Plate	0.00	4.7	-0.53	26.0	LDV/WG, z_m=1.0cm
12	LDV8BASE	NB	Plate	0.00	4.7	-0.53	26.0	LDV/WG, z_m=0.6cm
13	LDV9BASE	NB	Plate	0.00	4.7	-0.53	26.0	LDV/WG, z_m=0.3cm
14	LDVABASE	NB	Plate	0.00	4.7	-0.53	26.0	LDV/WG, z_m=0.2cm
15	LDVBBASE	NB	Plate	0.00	4.7	-0.53	26.0	LDV/WG, z_m=0.1cm
16	LDVCBASE	NB	Plate	0.00	4.7	-0.53	26.0	LDV/WG, z_m=0.07cm
17	LDV1A	NB	Rock	0.00	4.7	0.05	26.0	LDV/WG, z_m=5.0cm
18	LDV2A	NB	Rock	0.00	4.7	0.05	26.0	LDV/WG, z_m=5.0cm
19	LDV3A	NB	Rock	0.00	4.7	0.05	26.0	LDV/WG, z_m=2.0cm
20	LDV4A	NB	Rock	0.00	4.7	0.05	26.0	LDV/WG, z_m=2.0cm
21	LDV5A	NB	Rock	0.00	4.7	0.05	26.0	LDV/WG, z_m=1.0cm
22	LDV6A	NB	Rock	0.00	4.7	0.05	26.0	LDV/WG, z_m=0.6cm
23	LDV7A	NB	Rock	0.00	4.7	0.05	26.0	LDV/WG, z_m=0.6cm
24	LDV8A	NB	Rock	0.00	4.7	0.05	26.0	LDV/WG, z_m=0.3cm
25	LDV9A	NB	Rock	0.00	4.7	0.05	26.0	LDV/WG, z_m=0.3cm

Run #	Run File	Wave Type	Rock/ Plate	Tank Slope	H (cm)	x/L (cm)	h (cm)	Type of Observation
26	LDVAA	NB	Rock	0.00	4.7	0.05	26.0	LDV/WG, z_m=0.2cm
27	LDVBA	NB	Rock	0.00	4.7	0.05	26.0	LDV/WG, z_m=0.1cm
28	LDVCA	NB	Rock	0.00	4.7	0.05	26.0	LDV/WG, z_m=0.07cm
29	LDVDA	NB	Rock	0.00	4.7	0.05	26.0	LDV/WG, z_m=0.05cm
30	LDVEA	NB	Rock	0.00	4.7	0.05	26.0	LDV/WG, z_m=0.1cm
31	LDVFA	NB	Rock	0.00	4.7	0.05	26.0	LDV/WG, z_m=0.3cm
32	LDVGA	NB	Rock	0.00	4.7	0.05	26.0	LDV/WG, z_m=0.03cm
33	LDV0A	NB	Rock	0.00	4.7	0.05	26.0	LDV/WG, z_m=0.01cm
34	LDV1B	NB	Rock	0.00	4.7	0.48	26.0	LDV/WG, z_m=5.0cm
35	LDV2B	NB	Rock	0.00	4.7	0.48	26.0	LDV/WG, z_m=2.0cm
36	LDV3B	NB	Rock	0.00	4.7	0.48	26.0	LDV/WG, z_m=1.0cm
37	LDV4B	NB	Rock	0.00	4.7	0.48	26.0	LDV/WG, z_m=0.5cm
38	LDV5B	NB	Rock	0.00	4.7	0.48	26.0	LDV/WG, z_m=0.2cm
39	LDV6B	NB	Rock	0.00	4.7	0.48	26.0	LDV, z_m=0.1cm
40	LDV7B	NB	Rock	0.00	4.7	0.48	26.0	LDV, z_m=0.05cm
41	LDV8B	NB	Rock	0.00	4.7	0.48	26.0	LDV, z_m=0.02cm
42	LDV1C	NB	Rock	0.00	4.7	0.91	26.0	LDV, z_m=5.0cm
43	LDV2C	NB	Rock	0.00	4.7	0.91	26.0	LDV, z_m=2.0cm
44	LDV3C	NB	Rock	0.00	4.7	0.91	26.0	LDV, z_m=1.0cm
45	LDV4C	NB	Rock	0.00	4.7	0.91	26.0	LDV, z_m=0.5cm
46	LDV5C	NB	Rock	0.00	4.7	0.91	26.0	LDV, z_m=0.2cm
47	LDV6C	NB	Rock	0.00	4.7	0.91	26.0	LDV, z_m=0.1cm
48	LDV7C	NB	Rock	0.00	4.7	0.91	26.0	LDV, z_m=0.05cm
49	LDV8C	NB	Rock	0.00	4.7	0.91	26.0	LDV, z_m=0.02cm
50	DISWAV1	NB	Plate	0.00	4.7	-0.99	26.0	WG
51	DISWAV2	NB	Plate	0.00	4.7	-0.70	26.0	WG
52	DISWAV3	NB	Plate	0.00	4.7	-0.37	26.0	WG
53	DISWAV4	NB	Plate	0.00	4.7	-0.10	26.0	WG
54	DISWAV5	NB	Rock	0.00	4.7	-0.10	26.0	WG
55	DISWAV6	NB	Rock	0.00	4.7	0.37	26.0	WG
56	DISWAV7	NB	Rock	0.00	4.7	0.67	26.0	WG
57	DISWAV8	NB	Rock	0.00	4.7	0.87	26.0	WG

Run #	Run File	Wave Type	Rock/ Plate	Tank Slope	H (cm)	h_b (cm)	h (cm)	Type of Observation
58	BKA1A/B	B	Rock	0.02	14.7	13.8	13.8	Video Overhead/WG
59	BKA2A/B	B	Rock	0.02	14.7	13.8	13.8	Video Overhead/WG
60	BKA3A/B	B	Rock	0.02	14.7	13.8	13.8	Video Overhead/WG
61	BKA4A/B	B	Rock	0.02	14.7	13.8	13.8	Video Overhead/WG
62	BKA5A/B	B	Rock	0.02	14.7	13.8	13.8	Video Overhead/WG
63	BKA6A/B	B	Rock	0.02	14.7	13.8	13.8	Video Overhead/WG
64	BKA7A/B	B	Rock	0.02	14.7	13.8	13.8	Video Overhead
65	BKA8A/B	B	Rock	0.02	14.7	13.8	13.8	Video Overhead

Run #	Run File	Wave Type	Rock/ Plate	Tank Slope	H (cm)	h_b (cm)	h (cm)	Type of Observation
66	BKA9A/B	B	Rock	0.02	14.7	13.8	13.8	Video Overhead
67	BKA10A/B	B	Rock	0.02	14.7	13.8	13.8	Video Overhead
68	BKA11A/B	B	Rock	0.02	14.7	13.8	13.8	Video Overhead
69	BKA12A/B	B	Rock	0.02	14.7	13.8	13.8	Video Overhead
70	BKA13A/B	B	Rock	0.02	14.7	13.8	13.8	Video Overhead
71	BKA14A/B	B	Rock	0.02	14.7	13.8	13.8	Video Overhead
72	BKA15A/B	B	Rock	0.02	14.7	13.8	13.8	Video Overhead
73	BKA16A/B	B	Rock	0.02	14.7	13.8	13.8	Video Overhead
74	BKA17A/B	B	Rock	0.02	14.7	13.8	13.8	Video Overhead
75	BKA18A/B	B	Rock	0.02	14.7	13.8	13.8	Video Overhead
76	BKA19A/B	B	Rock	0.02	14.7	13.8	13.8	Video Overhead
77	BKA20A/B	B	Rock	0.02	14.7	13.8	13.8	Video Overhead
78	BKB1A/B	B	Rock	0.02	14.7	13.8	13.1	Video Overhead
79	BKB2A/B	B	Rock	0.02	14.7	13.8	13.1	Video Overhead
80	BKB3A/B	B	Rock	0.02	14.7	13.8	13.1	Video Overhead
81	BKB4A/B	B	Rock	0.02	14.7	13.8	13.1	Video Overhead
82	BKB5A/B	B	Rock	0.02	14.7	13.8	13.1	Video Overhead
83	BKB6A/B	B	Rock	0.02	14.7	13.8	13.1	Video Overhead
84	BKB7A/B	B	Rock	0.02	14.7	13.8	13.1	Video Overhead
85	BKB8A/B	B	Rock	0.02	14.7	13.8	13.1	Video Overhead
86	BKB9A/B	B	Rock	0.02	14.7	13.8	13.1	Video Overhead
87	BKB10A/B	B	Rock	0.02	14.7	13.8	13.1	Video Overhead
88	BKB11A/B	B	Rock	0.02	14.7	13.8	13.1	Video Overhead
89	BKB12A/B	B	Rock	0.02	14.7	13.8	13.1	Video Overhead
90	BKB13A/B	B	Rock	0.02	14.7	13.8	13.1	Video Overhead
91	BKB14A/B	B	Rock	0.02	14.7	13.8	13.1	Video Overhead
92	BKB15A/B	B	Rock	0.02	14.7	13.8	13.1	Video Overhead
93	BKC1A/B	B	Rock	0.02	14.7	13.8	12.5	Video Overhead
94	BKC2A/B	B	Rock	0.02	14.7	13.8	12.5	Video Overhead
95	BKC3A/B	B	Rock	0.02	14.7	13.8	12.5	Video Overhead
96	BKC4A/B	B	Rock	0.02	14.7	13.8	12.5	Video Overhead
97	BKC5A/B	B	Rock	0.02	14.7	13.8	12.5	Video Overhead
98	BKC6A/B	B	Rock	0.02	14.7	13.8	12.5	Video Overhead
99	BKC7A/B	B	Rock	0.02	14.7	13.8	12.5	Video Overhead
100	BKC8A/B	B	Rock	0.02	14.7	13.8	12.5	Video Overhead
101	BKC9A/B	B	Rock	0.02	14.7	13.8	12.5	Video Overhead
102	BKC10A/B	B	Rock	0.02	14.7	13.8	12.5	Video Overhead
103	BKC11A/B	B	Rock	0.02	14.7	13.8	12.5	Video Overhead
104	BKC12A/B	B	Rock	0.02	14.7	13.8	12.5	Video Overhead
105	BKC13A/B	B	Rock	0.02	14.7	13.8	12.5	Video Overhead
106	BKC14A/B	B	Rock	0.02	14.7	13.8	12.5	Video Overhead
107	BKC15A/B	B	Rock	0.02	14.7	13.8	12.5	Video Overhead

Run #	Run File	Wave Type	Rock/ Plate	Tank Slope	H (cm)	h_b (cm)	h (cm)	Type of Observation
108	LDVA1	B	Rock	0.02	14.7	13.8	14.0	LDV/WG, z_m=5.0cm
109	LDVA2	B	Rock	0.02	14.7	13.8	14.0	LDV/WG, z_m=2.0cm
110	LDVA3	B	Rock	0.02	14.7	13.8	14.0	LDV/WG, z_m=1.0cm
111	LDVA4	B	Rock	0.02	14.7	13.8	14.0	LDV/WG, z_m=0.5cm
112	LDVA5	B	Rock	0.02	14.7	13.8	14.0	LDV/WG, z_m=0.5cm
113	LDVA6	B	Rock	0.02	14.7	13.8	14.0	LDV/WG, z_m=0.5cm
114	LDVA7	B	Rock	0.02	14.7	13.8	14.0	LDV/WG, z_m=0.2cm
115	LDVA8	B	Rock	0.02	14.7	13.8	14.0	LDV/WG, z_m=0.2cm
116	LDVA9	B	Rock	0.02	14.7	13.8	14.0	LDV/WG, z_m=0.2cm
117	LDVA10	B	Rock	0.02	14.7	13.8	14.0	LDV/WG, z_m=0.2cm
118	LDVA11	B	Rock	0.02	14.7	13.8	14.0	LDV/WG, z_m=0.2cm
119	LDVA12	B	Rock	0.02	14.7	13.8	14.0	LDV/WG, z_m=0.1cm
120	LDVA13	B	Rock	0.02	14.7	13.8	14.0	LDV/WG, z_m=0.1cm
121	LDVA14	B	Rock	0.02	14.7	13.8	14.0	LDV/WG, z_m=0.1cm
122	LDVA15	B	Rock	0.02	14.7	13.8	14.0	LDV/WG, z_m=0.1cm
123	LDVB1	B	Rock	0.02	14.7	13.8	13.8	LDV/WG, z_m=5.0cm
124	LDVB2	B	Rock	0.02	14.7	13.8	13.8	LDV/WG, z_m=2.0cm
125	LDVB3	B	Rock	0.02	14.7	13.8	13.8	LDV/WG, z_m=1.0cm
126	LDVB4	B	Rock	0.02	14.7	13.8	13.8	LDV/WG, z_m=0.6cm
127	LDVB5	B	Rock	0.02	14.7	13.8	13.8	LDV/WG, z_m=0.5cm
128	LDVB6	B	Rock	0.02	14.7	13.8	13.8	LDV/WG, z_m=0.2cm
129	LDVB7	B	Rock	0.02	14.7	13.8	13.8	LDV/WG, z_m=0.2cm
130	LDVB8	B	Rock	0.02	14.7	13.8	13.8	LDV/WG, z_m=0.2cm
131	LDVB9	B	Rock	0.02	14.7	13.8	13.8	LDV/WG, z_m=0.2cm
132	LDVB10	B	Rock	0.02	14.7	13.8	13.8	LDV/WG, z_m=0.1cm
133	LDVB11	B	Rock	0.02	14.7	13.8	13.8	LDV/WG, z_m=0.1cm
134	LDVB12	B	Rock	0.02	14.7	13.8	13.8	LDV/WG, z_m=0.1cm
135	LDVB13	B	Rock	0.02	14.7	13.8	13.8	LDV/WG, z_m=0.1cm
136	LDVC1	B	Rock	0.02	14.7	13.8	13.6	LDV/WG, z_m=5.0cm
137	LDVC2	B	Rock	0.02	14.7	13.8	13.6	LDV/WG, z_m=1.9cm
138	LDVC3	B	Rock	0.02	14.7	13.8	13.6	LDV/WG, z_m=1.0cm
139	LDVC4	B	Rock	0.02	14.7	13.8	13.6	LDV/WG, z_m=0.5cm
140	LDVC5	B	Rock	0.02	14.7	13.8	13.6	LDV/WG, z_m=0.5cm
141	LDVC6	B	Rock	0.02	14.7	13.8	13.6	LDV/WG, z_m=0.2cm
142	LDVC7	B	Rock	0.02	14.7	13.8	13.6	LDV/WG, z_m=0.2cm
143	LDVC8	B	Rock	0.02	14.7	13.8	13.6	LDV/WG, z_m=0.2cm
144	LDVC9	B	Rock	0.02	14.7	13.8	13.6	LDV/WG, z_m=0.1cm
145	LDVC10	B	Rock	0.02	14.7	13.8	13.6	LDV/WG, z_m=0.1cm
146	LDVC11	B	Rock	0.02	14.7	13.8	13.6	LDV/WG, z_m=0.1cm
147	LDVC12	B	Rock	0.02	14.7	13.8	13.6	LDV/WG, z_m=0.1cm
148	LDVD1	B	Rock	0.02	14.7	13.8	13.1	LDV/WG, z_m=5.0cm
149	LDVD2	B	Rock	0.02	14.7	13.8	13.1	LDV/WG, z_m=2.0cm
150	LDVD3	B	Rock	0.02	14.7	13.8	13.1	LDV/WG, z_m=1.0cm

Run #	Run File	Wave Type	Rock/ Plate	Tank Slope	H (cm)	h_b (cm)	h (cm)	Type of Observation
151	LDVD4	B	Rock	0.02	14.7	13.8	13.1	LDV/WG, z_m=0.5cm
152	LDVD5	B	Rock	0.02	14.7	13.8	13.1	LDV/WG, z_m=0.5cm
153	LDVD6	B	Rock	0.02	14.7	13.8	13.1	LDV/WG, z_m=0.5cm
154	LDVD7	B	Rock	0.02	14.7	13.8	13.1	LDV/WG, z_m=0.2cm
155	LDVD8	B	Rock	0.02	14.7	13.8	13.1	LDV/WG, z_m=0.2cm
156	LDVD9	B	Rock	0.02	14.7	13.8	13.1	LDV/WG, z_m=0.2cm
157	LDVD10	B	Rock	0.02	14.7	13.8	13.1	LDV/WG, z_m=0.1cm
158	LDVD11	B	Rock	0.02	14.7	13.8	13.1	LDV/WG, z_m=0.1cm
159	LDVD12	B	Rock	0.02	14.7	13.8	13.1	LDV/WG, z_m=0.1cm
160	LDVD13	B	Rock	0.02	14.7	13.8	13.1	LDV/WG, z_m=0.1cm
161	LDVE1	B	Rock	0.02	14.7	13.8	12.5	LDV/WG, z_m=5.0cm
162	LDVE2	B	Rock	0.02	14.7	13.8	12.5	LDV/WG, z_m=2.0cm
163	LDVE3	B	Rock	0.02	14.7	13.8	12.5	LDV/WG, z_m=2.0cm
164	LDVE4	B	Rock	0.02	14.7	13.8	12.5	LDV/WG, z_m=1.0cm
165	LDVE5	B	Rock	0.02	14.7	13.8	12.5	LDV/WG, z_m=0.5cm
166	LDVE6	B	Rock	0.02	14.7	13.8	12.5	LDV/WG, z_m=0.2cm
167	LDVE7	B	Rock	0.02	14.7	13.8	12.5	LDV/WG, z_m=0.2cm
168	LDVE8	B	Rock	0.02	14.7	13.8	12.5	LDV/WG, z_m=0.2cm
169	LDVE9	B	Rock	0.02	14.7	13.8	12.5	LDV/WG, z_m=0.1cm
170	LDVE10	B	Rock	0.02	14.7	13.8	12.5	LDV/WG, z_m=0.1cm
171	LDVE11	B	Rock	0.02	14.7	13.8	12.5	LDV/WG, z_m=0.1cm
172	SLDVA1	B	Plate	0.02	14.7	13.8	14.0	LDV/WG, z_m=5.0cm
173	SLDVA2	B	Plate	0.02	14.7	13.8	14.0	LDV/WG, z_m=2.0cm
174	SLDVA3	B	Plate	0.02	14.7	13.8	14.0	LDV/WG, z_m=1.0cm
175	SLDVA4	B	Plate	0.02	14.7	13.8	14.0	LDV/WG, z_m=0.5cm
176	SLDVA5	B	Plate	0.02	14.7	13.8	14.0	LDV/WG, z_m=0.2cm
177	SLDVA6	B	Plate	0.02	14.7	13.8	14.0	LDV/WG, z_m=0.2cm
178	SLDVA7	B	Plate	0.02	14.7	13.8	14.0	LDV/WG, z_m=0.1cm
179	SLDVB1	B	Plate	0.02	14.7	13.8	13.8	LDV/WG, z_m=5.0cm
180	SLDVB2	B	Plate	0.02	14.7	13.8	13.8	LDV/WG, z_m=2.0cm
181	SLDVB3	B	Plate	0.02	14.7	13.8	13.8	LDV/WG, z_m=1.0cm
182	SLDVB4	B	Plate	0.02	14.7	13.8	13.8	LDV/WG, z_m=0.5cm
183	SLDVB5	B	Plate	0.02	14.7	13.8	13.8	LDV/WG, z_m=0.2cm
184	SLDVB6	B	Plate	0.02	14.7	13.8	13.8	LDV/WG, z_m=0.1cm
185	SLDVC1	B	Plate	0.02	14.7	13.8	13.6	LDV/WG, z_m=5.0cm
186	SLDVC2	B	Plate	0.02	14.7	13.8	13.6	LDV/WG, z_m=2.0cm
187	SLDVC3	B	Plate	0.02	14.7	13.8	13.6	LDV/WG, z_m=1.0cm
188	SLDVC4	B	Plate	0.02	14.7	13.8	13.6	LDV/WG, z_m=0.5cm
189	SLDVC5	B	Plate	0.02	14.7	13.8	13.6	LDV/WG, z_m=0.2cm
190	SLDVC6	B	Plate	0.02	14.7	13.8	13.6	LDV/WG, z_m=0.1cm
191	SLDVD1	B	Plate	0.02	14.7	13.8	13.1	LDV/WG, z_m=5.0cm
192	SLDVD2	B	Plate	0.02	14.7	13.8	13.1	LDV/WG, z_m=2.0cm
193	SLDVD3	B	Plate	0.02	14.7	13.8	13.1	LDV/WG, z_m=1.0cm

Run #	Run File	Wave Type	Rock/ Plate	Tank Slope	H (cm)	h_b (cm)	h (cm)	Type of Observation
194	SLDVD4	B	Plate	0.02	14.7	13.8	13.1	LDV/WG, z_m=0.5cm
195	SLDVD5	B	Plate	0.02	14.7	13.8	13.1	LDV/WG, z_m=0.2cm
196	SLDVD6	B	Plate	0.02	14.7	13.8	13.1	LDV/WG, z_m=0.1cm
197	SLDVE1	B	Plate	0.02	14.7	13.8	12.5	LDV/WG, z_m=5.0cm
198	SLDVE2	B	Plate	0.02	14.7	13.8	12.5	LDV/WG, z_m=2.0cm
199	SLDVE3	B	Plate	0.02	14.7	13.8	12.5	LDV/WG, z_m=1.0cm
200	SLDVE4	B	Plate	0.02	14.7	13.8	12.5	LDV/WG, z_m=0.5cm
201	SLDVE5	B	Plate	0.02	14.7	13.8	12.5	LDV/WG, z_m=0.2cm
202	SLDVE6	B	Plate	0.02	14.7	13.8	12.5	LDV/WG, z_m=0.1cm
203	1A1A/B	B	Rock	0.02	9.9	10.1	10.1	Video Overhead
204	1A2A/B	B	Rock	0.02	9.9	10.1	10.1	Video Overhead
205	1A3A/B	B	Rock	0.02	9.9	10.1	10.1	Video Overhead
206	1A4A/B	B	Rock	0.02	9.9	10.1	10.1	Video Overhead
207	1A5A/B	B	Rock	0.02	9.9	10.1	10.1	Video Overhead
208	1A6A/B	B	Rock	0.02	9.9	10.1	10.1	Video Overhead
209	1A7A/B	B	Rock	0.02	9.9	10.1	10.1	Video Overhead
210	1A8A/B	B	Rock	0.02	9.9	10.1	10.1	Video Overhead
211	1A9A/B	B	Rock	0.02	9.9	10.1	10.1	Video Overhead
212	1A10A/B	B	Rock	0.02	9.9	10.1	10.1	Video Overhead
213	1A11A/B	B	Rock	0.02	9.9	10.1	10.1	Video Overhead/WG
214	1A12A/B	B	Rock	0.02	9.9	10.1	10.1	Video Overhead/WG
215	1A13A/B	B	Rock	0.02	9.9	10.1	10.1	Video Overhead/WG
216	1A14A/B	B	Rock	0.02	9.9	10.1	10.1	Video Overhead/WG
217	1A15A/B	B	Rock	0.02	9.9	10.1	10.1	Video Overhead/WG
218	1B1A/B	B	Rock	0.02	9.9	10.1	10.1	Video Overhead/WG
219	1B2A/B	B	Rock	0.02	9.9	10.1	9.4	Video Overhead/WG
220	1B3A/B	B	Rock	0.02	9.9	10.1	9.4	Video Overhead/WG
221	1B4A/B	B	Rock	0.02	9.9	10.1	9.4	Video Overhead/WG
222	1B5A/B	B	Rock	0.02	9.9	10.1	9.4	Video Overhead
223	1B6A/B	B	Rock	0.02	9.9	10.1	9.4	Video Overhead
224	1B7A/B	B	Rock	0.02	9.9	10.1	9.4	Video Overhead
225	1B8A/B	B	Rock	0.02	9.9	10.1	9.4	Video Overhead/WG
226	1B9A/B	B	Rock	0.02	9.9	10.1	9.4	Video Overhead/WG
227	1B10A/B	B	Rock	0.02	9.9	10.1	9.4	Video Overhead/WG
228	1B11A/B	B	Rock	0.02	9.9	10.1	9.4	Video Overhead/WG
229	1B12A/B	B	Rock	0.02	9.9	10.1	9.4	Video Overhead/WG
230	1B13A/B	B	Rock	0.02	9.9	10.1	9.4	Video Overhead/WG
231	1B14A/B	B	Rock	0.02	9.9	10.1	9.4	Video Overhead/WG
232	1B15A/B	B	Rock	0.02	9.9	10.1	9.4	Video Overhead/WG
233	1C1A/B	B	Rock	0.02	9.9	10.1	8.8	Video Overhead/WG
234	1C2A/B	B	Rock	0.02	9.9	10.1	8.8	Video Overhead/WG
235	1C3A/B	B	Rock	0.02	9.9	10.1	8.8	Video Overhead/WG
236	1C4A/B	B	Rock	0.02	9.9	10.1	8.8	Video Overhead/WG

Run #	Run File	Wave Type	Rock/ Plate	Tank Slope	H (cm)	h_b (cm)	h (cm)	Type of Observation
237	1C5A/B	B	Rock	0.02	9.9	10.1	8.8	Video Overhead/WG
238	1C6A/B	B	Rock	0.02	9.9	10.1	8.8	Video Overhead/WG
239	1C7A/B	B	Rock	0.02	9.9	10.1	8.8	Video Overhead/WG
240	1C8A/B	B	Rock	0.02	9.9	10.1	8.8	Video Overhead/WG
241	1C9A/B	B	Rock	0.02	9.9	10.1	8.8	Video Overhead/WG
242	1C10A/B	B	Rock	0.02	9.9	10.1	8.8	Video Overhead/WG
243	1C11A/B	B	Rock	0.02	9.9	10.1	8.8	Video Overhead/WG
244	1C12A/B	B	Rock	0.02	9.9	10.1	8.8	Video Overhead/WG
245	1C13A/B	B	Rock	0.02	9.9	10.1	8.8	Video Overhead/WG
246	1C14A/B	B	Rock	0.02	9.9	10.1	8.8	Video Overhead/WG
247	1C15A/B	B	Rock	0.02	9.9	10.1	8.8	Video Overhead/WG
248	2A1A/B	B	Rock	0.02	7.6	7.9	7.9	Video Ovhd/Side/WG
249	2A2A/B	B	Rock	0.02	7.6	7.9	7.9	Video Ovhd/Side/WG
250	2A3A/B	B	Rock	0.02	7.6	7.9	7.9	Video Ovhd/Side/WG
251	2A4A/B	B	Rock	0.02	7.6	7.9	7.9	Video Ovhd/Side/WG
252	2A5A/B	B	Rock	0.02	7.6	7.9	7.9	Video Ovhd/Side/WG
253	2A6A/B	B	Rock	0.02	7.6	7.9	7.9	Video Ovhd/Side/WG
254	2A7A/B	B	Rock	0.02	7.6	7.9	7.9	Video Ovhd/Side/WG
255	2A8A/B	B	Rock	0.02	7.6	7.9	7.9	Video Ovhd/Side/WG
256	2A9A/B	B	Rock	0.02	7.6	7.9	7.9	Video Ovhd/Side/WG
257	2A10A/B	B	Rock	0.02	7.6	7.9	7.9	Video Ovhd/Side/WG
258	2A12A/B	B	Rock	0.02	7.6	7.9	7.9	Video Overhead/WG
259	2A12A/B	B	Rock	0.02	7.6	7.9	7.9	Video Overhead/WG
260	2A13A/B	B	Rock	0.02	7.6	7.9	7.9	Video Overhead/WG
261	2A14A/B	B	Rock	0.02	7.6	7.9	7.9	Video Overhead/WG
262	2A15A/B	B	Rock	0.02	7.6	7.9	7.9	Video Overhead/WG
263	2B1A/B	B	Rock	0.02	7.6	7.9	7.1	Video Ovhd/Side/WG
264	2B2A/B	B	Rock	0.02	7.6	7.9	7.1	Video Ovhd/Side/WG
265	2B3A/B	B	Rock	0.02	7.6	7.9	7.1	Video Ovhd/Side/WG
266	2B4A/B	B	Rock	0.02	7.6	7.9	7.1	Video Ovhd/Side/WG
267	2B5A/B	B	Rock	0.02	7.6	7.9	7.1	Video Ovhd/Side/WG
268	2B6A/B	B	Rock	0.02	7.6	7.9	7.1	Video Ovhd/Side/WG
269	2B7A/B	B	Rock	0.02	7.6	7.9	7.1	Video Ovhd/Side/WG
270	2B8A/B	B	Rock	0.02	7.6	7.9	7.1	Video Ovhd/Side/WG
271	2B9A/B	B	Rock	0.02	7.6	7.9	7.1	Video Ovhd/Side/WG
272	2B10A/B	B	Rock	0.02	7.6	7.9	7.1	Video Ovhd/Side/WG
273	2B11A/B	B	Rock	0.02	7.6	7.9	7.1	Video Overhead/WG
274	2B12A/B	B	Rock	0.02	7.6	7.9	7.1	Video Overhead/WG
275	2B13A/B	B	Rock	0.02	7.6	7.9	7.1	Video Overhead/WG
276	2B14A/B	B	Rock	0.02	7.6	7.9	7.1	Video Overhead/WG
277	2B15A/B	B	Rock	0.02	7.6	7.9	7.1	Video Overhead/WG
278	2C1A/B	B	Rock	0.02	7.6	7.9	6.5	Video Ovhd/Side/WG
279	2C2A/B	B	Rock	0.02	7.6	7.9	6.5	Video Ovhd/Side/WG

Run #	Run File	Wave Type	Rock/ Plate	Tank Slope	H (cm)	h_b (cm)	h (cm)	Type of Observation
280	2C3A/B	B	Rock	0.02	7.6	7.9	6.5	Video Ovhd/Side/WG
281	2C4A/B	B	Rock	0.02	7.6	7.9	6.5	Video Ovhd/Side/WG
282	2C5A/B	B	Rock	0.02	7.6	7.9	6.5	Video Ovhd/Side/WG
283	2C6A/B	B	Rock	0.02	7.6	7.9	6.5	Video Ovhd/Side/WG
284	2C7A/B	B	Rock	0.02	7.6	7.9	6.5	Video Ovhd/Side/WG
285	2C8A/B	B	Rock	0.02	7.6	7.9	6.5	Video Ovhd/Side/WG
286	2C9A/B	B	Rock	0.02	7.6	7.9	6.5	Video Ovhd/Side/WG
287	2C10A/B	B	Rock	0.02	7.6	7.9	6.5	Video Ovhd/Side/WG
288	2C11A/B	B	Rock	0.02	7.6	7.9	6.5	Video Overhead/WG
289	2C12A/B	B	Rock	0.02	7.6	7.9	6.5	Video Overhead/WG
290	2C13A/B	B	Rock	0.02	7.6	7.9	6.5	Video Overhead/WG
291	2C14A/B	B	Rock	0.02	7.6	7.9	6.5	Video Overhead/WG
292	2C15A/B	B	Rock	0.02	7.6	7.9	6.5	Video Overhead/WG
293	3A1A/B	B	Rock	0.02	11.9	11.8	11.8	Video Ovhd/Side/WG
294	3A2A/B	B	Rock	0.02	11.9	11.8	11.8	Video Ovhd/Side/WG
295	3A3A/B	B	Rock	0.02	11.9	11.8	11.8	Video Ovhd/Side/WG
296	3A4A/B	B	Rock	0.02	11.9	11.8	11.8	Video Ovhd/Side/WG
297	3A5A/B	B	Rock	0.02	11.9	11.8	11.8	Video Ovhd/Side/WG
298	3A6A/B	B	Rock	0.02	11.9	11.8	11.8	Video Ovhd/Side/WG
299	3A7A/B	B	Rock	0.02	11.9	11.8	11.8	Video Ovhd/Side/WG
300	3A8A/B	B	Rock	0.02	11.9	11.8	11.8	Video Ovhd/Side/WG
301	3A9A/B	B	Rock	0.02	11.9	11.8	11.8	Video Ovhd/Side/WG
302	3A10A/B	B	Rock	0.02	11.9	11.8	11.8	Video Ovhd/Side/WG
303	3A13A/B	B	Rock	0.02	11.9	11.8	11.8	Video Overhead/WG
304	3A13A/B	B	Rock	0.02	11.9	11.8	11.8	Video Overhead/WG
305	3A13A/B	B	Rock	0.02	11.9	11.8	11.8	Video Overhead/WG
306	3A14A/B	B	Rock	0.02	11.9	11.8	11.8	Video Overhead/WG
307	3A15A/B	B	Rock	0.02	11.9	11.8	11.8	Video Overhead/WG
308	3B1A/B	B	Rock	0.02	11.9	11.8	11.1	Video Ovhd/Side/WG
309	3B2A/B	B	Rock	0.02	11.9	11.8	11.1	Video Ovhd/Side/WG
310	3B3A/B	B	Rock	0.02	11.9	11.8	11.1	Video Ovhd/Side/WG
311	3B4A/B	B	Rock	0.02	11.9	11.8	11.1	Video Ovhd/Side/WG
312	3B5A/B	B	Rock	0.02	11.9	11.8	11.1	Video Ovhd/Side/WG
313	3B6A/B	B	Rock	0.02	11.9	11.8	11.1	Video Ovhd/Side/WG
314	3B7A/B	B	Rock	0.02	11.9	11.8	11.1	Video Ovhd/Side/WG
315	3B8A/B	B	Rock	0.02	11.9	11.8	11.1	Video Ovhd/Side/WG
316	3B9A/B	B	Rock	0.02	11.9	11.8	11.1	Video Ovhd/Side/WG
317	3B10A/B	B	Rock	0.02	11.9	11.8	11.1	Video Ovhd/Side/WG
318	3B11A/B	B	Rock	0.02	11.9	11.8	11.1	Video Overhead/WG
319	3B12A/B	B	Rock	0.02	11.9	11.8	11.1	Video Overhead/WG
320	3B13A/B	B	Rock	0.02	11.9	11.8	11.1	Video Overhead/WG
321	3B14A/B	B	Rock	0.02	11.9	11.8	11.1	Video Overhead/WG
322	3B15A/B	B	Rock	0.02	11.9	11.8	11.1	Video Overhead/WG

Run #	Run File	Wave Type	Rock/ Plate	Tank Slope	H (cm)	h_b (cm)	h (cm)	Type of Observation
323	3C1A/B	B	Rock	0.02	11.9	11.8	10.5	Video Ovhd/Side/WG
324	3C2A/B	B	Rock	0.02	11.9	11.8	10.5	Video Ovhd/Side/WG
325	3C3A/B	B	Rock	0.02	11.9	11.8	10.5	Video Ovhd/Side/WG
326	3C4A/B	B	Rock	0.02	11.9	11.8	10.5	Video Ovhd/Side/WG
327	3C5A/B	B	Rock	0.02	11.9	11.8	10.5	Video Ovhd/Side/WG
328	3C6A/B	B	Rock	0.02	11.9	11.8	10.5	Video Ovhd/Side/WG
329	3C7A/B	B	Rock	0.02	11.9	11.8	10.5	Video Ovhd/Side/WG
330	3C8A/B	B	Rock	0.02	11.9	11.8	10.5	Video Ovhd/Side/WG
331	3C9A/B	B	Rock	0.02	11.9	11.8	10.5	Video Ovhd/Side/WG
332	3C10A/B	B	Rock	0.02	11.9	11.8	10.5	Video Ovhd/Side/WG
333	3C11A/B	B	Rock	0.02	11.9	11.8	10.5	Video Overhead/WG
334	3C12A/B	B	Rock	0.02	11.9	11.8	10.5	Video Overhead/WG
335	3C13A/B	B	Rock	0.02	11.9	11.8	10.5	Video Overhead/WG
336	3C14A/B	B	Rock	0.02	11.9	11.8	10.5	Video Overhead/WG
337	3C15A/B	B	Rock	0.02	11.9	11.8	10.5	Video Overhead/WG
338	L24A1	B	Rock	0.02	14.7	13.8	13.8	LDV/WG, z_m=5.0cm
339	L24A2	B	Rock	0.02	14.7	13.8	13.8	LDV/WG, z_m=0.3cm
340	L24A2A	B	Rock	0.02	14.7	13.8	13.8	LDV/WG, z_m=0.3cm
341	L24A3	B	Rock	0.02	14.7	13.8	13.8	LDV/WG, z_m=0.2cm
342	L24A3A	B	Rock	0.02	14.7	13.8	13.8	LDV/WG, z_m=0.2cm
343	L24A4	B	Rock	0.02	14.7	13.8	13.8	LDV/WG, z_m=0.1cm
344	L24A4A	B	Rock	0.02	7.6	13.8	13.8	LDV/WG, z_m=0.1cm
345	L24A4B	B	Rock	0.02	7.6	13.8	13.8	LDV/WG, z_m=0.1cm
346	L24B1	B	Rock	0.02	7.6	13.8	13.1	LDV/WG, z_m=5.0cm
347	L24B2	B	Rock	0.02	7.6	13.8	13.1	LDV/WG, z_m=0.3cm
348	L24B3	B	Rock	0.02	7.6	13.8	13.1	LDV/WG, z_m=0.2cm
349	L24B4	B	Rock	0.02	7.6	13.8	13.1	LDV/WG, z_m=0.1cm
350	L24C1	B	Rock	0.02	7.6	13.8	12.5	LDV/WG, z_m=5.0cm
351	L24C2	B	Rock	0.02	7.6	13.8	12.5	LDV/WG, z_m=0.3cm
352	L24C3	B	Rock	0.02	7.6	13.8	12.5	LDV/WG, z_m=0.2cm
353	L24C3A	B	Rock	0.02	7.6	13.8	12.5	LDV/WG, z_m=0.2cm
354	L24C4	B	Rock	0.02	7.6	13.8	12.5	LDV/WG, z_m=0.1cm
355	L14C1	B	Rock	0.02	7.6	7.9	6.5	LDV/WG, z_m=5.0cm
356	L14C2	B	Rock	0.02	7.6	7.9	6.5	LDV/WG, z_m=2.0cm
357	L14C3	B	Rock	0.02	7.6	7.9	6.5	LDV/WG, z_m=1.0cm
358	L14C4	B	Rock	0.02	7.6	7.9	6.5	LDV/WG, z_m=0.5cm
359	L14C5	B	Rock	0.02	7.6	7.9	6.5	LDV/WG, z_m=0.3cm
360	L14C6	B	Rock	0.02	7.6	7.9	6.5	LDV/WG, z_m=0.2cm
361	L14C7	B	Rock	0.02	7.6	7.9	6.5	LDV/WG, z_m=0.1cm
362	L14C7A	B	Rock	0.02	7.6	7.9	6.5	LDV/WG, z_m=0.1cm
363	L14C7B	B	Rock	0.02	7.6	7.9	6.5	LDV/WG, z_m=0.1cm
364	L14B1	B	Rock	0.02	7.6	7.9	7.1	LDV/WG, z_m=5.0cm
365	L14B2	B	Rock	0.02	7.6	7.9	7.1	LDV/WG, z_m=2.0cm

Run #	Run File	Wave Type	Rock/ Plate	Tank Slope	H (cm)	h_b (cm)	h (cm)	Type of Observation
366	L14B3	B	Rock	0.02	7.6	7.9	7.1	LDV/WG, z_m=1.0cm
367	L14B4	B	Rock	0.02	7.6	7.9	7.1	LDV/WG, z_m=0.5cm
368	L14B5	B	Rock	0.02	7.6	7.9	7.1	LDV/WG, z_m=0.3cm
369	L14B5A	B	Rock	0.02	7.6	7.9	7.1	LDV/WG, z_m=0.3cm
370	L14B6	B	Rock	0.02	7.6	7.9	7.1	LDV/WG, z_m=0.2cm
371	L14B7	B	Rock	0.02	7.6	7.9	7.1	LDV/WG, z_m=0.1cm
372	L14B7A	B	Rock	0.02	7.6	7.9	7.1	LDV/WG, z_m=0.1cm
373	L14A1	B	Rock	0.02	7.6	7.9	7.9	LDV/WG, z_m=5.0cm
374	L14A2	B	Rock	0.02	7.6	7.9	7.9	LDV/WG, z_m=2.0cm
375	L14A3	B	Rock	0.02	7.6	7.9	7.9	LDV/WG, z_m=1.0cm
376	L14A4	B	Rock	0.02	7.6	7.9	7.9	LDV/WG, z_m=0.5cm
377	L14A5	B	Rock	0.02	7.6	7.9	7.9	LDV/WG, z_m=0.3cm
378	L14A6	B	Rock	0.02	7.6	7.9	7.9	LDV/WG, z_m=0.2cm
379	L14A6A	B	Rock	0.02	7.6	7.9	7.9	LDV/WG, z_m=0.2cm
380	L14A7	B	Rock	0.02	7.6	7.9	7.9	LDV/WG, z_m=0.1cm
381	L14A7A	B	Rock	0.02	7.6	7.9	7.9	LDV/WG, z_m=0.1cm
382	L14A7B	B	Rock	0.02	7.6	7.9	7.9	LDV/WG, z_m=0.1cm
383	L19A1	B	Rock	0.02	9.9	10.1	10.1	LDV/WG, z_m=5.0cm
384	L19A2	B	Rock	0.02	9.9	10.1	10.1	LDV/WG, z_m=2.0cm
385	L19A3	B	Rock	0.02	9.9	10.1	10.1	LDV/WG, z_m=1.0cm
386	L19A4	B	Rock	0.02	9.9	10.1	10.1	LDV/WG, z_m=0.5cm
387	L19A5	B	Rock	0.02	9.9	10.1	10.1	LDV/WG, z_m=0.3cm
388	L19A5A	B	Rock	0.02	9.9	10.1	10.1	LDV/WG, z_m=0.3cm
389	L19A6	B	Rock	0.02	9.9	10.1	10.1	LDV/WG, z_m=0.2cm
390	L19A6A	B	Rock	0.02	9.9	10.1	10.1	LDV/WG, z_m=0.2cm
391	L19A7	B	Rock	0.02	9.9	10.1	10.1	LDV/WG, z_m=0.1cm
392	L19A7A	B	Rock	0.02	9.9	10.1	10.1	LDV/WG, z_m=0.1cm
393	L21A1	B	Rock	0.02	11.9	11.8	11.8	LDV/WG, z_m=5.0cm
394	L21A2	B	Rock	0.02	11.9	11.8	11.8	LDV/WG, z_m=2.0cm
395	L21A3	B	Rock	0.02	11.9	11.8	11.8	LDV/WG, z_m=1.0cm
396	L21A4	B	Rock	0.02	11.9	11.8	11.8	LDV/WG, z_m=0.5cm
397	L21A5	B	Rock	0.02	11.9	11.8	11.8	LDV/WG, z_m=0.3cm
398	L21A5A	B	Rock	0.02	11.9	11.8	11.8	LDV/WG, z_m=0.3cm
399	L21A6	B	Rock	0.02	11.9	11.8	11.8	LDV/WG, z_m=0.2cm
400	L21A6A	B	Rock	0.02	11.9	11.8	11.8	LDV/WG, z_m=0.2cm
401	L21A7	B	Rock	0.02	11.9	11.8	11.8	LDV/WG, z_m=0.1cm
402	L21A7A	B	Rock	0.02	11.9	11.8	11.8	LDV/WG, z_m=0.1cm
403	LP21A1	B	Plate	0.02	11.9	11.8	11.8	LDV/WG, z_m=5.0cm
404	LP21A2	B	Plate	0.02	11.9	11.8	11.8	LDV/WG, z_m=2.0cm
405	LP21A2A	B	Plate	0.02	11.9	11.8	11.8	LDV/WG, z_m=2.0cm
406	LP21A3	B	Plate	0.02	11.9	11.8	11.8	LDV/WG, z_m=1.0cm
407	LP21A4	B	Plate	0.02	11.9	11.8	11.8	LDV/WG, z_m=0.5cm
408	LP21A5	B	Plate	0.02	11.9	11.8	11.8	LDV/WG, z_m=0.3cm

Run #	Run File	Wave Type	Rock/ Plate	Tank Slope	H (cm)	h_b (cm)	h (cm)	Type of Observation
409	LP21A6	B	Plate	0.02	11.9	11.8	11.8	LDV/WG, z_m=0.2cm
410	LP21A7	B	Plate	0.02	11.9	11.8	11.8	LDV/WG, z_m=0.1cm
411	LP19A7	B	Plate	0.02	9.9	11.8	11.8	LDV/WG, z_m=0.1cm
412	LP19A6	B	Plate	0.02	9.9	10.1	10.1	LDV/WG, z_m=0.2cm
413	LP19A5	B	Plate	0.02	9.9	10.1	10.1	LDV/WG, z_m=0.3cm
414	LP19A4	B	Plate	0.02	9.9	10.1	10.1	LDV/WG, z_m=0.5cm
415	LP19A3	B	Plate	0.02	9.9	10.1	10.1	LDV/WG, z_m=1.0cm
416	LP19A2	B	Plate	0.02	9.9	10.1	10.1	LDV/WG, z_m=2.0cm
417	LP19A1	B	Plate	0.02	9.9	10.1	10.1	LDV/WG, z_m=5.0cm
418	LP14A1	B	Plate	0.02	7.6	7.9	7.9	LDV/WG, z_m=5.0cm
419	LP14A2	B	Plate	0.02	7.6	7.9	7.9	LDV/WG, z_m=2.0cm
420	LP14A3	B	Plate	0.02	7.6	7.9	7.9	LDV/WG, z_m=1.0cm
421	LP14A4	B	Plate	0.02	7.6	7.9	7.9	LDV/WG, z_m=0.5cm
422	LP14A5	B	Plate	0.02	7.6	7.9	7.9	LDV/WG, z_m=0.3cm
423	LP14A6	B	Plate	0.02	7.6	7.9	7.9	LDV/WG, z_m=0.2cm
424	LP14A7	B	Plate	0.02	7.6	7.9	7.9	LDV/WG, z_m=0.1cm
425	LP14B1	B	Plate	0.02	7.6	7.9	7.1	LDV/WG, z_m=5.0cm
426	LP14B2	B	Plate	0.02	7.6	7.9	7.1	LDV/WG, z_m=2.0cm
427	LP14B3	B	Plate	0.02	7.6	7.9	7.1	LDV/WG, z_m=1.0cm
428	LP14B4	B	Plate	0.02	7.6	7.9	7.1	LDV/WG, z_m=0.5cm
429	LP14B5	B	Plate	0.02	7.6	7.9	7.1	LDV/WG, z_m=0.3cm
430	LP14B6	B	Plate	0.02	7.6	7.9	7.1	LDV/WG, z_m=0.2cm
431	LP14B7	B	Plate	0.02	7.6	7.9	7.1	LDV/WG, z_m=0.1cm
432	LP14C1	B	Plate	0.02	7.6	7.9	6.5	LDV/WG, z_m=5.0cm
433	LP14C2	B	Plate	0.02	7.6	7.9	6.5	LDV/WG, z_m=2.0cm
434	LP14C3	B	Plate	0.02	7.6	7.9	6.5	LDV/WG, z_m=1.0cm
435	LP14C4	B	Plate	0.02	7.6	7.9	6.5	LDV/WG, z_m=0.5cm
436	LP14C5	B	Plate	0.02	7.6	7.9	6.5	LDV/WG, z_m=0.3cm
437	LP14C6	B	Plate	0.02	7.6	7.9	6.5	LDV/WG, z_m=0.2cm
438	LP14C7	B	Plate	0.02	7.6	7.9	6.5	LDV/WG, z_m=0.1cm
439	STST23	B	Rock	0.02	N/A	N/A	13.8	LDV, z_m=5.0cm
440	STST21	NB	Rock	0.02	N/A	N/A	13.8	LDV, z_m=5.0cm
441	STST19	NB	Rock	0.02	N/A	N/A	13.8	LDV, z_m=5.0cm
442	STST17	NB	Rock	0.02	N/A	N/A	13.8	LDV, z_m=5.0cm
443	STST15	NB	Rock	0.02	N/A	N/A	13.8	LDV, z_m=5.0cm
444	STST13	NB	Rock	0.02	N/A	N/A	13.8	LDV, z_m=5.0cm
445	STST11	NB	Rock	0.02	N/A	N/A	13.8	LDV, z_m=5.0cm
446	STST09	NB	Rock	0.02	N/A	N/A	13.8	LDV/WG, z_m=5.0cm
447	N22A1	NB	Rock	0.02	13.1	12.8	13.8	LDV/WG, z_m=5.0cm
448	N16A1	NB	Rock	0.02	9.5	10.1	13.8	LDV/WG, z_m=5.0cm
449	N22A2	NB	Rock	0.02	13.1	12.8	13.8	LDV/WG, z_m=2.0cm
450	N16A2	NB	Rock	0.02	9.5	10.1	13.8	LDV/WG, z_m=2.0cm
451	N22A3	NB	Rock	0.02	13.1	12.8	13.8	LDV/WG, z_m=1.0cm

Run #	Run File	Wave Type	Rock/ Plate	Tank Slope	H (cm)	h_b (cm)	h (cm)	Type of Observation
452	N16A3	NB	Rock	0.02	9.5	10.1	13.8	LDV/WG, z_m=1.0cm
453	N22A4	NB	Rock	0.02	13.1	12.8	13.8	LDV/WG, z_m=0.5cm
454	N16A4	NB	Rock	0.02	9.5	10.1	13.8	LDV/WG, z_m=0.5cm
455	N22A5	NB	Rock	0.02	13.1	12.8	13.8	LDV/WG, z_m=0.3cm
456	N22A6	NB	Rock	0.02	13.1	12.8	13.8	LDV/WG, z_m=0.3cm
457	N16A5	NB	Rock	0.02	9.5	10.1	13.8	LDV/WG, z_m=0.3cm
458	N22A7	NB	Rock	0.02	13.1	12.8	13.8	LDV/WG, z_m=0.2cm
459	N22A8	NB	Rock	0.02	13.1	12.8	13.8	LDV/WG, z_m=0.2cm
460	N16A6	NB	Rock	0.02	9.5	10.1	13.8	LDV/WG, z_m=0.2cm
461	N22A9	NB	Rock	0.02	13.1	12.8	13.8	LDV/WG, z_m=0.1cm
462	N22A10	NB	Rock	0.02	13.1	12.8	13.8	LDV/WG, z_m=0.1cm
463	N16A7	NB	Rock	0.02	9.5	10.1	13.8	LDV/WG, z_m=0.1cm
464	WAV221	NB	Rock	0.02	13.1	12.8	13.8	Video Overhead/WG
465	WAV222	NB	Rock	0.02	13.1	12.8	13.8	Video Overhead/WG
466	WAV223	NB	Rock	0.02	13.1	12.8	13.8	Video Overhead/WG
467	WAV224	NB	Rock	0.02	13.1	12.8	13.8	Video Overhead/WG
468	WAV225	NB	Rock	0.02	13.1	12.8	13.8	Video Overhead/WG
469	WAV226	NB	Rock	0.02	13.1	12.8	13.8	Video Overhead/WG
470	WAV227	NB	Rock	0.02	13.1	12.8	13.8	Video Overhead/WG
471	WAV228	NB	Rock	0.02	13.1	12.8	13.8	Video Overhead/WG
472	WAV229	NB	Rock	0.02	13.1	12.8	13.8	Video Overhead/WG
473	WAV2210	NB	Rock	0.02	13.1	12.8	13.8	Video Overhead/WG
474	WAV2211	NB	Rock	0.02	13.1	12.8	13.8	Video Overhead/WG
475	WAV2212	NB	Rock	0.02	13.1	12.8	13.8	Video Overhead/WG
476	WAV2213	NB	Rock	0.02	13.1	12.8	13.8	Video Overhead/WG
477	WAV2214	NB	Rock	0.02	13.1	12.8	13.8	Video Overhead/WG
478	WAV2215	NB	Rock	0.02	13.1	12.8	13.8	Video Overhead/WG
479	WAV161	NB	Rock	0.02	9.5	10.1	13.8	Video Overhead/WG
480	WAV162	NB	Rock	0.02	9.5	10.1	13.8	Video Overhead/WG
481	WAV163	NB	Rock	0.02	9.5	10.1	13.8	Video Overhead/WG
482	WAV164	NB	Rock	0.02	9.5	10.1	13.8	Video Overhead/WG
483	WAV165	NB	Rock	0.02	9.5	10.1	13.8	Video Overhead/WG
484	WAV166	NB	Rock	0.02	9.5	10.1	13.8	Video Overhead/WG
485	WAV167	NB	Rock	0.02	9.5	10.1	13.8	Video Overhead/WG
486	WAV168	NB	Rock	0.02	9.5	10.1	13.8	Video Overhead/WG
487	WAV169	NB	Rock	0.02	9.5	10.1	13.8	Video Overhead/WG
488	WAV1610	NB	Rock	0.02	9.5	10.1	13.8	Video Overhead/WG
489	WAV1611	NB	Rock	0.02	9.5	10.1	13.8	Video Overhead/WG
490	WAV1612	NB	Rock	0.02	9.5	10.1	13.8	Video Overhead/WG
491	WAV1613	NB	Rock	0.02	9.5	10.1	13.8	Video Overhead/WG
492	WAV1614	NB	Rock	0.02	9.5	10.1	13.8	Video Overhead/WG
493	WAV1615	NB	Rock	0.02	9.5	10.1	13.8	Video Overhead/WG
494	SWAV241	NB	Rock	0.02	14.7	13.8	13.8	Video Sideview/WG

Run #	Run File	Wave Type	Rock/ Plate	Tank Slope	H (cm)	h_b (cm)	h (cm)	Type of Observation
495	SWAV242	NB	Rock	0.02	14.7	13.8	13.8	Video Sideview/WG
496	SWAV221	NB	Rock	0.02	13.1	12.8	13.8	Video Sideview/WG
497	SWAV222	NB	Rock	0.02	13.1	12.8	13.8	Video Sideview/WG
498	SWAV161	NB	Rock	0.02	9.5	10.1	13.8	Video Sideview/WG
499	SWAV162	NB	Rock	0.02	9.5	10.1	13.8	Video Sideview/WG
500	SWAV191	B	Rock	0.02	9.9	10.1	10.1	Video Sideview/WG
501	SWAV192	B	Rock	0.02	9.9	10.1	10.1	Video Sideview/WG
502	SWAV141	B	Rock	0.02	7.6	7.9	7.9	Video Sideview/WG
503	SWAV142	B	Rock	0.02	7.6	7.9	7.9	Video Sideview/WG

APPENDIX C

ERROR ANALYSIS FOR LASER DOPPLER SYSTEM

The Doppler shift in the frequency of the observed scattered light from a particle is

$$\Delta \upsilon = \frac{n}{\lambda} \vec{q} \cdot (\vec{e}_i - \vec{e}_o) \tag{C.1}$$

where $\Delta\upsilon$ is the difference between the frequency of the incident beam and the observed frequency, n is the index of refraction of water, λ is the vacuum wavelength of the laser, $\vec{q}$ is the particle velocity, and $\vec{e}_i$ and $\vec{e}_o$ are unit vectors in the scatter beam and observation directions respectively.

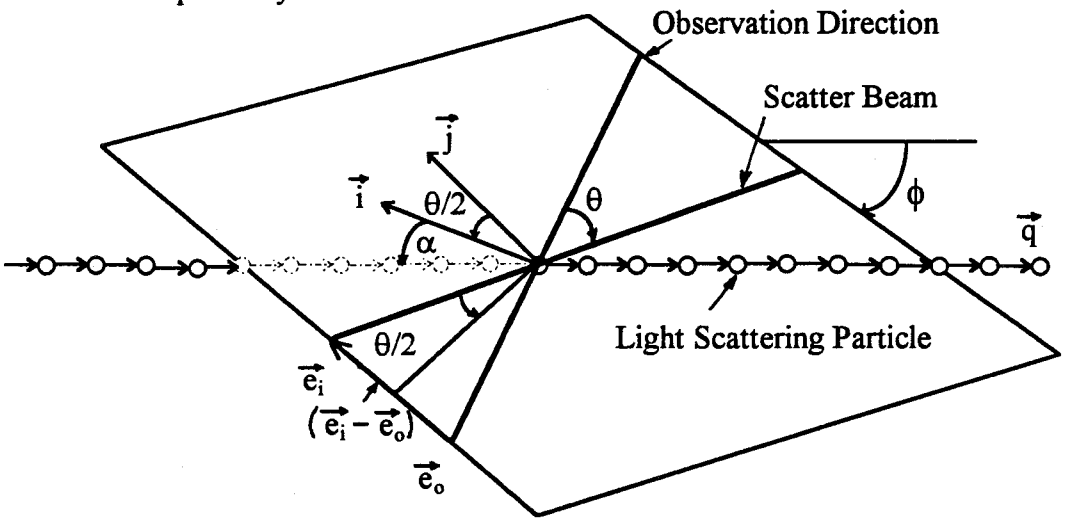

FIG. C.1. Geometry of LDV Plane of Observation.

Figure C.1 represents the plane of observation defined by the observation and scatter beam directions inclined at an angle φ from the horizontal. In this plane the quantity $(\vec{e}_i - \vec{e}_o)$ is given by the relation

$$(\vec{e}_i - \vec{e}_o) = 2 \sin \frac{\theta}{2} \vec{i} \tag{C.2}$$

where $\vec{i}$ is the unit vector perpendicular to the bisector of $\vec{e}_i$ and $\vec{e}_o$. The actual observed Doppler shift measures the velocity component in the direction $\vec{i}$ rather than in the direction directly perpendicular to the scatter beam:

$$\Delta \upsilon = \frac{n}{\lambda}\left(\vec{q}\cdot\vec{i}\right)\left(2\sin\frac{\theta}{2}\right) = \frac{n}{\lambda}\left(|q|\cos\alpha\right)\left(2\sin\frac{\theta}{2}\right) \qquad (C.3)$$

Here α is the angle between the water particle velocity vector and the unit vector $\vec{i}$.

For small $\theta/2$, $(\vec{q}\cdot\vec{i})$ is very close to the component of $\vec{q}$ in the direction perpendicular to the scatter beam and lying in the plane of $\vec{e}_i$ and $\vec{e}_o$. Call this unit vector $\vec{j}$, which is the actual desired direction of the measurements.

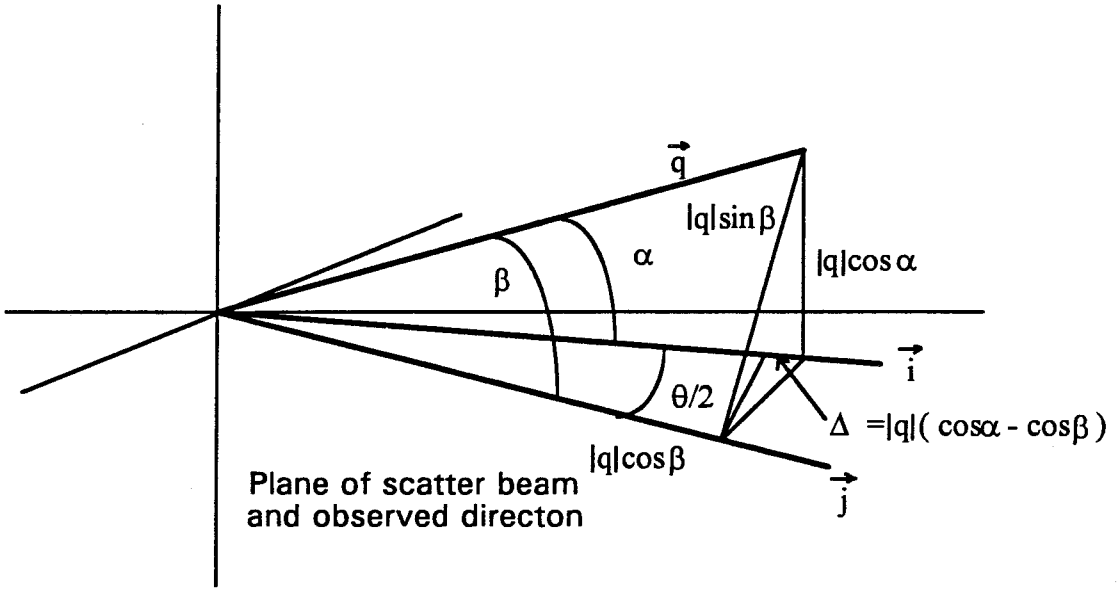

FIG. C.2. Projection of Water Particle Velocity $\vec{q}$ in directions $\vec{i}$ and $\vec{j}$.

Figure C.2 shows the relative difference Δ of the projection of $\vec{q}$ on $\vec{i}$ and $\vec{j}$. The angle of the water particle velocity to the unit vector $\vec{j}$ is given by β. By observation, it is obvious that the projection of $\vec{q}$ on $\vec{i}$ and $\vec{j}$ is identical ($\Delta = 0$) when $\vec{q}$ lies directly above the bisector of the angle $\theta/2$. The greatest difference between $|q|\cos\alpha$ and $|q|\cos\beta$ will occur when $\vec{q}$ lies on the plane of $\vec{i}$ and $\vec{j}$ so that $\vec{q}$ is outside the $\theta/2$ angle (shown in Figure C.3).

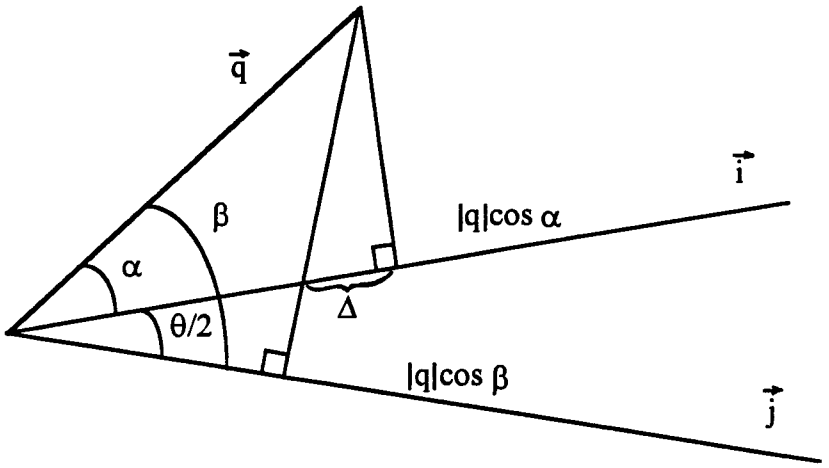

FIG. C.3. Geometry for Maximum Error in Doppler Analysis.

To determine the magnitude of Δ, select the worst case of $\alpha + \theta/2 = \beta$.

$$\begin{aligned}\Delta &= |q|[\cos\alpha - \cos(\alpha + \theta/2)] \\ &= |q|(\cos\alpha - \cos\alpha\cos\theta/2 + \sin\alpha\sin\theta/2)\end{aligned} \tag{C.4}$$

The present Laser Doppler system is configured with $\theta \approx 3°$ so that

$$\Delta = |q|(.0014\cos\alpha + .0523\sin\alpha) \tag{C.5}$$

Maximizing this expression with respect to the angle α:

$$-.0014\sin\alpha + .0523\cos\alpha = 0 \Rightarrow \tan\alpha = 37.36,\ \alpha = 88.5° \tag{C.6}$$

So the maximum possible error in Δ is

$$\frac{\Delta}{|q|} = 0.0523 \approx 5\%. \tag{C.7}$$

This maximum occurs when the water particle velocity vector is traveling in a path perpendicular to $\vec{j}$ (direction of $-\vec{e}_i$). With the current laser configuration this direction is across the width of the tank. Since the generated flows are plane flows; errors of this

magnitude can only occur at very low water particle velocities where the cross tank component of the velocity may be a significant portion of the total velocity.

APPENDIX D

DERIVATION OF ROTATION TIME FOR SPHERICAL PARTICLE

The rate of rotation of a particle resting on a bed of similar particles is governed by the net excess of the overturning moment due to hydrodynamic forces over the restoring moment due to self weight. For a spherical particle, the equations for these moments, as

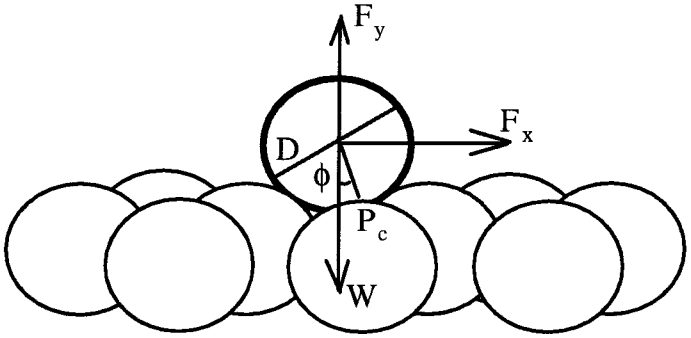

FIG. D.1. Schematic for particle resting on bed of particles.

presented in Chapter 4, are:

$$\text{Overturning Moment,}\quad M_H = F_x \frac{\alpha_m D}{2}\cos\varphi + F_y \frac{\alpha_m D}{2}\sin\varphi \tag{D.1}$$

$$\text{Restoring Moment,}\quad M_R = W\frac{\alpha_m D}{2}\sin\varphi \tag{D.2}$$

Here, as in Chapter 4, F_x and F_y are the horizontal and vertical components of the hydraulic force, W is the submerged particle weight, φ is the contact angle of the particle to the bed (estimated to be 30 degrees), and α_m (estimated to be 0.86) is based on the particle bed geometry. The applied forces for a sphere are:

$$F_x = \frac{1}{2}\rho C_D \frac{\pi D^2}{4} u^2 + \rho C_m \frac{\pi D^3}{6}\frac{du}{dt} \tag{D.3}$$

$$F_y = \frac{1}{2}\rho C_D \frac{\pi D^2}{4} v^2 + \rho C_m \frac{\pi D^3}{6}\frac{dv}{dt} + \frac{1}{2}\rho C_L \frac{\pi D^2}{4} u^2 \tag{D.4}$$

The angular acceleration $\ddot{\varphi}$ of the center of mass of the spherical particle is

$$M_H - M_R = -I\ddot{\varphi} \tag{D.5}$$

where I is the moment of inertia about the contact point,

$$I = \frac{2}{5}mr^2 + mr^2, \qquad \text{where} \quad m = \frac{4}{3}\pi r^3 (\rho_s - \rho). \tag{D.6}$$

Angular acceleration is negative since the angle φ is decreasing in the direction of motion.

Method 1

As a first order approximation one may assume that the net moment on the particle remains constant during the time of rotation. The linear acceleration at the center of mass of the sphere is then $-r\ddot{\varphi} = \frac{r(M_H - M_R)}{I}$ and the time, t, for the center of mass to travel the distance $-r\varphi$ (from $\varphi = 30°$ to the vertical) is:

$$t = \sqrt{\frac{2r\varphi}{r\ddot{\varphi}}} = \sqrt{\frac{2\varphi I}{M_H - M_R}} \tag{D.7}$$

This time for rotation is only approximate since as φ changes, the contributions of the vertical and horizontal applied forces as well as the contribution of the submerged weight of the particle also change. Since the net moment on the particle increases with decreasing contact angle, the time of rotation calculated by this method can be considered as an upper bound for the actual time it takes for a particle to rotate from φ_0 to the vertical.

Method 2

In order to incorporate the effects of the changing contact angle φ into the time of rotation, it is necessary to express the net moment in terms of the x and y direction force components:

$$-I\ddot{\varphi} = \frac{\alpha_m D}{2}\left[F_x \cos\varphi + (F_y - W)\sin\varphi\right]. \tag{D.8}$$

Let $C_1 = \dfrac{\alpha_m D}{2I}$, so

$$\ddot{\varphi} + C_1 \left[F_x \cos\varphi + \left(F_y - W \right) \sin\varphi \right] = 0 \qquad \text{(D.9)}$$

It is convenient to express the forces in polar form:

Let $F_x = C_2 \sin\beta, \quad F_y - W = C_2 \cos\beta$

$$\beta = \tan^{-1}\left(\frac{F_x}{F_y - W} \right), \quad C_2 = \sqrt{F_x^2 + \left(F_y - W \right)^2} \qquad \text{(D.10)}$$

Substituting into equation (D.9),

$$\ddot{\varphi} + C_1 C_2 \left[\cos\varphi \sin\beta + \sin\varphi \cos\beta \right] = 0. \qquad \text{(D.11)}$$

The quantity in parentheses can be expressed as the sum of two angles:

$$\ddot{\varphi} + C_3 \left[\sin(\varphi + \beta) \right] = 0, \quad C_3 = C_1 C_2. \qquad \text{(D.12)}$$

If we assume that $F_X, F_y \neq f(\varphi, t)$ so that $\beta \neq f(\varphi, t)$, then

$$\varphi' = \varphi + \beta , \qquad \frac{d\varphi'}{dt} = \frac{d\varphi}{dt}$$

and

$$\ddot{\varphi}' + C_3 \sin\varphi' = 0. \qquad \text{(D.13)}$$

To integrate,

set $\xi = \dot{\varphi}'$, $\quad \dfrac{d\xi}{dt} = \dfrac{d\xi}{d\varphi'} \dfrac{d\varphi'}{dt} = \xi \dfrac{d\xi}{d\varphi'}$

This yields

$$\xi \, d\xi + C_3 \sin\varphi' \, d\varphi' = 0. \qquad \text{(D.14)}$$

Integrating and applying the initial conditions $\varphi'(0) = \varphi_o'$ and $\dot{\varphi}'(0) = 0$,

$$\frac{\dot{\varphi}'^2}{2} - C_3 \cos\varphi' = -C_3 \cos\varphi_0' . \tag{D.15}$$

Solving for $\dot{\varphi}$ (choose the negative root since φ is decreasing) and integrating:

$$-\int_{\varphi_o'}^{\beta} \frac{d\varphi'}{\sqrt{\cos\varphi' - \cos\varphi_0'}} = \int_{\beta}^{\varphi_o'} \frac{d\varphi'}{\sqrt{\cos\varphi' - \cos\varphi_0'}} = \sqrt{2C_3}\int_0^t dt. \tag{D.16}$$

The integral on the left of equation (D.16) cannot be solved in terms of elementary functions but falls under the classification of an elliptic integral of the first kind:

$$F(k,\varphi') = \int_0^{\varphi} \frac{d\varphi'}{\sqrt{1 - k^2 \sin^2\varphi'}} \quad (0 < k < 1) \tag{D.20}$$

In order to express the integral in (D.19) in the above form, make the substitution:

$$\cos\varphi' = 1 - 2\sin^2(\varphi'/2)$$

This results in

$$\int_{\beta}^{\varphi_0'} \frac{d\varphi'}{\sqrt{2\left(\sin^2(\varphi_0'/2) - \sin^2(\varphi'/2)\right)}} = \sqrt{2C_3}\, t, \tag{D.21}$$

which may be rewritten as

$$\frac{k}{\sqrt{2}} \int_{\beta}^{\varphi_0'} \frac{d\varphi'}{\sqrt{1 - k^2 \sin^2(\varphi'/2)}} = \sqrt{2C_3}\, t, \quad \text{where } k = \frac{1}{\sin\left(\varphi_o'/2\right)}. \tag{D.22}$$

Letting $\psi = \varphi'/2$ and $\psi_0 = \varphi_0'/2$, then $d\psi = \frac{1}{2}d\varphi'$, and

$$k \int_{\beta/2}^{\psi_o} \frac{d\psi}{\sqrt{1 - k^2 \sin^2\psi}} = \sqrt{C_3}\, t \tag{D.23}$$

This is in the desired form, however, $k > 1$.

As a final step,

Let $k \sin\psi = \sin\chi$, $k\cos\psi\, d\psi = \cos\chi\, d\chi$. Equation (D.23) becomes

$$k \int_{\sin^{-1}(k\sin\beta/2)}^{\chi_o} \frac{\cos\chi\, d\chi}{k\cos\psi\sqrt{1-\sin^2\chi}} = \int_{\sin^{-1}(k\sin\beta/2)}^{\chi_o} \frac{d\chi}{\cos\psi}$$

$$= \int_{\sin^{-1}(k\sin\beta/2)}^{\chi_o} \frac{d\chi}{\sqrt{1-\frac{\sin^2\chi}{k^2}}} = \sqrt{C_3 t} \qquad \text{(D.24)}$$

and reduces to the desired form:

$$\int_{\sin^{-1}(k\sin\beta/2)}^{\chi_o} \frac{d\chi}{\sqrt{1-(\sin\varphi_o'/2)^2(\sin^2\chi)}} = \sqrt{C_3}\, t. \qquad \text{(D.25)}$$

Substituting into the elliptic integral format

$$t = \frac{1}{\sqrt{C_3}}\left\{F\left[\sin\left(\varphi_o'/2\right), \sin^{-1}\left(k\sin\left(\varphi_o'/2\right)\right)\right] - F\left[\sin\left(\varphi_o'/2\right), \sin^{-1}\left(k\sin\left(\beta/2\right)\right)\right]\right\} \qquad \text{(D.26)}$$

which can be simplified as:

$$t = \frac{1}{\sqrt{C_3}}\left\{F\left[\sin\frac{\varphi_o'}{2}, \frac{\pi}{2}\right] - F\left[\sin\frac{\varphi_o'}{2}, \sin^{-1}\left(\frac{\sin\frac{\beta}{2}}{\sin\frac{\varphi_o+\beta}{2}}\right)\right]\right\}, \quad \textit{for} \quad C_3 = \frac{\alpha_m D}{2I}\sqrt{F_x^2 + (F_y - W)^2}$$

$$\text{and} \quad \varphi_o' = \left(\varphi_o + \tan^{-1}\left[\frac{F_x}{F_y - W}\right]\right) \qquad \text{(D.27)}$$

Example:

For the case of the 5 mm sphere as presented in chapter 4, choose two sets of forces which both result in a net positive moment. The estimated rotation times are as follows:

	Case I	Case II
F_x (dynes)	150	300
F_y (dynes)	0	180
W (dynes)	96	96
M_H(dyne-cm)	27.9	75.2
M_R(dyne-cm)	10.3	10.3
I (g-cm^2)	0.0085	0.0085
φ_o	30°	30°
t by Method 1	0.022 sec	.0118 sec
β	-57.4°	74.4°
$\varphi_o'/2$	-13.7°	52.2°
C_3	4502	7882
F[k, π/2] - F[k,β/2]	1.68 - 0.51****	1.96 - 0.92
t by Method 2	0.017 sec	0.0117 sec

Table D.1. Example of Rotation Times for a Spherical Particle.

It appears from this analysis, that Method 1 is fairly accurate when the restoring moment is small compared to the overturning moment. When the two moments are only slightly out of balance, the change in moment due to change in the contact angle (Method 2) must be considered.

**** Note that for Case I where $\beta < -\varphi$, the substitution $k \sin\beta/2 = \sin\chi$ cannot be made since the ratio $\dfrac{\sin \beta/2}{\sin \varphi_o'/2}$ is greater than unity. For cases where $\beta < -\varphi$, the solution for rotation time is:

$$t = \frac{1}{\sqrt{C_3}} \left\{ F\left[\sin\frac{\beta}{2}, \frac{\pi}{2} \right] - F\left[\sin\frac{\beta}{2}, \sin^{-1}\left(\frac{\sin\dfrac{\varphi_o + \beta}{2}}{\sin\dfrac{\beta}{2}} \right) \right] \right\}, \qquad \text{(D.27a)}$$

with φ_o' and C_3 defined as before.